Simple Scalable Superstrate Cells with Good Thermal Stability and High Voc

Davies-Brenchley, Kaya

Award date:
2023

Awarding institution:
University of Bath

Simple Scalable Superstrate Cells with Good Thermal Stability and High V_{oc}

Kaya E. Davies-Brenchley

A Thesis submitted for the degree of Doctor of Philosophy

University of Bath

Department of Chemistry

February 2023

Copyright

Signature of Author: 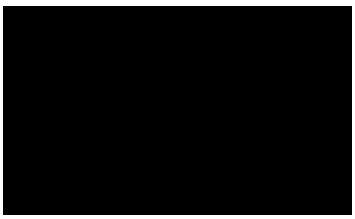

Kaya Davies-Brenchley

Declaration of any previous submission of the work

The material presented here for examination for the award of a higher degree by research has / has not been incorporated into a submission for another degree.

Declaration of authorship

I am the author of this thesis, and the work described therein was carried out by myself personally, with the exception of the XPS measurements in Chapters 5 and 6, which were carried at the EPSRC National Facility for XPS (‘HarwellXPS’), operated by Cardiff University and UCL, under contract No. PR16195.

Kaya Davies-Brenchley

Acknowledgements

First of off I must thank my supervisor Petra for a) offering me a PhD position in the first place and b) for her support over the last 4 years. I am grateful for all of your help and for reassuring me every couple months, when I had a meltdowns, that things were okay and that I wouldn't fail.

I would also like to thank the whole Cameron group (past and present members), but especially Matt P, Matt C, Rob, Philippa and Celine. Thank you for providing friendship, laughs and support in equal measures.

Next, I thank the PVCDT for the opportunities they have provided me with through my PhD and the ongoing Covid support. Also to the whole of C5 – I had the best first year of my PhD, making good friends, memories, seeing a good chunk of England, getting drunk and eating good food.

I owe huge thanks to my family and friends, old and new. Thank you to Abbie, Helen, Anna and Mollie for always encouraging me (not only throughout my PhD, but also for the last 10 ish years) and for having excellent pets I could use as emotional support animals. Thanks for providing fun and for listening to my moaning and general grumpiness throughout this time, I owe you many, many drinks. Thanks to Helena Dodd, for providing encouragement from afar, I am glad we have both made it through our PhDs. Emily and Liam also deserve a shout out for becoming excellent new friends. I enjoyed our constant swap of baked goods and pub trips whilst you were living in Bath, and boardgames and craft beer/wine nights were always an excellent weekend distraction.

To my Mum and Dad – thanks for the support (financial and otherwise), throughout this period of my life. Thank you for putting up with me living at home throughout the writing period, I know it was hard.

Finally, the biggest thank you in the universe goes to my fiancé George. Without you, I really would not have made it to the end. Thanks for putting up with the crying, the grumpiness and incessant worrying. Thanks for proof reading everything I have written - you may be one of only 4 people that will possibly read this thesis. Thank you for me providing some huge amounts of joy, adventure and laughs, despite me often struggling to enjoy my PhD.

Abstract

Perovskite solar cells (PSCs) have attracted immense attention since they first came to light in 2010. They have demonstrated extraordinary performance, with efficiencies increasing from 3.8 % to > 25 %, in a short space of time. The success of PSCs can be related to their excellent optoelectronic properties and facile, low-cost fabrication processes. However, the main issue preventing the widespread use of perovskite devices is their instability to air and moisture. The all-inorganic $CsPbBr_3$ perovskite, possesses features that make it considerably more stable than then commonly used perovskite absorber materials, which often contain organic cations. Furthermore, $CsPbBr_3$ has a large band gap (2.3 V) thus only visible light with a wavelength of ≈ 530 nm or higher can be absorbed and used to generate charge carriers. Consequently, the Power Conversion Efficiency (PCEs that) can be achieved by $CsPbBr_3$ based PSCs are significantly lower than the leading PSC devices in the field; the top $CsPbBr_3$ devices have reached efficiencies of ≈ 11 %.

Whilst the large band gap of $CsPbBr_3$ renders these devices less suitable for direct light to energy conversion, it bestows them with other useful properties, such as being able to achieve high V_{OC} values (> 1.4 V) using carbon based $CsPbBr_3$ devices. This is greater than the required thermodynamic potential for water oxidation of 1.23 V. This offers $CsPbBr_3$ PSCs applications as photoanodes for water splitting. Consequently, this paves the way for PSCs to potentially be used to produce solar fuels such as hydrogen gas. Previously, $CsPbBr_3$ based PSCs have been encapsulated using a commercially available Graphite Sheet (GS), functionalised with an iridium-based water oxidation catalyst (WOC) on the surface. Whilst $CsPbBr_3$ has increased air and heat stability, it is still unstable to moisture and will degrade when exposed to water. Thus, operating $CsPbBr_3$ based photoanodes for water oxidation, in direct contact with water, remains a challenge.

Expanding on previous work, three strategies for the improvement of$TiO_2|CsPbBr_3|$Carbon|GSWOC photoanodes were identified: i) Improving the V_{OC} of the planar $CsPbBr_3$ devices used, to increase the photovoltage and reduce the amount of external bias required for water oxidation to occur. ii) Increasing the WOC loading on the surface of the GS to help increase the amount of water oxidation and thus the photocurrent produced. iii) Improving the encapsulation of the $CsPbBr_3$ photoanode to extend the lifetime of the device in aqueous conditions.

Overall, the methods used for increasing the concentration of the WOC on the surface of the GS appeared unsuccessful. However, the open circuit voltage of the planar carbon devices was improved to values often > 1.45 V. Furthermore, using an electrochemical flow-based system the lifetime of the device was successfully extended to over 550 h under operating conditions, which may be a record for the lifetime of a lead halide perovskite photoelectrode in direct contact with an aqueous solution under illumination

Contents

Acknowledgements 4

Abstract 5

Table of Abbreviations 10

Chapter 1. Introduction 13

1.1. Global Energy Needs and Issues 13

1.2. The Solar Resource 15

1.3. Solar cell Technologies 17

1.4. Perovskite Solar Cells Overview 21

1.4.1. PSC Device Architectures 22

1.4.2. Issues with PSCs 26

1.4.3. Cesium Containing Perovskite Solar cells 27

1.5. Hydrogen Production 29

1.5.1. Water Splitting 31

1.6. References 36

Chapter 2. Theory 46

2.1. Semiconductors 46

2.1.1. Recombination 48

2.2. The Fermi Level 50

2.2.1. Quasi Fermi Levels 51

2.3. The P-N Junction in Semiconductors 52

2.3.1. Impurities and Doping 52

2.3.2. Junctions 54

2.3.3. Junctions in Perovskite Solar Cells 57

2.4. Solar cell parameters and device analysis 59

2.4.1. Detailed Balance and the Shockley-Queisser Limit 63

2.5. Band Gap determination Via the Optical Measurements of Thin Films 64

2.5.1. Tauc Plots 68

2.6. Using semiconductors for Water Splitting 70

2.7. References.....76

Chapter 3. Experimental Methods.....79

3.1. $CsPbBr_3$ Thin Film Deposition and Solar Cell Fabrication Materials and Methods 79

3.1.1. FTO Glass Preparation.....79

3.1.2. c-TiO_2 Deposition.....79

3.1.3. m-TiO_2 Deposition.....79

3.1.4. SnO_2 Deposition.....80

3.1.5. $PbBr_2$ Deposition.....80

3.1.6. $CsPbBr_3$ Conversion.....80

3.1.7. Carbon electrode deposition.....81

3.1.8. B Site Substitution in $CsPbBr_3$.....81

3.2. $CsPbBr_3$ Devices for Water Oxidation.....81

3.2.1. $CsPbBr_3$ Device Encapsulation.....81

3.3. Characterisation methods.....83

3.3.1. X-ray Diffraction.....83

3.3.2. UV/Vis Spectroscopy.....83

3.3.3. Atomic Force Microscopy (AFM).....83

3.3.4. J-V Measurements.....83

3.3.5. Incident Photon to Current Efficiency (IPCE) Measurement.....84

3.3.6. Scanning Electron Microscopy (SEM) & Energy Dispersive X-ray (EDX).....84

3.3.7. Fourier-Transform Infrared Spectroscopy.....84

3.3.8. X-Ray Photoelectron Spectroscopy (XPS) Measurements.....84

3.4. Electrochemical Measurements.....85

3.4.1. Linear Sweep Voltammetry (LSV).....85

3.4.2. Cyclic Voltammetry (CV).....85

3.4.3. Chronoamperommetry.....86

3.4.4. Open Circuit Potential (OCP) and Photovoltage Measurements.....86

Chapter 4. Planar Carbon $CsPbBr_3$ Baseline Device Improvement.....87

4.1. Introduction 87

4.2. $CsPbBr_3$ Thin film deposition methods 89

4.3. Improvements to $CsPbBr_3$ Planar Carbon PSCs 98

4.3.1. ETL modification 98

4.3.2. Rinsing Step 102

4.3.3. $PbBr_2$ Annealing Temperature 106

4.4. Conclusions and future work 112

4.5. References 113

Chapter 5 Investigation into the Effects of Transition Metal Ions in $CsPbBr_3$ Planar Carbon Devices 117

5. Introduction 117

5.2. Partial Pb^{2+} Site Substitution with Metal Ions 120

5.2.1. UV/Vis Analysis 121

5.2.2. Analysis Using X-rays 122

5.2.3. AFM Analysis 128

5.2.4. Device Performance 133

5.3. Conclusion and Future Work 148

5.4. References 151

Chapter 6. Ir-Based Water Oxidation Catalyst Interactions with Graphite Surfaces 153

6.1. Introduction 153

6.2. WOC On Untreated 70 µm Thickness GS 156

6.2.1. UV/Ozone treated GS (70 µm) 161

6.2.2. Electrochemical GS (70 µm) Oxidation 163

6.2.3. Electrochemical and UV/Ozone GS (70 µm) Oxidation 168

6.2.4. TiO_2 modified GS (70 µm) Surface 170

6.2.5. Summary and Comparison of the GS (70 µm) Modification Methods 173

6.3. WOC On Untreated 25 µm Thickness GS 176

6.4. WOC On Untreated 160 µm Thickness GS 178

6.5. Summary and Conclusion 179

6.6. References 181

Chapter 7. New and Improved CsPbBr3 Photoanodes 184

7.1. Introduction 184

7.2. Improved $CsPbBr_3$ Photoanode Encapsulation for Water Oxidation 188

7.2.1. Water oxidation setup tests 189

7.2.2. Water Oxidation Long Term Performance Tests 193

7.3. Water Oxidation using GS with Surface modification 201

7.3.1. GS Without a Self-Adhesive Layer 204

7.4. Conclusions and Further Work 206

7.5. References 208

Chapter 8. Conclusion 210

Appendix 1. 214

Appendix 2. 220

Appendix 3. 235

Table of Abbreviations

A.M. 0	Air Mass 0
A.M. 1.5	Air Mass 1.5
AFM	Atomic Force Microscopy
AWE	Alkaline Water Electrolyser
CB	Conduction Band
CBM	Conduction Band Maxima
CE	Counter Electrode
CIGS	Copper Inidium Gallium Selenide
CIS	CuInSe2
CP*	Pentamethyl-cyclopentadienyl
c-TiO2	Compact TiO2
CV	Cyclic Voltammetry
DLS	Dynamic Light Scattering
DMF	Dimethyl Formamide
DMSO	Dimethyl Sulfoxide
EDX	Energy Dispersive X-Ray
EF	Fermi Level
Eg	Band Gap
EQE	External Quantumn Efficiency
ETL	Electron Transport Layer
FA	Formamidinium
FF	Fill Factor
FTIR	Fourier-transform Infrared Spectroscopy
FTO	Fluorine doped Tin Oxide
GDP	Gross Domestic Produce
GO	Graphene Oxide
GS	Graphite Sheet
HER	Hydrogen Evolution Reaction
het-WOC	Heterogeneous Water Oxidation Catalyst
hom-WOC	Homogeneous Water Oxidation Catalyst
HTL	Hole Transport Layer

IPA	Propan-2-ol
IPCC	Internation Panel on Climate Change
IPCE	Incident Photon to current Conversion Efficiency
ITO	Indium Doped Tin Oxide
Jsc	Short Circuit Current
LCAO	Linear Combination of Atomic Orbitals
Li-TFSI	bis(trifluoromethane)sulfonimide lithium salt
MA	Methyl Ammonium
MAPI	Methyl Ammonium Lead Bromide
MO	Molecular OrbitaL
MP	Maximum Power Point
m-TiO2	Mesoporous TiO2
NREL	The National Renewable Energy Laboratory
OCP	Open Cicuit Potential
OER	Oxygen Evolution Reaction
PS	Power Density
PCBM	Phenyl-C61-butyric acid methyl ester
PCE	Photon Conversion Efficiency
PEAI	Phenylethylammonium Iodide
PEC	Photoelectrochemical
PEDOT:PSS	Poly(3-hexythiophene-2,5-diyl):polystyrene sulfonate
PEM	Polymer Electrolyte Membrane
PSCs	Perovskite Solar Cells
PTAA	Poly[bis(4-phenyl)(2,4,6-trimethylphenyl)amine
PV	Photovoltaic
RDS	Rate Determining Step
RHE	Reversible Hydrogen Electrode
Rs	Series Resistance
RSH	Shunt Resistance
SHE	Standard Hydrogen Electrode
Spiro-OMeTAD	2,2',7,7'-Tetrakis[N,N-di(4-methoxyphenyl)amino]-9,9'-spirobifluorene
STH	Solar to Hydrogen
TCO	Transparent Conducting Oxide
TM	Transition Metal
UN	United Nations
UV	Ultra-Violet

UV360	2,2’-methylenebis(4-*ter*-octyl-6-benzotriazole phenol
VB	Valence Band
Vbi	Built In Bias
VBM	Valence Band Maxima
Voc	Open Circuit Voltage
WE	Working Electrode
WOC	Water Oxidation Catalyst
XPS	X-Ray Photoelectron Spectroscopy
XRD	X-ray Diffraction

Chapter 1. Introduction

1.1. Global Energy Needs and Issues

The world's energy demand is ever increasing; the annual increase in total global population and GDP is coupled with a large increase in the consumption of energy. [1] Currently, the largest global sources of energy are oil, coal and natural gas (Figure 1).

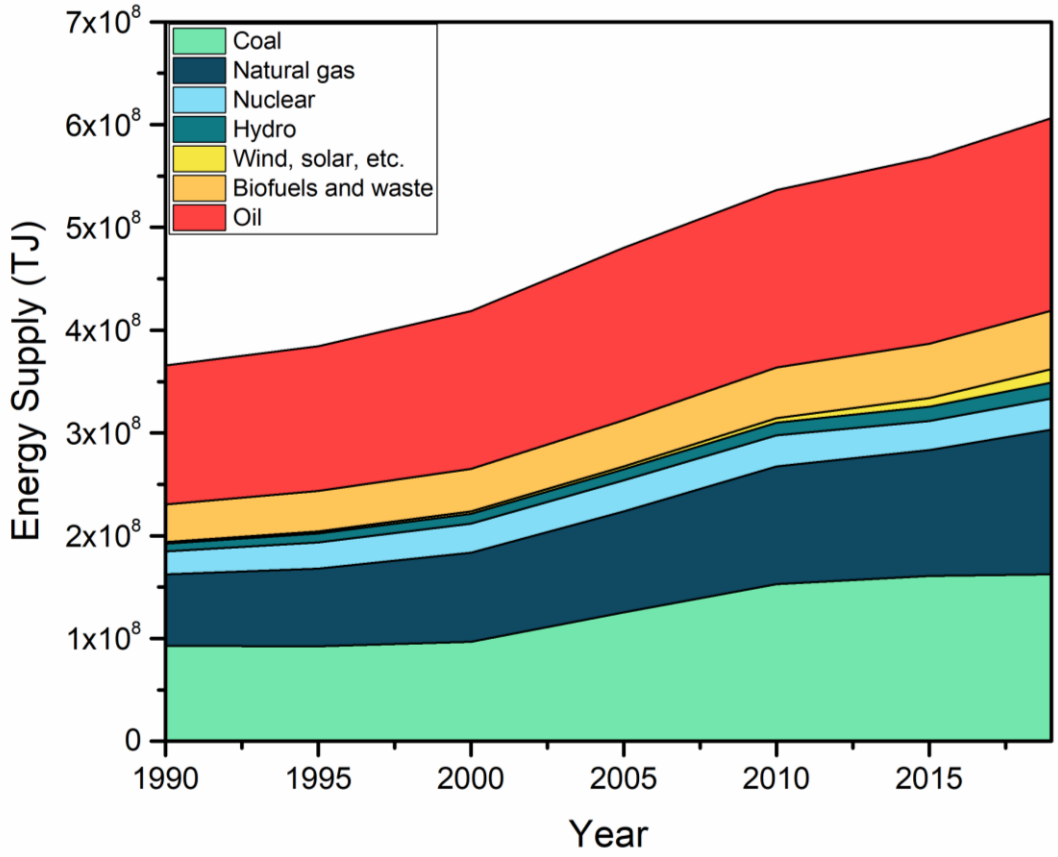

Figure 1: Total world energy supply by source from 1990-2019. Graph reproduced based on IEA data (2022), Energy Statistics Data Browser, All rights reserved. [2]

Oil, coal and natural gas are types of non-renewable energy sources, commonly referred to as *'fossil fuels'*. They are hydrocarbon containing fuel sources that have been formed naturally in the earth's crust from the remains of living organisms. These sources of energy are finite. Thus, the widespread use of non-renewable energy sources presents a global dilemma. Three key drivers that should encourage a shift in global energy usage towards renewable sources can be identified.

Firstly, it is necessary to increase the global energy supply, in order to keep up with the rapidly increasing energy demand; global primary energy demand increased by 5.8 % in 2021. [3] There are two main factors contributing towards this increase in demand; countries around the world are

becoming increasingly developed, causing an increase in transport and technology usage; and the rise in global population. According to the United Nations (UN), the total world population reached 7, 900, 000 in 2021 and is on course to reach over 9, 700, 000 by 2050. [4]

Secondly, there is a need to improve the global distribution of energy sources. Currently, in most parts of the world, there is a strong reliance on oil and gas imports from oil/gas rich regions. For example, in 2019 net imports of oil, gas and coal contributed towards 35 % of the UK's energy needs. [5] It is important to recognise that global conflicts can jeopardise the stability of energy imports. This was exemplified by the 2022 Russian invasion of Ukraine, which has led to Russia, the world's largest natural gas exporter, to restrict the export of its gas supplies to Europe. [6] An increase in the use of renewable energy sources would help to meet current and future global energy demand. There would be an alleviation of pressure to find new sources of fossil fuels, and the reliance on energy imports would be reduced by allowing a greater proportion of energy to be produced using a country's own resources. This would help improve overall global energy security.

Finally, there is an urgent need to reduce the rate of global heating. The importance of limiting the average global temperature rise to below 1.5 °C, in order to avoid the most catastrophic effects of climate change, has been highlighted by the International Panel on Climate Change (IPCC). [7] The IPCC's 2021 report noted that global heating, as caused by human emissions, has already reached an increase of 1.1 °C since 1750. The biggest effects of global heating include; sea level rise and an increase in severe weather patterns, leading to increased frequency of droughts, wildfires and extreme rainfall. [8] The use of fossil fuels is associated with the production of greenhouse gasses, such as CO_2, which are released into the atmosphere upon their combustion. Arrhenius first established the link between CO_2 emissions and the global temperature in 1896, highlighting at the time that fossil fuel usage should be limited. [9] Therefore, there is a great need to reduce our fossil fuel consumption to reduce the levels of atmospheric CO_2 and other greenhouse gasses, thus keeping global warming to a minimum.

Furthermore, a shift in energy source usage, away from fossil fuels, towards renewable sources, would contribute towards improved air quality and decreased environmental pollution. Energy is extracted from fossil fuels through combustion, releasing various gasses (e.g. CO_x, SO_x, and NOx) and various carbon particulates, such as ash and soot, into the air. Once in the air these pollutants can undergo secondary reactions, upon exposure to UV light or water, leading to the presence of other harmful pollutants, such as ground level ozone, peroxyacetyl nitrate and sulphuric and nitric acid. [10] This air pollution can cause damage to human health, animals, crops and structures. [11] In 2019, nearly 18 % of total deaths in India could be attributed to air pollution, with the majority of deaths being a direct cause of particulate matter pollution. [12] Health issues and deaths as a result of air pollution have economic consequences; disease, attributable to air pollution, can have a negative

effect on economic growth through reduced productivity and labour supply, and also through an increase in state health care expenditures. [12] This further highlights the need for the use of '*clean*' renewable energy sources.

Renewable energy sources include but are not limited to solar, wind, geothermal and hydro energy. The graph in Figure 1 shows that the proportion of use of these sources has increased since 1990; however, they still make up a small proportion of the total global energy usage.

The work in this thesis primarily focuses on solar energy. Theoretically, it would be possible to meet our current energy needs with solar energy as the primary renewable source. It has been determined that in order to satisfy global needs, approximately 0.1 % of Earth's surface would need to be covered with solar panels that had an light to photon conversions efficiency of 10 %. [13] However, whilst in theory this sounds trivial, Earth has a surface area of approximately 510, 064, 472 Km^2, [14] thus in reality 0.1 % of Earth's surface is a very large area, additionally, over 70% of Earth' surface is water, further limiting available space for solar panels. To be fully reliant on renewable energy, it is important to diversify our energy sources, meaning that it is important to consider a mixture of different renewable energy sources.

1.2. The Solar Resource

Energy from the sun has always been a fundamental resource for most natural processes on earth. In one hour, the sun can provide enough energy to the earth's surface, to meet the demands of the entire population on Earth, for one year, [15] therefore it seems obvious that we should attempt to harness this energy. The power density at the surface of the sun is calculated to be 62 MW m^{-2}; however, at the top of the Earth's atmosphere, this is reduced to 1353 W m^{-2}. As light passes through the Earth's atmosphere, it is scattered by molecules that are present in the atmosphere, resulting in a reduction in the power density at the surface, thus the surface of the Earth receives around 1000 W m^{-2} in energy from the sun. It also means that the spectrum of light that reaches the Earth's surface is vastly different to that at the top of the Earth's atmosphere. [16] The spectrum of light that reaches the top of the Earth's atmosphere is referred to Air Mass 0 (A.M 0) and the spectrum of light that reaches the surface is referred to as Air Mass 1.5 (A.M 1.5). Figure 2 shows the differences between A.M 0 and A.M 1.5.

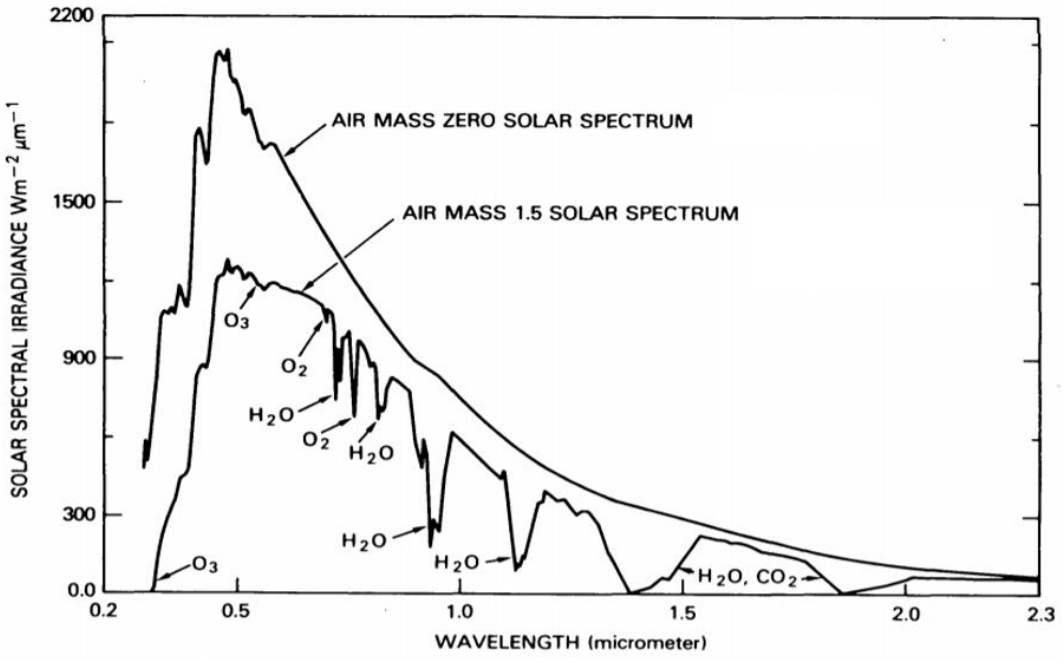

Figure 2: The A.M. 0 solar spectrum, received at the top of the earth's atmosphere, compared to the A.M 1.5 solar spectrum, received at the earth's surface. Image from NASA. [17]

Light with a wavelength of < 300 nm is filtered out by molecules in the atmosphere such as O_3 and N_2 which absorb the light at these wavelengths. The presence of H_2O, O_2 and CO_2 result in various other wavelengths of light also being filtered out by the atmosphere. [16] However, it is worth noting that the A.M. 1.5 spectrum corresponds to the sun being at a constant angle of elevation of 42 ° which is the standard spectrum received at temperate latitudes. Actual irradiances will also vary because of daily and seasonal changes in both the weather and the orientation of the earth with respect to the sun. [16] The A.M 1.5 spectrum radiation is often referred to as one sun radiation.

The term solar energy refers to any form of energy that can be obtained from the sun's electromagnetic radiation. As a result, this encompasses photovoltaic (PV), thermal and chemical energies. However, the work in this thesis predominantly focuses on PV. To most effectively harness the sun's energy, an ideal photovoltaic material should absorb visible light (≈ 350 – 700 nm) as this is where the solar irradiance is strongest at the Earth's surface. The most efficient solar energy collection is also achieved when the PV material is directly facing the sun, however in reality, if the device is fixed, it will not be facing the sun directly the majority of the time due to changes in the earths position relative to the sun throughout the day.

Finally, it is important to address the issue of energy storage. Solar energy can only be generated during the daytime, meaning in order to fully rely on solar energy as a resource, it is necessary to have the means to store the excess energy generated, so that power is available at night. There are a

range of energy storage mediums available including batteries, which store electrical energy as chemical energy. However, research is ongoing to improve battery technologies that have good volumetric energy density and are able to withstand the high cycling rates required for efficient use. [18] Pumped hydro storage can also be used for energy storage, where by during periods of low energy demand, electricity is used to pump water from a lower reservoir to an upper reservoir. When demand is high, the water can flow from the upper reservoir back to the lower one whilst turning turbines to generate electricity. The main advantage of this energy storage technique is that the technology is already available. There are many other energy storage methods; nonetheless, it is worth noting that the production of hydrogen using renewable electricity can also act as an energy storage method as this is discussed in section 1.5. [19]

1.3. Solar cell Technologies

Edmond Becquerel first reported the photovoltaic effect in 1839 when he observed that, upon shining light on a silver-coated platinum electrode immersed in an electrolyte solution, an electric current was produced. [20] Later in 1883, Charles Fritts constructed the first photoelectric module using a thin layer of selenium coated with a semi-transparent gold layer. It was observed that a continuous current was produced on exposure to not only direct sunlight, but also dim/diffuse daylight or even lamp light. [21] Despite these advances, the first silicon solar cell, with the well-known p-n junction, was not produced until 1954, and was reported with an efficiency of 6 %. [22] After this discovery, applications for these solar cells split into two categories; there was a small market for providing energy for powering toys, but a much bigger market for space applications. By 1971, 50 US satellites were launched into orbit, all equipped with silicon solar cells. [23] Over the following year, attempts at enhancing light absorption and reducing the recombination of charge carriers were successful and the efficiency of silicon solar cells increased rapidly; today the best silicon devices reach efficiencies over 26 %. [24] However, it is well accepted that there is scaling gap between lab scale devices and commercial devices and commercial technologies can be expected to reach 60 – 80 % of their laboratory record efficiency, [25] thus commercial silicon solar modules only reach around 15 % efficiency. [23] Silicon is extremely abundant within the Earth's crust, it is non-toxic and has a fundamental band gap of 1.1 eV at room temperature (Chapter 2.1); whilst this is not ideal band gap value of 1.39 eV, it is still within range for an effective solar semiconductor. [26] There are two main classes of silicon solar cells; single crystal and polycrystalline and although single crystal silicon cells can reach higher efficiencies, polycrystalline cells are less expensive to manufacture. Silicon technology largely dominates the market, making up for more than 90 % of solar cells produced. [27] The high purity silicon that is required for efficient solar cells originally led to high production cost of these devices, however, in recent years the average PV module price has dropped rapidly. [28] Prices

dropped from ≈ $0.80 /Wp in 2014 to ≈ $0.20 /Wp in 2020; this was in part due to a decline in manufacturing costs coupled with an increase in efficiency and module power. [29] The drop in price has meant that PV is becoming more accessible and can be rolled out further. Ongoing research into silicon solar cells focuses on a number of strategies to improve the efficiency of silicon solar cells and to further reduce manufacturing costs. For example, improving the optical surface properties of the silicon crystal by reducing the reflection of the light hitting the device, thus increasing the absorption of light into the cell. This is often done by texturing the front surface of the silicon or by applying anti reflection coatings. Other strategies include producing thinner silicon slices, using cheaper metal contacts and optimising the doping process, to reduce recombination and reduce series resistance. [23, 30, 31]

A range of alternative semiconductors also been developed for use in photovoltaic devices. The III-V class of semiconductors are commonly used; these semiconductors contain an alloy of atoms from group III and V in the periodic table. These materials are more effective optical absorbers than silicon as they have a direct band gap, as opposed to silicon, which has an indirect band gap. Gallium arsenide (GaAs) is a widely studied III-V semiconductor with a band gap of 1.4 eV and an absorption coefficient that is approximately 10 times that of silicon at visible wavelengths of light. [16] As a result, this meant that GaAs solar cells could be produced in 1976 with efficiencies of 22 %. [23] The impressive optical properties of GaAs result in a much thinner layer of semiconductor being required for solar cell applications, reducing the overall weight of the devices. GaAs devices also perform better at elevated temperatures than silicon does. Despite these advantages, high purity GaAs is expensive, and the resulting cost of GaAs solar cell production is greater than that of silicon, with the cost of GaAs devices reaching nearly 1000 times the price of silicon. [32] Consequently, there is a barrier to the use of GaAs as a widespread, commercially available technology, and the high fabrication costs mean GaAs is primarily used for space applications. [33]

As a result of single crystal materials being more expensive to produce, interest grew in finding semiconductors that were less expensive and could be processed more quickly. This led to the discovery of a number of thin film semiconductors materials that could be fabricated using existing chemical/physical deposition techniques. As a result, a number of polycrystalline PV technologies were produced. A polycrystalline material is composed of crystallites in which the semiconductor crystal grains are arranged at random orientations in relation to each other. Whilst polycrystalline semiconductors are less expensive to make, the presence of the grain boundaries can negatively affect the charge transport and recombination properties of the material.

$CuInSe_2$ (CIS) is a popular thin film material for solar cells with a direct bandgap and a high absorption coefficient. This material can be made in both p-type and n-type forms (see Chapter 2.3) and demonstrates stable electrical properties over a wide stoichiometric range. However, CIS has a

bandgap of 1.1 eV, which is below the ideal band gap value. Therefore, gallium can be partially substituted for indium, making copper indium gallium selenide (CIGS), to widen the band gap thus improving the PV performance of the devices, with the highest performing CIGS devices reaching 23.4 %. [34, 35]

Cadmium telluride (CdTe) is another popular thin film semiconductor material, which can also be prepared in n-type or p-type forms. It has an attractive band gap of 1.44 eV, within the ideal band gap range. [34] CdTe PV technology was commercialised by First Solar with lab scale devices that topped efficiencies of 22.1 %. [36] CdTe adopts the same crystal structure as GaAs, however, possess poorer transport properties and has toxicity issues. [34] These issues are outweighed by the inexpensive processing required.

Within the last decade, thin film solar cells, using materials with the perovskite crystal structure have gained much attention. The first lead-halide perovskite solar cell (PSC) devices were reported in 2009, achieving an efficiency of only 3.8 %. [37] However, since then efficiencies have soared and now stand at 25.7 % for a single junction lab scale device. [38] Perovskites are attractive materials as the bandgap can be tuned within the ideal band gap range by altering the ions and stoichiometry used. [39] Perovskites are also made from inexpensive, earth abundant materials and are easy to process. [40] Perovskite technology is in the process of being commercialised by Oxford PV for use in tandem with silicon solar cells. [41]

In further pursuit of the highest efficiency solar cells possible, attempts to overcome the 30 % Schockley-Queisser limit (see Chapter 2.4.1) have been investigated. These attempts include technologies such as: tandem/multi-junction devices to allow for a larger portion of sunlight to be absorbed; [42] the use of solar concentrators which collect and direct solar radiation towards a single focal point to increase the overall number of '*suns*' hitting the surface of the solar cells; [43] the use of up or down light conversion so that a greater range of the solar spectrum can be fully utilised; [44] and also the use of hot carrier solar cells. [45] However, these methods will not be explored in depth within this work.

The National Renewable Energy Laboratory (NREL) chart shown in Figure 3, demonstrates the advancements made in all PV technology from 1976 to present day, with the highest efficiency device being a four-junction or more, tandem cell with a solar concentrator reaching 47.1 %. Despite this, PSCs are the main focus of this thesis.

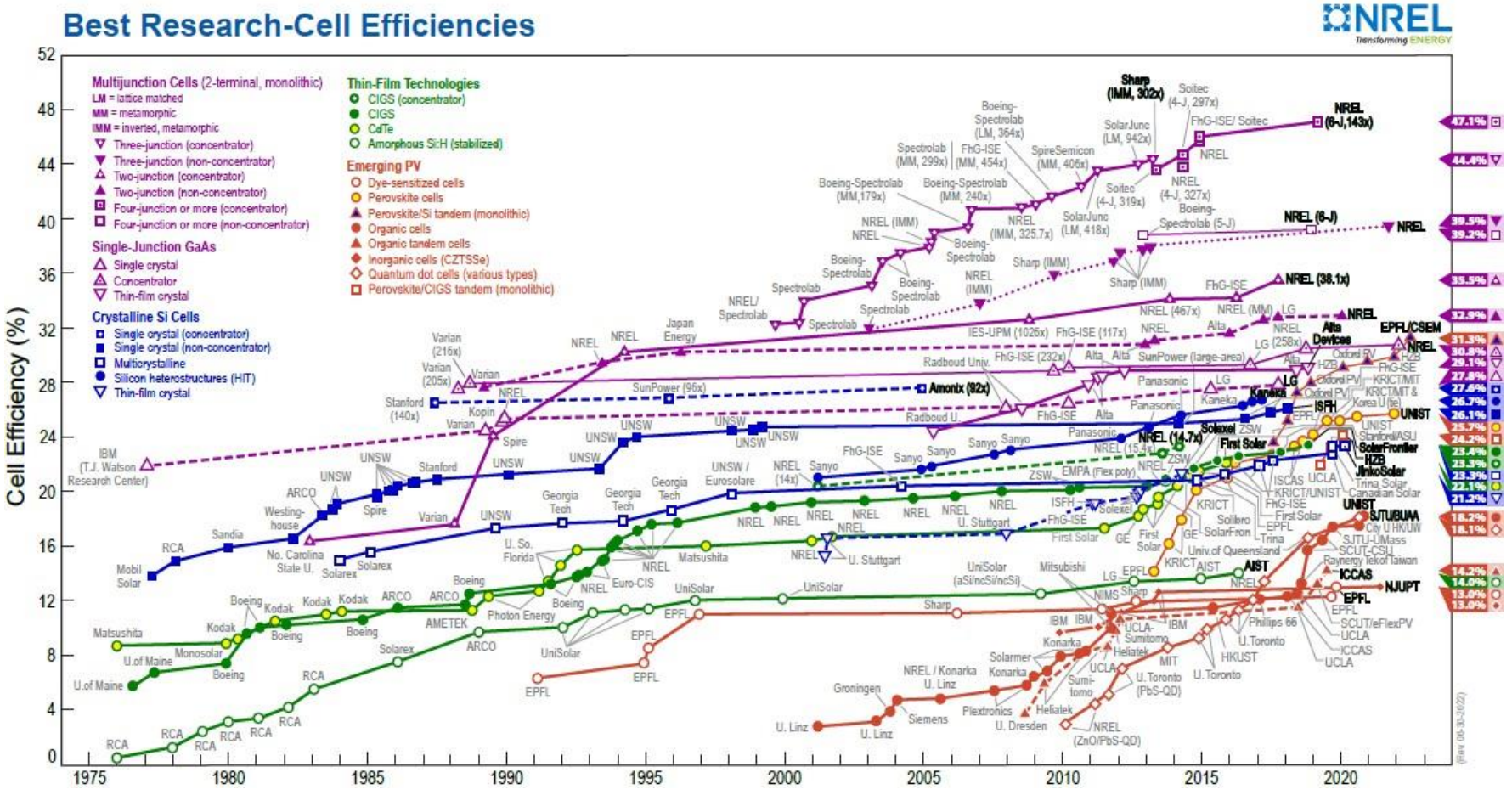

Figure 3: NREL best research-cell efficiency chart from 1976 – 2022. This plot is courtesy of the National Renewable Energy Laboratory, Golden, CO. [46]

1.4. Perovskite Solar Cells Overview

The term perovskite refers to the crystal structure of $CaTiO_2$, which has a cubic unit cell and the general formula ABX_3, whereby the A site is a monovalent cation, the B site is a divalent cation and the X site is a monovalent anion. In many materials with the perovskite structure, the X site is occupied by O; however, for perovskite materials that are used as solar absorber materials, the X site is usually occupied by a halide anion. The perovskite crystal structure is shown in Figure 4 and displays the interstitial A site cation between corner sharing BX_6 octahedra.

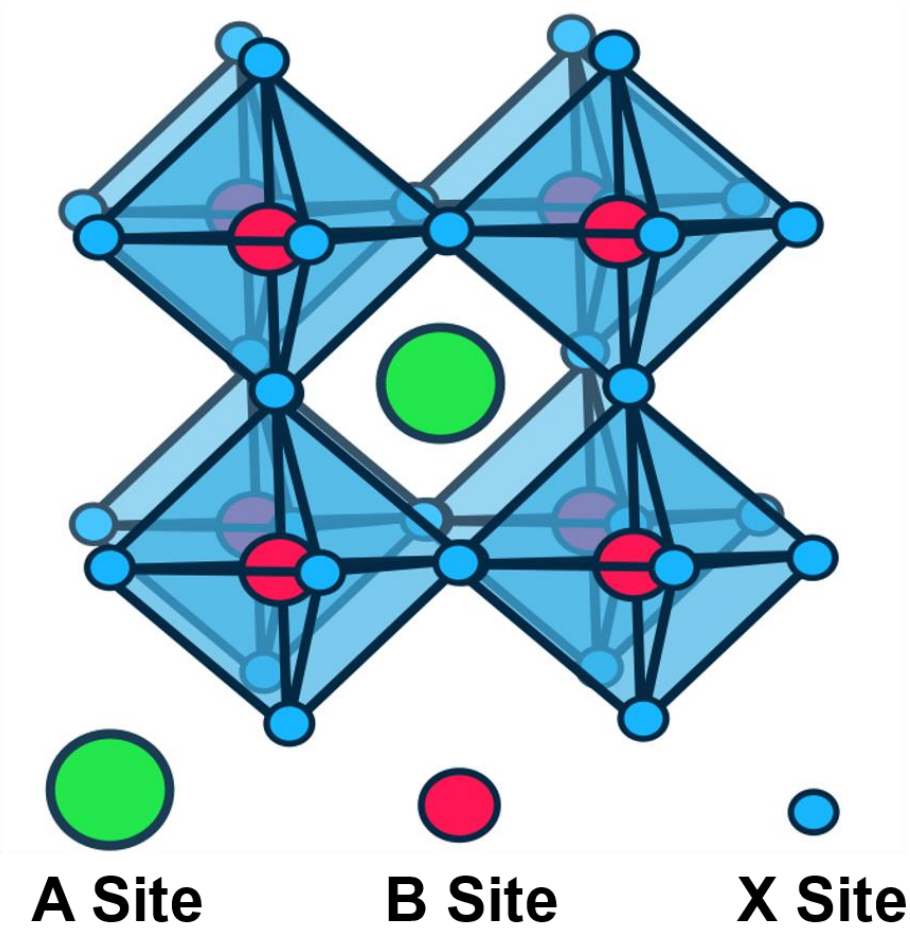

Figure 4: The perovskite crystal structure.

Popular materials used in PSCs contain Pb^{2+} cations on the B site and I^- anions on the X site. [47, 40, 48]

The Goldschmidt tolerance factor can be calculated using Equation 1 and can be used to geometrically assess whether the perovskite structure is able to form or not for a given chemical formula. [49]

$$t = \frac{r_a + r_x}{\sqrt{2}\,(r_b + r_x)}$$

(1)

The equation produces a value that is used determine whether or not the A site cation can fit within the cavities of the BX_6 octahedra. A value of between 0.8 – 1 indicates a perfect fit and the perovskite crystal structure will form. However, lower values of the tolerance factor will give less symmetric structures, with distorted pseudo perovskite structures often forming. [49] The equation was originally used to assess perovskite materials containing oxide or fluoride anions, which are small and highly electronegative anions. When considering systems containing larger and heavier halide anions, revised values of the ionic radii should be used, enabling the consideration of a greater range of materials for use in PSCs. [50]

The perovskites chosen as absorber materials in PSCs have a number of attractive optoelectronic properties that favour PV applications. They often display a sharp optical band gap with low Urbach energy values and it is possible to tune the band gap values throughout a broad range of wavelengths by altering the ratio of ions present in the material. [39, 40, 51] Lead halide perovskites possess low excition binding energies, on the thermal energy scale, allowing for facile charge carrier separation.[52] As a product of good carrier mobility and lifetimes, along with lower concentrations of trap densities, they have electron-hole diffusion lengths on the μm scale; this helps to increase charge extraction from the perovskite. [53] These materials are also attractive as they can be processed using a wide variety of methods, making them a versatile material with potential for upscaling the fabrication process. Methods that are commonly used for perovskite deposition include: spin coating, [54] chemical vapour deposition, [55] thermal evaporation, [56] dip coating, [57] and ink jet printing. [56]

1.4.1. PSC Device Architectures

There are a number of different device architectures that can be employed to make PSCs, and this allows flexibility in the range of materials that can be used. In order to make a successful device, the perovskite layer must be contacted with two different materials, with the appropriate band structures for light absorption and correct energy levels to enable the extraction of the photogenerated electrons and holes. As a result, most thin film solar cells, not just PSCs, are based on glass, coated with a transparent conducting oxide (TCO) material, such as fluorine doped tin oxide (FTO) or indium doped tin oxide (ITO). These materials must enable transmission of the solar spectrum so that the light can reach the absorber layer below.

They are important as they act as electrode materials, structural templates and diffusion barriers, as well as controlling the contact work function. [58]

The perovskite layer acts as an intrinsic semiconductor light absorber layer. A class of materials termed electron transport layers (ETL) and hole transport layers (HTL) are needed in PSCs to sandwich the perovskite layer; the ETL acts as an n-type layer and the HTL acts as p-type layer. The ETL requires the correct conduction and valance band alignment to allows for the extraction of photogenerated electrons from the perovskite and transports them towards the contact, whilst not allowing for the transport of the photogenerated holes. A range of different ETL materials can be used, such as metal oxides or organic materials. TiO_2 is the most commonly used metal oxide ETL and it can be used in either a thin compact planar layers or in a mesoporous layer. [59, 60] However, a thin planar layer of SnO_2 is also often used and boasts advantages over TiO_2 such as higher electron mobility, better stability and lower processing temperatures. [61] Organic ETL materials such as phenyl-C61-butyric acid methyl ester (PCBM) are also popular in inverted architecture devices. On the other hand, the HTL requires the correct band alignment to allow for the extraction of the photogenerated holes, whilst not allowing for the transport of the photogenerated electrons. The organic material 2,2',7,7'-tetrakis[N,N-di(4-methoxyphenyl)amino]-9,9'-spirobifluorene (Spiro-OMeTAD) is the most popular HTL for high performing PSCs, however it must first be doped with bis(trifluoromethane) sulfonimide lithium salt (Li-TFSI) to increase the conduction properties. [62] On the other hand, dopant free materials can also be used, for example poly(3-hexylthiophene-2,5-diyl): polystyrene sulfonate (PEDOT:PSS). Inorganic HTLs such as CuO or NiO_x are also reported; whilst these materials require much higher annealing temperatures, they are lower cost and often more stable. [63]

Most PSC devices today are solid state with planar heterojunctions. [53, 59] The ETL, perovskite layer and HTL can be arranged in different ways to achieve a range of PSC device architectures. Figure 5 shows three commonly used device architectures.

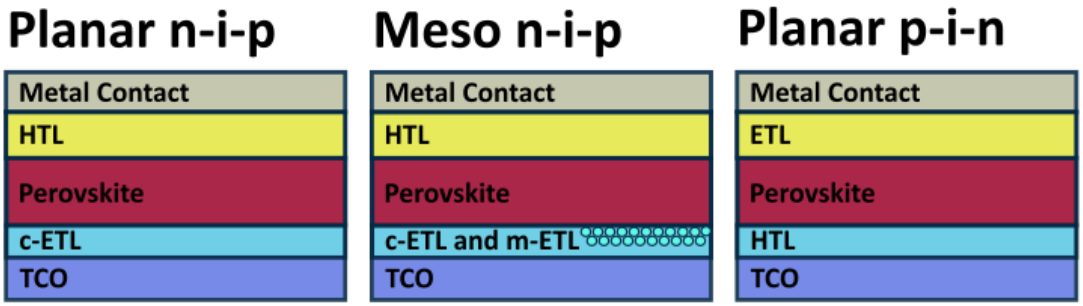

Figure 5: Common PSC device architectures. Planar n-i-p (regular) (left), mesoporous n-i-p (regular) (centre) and planar p-i-n (inverted) (right).

The regular, planar n-i-p architecture is the most commonly used device architecture. [53, 64] These devices start with a TCO, then employ an ETL, this is often accompanied by an added mesoporous layer of the ETL, before the perovskite absorber layer is added. The mesoporous ETL framework allows for increased contact between the ETL and the perovskite as the perovskite is able to infiltrate into the pores within the material. This can improve the perovskite grain size and increase electron extraction from the perovskite. [65] The HTL is deposited on top of the perovskite, before a metal contact is applied to enable charge extraction from the device.

The inverted, planar p-i-n, structures consist of a HTM deposited upon the TCO, followed by the perovskite absorber layer. The ETL is then deposited on top of the perovskite, before the metal contact is added. Low temperature ETLs are needed here, as many perovskites are unstable at high temperatures. The inverted device architecture has advantages such as lower fabrication costs, added stability and new solar cell applications, such as for use in flexible solar cells. [66] However, they have not managed to achieve the top efficiencies that can be achieved by the regular devices. [67]

1.4.1.1. Carbon Based PSCs

Carbon can be used as a counter electrode in PSCs to replace expensive noble metal back electrode materials such as silver and gold. They are suitable as they have similar work functions; for example carbon has a work function of – 5.0 eV whereas silver has a work function of – 5.1 eV. [68] Additionally, it was found that carbon could replace the expensive HTL materials as the work function is well aligned with the perovskite valence band for hole extraction. [69, 70] Other advantages of using a carbon electrode include the fact that it is a highly stable material, which is hydrophobic in nature, thus helping to protect the perovskite layer underneath from moisture and extending the lifetime of the device. [69] The carbon layer is often

screen printed or doctor bladed onto the perovskite layer in paste form, [71, 72] avoiding the need for energy intensive deposition techniques such as vacuum processing; this is advantageous for scale up purposes.

Carbon based PSCs can be prepared in two different manners, yielding either a planar or a mesoporous architecture. Figure 6 shows the differences between the planar and mesoporous carbon devices.

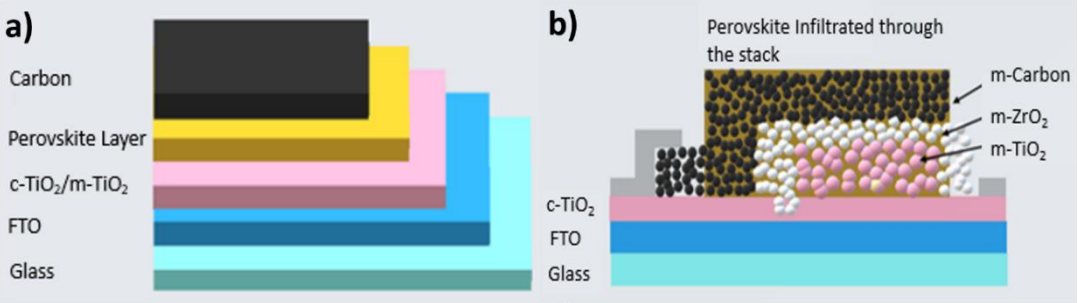

Figure 6: a) Example planar carbon device and b) example mesoporous carbon device architectures.

The planar carbon devices consist of an ETL deposited upon a TCO. The perovskite layer is then deposited directly onto the ETL (this can be just a compact layer or a compact and mesoporous layer), then finally the carbon layer is blade coated onto the perovskite layer. The mesoporous devices consist of a compact ETL layer deposited onto a TCO. Three subsequent mesoporous layers are then deposited on top of the compact ETL layer; a mesoporous ETL layer, an insulating spacer layer and then the carbon layer. The insulating spacer layer, in this example *m*-ZrO_2, is required to prevent contact between the HTL acting carbon and the ETL layers, ensuring better photogenerated charge separation. [71] Here the perovskite is dropped onto of the carbon layer after the mesoporous stack has been fabricated, and the perovskite will infiltrate into the holes in the mesoporous layers, all the way to the bottom of the stack. The size of the perovskite grains is determined by the size of the pores in the *m*-carbon layer. [71]

However, in most cases the carbon paste must be annealed at high temperatures in order to remove solvents and binder molecules from the paste to make it an effective conductor. [69, 71] This can pose issues for the fabrication of planar carbon PSCs, as many perovskite materials containing organic cations are not thermally stable enough to withstand the high temperatures required for the carbon annealing step. On the other hand, during the fabrication of the mesoporous carbon PSCs, all the layers in the device, including the carbon layer, must be annealed before the perovskite is introduced to the stack. As a result, the mesoporous carbon-based PSC architecture is more suitable for a wider range of materials. However, there are a growing number of low temperature carbon pastes that have been developed and it is also

possible to anneal the carbon layer using infrared radiation; this opens up the possibility of using other materials, which cannot withstand high temperatures, in the planar carbon PSC devices. [73, 74]

Unfortunately, the photon conversion efficiency (PCE) of carbon-based devices struggles to reach the high efficiencies reached by devices with more conventional HTLs. This is due to the fact that the carbon has high conductivity in the plane of the graphite sheet, but lower conductivity between carbon layers. The poor hole selectivity of the carbon and a poor contact between the perovskite layer and the carbon also contribute to the lower PCEs exhibited by carbon-based PSCs. [75]

1.4.2. Issues with PSCs

Despite the initial interest in PSCs and the high efficiencies that have been reported, PSCs are not without issues. The long-term stability of PSCs is a significant problem for the use of these devices. It is important that solar cells are able to function in atmospheric, everyday conditions, and many perovskite materials demonstrate an instability to oxygen and light. However, the biggest factor in perovskite degradation is moisture. Upon initial exposure to moisture, reversible hydrates of the perovskite are formed, but continued exposure to moisture and light causes irreversible damage and normally leads to full degradation of the perovskite back to the PbX_2 starting material. [76, 77] Moisture from the ambient atmosphere is enough to cause this irreversible degradation, hence many PSCs are fabricated in a dry, inert atmosphere and are further encapsulated before being exposed to ambient atmospheric conditions in an attempt to prolong the lifetime of the device. [67, 78]

A further issue is the hysteresis in the current-voltage characteristics of PSCs, which is a commonly reported phenomenon, not observed in other solar technologies such as silicon. [79, 80] Different amounts of hysteresis can be observed depending on the voltage scan rate used to measure the device. [81] This effect is now primarily attributed to the ion migration that occurs within the sample under the measurement conditions, [82] however, the hysteresis effect can be exacerbated by inefficient charge extraction at the interfaces. [65] Hysteresis makes determining the true performance efficiency of PSCs difficult and it has been argued that some practical guidelines on the measurement of PSCs should be established so that the effects can be better compared across different devices and laboratories. [83]

Finally, there are issues surrounding the toxicity of the materials used in PSCs. Lead is a well-known poisonous material and long term exposure to lead can cause a range of health issues, including anaemia, increased blood pressure, severe kidney damage, reduction in fertility and can result in death. [84] If PSCs were widely employed, it would be difficult to exclude the

possibility of lead leaking into the environment, even if rigorous encapsulation and strict recycling procedures were used. [85] The consensus is that the lead content in PSCs is low enough to be safe, however, substitutes for lead such as bismuth would provide a safer alternative and pose less of a risk. [86] Furthermore, there are concerns that the leaching of halide ions, particularly iodide, could have adverse effects on the environment. [87]

1.4.3. Cesium Containing Perovskite Solar cells

The very first PSCs used methyl ammonium lead iodide ($CH_3NH_3PbI_3$), commonly referred to as MAPI, as the perovskite absorber layer. The organic cation methylamonnium (MA) was used as the A-site cation in these PSCs, thus has subsequently been extensively researched. [37, 88, 89] MAPI has a band gap of 1.5 eV which is close to the value of the ideal band gap for efficient light absorption. [51] However, a range of other A site cations have also been investigated. Formamidinium (FA) is another organic A-site cation that has been well studied; $FAPbI_3$ devices have shown improved optoelectronic properties over MAPI. For example, it has a band gap of 1.48 eV, which is slightly closer to the ideal band gap. [40] Furthermore, the FA cation has a larger ionic radius of 2.79 Å compared to MA (2.70 Å), [90] thus allowing for the formation of a more symmetrical perovskite structure and allowing $FAPbI_3$ to be more thermally stable than $MAPbI_3$. [91] Single junction $FAPbI_3$ devices have reached efficiencies of up to 25.6 %. [92] Nonetheless, devices containing organic A site cations suffer from an instability to moisture, heat and light, which causes irreversible degradation to the perovskite layer, and decreases the overall performance of the devices. [77, 93] Recently most devices use a mixture of the MA^+ and FA^+ cations on the A site, along with Cs^+ as a third cation. This triple cation mixture is normally combined with a mixture of iodide and bromide anions on the X site, and these single junction devices have reached efficiencies of over 21 %. [90] Triple cation devices have increased in popularity, as adding a small amount of cesium to the organic A site cations has been shown to result in highly monolithic grains of more pure perovskite with increased stability, as well as fabrication being more reproducible. [90, 94, 95] Furthermore, whilst iodide remains popular as the X-site anion, mixed iodide/bromide compositions provide a range of benefits. Firstly, by increasing the amount of bromide in the sample, the band gap of the material increases, meaning that the band gap of the sample can be tuned to the desired application. [40] Additionally, increasing the bromide content can increase the stability of the sample to oxygen and light and even help supress ion migration in the samples. [96, 97]

Completely substituting the A site cation with the inorganic cation Cs^+, to make fully inorganic perovskite PSCs, such as $CsPbI_3$ or $CsPbBr_3$, can help overcome the instability issues discussed above. These perovskites have increased moisture and thermal stability and are able to withstand temperatures above 300 °C. [71] $CsPbI_3$ initially attracted a lot of attention as above

310 °C it forms a cubic black, perovskite phase material with a band gap of 1.73 eV. [98] These $CsPbI_3$ devices have reached efficiencies of over 18 %, [99] however, the black perovskite phase is unstable at room temperature in ambient conditions, where it readily undergoes a phase transition back into a yellow non-photoactive phase. [98] There have been many attempts to stabilise the black $CsPbI_3$ phase through the use of additives such as phenylethylammonium iodide (PEAI) or various polymers, [48, 100] yet the long term stability is still an issue for the widespread use of $CsPbI_3$.

$CsPbBr_3$ is another all-inorganic perovskite that is more stable than other perovskites such as $MAPbI_3$ and $CsPbI_3$. Unlike $CsPbI_3$ it does not undergo a phase transition at room temperature in ambient air. In fact, it is fully processable in ambient air as possesses good thermal stability. [71] The majority of work in this thesis focuses on $CsPbBr_3$ PSCs and their applications.

1.4.3.1. $CsPbBr_3$ PSCs

$CsPbBr_3$ has a Goldschmidt tolerance factor of 0.92, suggesting that it is able to form a cubic perovskite phase. In actuality, $CsPbBr_3$ crystallises in the orthorhombic (Pnma) space group at room temperature. Here the corner sharing $[PbBr]_6^{4-}$ octahedra are tilted, presenting a pseudo perovskite structure. However, $CsPbBr_3$ undergoes two phase transitions; one phase transition to a tetragonal crystal structure (P4/mbm) occurs at 88 °C, and a final transition to cubic system (Pm-3m) is observed at 130 °C. [101] $CsPbBr_3$ perovskites are more thermally stable, and can be heated to temperatures above 300 °C. [102] Heating to these temperatures can help remove any undesirable Cs_4PbBr_6 or $CsPb_2Br_3$ phases. [102] However, once cooled back to room temperature, the orthorhombic phase is the most stable. [102] Figure 7 shows how the $[PbBr]_6^{4-}$ octahedra are tilted in the orthorhombic phase.

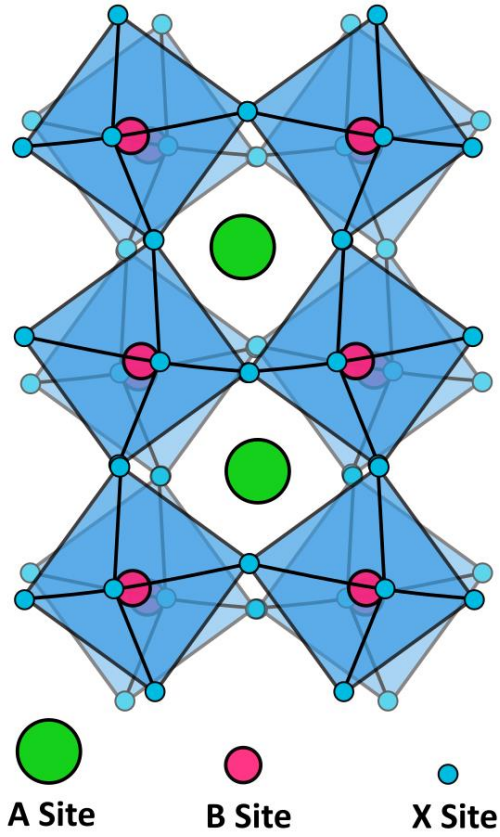

Figure 7: Orthorhombic Phase Perovskite Crystal Structure

$CsPbBr_3$ is a direct band gap semiconductor with a band gap of ≈ 2.3 eV at room temperature. [101, 103] $CsPbBr_3$ is yellow in colour and is a wide band gap semiconductor, with a band gap that is not close to the ideal band gap for efficient photon to electron conversion. This limits the efficiency of $CsPbBr_3$ devices and thus the most efficient devices only reach a PCE of ≈ 11 %. [104] On the other hand, as a result of this wide band gap, $CsPbBr_3$ devices are able to achieve a very large open circuit voltage (V_{OC}) and thus V_{OC}s greater than 1.3 V are regularly reported. [64, 104, 105] Reported methods for increasing the V_{OC} in $CsPbBr_3$ devices are discussed in detail in Chapter X. As a result of the wide band gap and large V_{OC}s, $CsPbBr_3$ PSCs have found potential applications in energy harvesting under indoor fluorescent lighting, [106] as well as in hydrogen production, through water splitting. [107]

1.5. Hydrogen Production

Hydrogen accounts for ≈ 90 % of all atoms in the universe and is the most abundant atom on earth. [108] Therefore alongside solar energy, hydrogen has the potential to form a part of a feasible solution to the global energy issues discussed in section 1.1. Hydrogen has a high energy density and, per weight, can produce three times more energy than methane or gasoline combustion, [109] demonstrating its potential as a reliable energy carrier. Despite this, it is

important to mention that hydrogen storage is a key issue. Whilst hydrogen has good energy density, a large amount of space is required for storage. Under normal storage conditions, the volume required for hydrogen storage is around 3000 times more than that required for gasoline providing an equivalent amount of energy. [110] Nonetheless, the combustion of H_2 produces only water vapour and therefore hydrogen has the potential to be one of the 'cleanest' sources of energy available. However, this is only true if the hydrogen is produced from renewable sources. Hydrogen can also be used as an energy storage medium to allow the storage of excess energy produced by renewable systems, such as solar power. Nonetheless, despite being the most abundant atom on earth, most of it is 'locked up' in a range of molecules such as water, hydrocarbons or hydrides, thus to obtain free H_2 that can be used for energy, it must be liberated from these sources.

Currently, most of the hydrogen produced comes from fossil fuels such as natural gas and oil. However, the majority of this hydrogen is not being used for energy purposes, but for purposes such as refining oil or in chemical industries to synthesise molecules such as ammonia. [111] Obtaining hydrogen from hydrocarbons can be done using a range of different methods such as steam reforming or partial oxidation reactions. [112] Steam reforming is advantageous as it does not require oxygen, can be performed at lower temperatures than partial oxidation and produces the product with the highest H_2 to CO ratio. Partial oxidation has advantages such as the fact it does not require a catalyst and it is less susceptible to sulphur poisoning than steam reforming, but results in a lower H_2 to CO ratio. Steam reforming is the most commonly used process for hydrogen production in industry. [113]

Hydrogen can also be produced by conversion from biomass; this is considered a more sustainable source of H_2 than that from fossil fuels. A large range of biomass resources can be used to produce hydrogen such as: crops, agricultural waste, forestry waste and community waste. The techniques used for H_2 production from biomass fall into two categories, thermochemical or biological. [112] These thermochemical processes involve heat and include: combustion, pyrolysis and gasification. The main aim of combustion is to produce heat or electricity through the direct burning of biomass. This electricity can then be used for the production of hydrogen using other methods. The main aim of pyrolysis is to obtain bio-oils or charcoal from the biomass, whereas the main aim of gasification is to obtain gaseous products, both of these products can then undergo the conventional hydrogen conversion techniques that is used for extraction of H_2 from fossil fuels. [112] Biological processes from biomass include fermentation, which uses anaerobic bacteria to break down the biomass. However, for fermentative processes the biomass that is used must be fully biodegradable and have a high carbohydrate content, therefore the sources of biomass that can be used are more limited and those such as pure sugars are preferred. [113]

1.5.1. Water Splitting

Given the fact it covers more than 70 % of the earth's surface, it could be argued that water is one of the most logical sources for large-scale hydrogen production. Hydrogen can be obtained from water using a range of processes such as electrolysis, thermolysis, thermochemical cycles and photolysis. [111] Water can be split into Hydrogen and oxygen gas thermally at temperatures above 2000 K, however, at 2000 K the degree of bond dissociation is only 1 %; this increases to 34 % at 3000 K. These high temperatures are due to the undesirable thermodynamic process of splitting water, which has a standard Gibbs free energy of 237 kJ/mol, [114] and means that the thermolysis of water is not a sustainable way of producing hydrogen from H_2O. [111] Thermochemical cycles can be used to reduce the temperatures required to split water in a more sustainable manner; typically the temperatures required are in the range of 700 – 2000 K. [115] Popular cycles include the two step zinc oxide cycle or the three step sulphur-iodine cycle. [116, 117] These thermochemical cycles perform water splitting through a repetitive series of chemical reactions. The chemicals used in the cycles are all recycled so that the only overall product of the reaction series is H_2 and O_2. However, using thermochemical cycles for the production of hydrogen is not as cost effective as other methods of hydrogen production and there are corrosion issues that need to be solved in order for this technique to be scaled up easily. [115]

The electrolysis of water refers to the process of passing an electric current through water to break the bonds in the H_2O molecules. This is performed in an electrochemical cell where H_2 gas forms at the cathode and O_2 gas is produced at the anode. Nicholson and Carlisle discovered the electrolysis of water in 1800 and the process has since been well studied. [108] In order for the hydrogen produced from water electrolysis to be sustainable, the electricity required to perform this must come from renewable sources. There are several main types of electrolysis systems for H_2 production. The alkaline water electrolyser (AWE) and the polymer electrolyte membrane (PEM) electrolyser are just two examples. The AWE consists of an anode and cathode, immersed in an alkaline solution, typically a KOH solution. This system requires a diaphragm to separate the electrodes and allow the transport of OH^- ions from one electrode to the other; the diaphragm also helps prevent the recombination of oxygen and hydrogen. The best industrial AWE systems can produce 1000 m^3/h of hydrogen. [118] However, drawbacks making the widespread scale up of this technology difficult, include a slow start up time, corrosion issues and complicated maintenance issues. [119, 118] The PEM electrolyser system consists of an anode and cathode separated by a polymer electrolyte membrane. The PEM typically is composed of Nafion ™, a sulfonated tetrafluroethylene based polymer, which allows the transport of protons from one electrode to the other. The

PEM electrolyser system has a faradaic efficiency of close to 100 %. Despite this, at present, the best systems can only produce 400 m^3/h of hydrogen. These systems also have high manufacturing costs, expensive metal electrodes and catalysts are also required. [119, 118]

1.5.1.2. Photocatalytic Water Splitting

It was discovered in 1972 that semiconductors can be used to split water without the need to apply external electric power. Fujishima and Honda found that when an electrochemical cell, in which a TiO_2 electrode was connected to a platinum back electrode, was illuminated with light, oxygen evolution occurred at the TiO_2 electrode and hydrogen evolution occurred at the platinum electrode. [120] This unlocked the potential to directly convert solar energy into chemical energy, in the form of hydrogen. Chemical fuels which are produced using solar energy are often termed solar fuels. [107] There are a number of routes for achieving solar powered water splitting; these are illustrated in Figure 8.

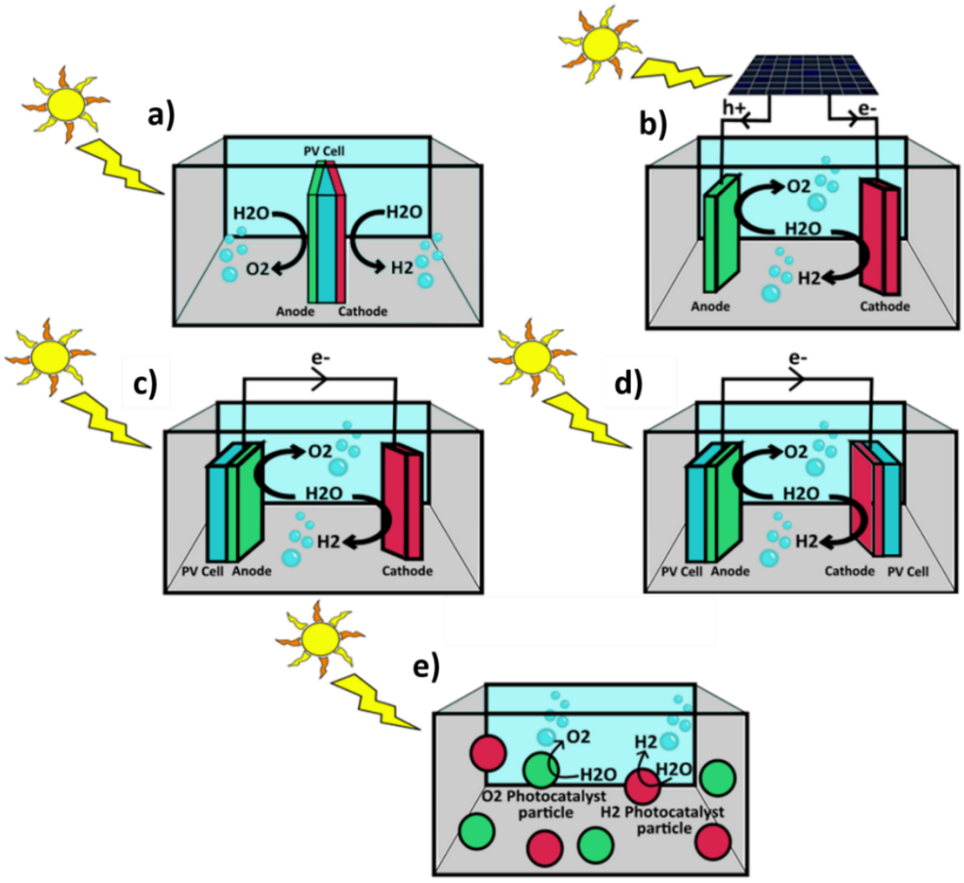

Figure 8: Schematic diagrams of different water splitting technologies a) fully integrated photovoltaic device for PEC (artificial leaf) b) non-integrated wired photovoltaic device with a separate anode and cathode c) partially integrated photoelectrode – electrode system d) unassisted partially integrated two photoelectrode system e) powdered photocalatylsts.

Generally, all of the photocatalytic water splitting systems, pictured in Figure 8, involve the generation of electrons and holes inside a semiconductor material, the electrons and holes are separated and transferred to the surface of the semiconductor, where they can be consumed by the water oxidation and reduction reactions.

The water splitting reaction is a thermodynamically uphill reaction, requiring a theoretical potential of 1.23 V. [121] However, due to the high kinetic barrier for oxygen evolution, additional potential, above the thermodynamic minimum, is required; this additional potential is termed the overpotential. Most industrial electrolysis cells use a potential between 1.8 – 2.0 V. In order to drive the water splitting reaction using solar energy, the semiconductor or solar cell used must generate a large enough voltage upon irradiation. Thus, most systems typically require the use of water oxidation and reduction catalysts to be applied at the surface, where water splitting is occurring, to reduce the amount of overpotential that must be applied. These catalysts are often based on expensive metals, for example platinum is widely regarded as the best water reduction catalyst, [122, 123] along with metal oxide compounds containing iridium or ruthenium for water oxidation. [124]

Water splitting can theoretically occur by using a single semiconductor or solar cell device as a light harvester, where upon irradiation, water oxidation occurs at the anode and water reduction at the cathode. These are fully integrated and wireless systems; they require no external potential and are driven only by solar light (Figure 8 (a)). They are inspired by photosynthesis and are often referred to as 'artificial leaves'. TiO_2 was a material first considered for this as it has a valance and conduction band edge that are appropriately placed for driving both the water oxidation and reduction reactions, However, TiO_2 has a large band gap of ≈ 3.2 eV and absorbs light mostly in the UV region. UV light only makes up around 5 % of the solar spectrum, thus under 1 sun irradiation, a solar to hydrogen (STH) conversion efficiency of < 1 % is achieved using wide band gap materials such as TiO_2. [125] Ye *et. Al.* achieved a higher STH of 4.3 % by employing a $BiVO_4$ photoanode with an organic semiconductor as the photocathode. [126] This method employs two different semiconductors in one device, allowing for the selection of semiconductors that have more appropriate band gaps for solar light absorption. These systems pose the most ideal structure for efficient water splitting as ohmic losses are reduced due to the fact that there is no need for long distance charge carrier transport though wires. However, these devices have not been studied in as great detail as the other systems, possibly due to complexities of the device fabrication. [127]

Water splitting using solar energy can also occur in the simplest form; energy can be generated directly from solar cells and this energy can be supplied to two non-photoactive electrodes, where the water oxidation and reduction reactions can occur. This is a non-integrated, hybrid

photovoltaic-photoelectrochemical system (Figure 8 (b)). These systems are capable of achieving some of the highest STH conversions efficiencies. For example, a tandem silicon solar cell, wired to a PEM reactor reached achieved a STH conversion efficiency of 18 %, however, this was with the use of a frensel lens to concentrate the sunlight to 500 suns. [128] A STH conversion efficiency of 17.6 % was achieved using a tandem silicon perovskite device, without a concentrator at 1 sun. [129] These systems avoid the need for water stable materials, meaning a greater range of materials can be considered and generally, the lifetime of these systems is longer.

Photoelectrochemical water splitting can be achieved by using a semiconductor or solar cell device as the light harvester in direct contact with the photoanode or cathode. This can be done using one device as the photoelectrode as pictured in Figure 8 (c), the photoelectrode is then connected through a wire to the counter electrode. Systems such as this include encapsulated perovskite solar cells, placed directly in the electrolyte. Wide band gap perovskites such as $CsPbBr_3$ work particularly well for these applications. However, even though these materials can reach voltages above 1.23 V, an externally applied bias is still required in order to reach the required potential for water splitting. [107, 130] Conversely, the system can also be set up with both a photoanode and photoelectrode, in a wired tandem system (Figure 8 (d)). These systems can achieve unbiased water splitting. Zhang *et al.* demonstrated unbiased water splitting over 120 h, with a STH efficiency of 3.24 % using a Mo-doped $BiVO_4$ photoanode and a Cu_2O based photocathode. [131] Park and co-workers, also demonstrated the potential of perovskite devices for water splitting in these systems. An unbiased system, using an encapsulated regular planar $FAPbI_3$ based perovskite for the photoanode and an encapsulated inverted $FAPbI_3$ based perovskite for the photocathode, was able to reach a STH efficiency of 10.65 %. [132] However, perovskites are highly unstable in water and currently issues with encapsulation mean that perovskites are not suitable for long-term water splitting applications in these partially integrated systems.

Finally, photocatalytic powders/particles can also be used for water splitting. These systems are the simplest and present the lowest cost solution for potential scale up. Here, photocatalyst powders are simply dispersed in water and irradiated with light. These systems often require the presence of an electron mediator species that is capable of transferring the photogenerated carriers between the H_2 and O_2 photocatalysts. [133] Suitable photocatalyst powders for H_2 evolution include doped $SrTiO_3$ powders, whilst $BiVO_4$ or WO_3 are suitable O_2 evolution photocatalysts. [134] Unfortunately, gas separation of the resulting H_2 and O_2 from these systems can be difficult, although the use of zeolite membranes has shown promise for providing a solution to this issue. [135, 136]

The work in this thesis focuses on the use of $CsPbBr_3$ photoanodes for use in partially integrated photoanode - electrode water splitting systems.

1.6. References

1 A. V. Komarova, I. V. Filimonova and A. A. Kartashevich, *Energy Reports*, 2022, **8**, 683–690.

2 IEA (2022), Energy Statistics Data Browser, https://www.iea.org/data-and-statistics/data-tools/energy-statistics-data-browser?country=WORLD&fuel=Energy supply&indicator=TESbySource, (accessed 9 September 2022).

3 BPstats, *BP Statistical Review of World Energy*, 2022.

4 U. N. Department of Economic and Social Affairs (Population Division), *World Population Prospects*, 2022.

5 Department for Business Energy & Industrial Strategy, *UK ENERGY IN BRIEF 2021*, 2021.

6 Nord Stream 1: Russia shuts major gas pipeline to Europe - BBC News, https://www.bbc.co.uk/news/world-europe-62732835, (accessed 21 September 2022).

7 V. Masson-Delmotte, P. Zhai, H.-O. Pörtner, D. Roberts, J. Skea, P. R. Shukla, A. Pirani, W. Moufouma-Okia, C. Péan, R. Pidcock, S. Connors, J. B. R. Matthews, Y. Chen, X. Zhou, M. I. Gomis, E. Lonnoy, T. Maycock, M. Tignor and T. Waterfield, *Global Warming of 1.5°C An IPCC Special Report*, 2018.

8 D. Qin, G. Plattner, M. Tignor, S. Allen, J. Boschung, A. Nauels, Y. Xia, V. Bex, P. Midgley, L. V Alexander, S. K. Allen Switzerland, N. Zealand, N. L. Bindoff, M. R. Allen, O. Boucher, D. Chambers and J. Hesselbjerg Christensen, *Summary for Policymakers in Climate Change 2013: The physical Science Basis, Contribution of the Working Group I to the Fifth Assessment Report of the Intergovernmental Panel on Climate Change*, Cambridge University Press, 2013.

9 S. Arrhenius, *Philos. Mag. J. Sci.*, 1896, **41**, 237–276.

10 J. Fuhrer, *Exp. 1995 413*, 1985, **41**, 286–301.

11 F. Barbir, T. N. Veziroğlu and H. J. Plass, *Int. J. Hydrogen Energy*, 1990, **15**, 739–749.

12 A. Pandey, M. Brauer, M. L. Cropper, K. Balakrishnan, P. Mathur, S. Dey, B. Turkgulu, G. A. Kumar, M. Khare, G. Beig, T. Gupta, R. P. Krishnankutty, K. Causey, A. J. Cohen, S. Bhargava, A. N. Aggarwal, A. Agrawal, S. Awasthi, F. Bennitt, S. Bhagwat, P. Bhanumati, K. Burkart, J. K. Chakma, T. C. Chiles, S.

Chowdhury, D. J. Christopher, S. Dey, S. Fisher, B. Fraumeni, R. Fuller, A. G. Ghoshal, M. J. Golechha, P. C. Gupta, R. Gupta, R. Gupta, S. Gupta, S. Guttikunda, D. Hanrahan, S. Harikrishnan, P. Jeemon, T. K. Joshi, R. Kant, S. Kant, T. Kaur, P. A. Koul, P. Kumar, R. Kumar, S. L. Larson, R. Lodha, K. K. Madhipatla, P. A. Mahesh, R. Malhotra, S. Managi, K. Martin, M. Mathai, J. L. Mathew, R. Mehrotra, B. V. M. Mohan, V. Mohan, S. Mukhopadhyay, P. Mutreja, N. Naik, S. Nair, J. D. Pandian, P. Pant, A. Perianayagam, D. Prabhakaran, P. Prabhakaran, G. K. Rath, S. Ravi, A. Roy, Y. D. Sabde, S. Salvi, S. Sambandam, B. Sharma, M. Sharma, S. Sharma, R. S. Sharma, A. Shrivastava, S. Singh, V. Singh, R. Smith, J. D. Stanaway, G. Taghian, N. Tandon, J. S. Thakur, N. J. Thomas, G. S. Toteja, C. M. Varghese, C. Venkataraman, K. N. Venugopal, K. D. Walker, A. Y. Watson, S. Wozniak, D. Xavier, G. N. Yadama, G. Yadav, D. K. Shukla, H. J. Bekedam, K. S. Reddy, R. Guleria, T. Vos, S. S. Lim, R. Dandona, S. Kumar, P. Kumar, P. J. Landrigan and L. Dandona, *Lancet Planet. Heal.*, 2021, **5**, 25–38.

13 M. Grätzel, *Philos. Trans. R. Soc. A Math. Phys. Eng. Sci.*, 2007, **365**, 993–1005.

14 By the Numbers | Earth – NASA Solar System Exploration, https://solarsystem.nasa.gov/planets/earth/by-the-numbers/, (accessed 23 August 2022).

15 P. A. Lynn, *Electricity from sunlight : An Introduction to Photovoltaics*, Wiley, 2010.

16 J. Nelson, *The Physics of Solar Cells*, Imperial College Press, London, 1st edn., 2003.

17 A. T. Mercherikunnel and J. C. Richmond, *Spectral Distribution of Solar Radiation*, NASA, 1980.

18 Q. Pang, X. Liang, C. Y. Kwok, J. Kulisch and L. F. Nazar, *Adv. Energy Mater.*, 2017, **7**, 1601630–160130.

19 H. Ibrahim, A. Ilinca and J. Perron, *Renew. Sustain. Energy Rev.*, 2008, **12**, 1221–1250.

20 A. E. Becquerel, *C. R. Hebd. Seances Acad. Sci.*, 1839, **9**, 561–567.

21 J. Perlin, *From Space to Earth - The Story of Solar Electricity*, Harvard University Press, 2002.

22 D. M. Chapin, C. S. Fuller and G. L. Pearson, *J. Appl. Phys.*, 1954, **25**, 676–677.

23 W. Palz, *Power for The World - The Emergence of Electricity From The Sun*, Jenny

Stanford Publishing, 2010.

24 K. Yoshikawa, H. Kawasaki, W. Yoshida, T. Irie, K. Konishi, K. Nakano, T. Uto, D. Adachi, M. Kanematsu, H. Uzu and K. Yamamoto, *Nat. Energy*, 2017, **2**, 1–8.

25 J. E. Carlé, M. Helgesen, O. Hagemann, M. Hösel, I. M. Heckler, E. Bundgaard, S. A. Gevorgyan, R. R. Søndergaard, M. Jørgensen, R. García-Valverde, S. Chaouki-Almagro, J. A. Villarejo and F. C. Krebs, *Joule*, 2017, **1**, 274–289.

26 T. Kita, Y. Harada and S. Asahi, *Energy Conversion Efficiency of Solar Cells*, Springer Singapore, 2019.

27 Fraunhofer Institute for Solar Energy Systems, in *Photovoltaics Report*, Freiburg, 2019.

28 A. Louwen, W. Van Sark, R. Schropp and A. Faaij, *Sol. Energy Mater. Sol. Cells*, 2016, **147**, 295–314.

29 G. M. Wilson, M. Al-Jassim, W. K. Metzger, S. W. Glunz, P. Verlinden, G. Xiong, L. M. Mansfield, B. J. Stanbery, K. Zhu, Y. Yan, J. J. Berry, A. J. Ptak, F. Dimroth, B. M. Kayes, A. C. Tamboli, R. Peibst, K. Catchpole, M. O. Reese, C. S. Klinga, P. Denholm, M. Morjaria, M. G. Deceglie, J. M. Freeman, M. A. Mikofski, D. C. Jordan, G. Tamizhmani and D. B. Sulas-Kern, *J. Phys. D. Appl. Phys.*, 2020, **53**, 493001.

30 Y. Dan, K. Seo, K. Takei, J. H. Meza, A. Javey and K. B. Crozier, *Nano Lett.*, 2011, **11**, 2527–2532.

31 H. Nakaya, M. Nishida, Y. Takeda, S. Moriuchi, T. Tonegawa, T. Machida and T. Nunoi, *Sol. Energy Mater. Sol. Cells*, 1994, **34**, 219–225.

32 K. A. Horowitz, T. W. Remo, B. Smith and A. J. Ptak, *A Techno-Economic Analysis and Cost Reduction Roadmap for III-V Solar Cells*, Golden, CO: National Renewable Energy Laboratory, 2018.

33 J. Li, A. Aierken, Y. Liu, Y. Zhuang, X. Yang, J. H. Mo, R. K. Fan, Q. Y. Chen, S. Y. Zhang, Y. M. Huang and Q. Zhang, *Front. Phys.*, 2021, **8**, 657.

34 A. Shah, P. Torres, R. Tscharner, N. Wyrsch and H. Keppner, *Science (80-.).*, 1999, **285**, 692–698.

35 Y. Hirai, Y. Kurokawa and A. Yamada, *Jpn. J. Appl. Phys.*, 2014, **53**, 12301.

36 Series 6, First Solar, http://www.firstsolar.com/Modules/Series-6, (accessed 8 March

2020).

37 A. Kojima, K. Teshima, Y. Shirai and T. Miyasaka, *J. Am. Chem. Soc.*, 2009, **131**, 6050–6051.

38 H. Kim, J. Lim, M. Sohail and M. K. Nazeeruddin, *Sol. RRL*, 2022, **6**, 2200013.

39 R. J. Sutton, G. E. Eperon, L. Miranda, E. S. Parrott, B. A. Kamino, J. B. Patel, M. T. Hörantner, M. B. Johnston, A. A. Haghighirad, D. T. Moore and H. J. Snaith, *Adv. Energy Mater.*, 2016, **6**, 1502458.

40 G. E. Eperon, S. D. Stranks, C. Menelaou, M. B. Johnston, L. M. Herz and H. J. Snaith, *Energy Environ. Sci.*, 2014, **7**, 982–988.

41 Perovskite solar cell leaders Oxford Photovoltaics (Oxford PV), https://www.oxfordpv.com/about-us, (accessed 8 March 2020).

42 R. E. Beal, D. J. Slotcavage, T. Leijtens, A. R. Bowring, R. A. Belisle, W. H. Nguyen, G. F. Burkhard, E. T. Hoke and M. D. McGehee, in *2017 IEEE 44th Photovoltaic Specialist Conference, PVSC 2017*, IEEE, 2017, vol. 7, pp. 1094–1099.

43 N. Sellami and T. K. Mallick, *Appl. Energy*, 2013, **102**, 868–876.

44 Y. Shang, S. Hao, C. Yang and G. Chen, *Nanomaterials*, 2015, 5, 1782–1809.

45 G. Wang, L. P. Liao, A. M. Elseman, Y. Q. Yao, C. Y. Lin, W. Hu, D. B. Liu, C. Y. Xu, G. D. Zhou, P. Li, L. J. Chen, J. J. Han, X. De Yang, R. Wu, X. Rao and Q. L. Song, *Nano Energy*, 2020, **68**, 104383.

46 Best Research-Cell Efficiency Chart | Photovoltaic Research | NREL, https://www.nrel.gov/pv/cell-efficiency.html, (accessed 31 August 2022).

47 C. Quarti, E. Mosconi, J. M. Ball, V. D'Innocenzo, C. Tao, S. Pathak, H. J. Snaith, A. Petrozza and F. De Angelis, *Energy Environ. Sci.*, 2016, **9**, 155–163.

48 K. Wang, Z. Jin, L. Liang, H. Bian, D. Bai, H. Wang, J. Zhang, Q. Wang and L. Shengzhong, *Nat. Commun.*, 2018, **9**, 1–8.

49 V. M. Goldschmidt, *Naturwissenschaften*, 1926, **21**, 478–485.

50 W. Travis, E. N. K. Glover, H. Bronstein, D. O. Scanlon and R. G. Palgrave, *Chem. Sci.*, 2016, **7**, 4548–4556.

51 S. De Wolf, J. Holovsky, S. J. Moon, P. Löper, B. Niesen, M. Ledinsky, F. J. Haug, J. H. Yum and C. Ballif, *J. Phys. Chem. Lett.*, 2014, **5**, 1035–1039.

52 K. Tanaka and T. Kondo, *Sci. Technol. Adv. Mater.*, 2003, **4**, 599–604.

53 S. D. Stranks, G. E. Eperon, G. Grancini, C. Menelaou, M. J. P. Alcocer, T. Leijtens, L. M. Herz, A. Petrozza and H. J. Snaith, *Science*, 2013, **342**, 341–4.

54 I. C. Smith, E. T. Hoke, D. Solis-Ibarra, M. D. McGehee and H. I. Karunadasa, *Angew. Chemie - Int. Ed.*, 2014, **53**, 11232–11235.

55 M. Liu, M. B. Johnston and H. J. Snaith, *Nature*, 2013, **501**, 395–398.

56 Z. Wei, H. Chen, K. Yan and S. Yang, *Angew. Chem. Int. Ed*, 2014, **53**, 13239–13243.

57 V. M. Koch, M. K. S. Barr, P. Büttner, I. Mínguez-Bacho, D. Döhler, B. Winzer, E. Reinhardt, D. Segets and J. Bachmann, *J. Mater. Chem. A*, 2019, **7**, 25112–25119.

58 E. Fortunato, D. Ginley, H. Hosono and D. C. Paine, *MRS Bull.*, 2007, **32**, 242–247.

59 G. Xing, B. Wu, S. Chen, J. Chua, N. Yantara, S. Mhaisalkar, N. Mathews and T. C. Sum, *Small*, 2015, **11**, 3606–3613.

60 M. Kulbak, D. Cahen and G. Hodes, *J. Phys. Chem. Lett*, 2015, **6**, 42.

61 K. Mahmood, S. Sarwar and M. T. Mehran, *RSC Adv.*, 2017, 7, 17044–17062.

62 M. Saliba, J. P. Correa-Baena, C. M. Wolff, M. Stolterfoht, N. Phung, S. Albrecht, D. Neher and A. Abate, *Chem. Mater.*, 2018, **30**, 4193–4201.

63 S. Li, Y. L. Cao, W. H. Li and Z. S. Bo, *Rare Met.*, 2021, **40**, 2712–2729.

64 G. Tong, T. Chen, H. Li, L. Qiu, Z. Liu, Y. Dang, W. Song, L. K. Ono, Y. Jiang and Y. Qi, *Nano Energy*, 2019, **65**, 104015.

65 J. Zhou, X. Wei, J. Zhu, X. Yang, H. Niu, L. Wan, P. Jiang, J. Xu, R. Zhou and G. Cao, *Sci. China Mater.*, 2020, **63**, 1151–1162.

66 V. Babu, R. Fuentes Pineda, T. Ahmad, A. O. Alvarez, L. A. Castriotta, A. Di Carlo, F. Fabregat-Santiago and K. Wojciechowski, *ACS Appl. Energy Mater.*, 2020, **3**, 5126–5134.

67 M. B. Islam, M. Yanagida, Y. Shirai, Y. Nabetani and K. Miyano, *ACS Omega*, 2017, **2**, 2291–2299.

68 Z. Ku, Y. Rong, M. Xu, T. Liu and H. Han, *Sci. Rep.*, 2013, **3**, 1–5.

69 A. Mei, X. Li, L. Liu, Z. Ku, T. Liu, Y. Rong, M. Xu, M. Hu, J. Chen, Y. Yang, M.

Grätzel and H. Han, *Science*, 2014, **345**, 295–298.

70 T. Minemoto and M. Murata, *Curr. Appl. Phys.*, 2014, **14**, 1428–1433.

71 I. Poli, J. Baker, J. Mcgettrick, F. De Rossi, S. Eslava, T. Watson and P. J. Cameron, *J. Mater. Chem. A*, 2018, **6**, 18677–18686.

72 Z. Liu, B. Sun, X. Liu, J. Han, H. Ye, Y. Tu, C. Chen, T. Shi, Z. Tang and G. Liao, *J. Mater. Chem. A*, 2018, **6**, 7409–7419.

73 F. Zhang, X. Yang, M. Cheng, J. Li, W. Wang, H. Wang and L. Sun, *J. Mater. Chem. A*, 2015, **3**, 24272–24280.

74 J. Baker, K. Hooper, S. Meroni, A. Pockett, J. McGettrick, Z. Wei, R. Escalante, G. Oskam, M. Carnie and T. Watson, *J. Mater. Chem. A*, 2017, **5**, 18643–18650.

75 D. Bogachuk, S. Zouhair, K. Wojciechowski, B. Yang, V. Babu, L. Wagner, B. Xu, J. Lim, S. Mastroianni, H. Pettersson, A. Hagfeldt and A. Hinsch, *Energy Environ. Sci.*, 2020, **13**, 3880–3916.

76 A. M. A. Leguy, Y. Hu, M. Campoy-Quiles, M. I. Alonso, O. J. Weber, P. Azarhoosh, M. Van Schilfgaarde, M. T. Weller, T. Bein, J. Nelson, P. Docampo and P. R. F. Barnes, *Chem. Mater.*, 2015, **27**, 3397–3407.

77 M. Salado, L. Contreras-Bernal, L. Caliò, A. Todinova, C. López-Santos, S. Ahmad, A. Borras, J. Idígoras and J. A. Anta, *J. Mater. Chem. A*, 2017, **5**, 10917–10927.

78 F. T. F. O'Mahony, Y. H. Lee, C. Jellett, S. Dmitrov, D. T. J. Bryant, J. R. Durrant, B. C. O'Regan, M. Graetzel, M. K. Nazeeruddin and S. A. Haque, *J. Mater. Chem. A*, 2015, **3**, 7219–7223.

79 H. J. Snaith, A. Abate, J. M. Ball, G. E. Eperon, T. Leijtens, N. K. Noel, S. D. Stranks, J. Tse, W. Wang, K. Wojciechowski and W. Zhang, *J. Phys. Chem. Lett*, 2014, **5**, 29.

80 W. Tress, N. Marinova, T. Moehl, S. M. Zakeeruddin, M. K. Nazeeruddin and M. Grätzel, *Energy Environ. Sci.*, 2015, **8**, 995–1004.

81 D. H. Kang and N. G. Park, *Adv. Mater.*, 2019, **31**, 1805214.

82 B. Chen, M. Yang, X. Zheng, C. Wu, W. Li, Y. Yan, J. Bisquert, K. Zhu and S. Priya, *J. Phys. Chem. Lett*, 2015, **6**, 4700.

83 M. V Khenkin, E. A. Katz, A. Abate, G. Bardizza, J. J. Berry, C. Brabec, F. Brunetti, V. Bulović, Q. Burlingame, A. Di Carlo, R. Cheacharoen, Y. B. Cheng, A.

Colsmann, S. Cros, K. Domanski, M. Dusza, C. J. Fell, S. R. Forrest, Y. Galagan, D. Di Girolamo, M. Grätzel, A. Hagfeldt, E. von Hauff, H. Hoppe, J. Kettle, H. Köbler, M. S. Leite, S. (Frank) Liu, Y. L. Loo, J. M. Luther, C. Q. Ma, M. Madsen, M. Manceau, M. Matheron, M. McGehee, R. Meitzner, M. K. Nazeeruddin, A. F. Nogueira, Ç. Odabaşı, A. Osherov, N. G. Park, M. O. Reese, F. De Rossi, M. Saliba, U. S. Schubert, H. J. Snaith, S. D. Stranks, W. Tress, P. A. Troshin, V. Turkovic, S. Veenstra, I. Visoly-Fisher, A. Walsh, T. Watson, H. Xie, R. Yıldırım, S. M. Zakeeruddin, K. Zhu and M. Lira-Cantu, *Nat. Energy*, 2020, **5**, 35–49.

84 A. L. Wani, A. Ara and J. A. Usmani, *Interdiscip. Toxicol.*, 2015, **8**, 55–64.

85 M. Ren, X. Qian, Y. Chen, T. Wang and Y. Zhao, *J. Hazard. Mater.*, 2022, **426**, 127848.

86 G. Schileo and G. Grancini, *J. Mater. Chem. C*, 2021, **9**, 67–76.

87 E. M. Hutter, R. Sangster, C. Testerink, B. Ehrler and C. M. M. Gommers, *iScience*, 2022, **25**, 103583.

88 A. Rizzo, F. Lamberti, M. Buonomo, N. Wrachien, L. Torto, N. Lago, S. Sansoni, R. Pilot, M. Prato, N. Michieli, M. Meneghetti, G. Meneghesso and A. Cester, *Sol. Energy Mater. Sol. Cells*, 2019, **189**, 43–52.

89 L. Gil-Escrig, G. Longo, A. Pertegá, C. Roldá n-Carmona, A. Soriano, M. Sessolo and H. J. Bolink, *Chem. Commun*, 2015, **51**, 569–571.

90 M. Saliba, T. Matsui, J.-Y. Seo, K. Domanski, J.-P. Correa-Baena, M. Khaja, S. M. Zakeeruddin, W. Tress, A. Abate, A. Hagfeldt and M. Grätzel, *Energy Environ. Sci.*, 2016, **9**, 1989–1997.

91 H. Chen, Y. Chen, T. Zhang, X. Liu, X. Wang and Y. Zhao, *Small Struct.*, 2021, **2**, 2000130.

92 J. Jeong, M. Kim, J. Seo, H. Lu, P. Ahlawat, A. Mishra, Y. Yang, M. A. Hope, F. T. Eickemeyer, M. Kim, Y. Jin Yoon, I. Woo Choi, B. Primera Darwich, S. Ju Choi, Y. Jo, J. Hee Lee, B. Walker, S. M. Zakeeruddin, L. Emsley, U. Rothlisberger, A. Hagfeldt, D. Suk Kim, M. Grätzel and J. Young Kim, *Nature*, 2021, **592**, 381.

93 A. F. Akbulatov, L. A. Frolova, N. N. Dremova, I. Zhidkov, V. M. Martynenko, S. A. Tsarev, S. Y. Luchkin, E. Z. Kurmaev, S. M. Aldoshin, K. J. Stevenson, P. A. Troshin and M. N. Mikheev, *J. Phys. Chem. Lett*, 2020, **11**, 333–339.

94 C. Wang, C. Zhang, S. Wang, G. Liu, H. Xia, S. Tong, J. He, D. Niu, C. Zhou, K.

Ding, Y. Gao and J. Yang, *Sol. RRL*, 2018, **2**, 1700209.

95 G. Zhou, J. Wu, Y. Zhao, Y. Li, J. Shi, Y. Li, H. Wu, D. Li, Y. Luo and Q. Meng, *ACS Appl. Mater. Interfaces*, 2018, **10**, 9503–9513.

96 A. Aziz, N. Aristidou, X. Bu, R. J. E. Westbrook, S. A. Haque and M. Saiful Islam, *Cite This Chem. Mater*, 2020, **32**, 400–409.

97 R. García-Rodríguez, D. Ferdani, S. Pering, P. J. Baker and P. J. Cameron, *J. Mater. Chem. A*, 2019, **7**, 22604–22614.

98 R. J. Sutton, M. R. Filip, A. A. Haghighirad, N. Sakai, B. Wenger, F. Giustino and H. J. Snaith, *ACS Energy Lett*, 2018, **3**, 56.

99 Z. Xu, N. Liu, X. Liu, W. Han, W. Xu, J. Zhang, L. Huang, Z. Hu and Y. Zhu, *Chem. Eng. J.*, 2023, **451**, 139047.

100 B. Li, Y. Zhang, L. Fu, T. Yu, S. Zhou, L. Zhang and L. Yin, *Nat. Commun.*, 2018, **9**, 1076.

101 C. C. Stoumpos, C. D. Malliakas, J. A. Peters, Z. Liu, M. Sebastian, J. Im, T. C. Chasapis, A. C. Wibowo, D. Y. Chung, A. J. Freeman, B. W. Wessels and M. G. Kanatzidis, *Cryst. Growth Des.*, 2013, **13**, 2722–2727.

102 C. Tenailleau, S. Aharon, B. El Cohen and L. Etgar, *Nanoscale Adv.*, 2019, **1**, 147–153.

103 M. Ezzeldien, S. Al-Qaisi, Z. A. Alrowaili, M. Alzaid, E. Maskar, A. Es-Smairi, T. V. Vu and D. P. Rai, *Sci. Reports 2021 111*, 2021, **11**, 1–12.

104 Q. Zhou, J. Duan, J. Du, Q. Guo, Q. Zhang, X. Yang, Y. Duan and Q. Tang, *Adv. Sci.*, 2021, **8**, 2101418.

105 X. Liu, X. Tan, Z. Liu, B. Sun, J. Li, S. Xi, T. Shi and G. Liao, *J. Power Sources*, 2019, **443**, 227269.

106 B. Li, B. Hou and G. A. J. Amaratunga, *InfoMat*, 2021, **3**, 445–459.

107 I. Poli, U. Hintermair, M. Regue, S. Kumar, E. V. Sackville, J. Baker, T. M. Watson, S. Eslava and P. J. Cameron, *Nat. Commun.*, 2019, **10**, 2097.

108 W. Grochala, *Nat. Chem.*, 2015, **7**, 264.

109 G. Nicoletti, N. Arcuri, G. Nicoletti and R. Bruno, *Energy Convers. Manag.*, 2015, **89**, 205–213.

110 N. Armaroli and V. Balzani, *ChemSusChem*, 2011, **4**, 21–36.

111 S. . Sherif, D. Y. Goswami, E. K. Stefanakos and A. Steinfield, *Handbook of Hydrogen Energy*, CRC Press, 2014.

112 A. M. Abdalla, S. Hossain, O. B. Nisfindy, A. T. Azad, M. Dawood and A. K. Azad, *Energy Convers. Manag.*, 2018, **165**, 602–627.

113 J. D. Holladay, J. Hu, D. L. King and Y. Wang, *Catal. Today*, 2009, **139**, 244–260.

114 T. Ohta, T. Takahashi, S. Ihara, S. Sato, N. Kamiya, K. Honda, A. Fujishima, T. Watanabe, A. Mitsui, S. Ono, M. Yamaguchi and W. Escher, in *Solar-Hydrogen Energy Systems*, Pergamon, 1979, pp. 25–33.

115 F. Safari and I. Dincer, *Energy Convers. Manag.*, 2020, **205**, 112182.

116 Y. Mao, Y. Gao, W. Dong, H. Wu, Z. Song, X. Zhao, J. Sun and W. Wang, *Appl. Energy*, 2020, **267**, 114860.

117 X. Vitart, A. Le Duigou and P. Carles, *Energy Convers. Manag.*, 2006, **47**, 2740–2747.

118 Y. Guo, G. Li, J. Zhou and Y. Liu, *IOP Conf. Ser. Earth Environ. Sci.*, 2019, **371**, 042022.

119 L. (Chemist) Zhang, H. Zhao, D. P. Wilkinson, X. Sun and J. Zhang, 240.

120 A. Fujishima and K. Honda, *Nature*, 1972, **238**, 37–38.

121 Z. Chen, H. N. Din and E. Miller, *Photoelectrochemical Water Splitting - Standards, Experimental Methods and Protocols*, Springer, 2016.

122 N. Cheng, S. Stambula, D. Wang, M. N. Banis, J. Liu, A. Riese, B. Xiao, R. Li, T. K. Sham, L. M. Liu, G. A. Botton and X. Sun, *Nat. Commun. 2016 71*, 2016, **7**, 1–9.

123 P. C. K. Vesborg, B. Seger and I. Chorkendorff, *J. Phys. Chem. Lett.*, 2015, **6**, 951–957.

124 J. D. Blakemore, R. H. Crabtree and G. W. Brudvig, *Chem. Rev.*, 2015, **115**, 12974–13005.

125 P. D. Nguyen, T. M. Duong and P. D. Tran, *J. Sci. Adv. Mater. Devices*, 2017, **2**, 399–417.

126 S. Ye, W. Shi, Y. Liu, D. Li, H. Yin, H. Chi, Y. Luo, N. Ta, F. Fan, X. Wang and C. Li, *J. Am. Chem. Soc.*, 2021, **143**, 12499–12508.

127 C. Moon and B. Shin, *Discov. Mater. 2022 21*, 2022, **2**, 1–16.

128 G. Peharz, F. Dimroth and U. Wittstadt, *Int. J. Hydrogen Energy*, 2007, **32**, 3248–3252.

129 S. K. Karuturi, H. Shen, A. Sharma, F. J. Beck, P. Varadhan, T. Duong, P. R. Narangari, D. Zhang, Y. Wan, J. H. He, H. H. Tan, C. Jagadish and K. Catchpole, *Adv. Energy Mater.*, 2020, **10**, 2000772.

130 L. F. Gao, W. J. Luo, Y. F. Yao and Z. G. Zou, *Chem. Commun.*, 2018, **54**, 11459–11462.

131 Y. Zhang, H. Lv, Z. Zhang, L. Wang, X. Wu, H. Xu, Y. Zhang, L. Wang, H. Xu, H. Lv, X. Wu and Z. Zhang, *Adv. Mater.*, 2021, **33**, 2008264.

132 R. Rhee, T. G. Kim, G. Y. Jang, G. Bae, J. H. Lee, S. Lee, S. Kim, S. Jeon and J. H. Park, *Carbon Energy*, 2022, **5**, 1–10.

133 A. Iwase, Y. H. Ng, Y. Ishiguro, A. Kudo and R. Amal, *J. Am. Chem. Soc*, 2011, **133**, 11054–11057.

134 Y. Sasaki, H. Nemoto, K. Saito and A. Kudo, *J. Phys. Chem. C*, 2009, **113**, 17536–17542.

135 R. Li, *Chinese J. Catal.*, 2017, **38**, 5–12.

136 N. Kosinov, J. Gascon, F. Kapteijn and E. J. M. Hensen, *J. Memb. Sci.*, 2016, **499**, 65–79.

Chapter 2. Theory

2.1. Semiconductors

In solid materials, such as those with crystalline structures, a large number of atoms come together to form an extended structure. Molecular orbital (MO) theory and the linear combination of atomic orbitals (LCAO) can be applied to the numerous of atoms in an extended solid, and their individual atomic orbitals can be viewed as a large number of energy levels. The interaction of an identical orbital from 'n' number of atoms, results in numerous energy levels that are so close together that they overlap and form a continuum of allowed energy levels. This continuum is often referred to as a 'band'. The filled orbitals make up the valence band (VB), whereas the unfilled orbitals make up the conduction band (CB). [1] These bands can have different energy positions and band spacing, which determine some of the key properties of the material (Figure 1).

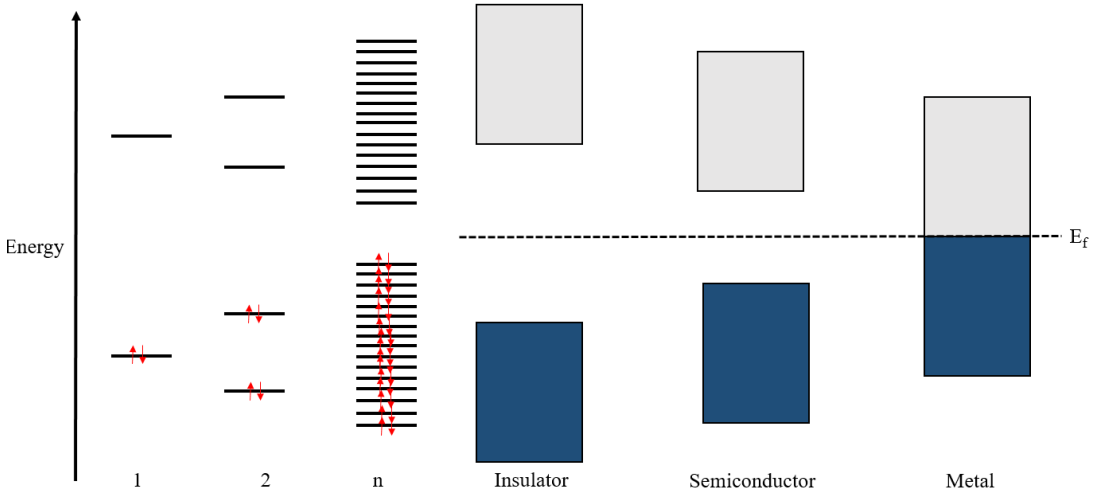

Figure 1: A representation of the expansion of MO theory from 1, 2 and n atoms. The relative energetic positions of the valance bands (blue) and conduction bands (grey) in insulators, semiconductors and metals are shown.

The energy difference between the VB and CB is known as the band gap and it has an energy of E_g. The energy at which the probability of an energy level being occupied by electrons is 50 % is often referred to as the Fermi level (E_f). Depending on the energy difference between the bands, some electrons may be excited to energy levels that lie above the Fermi level. In insulating materials, the band gap is large (> ~ 4 eV) [2] and as a result, a large amount of energy would be required in order to promote one electron from the VB to the CB. Consequently,

insulating materials, do not conduct electricity as there are no free electrons and these materials have high resistivity values. In metallic materials, there is no band gap and there is only one continuous band that is partially filled with electrons. As a result, only a small amount of energy is required to excite an electron from the VB to the CB. This allows metallic solids to be good conductors of electricity with low resistivity. However, semiconductors have a larger band gap than metallic materials, but a smaller band gap than insulating materials, often in the range of 0.5 – 3.5 eV. [2] Therefore, semiconductors have low intrinsic conductivity properties, as whilst electrons cannot travel freely between the VB and CB, at room temperature, a small number of electrons will have sufficient kinetic energy to be promoted across the band gap to the CB. The number of electrons with sufficient energy to be promoted increases with temperature. However, the energy difference between the VB and CB in semiconductors often means that visible or UV light with sufficient energy can result in the promotion of an electron across the band gap.

The band gap in semiconductors can be either direct or indirect. For a direct band gap, the energy minima of the CB is positioned directly above the energy maxima of the VB, *i.e.* they have the same value of the wave vector k. Subsequently, upon photoexcitation, an electron is easily promoted from the VB to the CB. In the case of an indirect bandgap, the VB maxima and CB minima are widely separated in k space (see Figure 2). As a result, the absorption of light alone cannot excite a valance electron across the band gap as there are no target energy states available in the conduction band that have both suitable energy and k vector. Consequently, the promotion of an electron from the VB to the CB minima requires a change in momentum of the electron, and the electron has to change energy as well as its wave vector k value. To excite an electron across an indirect band gap, the change in momentum that is required can be supplied by a phonon. However, phonon processes are slower, causing the absorption coefficient of materials with indirect band gaps to be smaller and more temperature dependent than that of those with direct band gaps. [3]

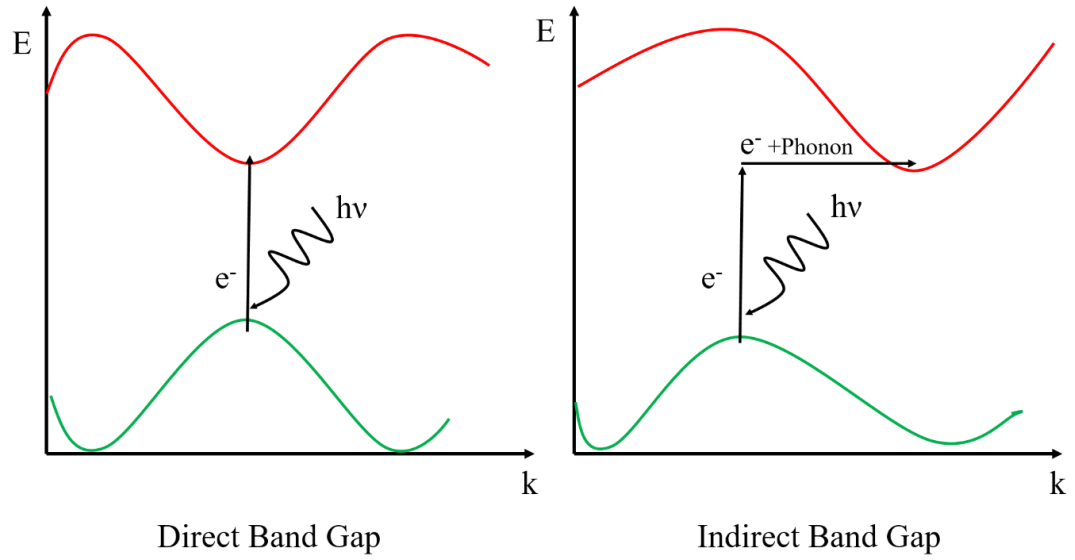

Figure 2: Schematic representation of a direct band gap (left) and an indirect band gap (right). The VB is shown in green whilst the CB is shown in red.

The promotion of an electron across the bandgap to the CB leaves behind a positively charged 'hole' in place of the electron in the VB. The positively charged hole in VB and negatively charged electron in the CB create an exciton pair and they are still loosely bound to each other through columbic interactions. However, conduction throughout the semiconductor requires the movement of both of these charge carriers in opposite direction, thus once the charge carriers have been photogenerated, it is necessary to separate the charges and transport them to opposite electrodes where they can be collected. [4] Furthermore, the dielectric constant of the semiconductor material can influence the excition binding and materials with high dielectric constants have lower excition binding energies. [5, 6] This results in faster electron – hole separation.

2.1.1. Recombination

If the charge carriers are not separated, the photoexcited electron will eventually recombine with the hole and no photocurrent will be produced. Recombination is an electronic relaxation event that occurs when a photoexcited electron is able to decay to a lower energy state and recombine with a hole, reducing the number of free charge carriers available. The amount of time that the charge carriers are able to stay in the photoexcited, without recombination, is referred to as the charge carrier lifetime. The longer the charge carrier lifetime, the more likely the charges are to be extracted. Recombination occurs through three main processes, which are shown in Figure 3. Radiative recombination occurs when a photoexcited electron decays from the CB to the VB with the emission of a photon, with energy equal to that of the band

gap. Radiative recombination processes can take place in semiconductors with both direct and indirect band gaps; however, phonon scattering is required for radiative recombination to occur in indirect band gap semiconductors. [7]

Recombination can also be non-radiative and occur through defect/trap states that exist within a material; this process is called Shockley-Read-Hall recombination. [8] It can be assumed that due to defects, a crystal will contain a density of defect traps (N_t), which will contribute to the recombination process. These defect trap states can sit at an energy in between the CB and VB. These traps may capture an electron from the conduction band, with the resulting energy loss of the electron converted into heat. Recombination will occur if the hole is also able to move to this trap state, before the electron is able to free itself and be thermally released back into the CB. The opposite can also occur, where it is the hole that becomes trapped first. Generally, if the defect level is close to the conduction band minimum (CBM) electrons will be more easily trapped, however, it is difficult to trap a hole here. On the other hand, , if the defect level is close to the valance band maxima (VBM), holes can be more easily trapped but electron trapping is more difficult. As a result, the recombination process is determined by the slower trapping rate of the electron or hole. This leads to trap states that lie close to the middle of the band gap in energy, providing the most effective route for recombination. [9]

Auger recombination is a third type of recombination. Here, a photogenerated electron will combine with a hole in the VB. Instead of emitting the energy difference in the form of light or heat, this energy is transferred to a second electron in the CB. The second electron will be excited within the CB, before thermalising back down to the CB minimum. [10]

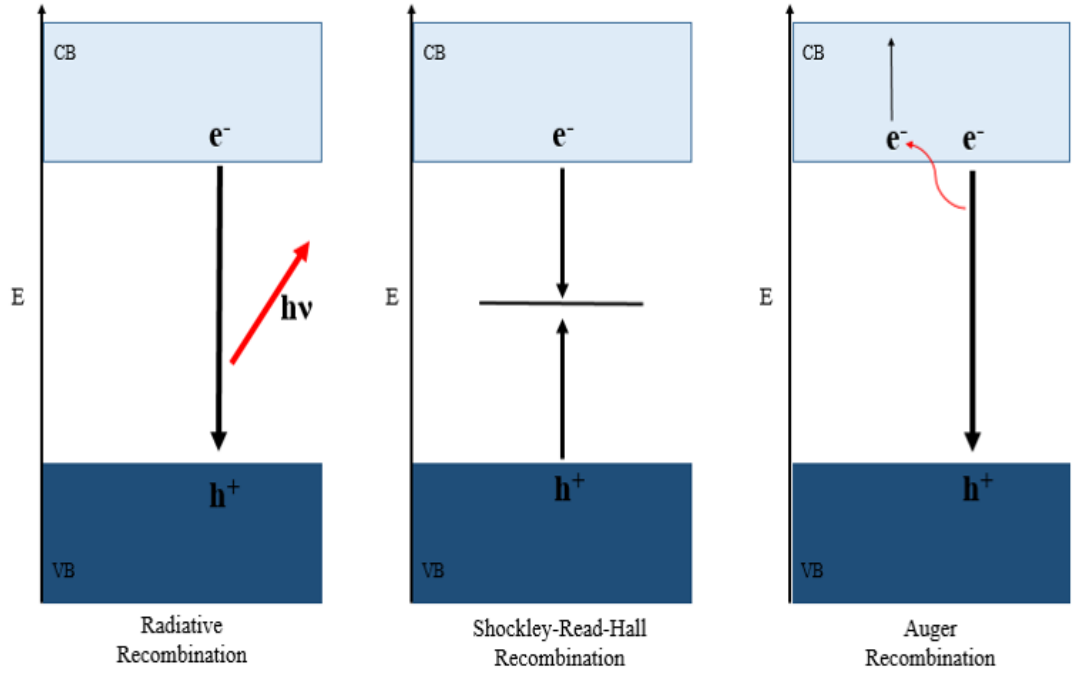

Figure 3: An illustration of different recombination pathways within semiconductors. Radiative recombination (left), Shockley-Read-Hall recombination (center) and Auger recombination (right).

2.2. The Fermi Level

The energy level, up to which the states are filled at absolute zero, is called the Fermi energy.[4] Whereas above absolute zero, the Fermi level can be defined as the energy level where there is a 50 % chance of an electron occupying that level at equilibrium. The electron occupation of the energy levels in a semiconductor is given by the Fermi-Dirac distribution function (f_E) (Eq. 1). Where E corresponds to the energy of an electron state, E_f is the Fermi level, k_B is the Boltzmann constant and T is the temperature.

$$f_E = \frac{1}{1 + exp^{(E-E_F)/k_BT}} \quad (1)$$

At absolute zero, the electrons in a material, have no kinetic energy, thus they always occupy the lowest available energy levels. The available energy levels are filled in order of increasing energy. However, at temperatures above 0 K, the electrons will have some kinetic energy and thus some electrons will be excited to energy levels above the Fermi level, leaving some unoccupied states below the Fermi level. For a semiconductor at absolute zero, the valence

band is completely filled with electrons, and the conduction band is completely empty. Therefore the Fermi energy will lie somewhere within the band gap. [4] This is illustrated below in Figure 4. [4]

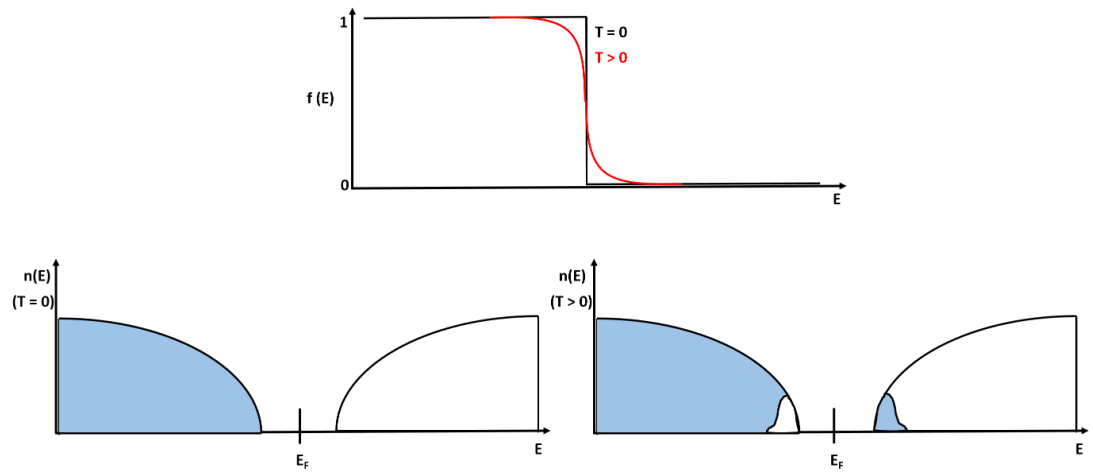

Figure 4: The effect of the Fermi-Dirac distribution on the energy distribution of electrons in a semiconductor with parabolic bands. The Fermi-Dirac distribution, f(E), is shown (top) where 1 and 0 are the probability of finding an electron and the effect of a temperature greater than 0 K is shown in red. The energy distribution of electrons, n(E), (below) is shown by the shaded area at 0 K (left) and temperatures above 0 K (right). The Fermi energy is denoted by E_f.

The Fermi level can be raised or lowered with changing temperature or by introducing impurities or dopants into the semiconductor. This changes the electronic properties of the semiconductor. This concept is discussed further in section 2.3.1.

2.2.1. Quasi Fermi Levels

The above section discusses a semiconductor at equilibrium, however, solar cells are designed to be operated under illumination, which disturbs this equilibrium. Both exposure to light, with an energy greater than E_g, and/or the application of an electrical bias, causes changes in the population of electrons and holes in the CB and VB. Instead, a separate '*quasi*' thermal equilibrium is reached separately, for both the electrons and holes. As a result, the electron population, within the CB, will redistribute as though they are at equilibrium with a common Fermi level and the hole population, within the VB, also will redistribute as though they are in equilibrium, with another common Fermi level. These are called the '*quasi*' Fermi levels, denoted E_{Fn} and E_{Fp} respectively, for both the electrons and holes (see Figure 5). However, it is important to note that this is only an approximation, hence the term '*quasi*'. This

approximation holds true due to the fact that the relaxation within the two bands occurs on a much faster time scale than relaxation between the bands (10^{-12} – 10^{-15} s Vs 10^{-6} – 10^{-9} s). [4, 11]

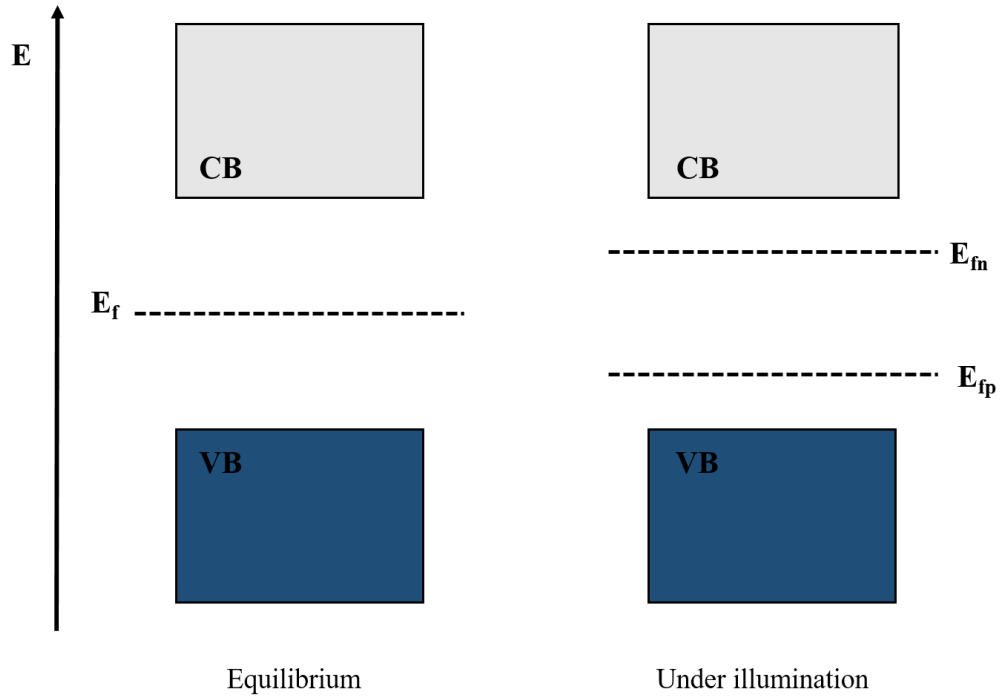

Figure 5: Fermi level (E_F) at equilibrium (left) and the Fermi level splitting under illumination, leading to the creation of the 'quasi' Fermi levels (E_{Fn}) and (E_{Fp}) (right).

Consequently, the quasi Fermi levels are often referred to as the spitting of the Fermi level and the difference in the splitting gives a chemical potential Δμ.

2.3. The p-n Junction in Semiconductors

2.3.1. Impurities and Doping

In an intrinsic semiconductor, there are no significant number of impurities within the crystal and the well-defined VB and CB are the only allowed energies, although some intrinsic defects and impurities will be present. The semiconductor crystal can be altered by introducing impurity atoms or structural defects into the lattice. This impurity, or defect, causes a change to the distribution of electronic energy levels on a local level and impurity/defect energy levels are created. If these impurity energy levels lie within the band gap, the Fermi level will change accordingly.

A semiconductor can be doped with '*donor*' atoms, which introduce or donate extra electrons into the crystal lattice; this is referred to n-type doping. The extra electrons provided by the

donor atoms are not required for bonding in the lattice and are surplus to requirement; hence, the electrons are only loosely bound to the donor atoms. Consequently, the donor atom can be ionised easily, resulting in a free electron and a positively charged donor atom. This results in the formation of a new donor energy state close to the CB edge. At absolute zero, this donor state is filled with electrons, thus the Fermi level must be raised to a position between the new donor energy state and the CB edge (see Figure 6). At temperatures above absolute zero, these extra electrons are easily promoted from the new donor level into the conduction band. This results in electrons being the majority carrier in n-type semiconductors and conduction within the material is mostly due to the movements of electrons. [4, 12] An example of this is, silicon doped with phosphorous atoms. Silicon atoms are tetravalent in a silicon crystal lattice, whereas phosphorous atoms have five valance electrons; the fifth electron is not needed for bonding.

Conversely, a semiconductor can be doped with '*acceptor*' atoms, which have too few valance electrons to be able to form all the required bonds within the crystal lattice; this is referred to as p- type doping. To compensate for the lack of electrons, the acceptor atom can remove a valance electron from another bond nearby. This has the effect of ionising the acceptor atom and creating a hole in the VB. This now results in a new acceptor energy state close to the VB. At absolute zero, the VB remains filled, whilst the acceptor level is empty, and the Fermi energy is lowered to a positon between the VB and the new acceptor energy state. In p-type semiconductors, the holes are the majority carriers and conduction is mostly due to the movement of holes. [4, 12] An example of a p-type semiconductor is silicon doped with boron. Boron is trivalent and can only form three bonds with the tetravalent silicon. Figure 6 illustrates the differences between intrinsic, n-type and p-type semiconductors.

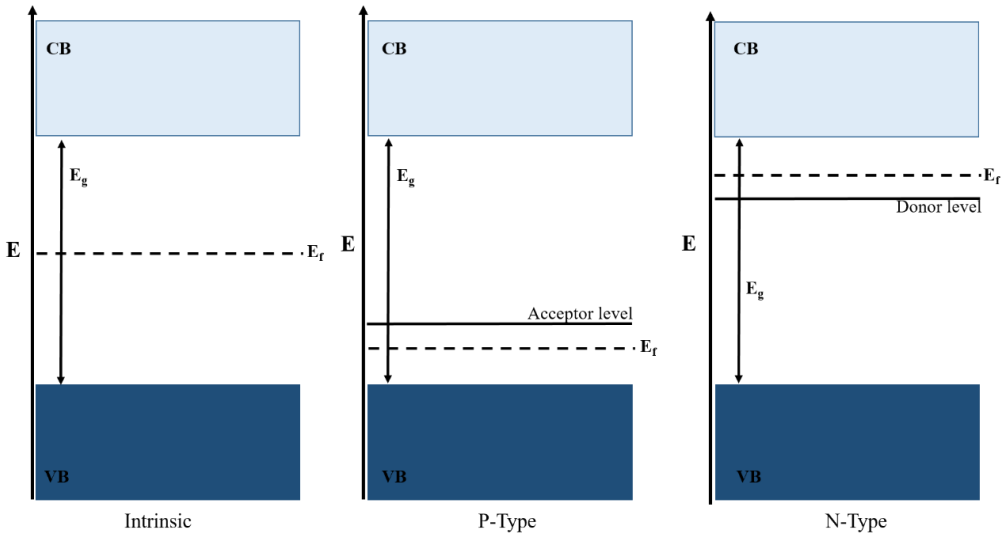

Figure 6: Energy level diagrams of an intrinsic semiconductor (left), a p-type semiconductor (centre) and an n-type semiconductor (right).

2.3.2. Junctions

In semiconductor solar cell devices, a junction between two electronically different materials provides the required driving force for the separation of the charge carriers. To achieve charge separation, light illumination or a bias application, must produce a gradient in at least one of the quasi fermi levels. By placing two electronically different materials together, with different work functions, a potential drop across the interface and a 'built in' electric field is established at equilibrium. Under illumination, where there are increased numbers of charge carriers, the presence of this electric field results in a net drift current. Electrons will move down the gradient towards a lower energy, whilst the holes will move up the gradient to higher energies. However, there is also a diffusion gradient present. The diffusion gradient arises from a change in the concentration of charge carriers across the material; this occurs if there are changes in the generation or removal rate of charge carriers. Thus, the diffusion gradient leads to the presence of a diffusion current, which often acts in the opposite direction to the drift current. Placing two electronically different materials together, which have different work functions, causes a gradient in the overall vacuum level/work function and leads to the presence of this built in electric field, this is shown in Figure 7. This is what happens when an n-type and p-type material are placed together at am interface, to form what is known as the p-n junction. The work function of the p-type material (Φ_p) is greater than the work function of the n-type material (Φ_n) and the electrostatic potential energy difference across the junction is equal to the difference in the work functions. This variation in electrostatic potential energy is represented by a change in the vacuum level(E_{vac}). When the two sides of the p-n junction are

isolated, the Fermi levels of the materials are independent of each other. However, when the two sides of the junction are brought together, the Fermi levels are required to equilibriate. Therefore, the CB minimum and VB maxima of the p-type material are at a higher energy than those of the n-type material. This causes band bending to occur in order to achieve continuity across the junction. The built-in field or bias (V_{bi}), is now not only equal to the difference in the work functions of the two materials, but also to the total amount of band bending. [4] Figure 7 demonstrates what happens when a p-type and n-type material are brought together to form a p-n junction under equilibrium.

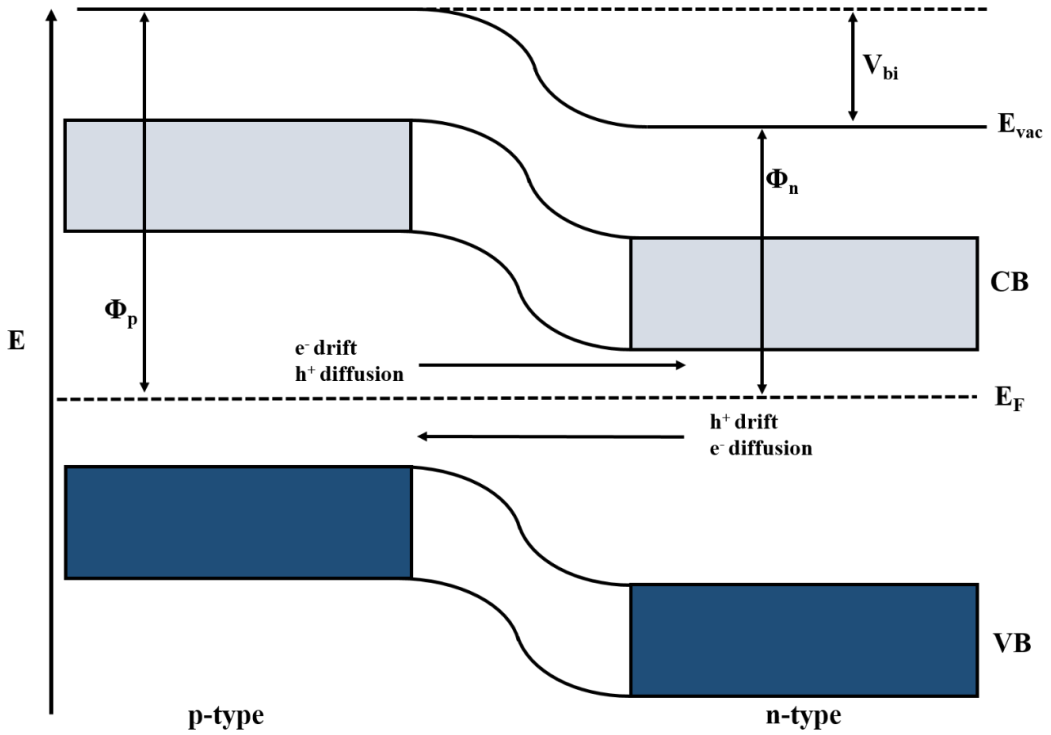

Figure 7: A band diagram of a p-n junction and charge carrier movement at equilibrium.

When applying an external bias to the p-n junction, the Fermi level on one side of the junction is raised with respect to the other, this alters the work function of the materials, thus changing the potential across the device. An applied negative bias leads to an increase in the depletion of charge carriers from the junction, whereas an applied positive bias injects carriers into the junction region. If the applied forward bias is equal to that of $V_{bi,}$ the built in bias of the device will be completely cancelled out. Therefore the asymmetry of the junction, which is essential for driving the photovoltaic effect, is removed. [4]

Under illumination, any electrons and holes that are generated at the junction between the p and n type semiconductors, will be immediately swept away due to the electric field. This region around the junction, is often called the depletion region or space charge region. In the depletion region, electrons are swept towards the n-type region, whilst holes are swept towards

the p-type region, thus separating the charge carriers and reducing their chance of recombination. Charge carriers that are generated away from the depletion region, will travel around in the VB and CB according to the diffusion gradient. Without the pull of the electric field, the charge carriers will travel an average distance, called the diffusion length, before they eventually recombine. Nonetheless, some of these carriers will enter the depletion region and also be swept away to the appropriate side. Only the minority carriers are able to cross the junction. This results in a net positive charge on the p-type side and a net negative charge on the n-type side. This build-up of positive and negative charges at opposite sides upon illumination, results in a potential difference, this potential difference is called the photovoltage (V). [13] When illuminated, or under bias, the splitting of the Fermi level that occurs is also equal to the voltage difference between the two contacts on either side of the junction. Therefore, the quasi-Fermi energies can be viewed as the energy of the mobile electrons and holes that are available to the external circuit. [14] This is shown in Figure 8.

An ohmic contact is made to the semiconductor, often with metal, to allow for the extraction of the charge carriers from the semiconductor, into the electrical circuit. Contacts are made on both the n-type side and the p-type side. When an ohmic contact with a semiconductor is formed, the semiconductor band will bend in a way that encourages the transport of the majority carriers across the semiconductor-metal junction. This also inhibits the transport of the minority carriers. Thus, in an n-type semiconductor-metal contact, both the VB and CB edges bend downward at the junction. The opposite is true for a p-type semiconductor-metal contact, and both the VB and CB edges bend upwards at the junction (see Figure 8).

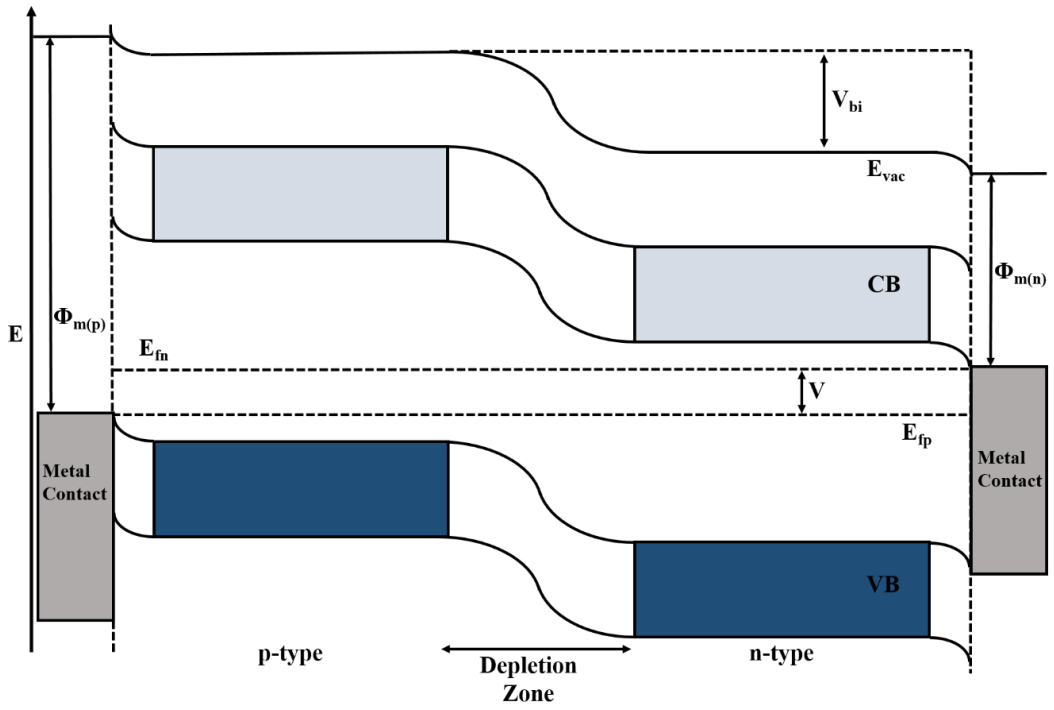

Figure 8: A band diagram of a p-n junction under illumination (or bias), with ohmic metal contacts. $\Phi_{m(n)}$ and $\Phi_{m(p)}$ refer to the work function of the two metal contacts.

The p-n junction is the classic model for solar cells and is the most widely used structure for semiconductor devices. Therefore, most silicon solar cells are based on the p-n junction. [4] However, other types of junctions are possible, such as; the p-i-n junction, where there is an intrinsic, undoped semiconductor layer between the p-type and n-type layers; [15] or p-n heterojunctions, where two different materials, with different band gaps are used to form a junction. [4]

2.3.3. Junctions in Perovskite Solar Cells

Perovskite solar cells work in a similar way to devices with a p-i-n (or n-i-p depending on the order of the layer arrangement) junction. Here, the ETL functions as the n-type layer and the HTL functions as the p-type layer. The perovskite layer functions as the intrinsic semiconductor layer. There are also heterojunctions present, as the perovskite is sandwiched between two non-perovskite materials with different band gaps and different work functions. When the three different materials are brought together, the electric field extends over a wider area than in a p-n junction and the potential drop will extend across the intrinsic layer. The band diagram of a simple n-i-p junction is shown in Figure 9.

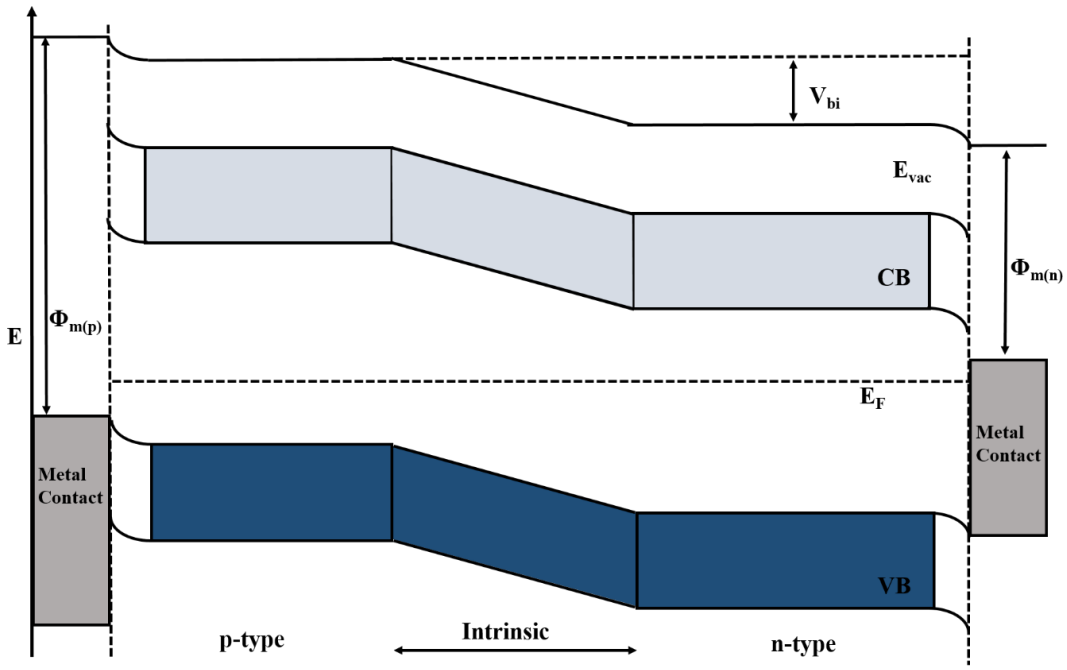

Figure 9: A band diagram for a simple p-i-n junction, at equilibrium in the dark.

However, in lead halide based PSCs, the presence of mobile ionic species can complicate the matter. The different ionic species can move on different time scales, resulting in the presence of both '*slow*' and '*fast*' moving ions. [16] The movement of an ionic species leaves a vacancy in its place, with the opposite charge, which can also migrate. The slow moving charges in the perovskite layer can accumulate at the interfaces between the perovskite and the two different transport layers. The migration is driven by the potential drop that is produced by the built in bias. The ion migration results in a net ionic charge that establishes an opposing electric field to the built-in field. Once a steady state has been achieved and the ionic species have accumulated at the interface, they effectively screen the electrons and holes from the potential drop across the intrinsic perovskite layer. [16, 17] The electric field within the bulk of the perovskite is neutralised. The effect of this is shown in Figure 10. As a result, ion migration within PSCs often has a profound effect on device performance and has been shown to cause hysteresis in the measurement of the devices. [18]

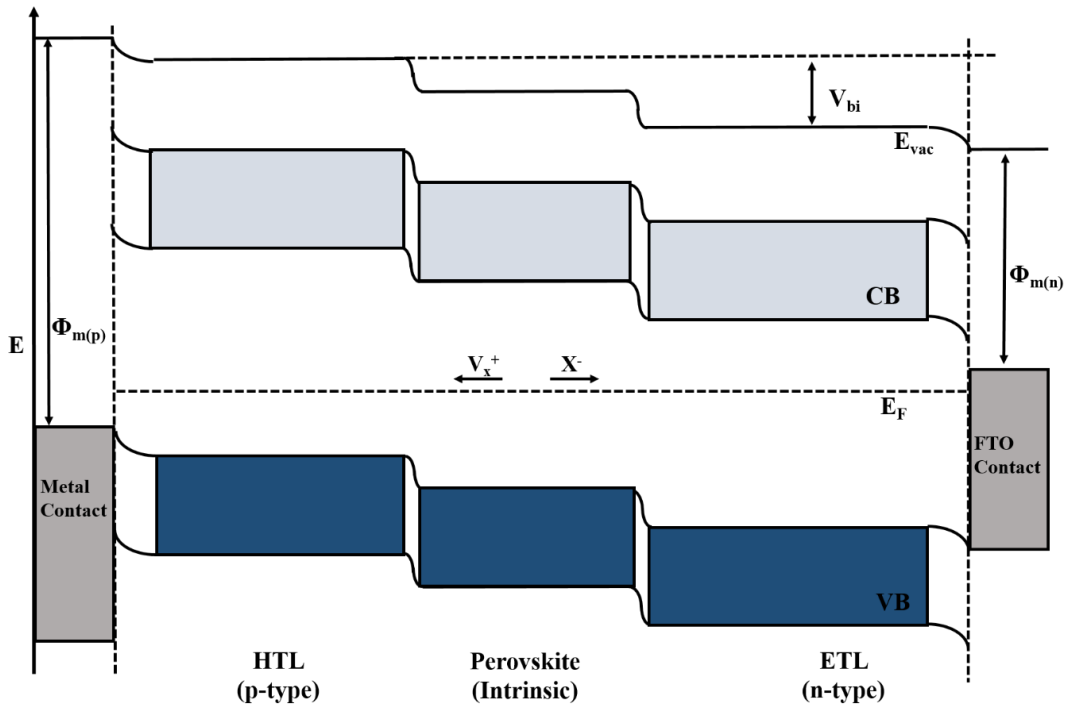

Figure 10: Band diagram showing the effect of mobile ion species in a perovskite p-i-n junction

The p-i-n design is often used in devices where carriers that are generated in the n and p-type layers are unlikely to contribute to the photocurrent. [4] This is the case with most PSCs as the ETL and HTL are often materials with large band gaps, thus they will not absorb a large proportion of visible light and charge carriers will not be generated in these layers. Hence, the perovskite layer is often referred to the absorber layer in PSCs.

The levels of the VBM and CBM in the ETL, perovskite and HTL can be easily altered either by using different materials, or by changing the electronic properties of the materials by doping. The appropriate band energy tailoring can alter the interface and thus can be used to improve the overall performance of PSCs. [19, 20, 21]

2.4. Solar cell parameters and device analysis

The contacts deposited on either side of the junctions within a device, allow for the collection of the photogenerated charge carriers. When these contacts are connected to an external circuit, current can be drawn from the device. The photogenerated current that is produced under short circuit conditions, when the cell is under illumination, is dependent upon the incident light that falls on the active area of the device. When a solar cell is under short circuit conditions, the overall voltage of the device is zero, the quasi fermi levels are equal and the maximum possible current can be drawn from the device. [4] The external quantum efficiency (EQE) of a device, gives the probability that one incident photon, possessing an energy of E,

will result in one electron being available to the external circuit. In an ideal solar cell, the short circuit current and light generated current would be equal, and the device would have a EQE of 100 %. However, due to various resistive loss mechanisms, this is not the case. As a convention, solar cells are measured and characterised under light with the AM 1.5 spectrum and using EQE, the photocurrent density at short circuit (J_{SC}) can be related to the incident spectrum of light that hits the device. Equation 2 shows the relationship between J_{SC} and EQE, where b_S is the incidental spectral photon flux density for energy (E) and q is the electronic charge. [4]

$$J_{SC} = q \int b_S(E) EQE(E) dE \quad (2)$$

In the dark, most photovoltaic devices behave like a diode. Therefore, under an applied bias, a current will flow across the device, often termed the dark current, acting in the opposite direction that the photogenerated current acts. The dark saturation current J_0 is a temperature dependent constant that is a property of the materials used. The dark current reduces the net current of the device from the short circuit value and therefore, the overall current produced by a device, under illumination, at a given applied voltage (V), is described by the sum of the short circuit photogenerated current and the dark current. Thus, the net current density (J) can be described by the ideal diode equation. However, as photovoltaic devices are not ideal diodes, an ideality factor (m) is included to account for any non-ideal behaviour. This is shown in Eq. 3. [4]

$$J = J_{SC} - J_0 \left(\exp {}^{qV}/_{mk_BT} - 1 \right) \quad (3)$$

The voltage that is observed when the net current is zero, is termed the open circuit voltage (V_{OC}). This voltage corresponds to the amount of bias on the solar cell junction that is present from the light generated current. [22] Under illumination, at V_{OC}, the splitting of the Fermi level causes the VB and CB of the perovskite to be flat (see Figure 11). Here the driving force for the collection of the charge carriers is cancelled out by the applied bias on the cell, thus, there is no photocurrent. The splitting of the Fermi levels represents the maximum V_{OC} that is theoretically achievable from the device. [23]

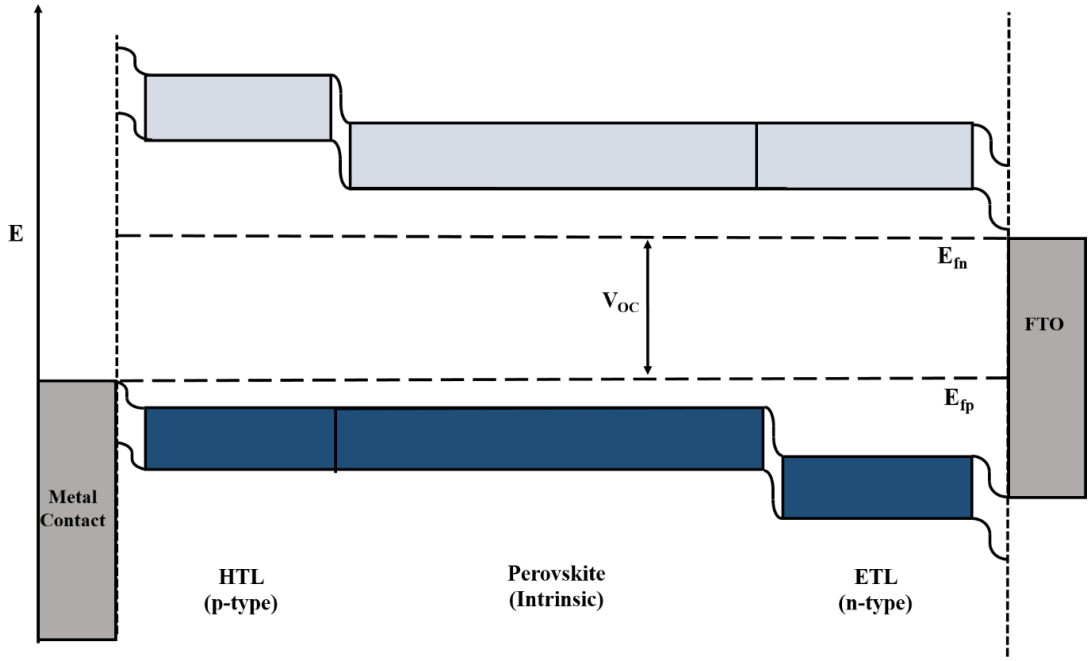

Figure 11: The schematic band diagram of a FTO/TiO_2/$MAPbI_3$/SpiroOMe-TAD/Au PSC under illumination at V_{OC}.

The V_{OC} of a device can be related to the J_{SC} and dark current of the device, using Eq. 4. [4]

$$V_{OC} = \frac{mkT}{q} \ln\left(\frac{J_{SC}}{J_O} + 1\right)$$

(4)

A photovoltaic device will generate power when there is an applied bias at a value between 0 and V_{OC}. Thus, the cell power density (P) can be calculated using Eq. 5. [4]

$$P = JV$$

(5)

The current density and voltage (J-V) characteristics of a photovoltaic device are measured to assess the over performance of the device. To carry out the J-V measurements, a device is placed under AM 1.5 illumination and the voltage is swept between V_{OC} and J_{SC} conditions. Before any measurements begin, a bias, often greater than the expected $V_{OC,}$ is applied to the device. This pre-bias application will cause the current to flow in the opposite direction to that of the photocurrent. The applied voltage will then begin to decrease towards 0 V, this is referred to as the reverse scan. During the reverse scan, when the applied bias reaches the V_{OC}, the net current density will be at a value of 0 mA cm^{-2}. When the applied bias reaches 0 V, the J_{SC} value is obtained. The applied bias then is swept back from 0 V to its original value; this

is referred to as the forward scan. A typical J-V curve that can be obtained from these measurements is displayed in Figure 12.

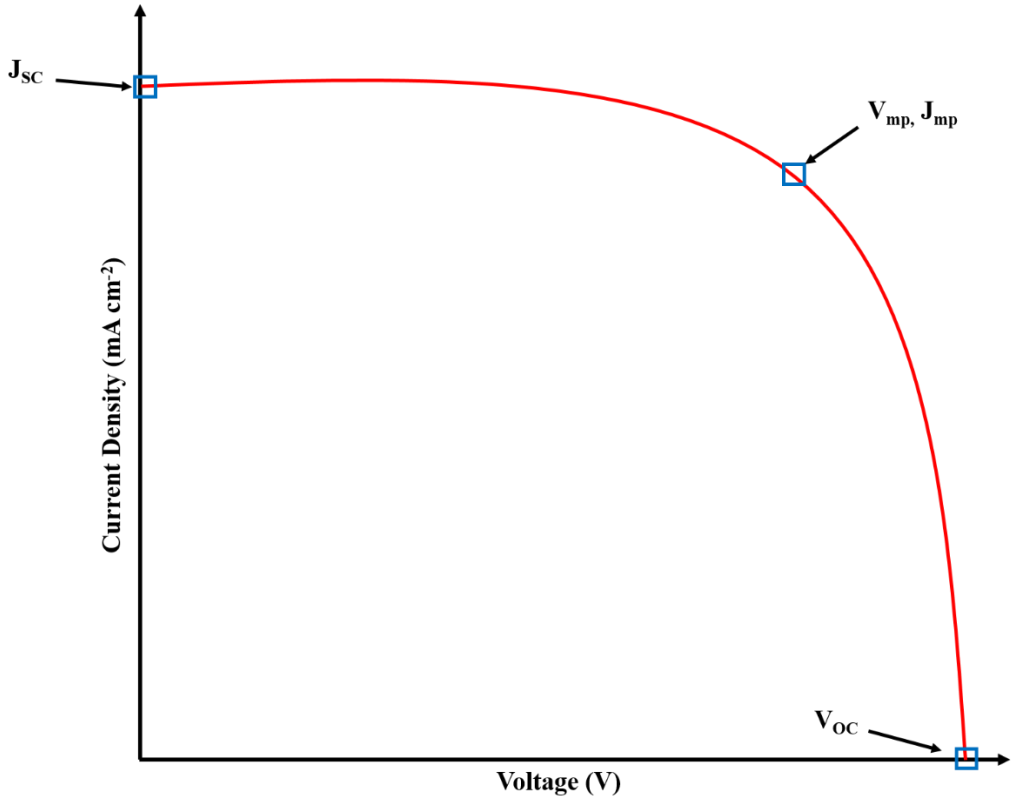

Figure 12: A representation of a current density – voltage (J-V) curve. The J_{SC}, V_{OV} and maximum power point (V_{mp}, J_{mp}) are indicated.

The power density of a device will reach a maximum at a voltage (V_{mp}) that is close to the V_{OC} and at the corresponding current density value (J_{MP}), that is close to the J_{SC}. This point is named the maximum power point (MP). This is the largest J-V product available, thus, to extract the most amount of power available from a device, solar cells should operate at the M_{PP}. [24] The ideal J-V curve would be rectangular and the device would provide a constant J_{SC} value, until the V_{OC} was reached where the current density would drop to 0 V. A term called the fill factor (FF) describes the squareness of the J-V curve, and can be calculated using the MP as shown in Eq. 6.

$$FF = \frac{P_{MP}}{J_{SC}V_{OC}} \quad (6)$$

Any resistance present in the device will have an effect on the FF. The two main parasitic resistances that affect performance are series resistance (R_S) and shunt resistance (R_{SH}). Series resistance arises from how resistive the materials within the solar cells are to current flow,

therefore, a series resistance will has the effect of reducing the FF of a device and a high series resistance will also reduce the J_{SC}. On the other hand, a low shunt resistance means that there are alternative current paths available for the light generated current; this reduces the overall amount of current that flows through the junctions. Shunt resistance also reduces the voltage. Thus, a low shunt resistance has the effect of the reducing the FF of a device. [4, 25]

The FF, V_{OC} and J_{SC}, along with the incident light power density (P_S), can be used to determine the power conversion efficiency (PCE, η) of a solar cell. For light that is equal to 1 sun, the P_S is 1000 W. [4] Eq. 7 gives the equation for calculating the PCE of a device.

$$\eta = \frac{J_{SC} V_{OC} FF}{P_S} \tag{7}$$

The PCE of a device is the parameter that is most commonly used to compare the performance of solar cells and as a result, the conditions of testing must be carefully controlled. Recognised test laboratories, such as those at N-Rel or Fraunhofer-ISE, independently confirm the efficiency of state of the art solar technologies under controlled conditions. [26]

2.4.1. Detailed Balance and the Shockley-Queisser Limit

Fundamentally, detailed balance provides a basis for finding the maximum theoretical efficiency of photovoltaic devices. The upper limit is a consequence of the laws of physics and atomic processes that occur in solar cells. The model considers an ideal case, where the material absorbs light perfectly and is not reflective, so that all photons with energy greater than E_g are absorbed and result in the generation of an electron-hole pair. It is also assumed that there is perfect collection of the charge carriers and radiative recombination is the only allowed recombination route. This means that photocurrent is only a function of the band gap and the incident spectrum of light falling on the device. The net photocurrent of the device is the difference between the absorbed photon flux, which is distributed over a wide energy range over E_g, and the emitted photon flux. The emitted flux is due to the recombination of electrons and holes so is concentrated around photon energies that are close to E_g. As a result, the lower the band gap, the higher the photocurrent. As the voltage applied to a device increases, the photocurrent decreases because the emitted photon flux increases. At the V_{OC}, the total absorbed flux is zero and the net photocurrent is also zero. If the voltage is increased past V_{OC}, the device would act as a light emitting device, with the emitted photon flux exceeding the absorbed photon flux.

The assumption listed above means that the PCE limit a device can approach, is dependent on the band gap energy and the incident spectrum. If the incident spectrum is fixed at AM 1.5, the PCE only depends on the band gap. Figure 13 shows how efficiency varies with the value of E_g.

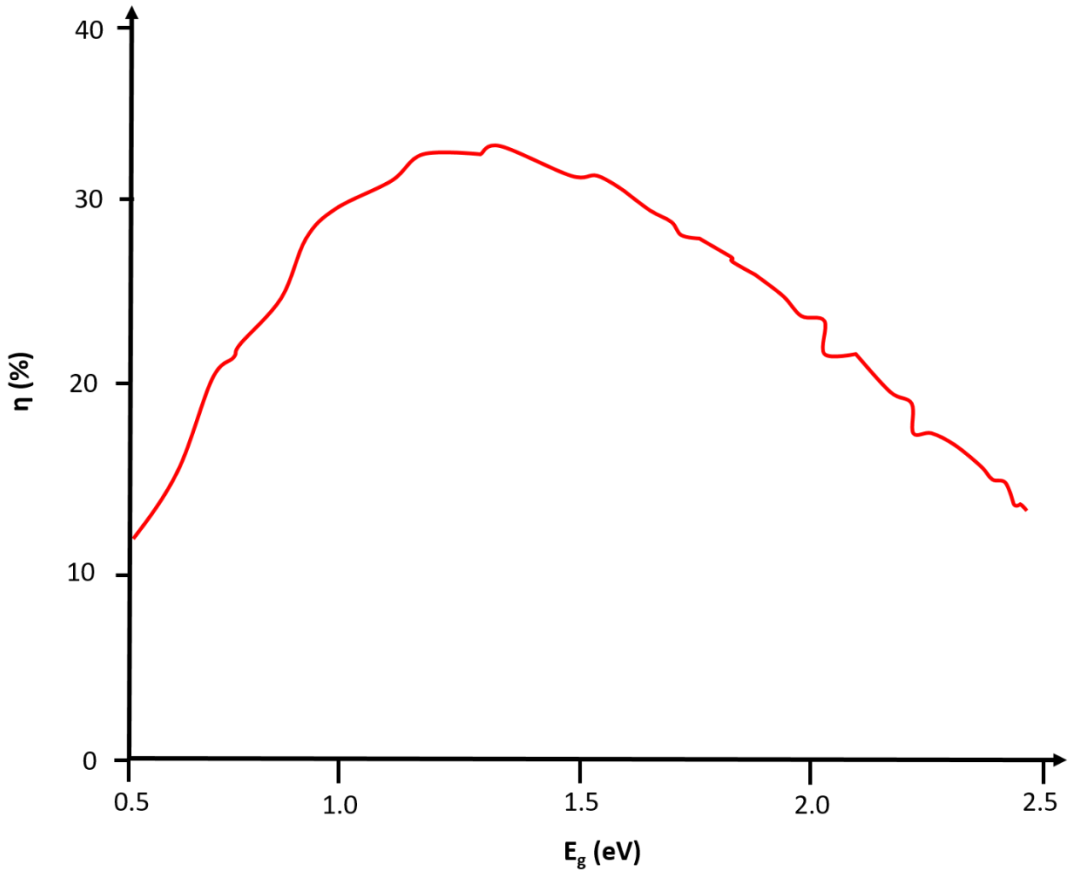

Figure 13: A sketch of the efficiency as a function of the band gap.

At small band gaps, the voltage produced by the device is too small to produce efficient devices as V_{OC} and V_{mp} must always be less than the band gap. On the other hand, if the band gap is too large, whilst the V_{OC} is large, the photocurrent is too small as the proportion of photons with $E \geq E_g$ is small. As a result, the maximum efficiency that can theoretically be reached by a single junction solar cell, hits approximately 33 % at a band gap value close to 1.4 eV. [4, 27]

2.5. Band Gap determination Via the Optical Measurements of Thin Films

Light can be used to examine most of the properties of a semiconductor, thus a range of optical measurements can be useful when characterising them. Absorption spectroscopy can be used

to determine the optical band of a material that lies in the near-infrared, visible and ultraviolet region of the electromagnetic spectrum. This technique is referred to as UV/Vis spectroscopy. At wavelengths of light that have an energy below the band gap, the absorption profile of a semiconductor is zero. However, once wavelengths of light, that have an energy equal to or greater than the band gap, have been reached, the absorption profile increases rapidly.

UV/Vis absorption spectroscopy is commonly used for the characterisation of solutions. Here, a solution in a clear vessel (e.g. a cuvette) is placed directly in the path of light of a given wavelength. When the beam of light hits a solution, some of the incident light will be absorbed by the sample, a small portion of the light will be reflected and the remaining light will be transmitted through the sample. If a clear cuvette is used to measure an absorbing solute, in a non-absorbing solvent, the amount of light that is reflected is small and is often negligible. However, a background scan, using the clear cuvette and solvent can be taken first, to account for the minimal amount of reflection. The relationship between the intensity of the incident light (I_0) and the transmitted intensity (I) allows the amount of light absorbed by the sample to be calculated. The Beer-Lambert law, shown in Eq. 8, describes the absorbance (A) of the sample.

$$A = \log\left(\frac{I_0}{I}\right) = \varepsilon CL \tag{8}$$

According to Beer's law, the amount of light absorbed by the sample, is directly proportional to the number of molecules of the absorbing species that are present in the path of the light. Therefore, the absorbance of a sample can also be related to the extinction coefficient of the sample (ε), the concentration (C), and the path length that the light takes through the sample (L). The molar extinction coefficient is a characteristic of the absorbing species in the chosen solvent that determines how strongly a species absorbs light at a given wavelength. [28]

However. The Beer-Lambert law no longer holds true for a solid thin film that is supported on a substrate. Therefore, it is not possible to directly measure the absorbance of a thin film. Instead, the transmitted and the reflected light is measured separately and then the amount of light that has been absorbed can then be calculated. When it comes to the measurement of thin films, the amount of light that is reflected is no longer negligible and the reflection of light at each of the various interfaces within the sample must be considered. Hence, there is no suitable 'blank' substrate for a solid film. The optical properties of a solid are governed by the interaction between the solid and the electric field of the electromagnetic wave and therefore the interaction between light and a solid is now governed by the progressive wave equation.

Thus, the relationship between the absorption of light in a solid species and the extinction coefficient is different, and is described by Eq. 9.

$$I = I_0 \exp\left(\frac{-4\pi f \varepsilon x}{c}\right)$$

(9)

Here, f is the frequency of light, x is the path length through the solid and c is the speed of light in a vacuum. For a solid, the absorption coefficient (α) can be related to the extinction coefficient as shown in Eq. 10.

$$\alpha = \frac{4\pi f \varepsilon}{c}$$

(10)

Radiation is absorbed by a solid to an extent that depends on both the wavelength of radiation and the thickness of the solid medium. Therefore, α can be described as the reciprocal of the depth of penetration of the incident light into the bulk solid. This gives the relationship shown in Eq. 11. Where x is the thickness of the solid. [29, 30]

$$I = I_0 \, e^{-\alpha x}$$

(11)

The multiple interfaces that the light will encounter within the sample must be considered. The incident light first experiences an interface between the ambient air and the front face of the thin film. Here, a portion of the light will be reflected (R) and the remaining portion of light ($(1\text{-}R)I_0$), will pass through the interface into the film. A fraction of the light will be absorbed by the solid film, as expressed above in Eq. 11, thus, the light intensity that had travelled through the bulk of the film, to the back interface is ($(1\text{-}R)I_0e^{-\alpha x}$). At the back interface, a fraction of the remaining light will be reflected back into the film ($R(1\text{-}R)I_0e^{-\alpha x}$). The leftover fraction of light ($(1\text{-}R)^2I_0e^{-\alpha x}$) is transmitted out of the back of the film. This is the light that is available to be detected.

However, the light reflected internally into the film, will travel through the thin film again to the front interface. Again some light is absorbed by the film during this process, so the light hits the front interface with an intensity of $R(1\text{-}R)I_0e^{-2ax}$. Here, some light is transmitted out of the front face of the film, whilst another internal reflections occurs. This process happens repeatedly inside the thin film and is depicted in Figure 14. [31, 32]

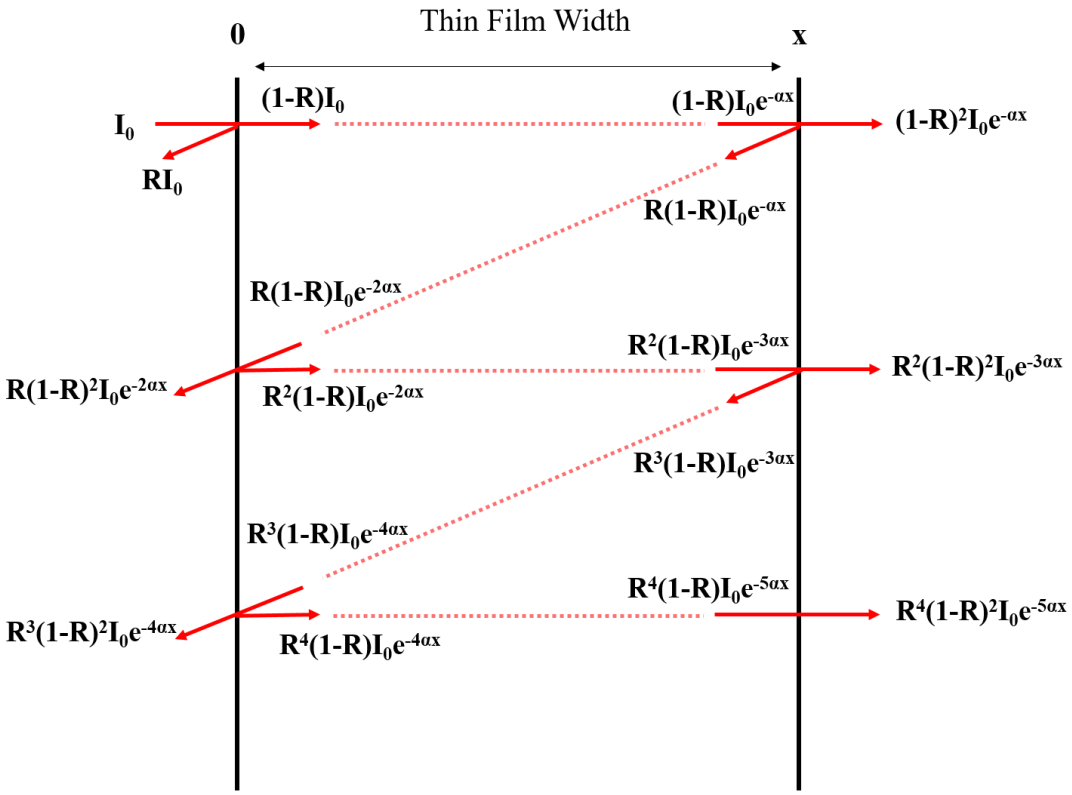

Figure 14: A schematic diagram of the interaction of light within a thin film.

The overall transmittance is a sum of all of the light, which is lost out of the back of the film. It can be expressed by the infinite series, shown in Eq. 12.

$$T = (1-R)^2 I_0 e^{-\alpha x} + R^2(1-R)^2 I_0 e^{-3\alpha x} + R^4(1-R)^2 I_0 e^{-5\alpha x} + \cdots \quad (12)$$

However, for ease, this series can be simplified to Eq. 13. [31]

$$T = \frac{(1-R)^2 e^{-\alpha x}}{(1-R)^2 e^{-2\alpha x}} \quad (13)$$

For materials which are highly absorbing, the αx term is very large and thus the second term in the denominator can be approximated to 0. This yields Eq. 14. This is case for most materials that are used as absorbers for solar cells.

$$T = (1-R)^2 e^{-\alpha x} \quad (14)$$

Thus, the absorbance can be calculated through the combination of Eq. 14 with Eq.11 and Eq. 8. This gives Eq. 15 and Eq. 16. [33]

$$T = \frac{I}{I_0}(1-R)^2$$

(15)

$$A = -\log\left(\frac{T}{(1-R)^2}\right)$$

(16)

The collection of the transmission spectrum is simple. The solid thin film, it is placed into the path of the beam and the light that is transmitted out of the other side is collected as the transmission spectrum. However, the reflection spectrum is more complicated. The overall reflection of the film is made up of the specular and diffuse reflections. Specular reflection occurs when the reflected light has an angle of reflection that matches the angle of incidence. The amount of specular reflection is higher in thin films with a smoother surface. The diffuse reflection has no singular defined angel of reflection and the light is reflected back at all angles. Thin films with a rougher surface have more diffuse reflection. [31] As a result, both types of reflection must be measured to obtain the reflection spectrum. To measure the reflection spectrum, the thin film is placed at the back of an integrating sphere. However, it is important that a low angle (often 8°) wedge is placed between the sphere and the sample. When the light hits the sample, the diffuse reflection is reflected back at all angles, thus the light is caught within the integrating sphere and collected. The 8° wedge is important for the measurement of the specular reflection. This prevents the problem whereby if the thin film surface was placed directly perpendicular in the path of the beam, the specular reflection would be reflected back in the direction of the incident beam, exiting the integrating sphere without being collected. With the use of the 8° wedge, the specular reflection is offset from the incident beam by 8°, causing it to be collected by the integrating sphere. Whilst this measurement provides a sufficiently good approximation of the reflection of a thin film sample, it is not completely accurate.

2.5.1. Tauc Plots

To estimate the band gap, it is possible to plot the thin film absorption vs photon energy. The point of the absorption onset is indicated by a sharp linear rise in absorption. The onset in absorption is caused by the band to band transition of electrons, when energy greater than the band gap energy is absorbed. The point of the onset can then be interpolated along the linear region of the graph to the X axis, where the band gap value can be determined. This method can provide an estimate of the band gap of a material. However, there can be issues when a material has multiple band edges at similar energies. Multiple band edges can occur as a result

of defects in the semiconductor crystal. Defects can result in a spread of energy levels and cause the density of states near the CB minima and VB maxima to decay with energy into the band gap, instead of there being a sharp cut off. Defects are particularly common on the surface of a thin films, due to the loss of coherence of the crystal at the surface. To make up for this, the surface atoms will relax in an attempt to minimise the surface energy. Consequently, the crystal lattice and the molecular orbitals at the surface will distort. These defects cause a slight difference in the band gap at varying points across the surface of the thin film, resulting in a more gradual absorption onset. This gradual onset is referred to as the Urbach tail. [4, 34] The Urbach tail can make determination of the onset more difficult, meaning it is hard to accurately determine the band gap. Thus, to mitigate these effects, the Tauc transformation can be performed on the data and a Tauc plot can be constructed. This requires a mathematical transformation which minimises the contribution of the Urbach tail. [35]

To conduct the Tauc transformation, $(\alpha h\nu)^{1/r}$ is plotted Vs photon energy, where α is the absorption coefficient, $h\nu$ is the photon energy and r corresponds to the type of band transition that is responsible for the absorption onset. For a direct, allowed transition r = ½. The Tauc plot will be flat at energies below the band gap. [36] The gradient of the plot will increase rapidly around the band gap energy and will become linear. By extrapolating the linear region of the plot towards the X axis intercept, the band gap energy can be found. In the case that the thickness of the thin film is unknown, the value of αx can be used instead and $(\alpha x h\nu)^{1/r}$ can be used for the Tauc transformation. This does not affect the overall shape of the Tauc plot, but has the effect of altering the scale of the plot. Nonetheless, the determination of the band gap does not change. Figure 15 demonstrates the Tauc plot.

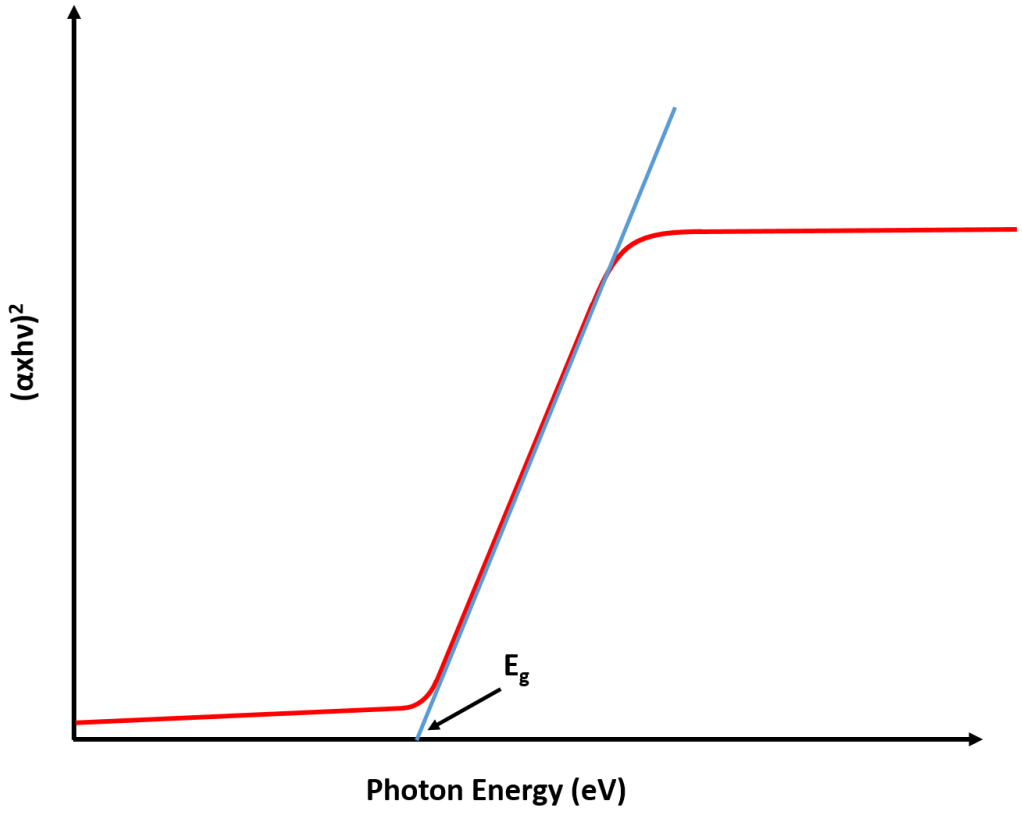

Figure 15: A sketch of a Tauc plot, indicating the band gap energy (E_g)

2.6. Using semiconductors for Water Splitting

Water splitting is the first step of photosynthesis and requires the conversion of water into hydrogen and oxygen gas, through the overall chemical equation shown in Eq. 17.

$$2H_2O\ (l) \rightarrow 2H_2\ (g) + \ O_2\ (g)$$

(17)

This can be split into two half equations; the water oxidation (oxygen evolution) and the water reduction (hydrogen evolution) equations, shown in Eq. 18 and 19 respectively. These equations describe water splitting under acidic conditions.

$$2H_2O\ \rightarrow 4H^+ + \ O_2 + 4e^-$$

(18)

$$4H^+ + 4e^-\ \rightarrow\ 2H_2$$

(19)

The water oxidation reaction has a required potential of 1.23 V (Vs SHE) whereas the water reduction reaction requires 0 V (Vs SHE). Thus, the overall water splitting reaction has a required thermodynamic potential of 1.23 V (Vs SHE). This means that water splitting is a process that is not thermodynamically spontaneous and it requires external energy. [37] However, due to the kinetic barriers of transferring four electrons, additional energy, above 1.23 V, is required. This extra energy is termed the overpotential. Water oxidation catalysts are often used to help reduce the amount of overpotential required. [38] When the required external voltage is applied to the electrodes, water oxidation occurs at the anode and water reduction occurs at the cathode. During the oxidation process, electrons are transferred from the water to an acceptor state in the electrode.

It is possible to use wide band gap semiconductors to provide the potential required for water oxidation. This can occur simply by placing the illuminated semiconductor in contact with the electrolyte as the photoanode. The holes that are generated by the semiconductor photoelectrochemical (PEC) anode are able to oxidise the water molecules, and the electrons flow around the circuit to the cathode. Consider a PEC electrode consisting of a thin layer of a semiconductor. A barrier junction is established at the interface between the surface of a semiconductor and liquid electrolyte. If the electrolyte contains a redox couple, charge can be transported to and from the surface of the semiconductor. Charge transfer will occur across the interface until equilibrium is established and the Fermi level of the semiconductor is equal to the redox potential of the electrolyte. This establishes a space charge layer in the semiconductor and causes there to be an electric field at the interface; this is essential for charge separation. This is shown in Figure 16. There will also be a built in bias, established in the dark condition, due to the difference in the vacuum levels of the semiconductor and counter electrode (CE)

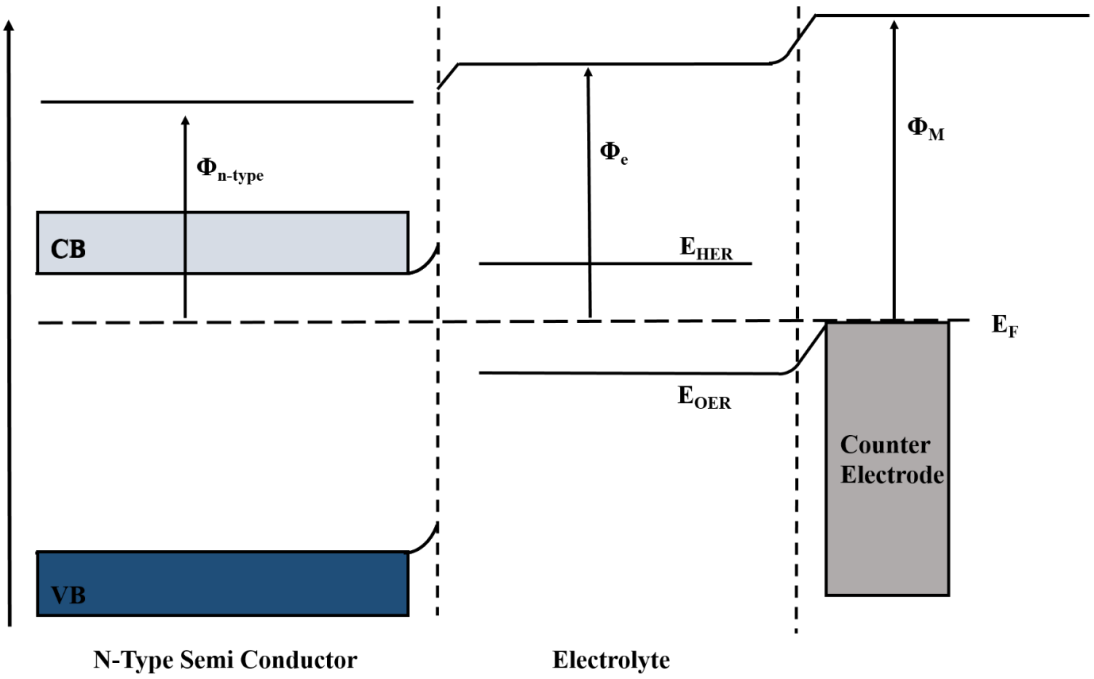

Figure 16: A schematic band diagram of an n-type semiconductor-electrolyte heterojunction at equilibrium. E_{HER} and E_{OER} are the standard potentials for the hydrogen evolution reaction and the oxygen evolution reaction respectively. $\Phi_{n\text{-}type}$ denotes the work function of the n-type semiconductor, Φ_e denotes the work function of the electrolyte and Φ_M denotes the work function of the metal counter electrode.

As a result of the space charge region in the semiconductor, a balancing charged layer is formed in the electrolyte. This layer is called the Helmholtz double layer, and results from a redistribution of ions or solvent molecules at the surface to counter the charge of the semiconductor surface; thus, there is a small potential drop across this layer. When a potential is applied to the metal counter electrode, the potential drops across the double layer at the electrode surface, as shown in Figure 16. The electrolyte has a redox potential (E°), referenced to the standard hydrogen electrode (SHE), this is essentially the Fermi level of the solution. [39] The electrolyte also has two energy levels, that of the oxidised form and that of the reduced form. In the case of water, this equates to the oxygen and hydrogen gas products from the oxygen evolution reaction (OER) and the hydrogen evolution reaction (HER). We can relate these to the standard potential energies for the two evolution reactions that occur simultaneously at the anode (OER) and the cathode (HER), these should be theoretically separated by 1.23 V. In order for water oxidation and reduction to occur, the energy levels of the electrolyte should lie within the band gap of the semiconductor, thus the semiconductor needs a band gap wide enough to accommodate this requirement. The three potentials are pH dependant, the position of these energies will change with respect to the vacuum level, however, the relative energy gap between the CB edge, and E_{HER} is not affected by pH. [40]

Under illumination, the Fermi level in the semiconductor will split, thus the concentrations of the photogenerated electron-hole pairs are defined by the quasi fermi levels. The quasi-Fermi levels are a representation of the electrochemical potential of the electrons and holes under illumination. [41] The redox potential of the electrolyte does not change. The band bending at the interface is also reduced. Figure 17, demonstrates the system under illumination.

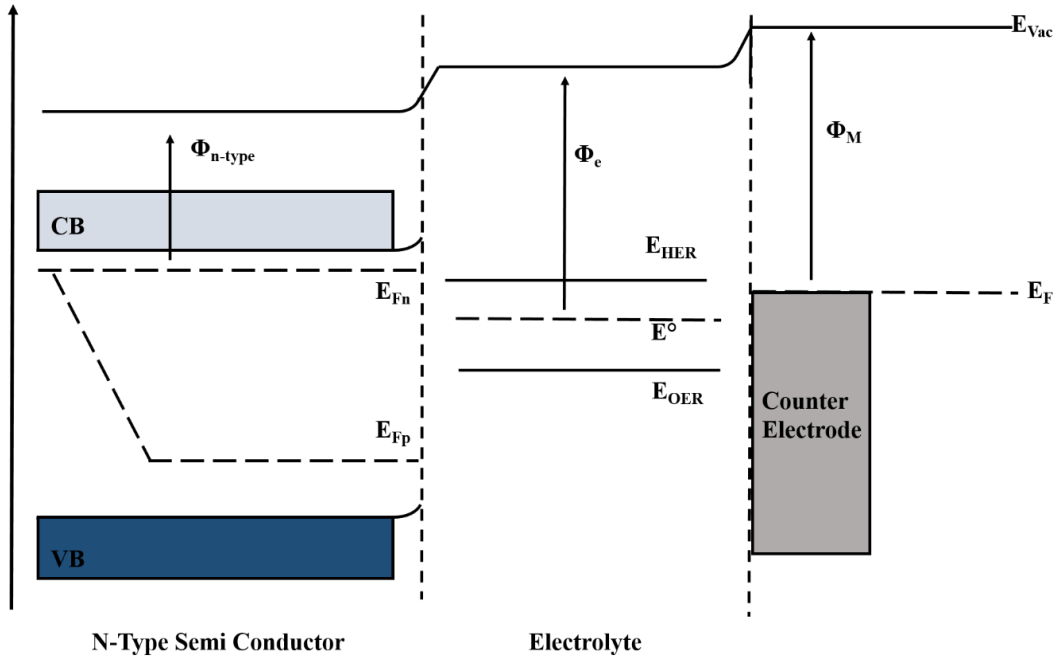

Figure 17: A simplified schematic band diagram of an n-type semiconductor-electrolyte heterojunction under illumination

Depending on the type of semiconductor doping, under illumination with light with $E \geq E_g$, charge carriers will be generated within the semiconductor and electrons will be transferred either to or from the semiconductor surface. In the case of the n-type semiconductor in Figure 17, electrons can flow from the electrolyte to the semiconductor surface, as there are unfilled energy levels in the conduction band of the semiconductor, that can accept an electron from the solution. Therefore, the semiconductor surface gains a negative charge. The electrolyte, close to the semiconductor working electrode (WE) gains a positive charge producing a photovoltage. The photovoltage can be described as a product of the electrostatic raising of the semiconductor Fermi level with respect to the redox potential. [42] The field in the space charge region means that photogenerated holes are able to flow from the semiconductor to the electrolyte, oxidising the water molecules. At the same time, the photogenerated electrons can flow through the external circuit, to the counter electrode (CE) to reduce the water. However, this will only occur if the VB potential is more positive than E_{OER} and the CB potential and the counter electrode Fermi level is more negative than $E_{HER.}$ [41] As a result, often the

application of an external bias is needed to raise the level of the CB and the E_{Fn}. A simplified band diagram of this is shown in Figure 18.

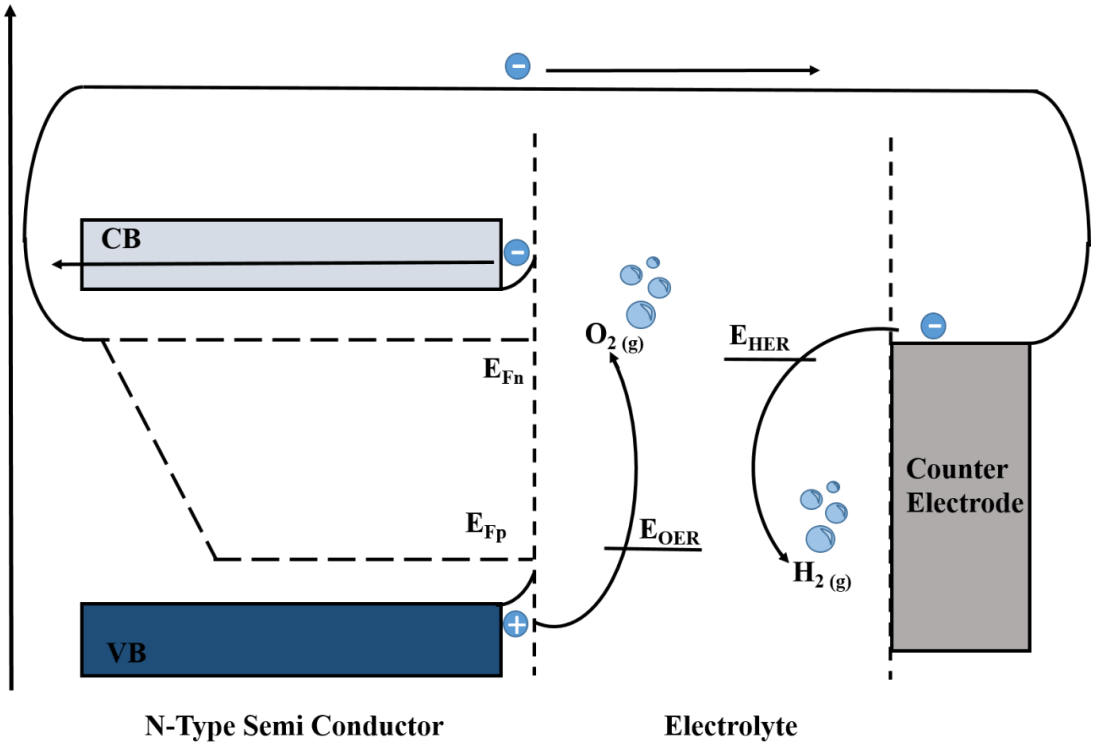

Figure 18: A simplified energy diagram for a n-type semiconductor photoannode, depicting water oxidation at the surface of the photoanode WE and water reduction at the cathode CE.

The Faradaic efficiency is a useful parameter for determining how efficient photoanodes are and can also help to verify that the photocurrent produced is a product of water splitting and is not due to photocorrosion of the electrodes. It is expressed as a ratio of the experimental gas evolution vs the theoretical gas evolution; this is shown in Eq. 20.

$$Faradaic\ Efficiency = \frac{Oxygen\ Evolution\ Measured}{\left(\frac{\left(\frac{J_{photo}\,A\,T}{e}\right)}{4}\right) / N_A}\ x\ 100\ \%$$

(20)

The theoretical gas evolution is calculated using J_{photo} as the photocurrent density (A cm^{-2}) that is generated over a time T (s), A is the illuminated area of the photoelectrode (cm^2), e is the charge of an electron and N_A is Avogadro's constant. The incident photon to current efficiency (IPCE) can also be used to assess the efficiency of a photoanode. Here the current is measured across a range of fixed incident wavelengths and the IPCE is defined as the number of photogenerated charge carriers that contribute to the photocurrent, per incident photon.

The solar to hydrogen conversion efficiency (η_{STH}) is also commonly quoted. The solar to hydrogen conversion efficiency expresses the ratio between the total energy input from sunlight at 1 sun irradiation and the total generated energy. This is expressed in Eq. 21.

$$\eta_{STH} = \frac{\Delta G\, r_{H2}}{P_{sun}\, A}$$

(21)

Where ΔG is the Gibbs free energy for the water splitting reaction of 237 kJ mol^{-1}, r_{H2} is the rate of the hydrogen production (mol s^{-1}), P_{sun} is the light intensity and A is the area of the illuminated photoelectrode (cm^2). [41] However, if an external bias is applied to the system, then added electrical energy must be subtracted. The solar to hydrogen efficiency can also be calculated easily using the Faradaic efficiency. [43] The equation is shown is Eq 22.

$$\eta_{STH} = \frac{J * 1.23\, V * \eta_F}{P_{Sun}}$$

(22)

Using a simple semiconductor surface as the photoanode presents some disadvantages. Many materials will react or degrade upon contact with water, especially under illumination. This is the case with perovskite materials. As a result, full photovoltaic devices can be protected or encapsulated and water oxidation can take place on the front surface of the device. [44] However, the band diagram here is more complicated, due to the multiple layers used in the device. This creates additional junctions within the device and the properties of the protecting layer, where the water oxidation reaction occurs, must also be considered.

2.7. References

1 J. Singleton, *Band theory and electronic properties of solids*, Oxford University Press, 7th edn., 2001.

2 M. L. Cohen and J. R. Chelikowsky, *Electronic Structure and Optical Properties of Semiconductors*, Springer, Berlin, 1989.

3 M. Fukuda, *Optical Semiconductor Devices*, John Wiley & Sons, Ltd, 1st edn., 1999.

4 J. Nelson, *The Physics of Solar Cells*, Imperial College Press, London, 1st edn., 2003.

5 Z. Yang, A. Surrente, K. Galkowski, N. Bruyant, D. K. Maude, A. A. Haghighirad, H. J. Snaith, P. Plochocka and R. J. Nicholas, *J. Phys. Chem. Lett.*, 2017, **8**, 1851–1855.

6 G. Li, P. Fu, Q. Yue, F. Ma, X. Zhao, S. Dong, X. Han, Y. Zhou and J. Wang, *Chem Catal.*, 2022, **2**, 1734–1747.

7 W. P. Dumke, *Phys. Rev.*, 1957, **105**, 139–144.

8 W. Shockley and W. T. Read, *Phys. Rev.*, 1952, **87**, 835–842.

9 J. H. Yang, L. Shi, L. W. Wang and S. H. Wei, *Sci. Rep.*, 2016, **6**, 21712.

10 A. Haug, *J. Phys. Chem. Solids*, 1988, **49**, 599–605.

11 N. Satō, *Electrochemistry at metal and semiconductor electrodes*, Elsevier, 1998.

12 J. Piprek, *Semiconductor Optoelectronic Devices*, Academic Press, 2003, vol. 9.

13 C. S. Solanki, *Solar photovoltaics : fundamentals, technologies and applications*, PHI Learning, 2015.

14 PV Lighthouse, https://www.pvlighthouse.com.au/cms/lectures/altermatt/principle/illumination, (accessed 22 October 2022).

15 R. Singh and B. J. Baliga, in *Cryogenic Operation of Silicon Power Devices*, Springer, Boston, MA, 1998, pp. 37–48.

16 N. Wu, D. Walter, A. Fell, Y. Wu and K. Weber, *J. Phys. Chem. C*, 2020, **124**, 219–229.

17 G. Richardson, S. E. J. O'Kane, R. G. Niemann, T. A. Peltola, J. M. Foster, P. J.

Cameron and A. B. Walker, *Energy Environ. Sci.*, 2016, **9**, 1476–1485.

18 S. Van Reenen, M. Kemerink and H. J. Snaith, *J. Phys. Chem. Lett.*, 2015, **6**, 3808–3814.

19 F. Cao, M. Wang and L. Li, *Nano Sel.*, 2020, **1**, 152–168.

20 L. Kavan, *Catal. Today*, 2019, **328**, 50–56.

21 X. Cao, G. Zhang, Y. Cai, L. Jiang, Y. Chen, X. He, Q. Zeng, Y. Jia, G. Xing and J. Wei, *Appl. Surf. Sci.*, 2020, **529**, 147119.

22 Open-Circuit Voltage | PVEducation, https://www.pveducation.org/pvcdrom/solar-cell-operation/open-circuit-voltage, (accessed 23 October 2022).

23 I. Mora-Seró, *Joule*, 2018, **2**, 585–587.

24 S. J. Fonash, *Solar cell device physics*, Academic Press/Elsevier, 2010.

25 Shunt Resistance | PVEducation, https://www.pveducation.org/pvcdrom/solar-cell-operation/shunt-resistance, (accessed 27 October 2022).

26 Best Research-Cell Efficiency Chart | Photovoltaic Research | NREL, https://www.nrel.gov/pv/cell-efficiency.html, (accessed 31 August 2022).

27 W. Shockley and H. J. Queisser, *J. Appl. Phys.*, 1961, **32**, 510–519.

28 D. N. Sathyanarayana, *Electronic absorption spectroscopy and related techniques*, Universities Press, 2001.

29 M. Quinten, *Optical Surface Metrology – Physical Basics*, Springer, Cham, 2019.

30 Absorption and extinction coefficient theory, https://www.reading.ac.uk/infrared/technical-library/substrate-optical-theory-introduction/absorption-and-extinction-coefficient-theory, (accessed 28 October 2022).

31 S. Perkowitz, *Optical characterization of semiconductors : infrared, Raman, and photoluminescence spectroscopy*, Academic Press, 1993.

32 O. S. Heavens, *Rep. Prog. Phys*, 1960, **23**, 1–5.

33 J. Gong and S. Krishnan, *Dye-Sensitized Solar Cells*, Academic Press, 2019.

34 L. . Freund and S. Suresh, *Thin Film Materials: Stress, Defect Formation and Surface Evolution*, Cambridge University Press, 2003.

35 J. Tauc, R. Grigorovici and A. Vancu, *Phys. status solidi*, 1966, **15**, 627–637.

36 O. (Olaf) Stenzel, *The physics of thin film optical spectra : an introduction*, Springer, 2005.

37 R. Sen, S. Das, A. Nath, P. Maharana, P. Kar, F. Verpoort, P. Liang and S. Roy, *Front. Chem.*, 2022, **10**, 414.

38 S. W. Sheehan, J. M. Thomsen, U. Hintermair, R. H. Crabtree, G. W. Brudvig and C. A. Schmuttenmaer, *Nat. Commun.*, 2015, **6**, 1–9.

39 H. Reiss, *J. Phys. Chem.*, 1985, **89**, 3783–3791.

40 T. T. Hien, N. D. Quang, C. Kim and D. Kim, *Nano Energy*, 2019, **57**, 660–669.

41 C. Jiang, S. J. A. Moniz, A. Wang, T. Zhang and J. Tang, *Chem. Soc. Rev.*, 2017, **46**, 4645–4660.

42 B. Miao, A. Iqbal and K. H. Bevan, *J. Phys. Chem. C*, 2019, **123**, 28593–28603.

43 O. J. Alley, K. Wyatt, M. A. Steiner, G. Liu, T. Kistler, G. Zeng, D. M. Larson, J. K. Cooper, J. L. Young, T. G. Deutsch and F. M. Toma, *Front. Energy Res.*, 2022, **10**, 685.

44 I. Poli, U. Hintermair, M. Regue, S. Kumar, E. V. Sackville, J. Baker, T. M. Watson, S. Eslava and P. J. Cameron, *Nat. Commun.*, 2019, **10**, 2097.

Chapter 3. Experimental Methods

3.1. $CsPbBr_3$ Thin Film Deposition and Solar Cell Fabrication Materials and Methods

All processes were conducted in ambient conditions, outside of a glovebox.

3.1.1. FTO Glass Preparation

Fluorine-doped Tin Oxide glass (TEC 15), with a thickness of 2.3 mm and resistivity of 15 Ω/sq (Sigma-Aldrich) was cut into 2.5 x 2.5 cm pieces. A line with ~ 5 mm thickness, was etched from one edge of the glass slide, using 2 M HCl and Zn powder (Sigma-Aldrich).

The cut and etched FTO glass was then cleaned thoroughly. It was placed in a vertical staining jar filled with 2% Hellmanex in deionised water and sonicated in an ultrasonic bath at 60 °C for 15 min. The Hellmanex solution was discarded and the jar was then sequentially filled with deionised water, acetone, isopropanol and ethanol. The glass was rinsed with deionised water and ultra-sonicated at 60°C between each step. The cleaned glass was dried quickly with nitrogen gas and placed in a UV/Ozone cleaner for 20 min before use.

3.1.2. c-TiO_2 Deposition

The *c*-TiO_2 precursor solution was prepared by diluting 549 µL of titamium diisopropoxide(bisacetylacetoneate) (75 wt% in IPA) (Sigma-Aldrich) in 10 mL of EtOH. The FTO glass substrates were preheated in a furnace at 500 °C for 10 min, before being transferred to a covered hotplate at 500 °C. The TiO_2 precursor solution was sprayed, using a chromatography sprayer, onto the surface of the substrates, whilst on the hotplate, periodically over 4 min at 30 s intervals. The substrates were then post annealed at 500 °C for 10 min in a furnace.

3.1.3. m-TiO_2 Deposition

The *m*-TiO_2 layer was deposited as follows. 30 NR-D titania paste (Greatcell Solar) diluted with EtOH (150 mg/mL) and stirred vigorously overnight. The solution was deposited onto the substrates through spin-coating 100 µL of solution at 4000 rpm for 10 s, before being dried on a hotplate at 120 °C for a few minutes, then annealed at 350 °C for 15 min and then further annealed in a furnace at 550 °C for 15 min. After cooling, the *m*-TiO_2 was doped with lithium using a solution of bis(trifluoromethane)sulfonimide lithium in acetonitrile (10 mg/mL). 100

μL of the solution was spin coated onto the substrates at 3000 rpm for 10 s, before being dried at 120 °C, then annealed at 350 °C and 550 °C for 15 min each.

3.1.4. SnO_2 Deposition

A solution of tin oxide (IV) (15 % in H_2O colloidal dispersion) (Alfa Aesar) and deionised water was prepared in a 1:5 ratio and placed in an ultrasonic bath at room temperature for 10 min. The solution was then filtered using a 0.45 μm PTFE filter. 130 μl of the filtered solution was spin coated onto the c-TiO_2 substrates at 4000 rpm for 30 s. The substrates were then annealed on a hot plate at 180 ° C for 1 h.

3.1.5. $PbBr_2$ Deposition

The $CsPbBr_3$ perovskite layer was deposited using a two-step method. A 1 M solution of $PbBr_2$ was prepared by dissolving $PbBr_2$ (98 %) (Sigma-Aldrich) in DMF (anhydrous) (Sigma-Aldrich) and stirred at 70 °C, before being filtered using a 0.45 μm PTFE filter. The substrates were held at 70 °C for ~ 5 min before 120 μL of $PbBr_2$ was deposited via spin coating at 2500 rpm for 30 s. The substrates were then annealed at temperatures between 70 - 90 °C for 45 min. After cooling to room temperature the $PbBr_2$ was converted to $CsPbBr_2$.

3.1.6. $CsPbBr_3$ Conversion

3.1.6.1. Dipping Method

A 0.08 M CsBr solution was prepared by dissolving CsBr (99.9 %) (Sigma-Aldrich) solution in MeOH at 50 °C. Glass staining jars were also preheated at 50 °C. The CsBr/MeOH solution was placed into the warmed staining jars and the $PbBr_2$ substrates were then immersed in the solution for 50 min, whilst the temperature was held at 50 °C. The substrates were then annealed on a hotplate 250 °C for 30 min.

3.1.6.2. Spin Coating Method

A 0.07 M CsBr solution was prepared by dissolving CsBr (99.9 %) (Sigma-Aldrich) solution in MeOH at 50 °C. 100 μL of the CsBr solution was deposited onto the substrates and left on the surface for 5 s, before spin coating at 3000 rpm for 30 s. The substrates were annealed at 250 °C for 5 min. The spin coating and annealing process is then repeated as many times as was necessary to achieve full conversion from $PbBr_3$ to $CsPbBr_3$. Often this process was repeated seven times.

3.1.7. Carbon electrode deposition

The substrates were cut in half. A carbon electrode was deposited directly on top of the $CsPbBr_3$ layer via doctor blading of the carbon paste (Sun Chemical) and the substrates were annealed in a furnace at 360 °C for 30 min. Finally silver conductive paint (RS Components) was painted on to the cells to create contacts.

3.1.8. B Site Substitution in $CsPbBr_3$

The following metal-bromide salts were used: $ZnBr_2$ (Anhydrous, 99.99 %) (Sigma-Aldrich), CuBr (Anhydrous, 99 %) (Sigma-Aldrich), $NiBr_2$ (Anhydrous, 99.99 %) (Sigma-Aldrich), $CoBr_2$ (Anhydrous, 97 %) (Alfa Aesar), $FeBr_2$ (Anhydrous, 98 %) (Sigma-Aldrich), $MnBr_2$ (Anhydrous, 99 %) (Alfa Aesar) and $TbBr_3$ (Anhydrous, 99.99 %) (Sigma-Aldrich). The powdered metal-bromide salts were added to $PbBr_2$ in the required ratios (0.2, 0.5, 1.0 and 3.0 %) and dissolved in DMF (anhydrous) (Sigma-Aldrich). The solutions were heated and stirred at 80 °C until dissolved and a clear solution was achieved. Sonication in a water bath at 80 °C was required for $NiBr_2$, $FeBr_2$ and $MnBr_2$. The metal ion containing $PbBr_2$ solutions were filtered using a 0.45 μm PTFE filter, and then deposited onto the substrate as described in section 3.1.5. The films were then converted to $CsPb_{1-X}M_XBr_3$ using the method described in section 3.1.5.

The $CsPb_{1-X}M_XBr_3$ devices were fabricated following the procedures described throughout section 3.1.

3.2. $CsPbBr_3$ Devices for Water Oxidation

3.2.1. $CsPbBr_3$ Device Encapsulation

Planar carbon $CsPbBr_3$ devices were encapsulated, first by sticking a self-adhesive graphite sheet (GS) (Panasonic, 1000W m^{-1} K^{-1}), with a thickness of either 25, 70 or 160 μm on top of the carbon layer. These encapsulated devices formed with TiO_2|$CsPbBr_3$|Carbon|GS photoanodes.

The device was then placed in front of a Teflon block, with a 1 cm diameter hole cut out and O-ring around the edges on either side. A glass microscope slide was placed the other side of the Teflon block and the stack was clamped together.

3.2.1.1. Graphite Sheet Preparation

Before being placed on the $CsPbBr_3$ device, the GS was soaked in a solution of [2-(pyridine-2-yl)-2 propanato]iridium(IV) dimer solution (1 mM in 0.1 M aqueous $NaIO_3$, Strem Chemicals) for 48 h. The GS was rinsed with deionised water and air dried.

3.2.1.2. Graphite Sheet Ozone Treatment

In some cases, the GS was pre-treated with UV/ozone before the WOC was applied. The GS was placed in a UV/Ozone cleaner for 2 h.

3.2.1.3. Graphite Sheet K_2HPO_4 Treatment

In some cases, the GS was pre-treated with K_2HPO_4 (1 M, aqueous) and held at 2 V Vs Ag/AgCl for 1 h.

3.2.1.4. Graphite Sheet without Adhesive Layer

In some cases, it was required to attach a GS layer, without the self-adhesive layer, to the $CsPbBr_3$ device. In this case, during the fabrication of the $CsPbBr_3$ devices, described in section 3.1, after the Carbon paste was applied (section 3.1.7), it was annealed at 100 °C for 5 min. A small amount of carbon paste was applied to one side of the GS using a cocktail stick, and the GS was then placed onto the carbon electrode of the $CsPbBr_3$ device. Pressure was applied to the GS, using a microscope slide, to ensure good contact with the carbon electrode below. A small weight was placed onto of the GS and the $CsPbBr_3$|GS devices were annealed at 360 °C for 30 min.

3.2.1.5. Graphite Sheet TiO_2 Treatment

In the cases where it was required to deposit c-TiO_2 onto the non-adhesive GS, the GS was first pre-heated in a furnace at 500 °C for 5 min. The TiO_2 precursor solution was prepared as described in section 3.1.2. The pre-heated GS substrates were placed onto a hot plate at 500 °C, and the TiO_2 precursor solution was sprayed onto the GS periodically at 30 s intervals. The substrates were sprayed between 4 and 12 times.

3.3. Characterisation methods

The common methods that have been used to characterise the materials and devices are outlined below. These methods have been used throughout the work in this thesis, unless stated otherwise.

3.3.1. X-ray Diffraction

Powder X-ray diffraction (XRD) patterns were collected from thin film samples using a STSDI P diffractometer in reflection mode. Cu Kα radiation (λ= 1.54056 Å) was used at 298 K.

3.3.2. UV/Vis Spectroscopy

Optical thin film transmission and reflectance measurements were obtained using a Perkin-Elmer Lambda 650S UV/Vis spectrometer. Baseline measurements were taken using FTO glass. Both transmission and reflectance measurments were collected in % T mode between the range of 800 – 350 nm. Tauc plots were constructed by plotting $(\alpha x h\nu)^{1/r}$ against the photon energy in eV. Where α is the absorption coefficient, x is the unknown thickness of the thin film and r = ½, corresponding to a direct and allowed transition. This is described in detail in Chapter 2. The absoption coefficient, αx, was calculated using Eq.1, where R is the reflectance and T is the transmission of light through a thin film.

$$\alpha x = \ln\left(\frac{(1-R)^2}{T}\right) \quad (1)$$

3.3.3. Atomic Force Microscopy (AFM)

AFM images were taken using a Nanosurf easy scan 2 FlexAFM system in phase contrast mode, using a ContAl-G tip.

3.3.4. J-V Measurements

J-V curves were measured using a solar simulator, Class AAA, with a HMI Lamp (200 W/ 70 V) under AM1.5, 1 sun light intensity and a Keithley 2601 A potentiostat. To calibrate the

light, a WPVS reference cell (Fraunhofer ISE) was used in accordance with international standard requirements of IEC 60904-2. Only the active area of the device was exposed and the non-active area was masked. The device was held at 1.6 V under illumination for 5 s, before scanning in reverse. The voltage was swept from 1.6 V to 0 V and then back to 1.6 V. A scan rate of 100 mV s^{-1} was used.

3.3.5. Incident Photon to Current Efficiency (IPCE) Measurement

The incident photon to current efficiency (IPCE) measurements were performed from 800 nm to 350 nm, with the light source passing through a monochromator. Calibration was carried out using a Bentham GaAs reference photodiode (0.47 PD) and this reference photodiode was used to assist the calculation of the IPCE of the measured device. The IPCE values were calculated as shown in Eq. 2. Where i_{sample} is the current measured from the sample, i_{Dioide} is the current measured from the reference diode and QE is the quantum efficiency of the reference diode.

$$IPCE = \frac{i_{Sample}}{i_{Didode}} \, x \, QE_{Didode} \qquad (2)$$

3.3.6. Scanning Electron Microscopy (SEM) & Energy Dispersive X-ray (EDX)

SEM images were taken using a JEOL JSM-6480LV at an acceleration voltage of 10 kV. Energy Dispersive X-ray (EDX) using an Oxford INCA X-ray analyser, was used for analysis of the elemental distribution throughout the sample.

3.3.7. Fourier-Transform Infrared Spectroscopy

FTIR spectra were collected using a Perkin Elmer Frontier FTIR instrument. Spectra were acquired between 800 and 3500 cm^{-1}.

3.3.8. X-Ray Photoelectron Spectroscopy (XPS) Measurements

XPS data collection was performed at the EPSRC National Facility for XPS (HarwellXPS), operated by Cardiff University and UCL. X-ray photoelectron spectroscopy (XPS) was performed on a Thermo Fisher Scientific K-alpha^{+} spectrometer. Samples were analysed using a micro-focused monochromatic Al X-ray source (72 W) using the "400-micron spot" mode, which provides an analysis defining elliptical X-ray spot of *ca*. 400 x 600 microns. Data was recorded at pass energies of 150 eV for survey scans and 40 eV for high resolution

scan with 1 eV and 0.1 eV step sizes respectively. Charge neutralisation of the sample was achieved using a combination of both low energy electrons and argon ions.

Data analysis was performed in CasaXPS v2.3.24 after calibrating the data to the lowest C(1s) component taken to have a value of 284.8 eV. Quantification was made using a Shirley type background and Scofield cross sections, with an electron energy dependence of -0.6.

3.4. Electrochemical Measurements

Throughout this thesis, electrochemical measurements were performed using a three electrode system. Pt wire and Ag/AgCL electrodes were used as the counter electrode and reference electrode, respectively. The measured potentials were converted to the reversible hydrogen electrode (RHE) scale using Eq. 3. Where V_{ref} is the potential measured at the reference electrode and E_{0vsSHE} is the potential of the reference electrode with respect to the standard hydrogen electrode (SHE).

$$V_{RHE} = V_{ref} + (0.059 * pH) + E_{0vsSHE} \quad (3)$$

3.4.1. Linear Sweep Voltammetry (LSV)

LSV measurements were collected to assess the performance of the TiO_2|$CsPbBr_3$|Carbon|GS photoelectrodes. LSV data was collected using a Compactstat Ivium potentiostat under simulated solar chopped, illumination (AM 1.5 G filtered 100 mW cm^{-2}), with a 100 W Xe source. Measurements were performed at a scan rate of 50 mV s^{-1}, in A 0.1 M KNO_3 solution, adjusted to pH 2.5 using HNO_3.

3.4.2. Cyclic Voltammetry (CV)

CV measurements were used to observe the Ir-based WOC on the surface of the GS. All CV measurements were performed using a Metrohm autolab potentiostat-galvanostat. A 0.1 M KNO_3 solution was used, adjusted to pH 2.5 using HNO_3. Measurements were performed at a scan rate of 50 mV s^{-1}, in A 0.1 M KNO_3 solution, adjusted to pH 2.5 using HNO_3.

3.4.3. Chronoamperommetry

Chronoamperommetry was performed on the TiO_2|$CsPbBr_3$|Carbon|GS based photoanodes. These measurements were carried out to observe the stability of the photocurrent. Potentials between 0 and 1.56 V were applied to the working electrode. In some cases the applied potential was raised by 0.2 V at 5 min intervals. The measurements were carried out using a Compactstat Ivium potentiostat under simulated solar illumination (AM 1.5 G filtered 100 mW cm^{-2}), with a 100 W Xe source. Measurements were performed in A 0.1 M KNO_3 solution, adjusted to pH 2.5 using HNO_3.

3.4.4. Open Circuit Potential (OCP) and Photovoltage Measurements

OCP measurements were performed in the PEC cell, when the current flowing through the system was set to 0 A. The photovoltage was calculated by subtracting the OCP value measured in the dark from the OCP value measured under 1 sun illumination (AM 1.5 G filtered, 100 mW cm^{-2}). Measurements were performed in A 0.1 M KNO_3 solution, adjusted to pH 2.5 using HNO_3.

Chapter 4. Planar Carbon $CsPbBr_3$ Baseline Device Improvement

4.1. Introduction

One of the first reports of $CsPbBr_3$ solar cells was by Kulbak *et. a*l. in 2015, [1] in which $CsPbBr_3$ was investigated as the absorber layer in a variety of common PSC architectures with different ETL and HTL materials. The report concluded that the cell architecture FTO/*c*-TiO_2/*m*-TiO_2/$CsPbBr_3$/PTAA/Au gave rise to the cells with the best efficiency of 5.95 %. Since 2015, the use of $CsPbBr_3$ as an absorber layer has continued to be investigated and the highest efficiency $CsPbBr_3$ devices are now reaching efficiencies above 10 %. [2, 3] In 2019 a $CsPbBr_3$ PSC was reported reaching an efficiency of 10.91 % with a simple n-i-p cell architecture of FTO/*c*-TiO_2/$CsPbBr_3$/spiro-OMeTAD/Ag. [4] However, this was topped by Zhou *et. al.* in 2021, who reported that an efficiency of 11.08 % could be reached using a planar carbon cell architecture, through the incorporation of $Ti_3C_2Cl_x$ MXene into the bulk and surface of the $CsPbBr_3$ film. [3]

Recently, HTM free $CsPbBr_3$ PSCs have become popular. [5] As previously mentioned in Chapter 1, many HTMs are made from expensive, organic materials, so there has been great interest in finding alternatives. When Kulbak *et. al.* investigated a mix of different device architectures, the use of no HTML at all was studied; the HTML free device exhibited an efficiency of 5.47 %. [1] Following this, many other HTM free $CsPbBr_3$ devices have published in the literature, with many choosing to use a planar carbon electrode, deposited directly on top of the perovskite layer. [6, 7, 8] The first report of planar carbon $CsPbBr_3$ PSCs comes from Liang *et. al.* in 2016, where FTO/c-TiO_2/m-TiO_2/$CsPbBr_3$/carbon devices were fabricated, achieving a champion cell with a PCE reaching 6.7 %, although, it was noted that the average PCE, over 40 devices, was 5.4 %. [9] Over the past 6 years, this efficiency has slowly improved due to focus on fixing a range of issues that exist within these devices. For example, interface engineering is a strategy that is often employed to improve the physical contact and the energy level difference, between two layers within the cells. In $CsPbBr_3$ planar carbon cells, there are two main interfaces that can be improved: the interface between the electron transport layer, often TiO_2, and the perovskite layer, or the interface between the perovskite and the carbon layer. Improving the interfaces can help remove the causes of severe charge recombination which may occur at either site; this is desirable for improving the JV characteristics of a device, and thus ultimately the efficiency.

There are numerous studies in the literature that seek to improve the interface between the ETL and the $CsPbBr_3$. Liu *et. al.* proposed a bilayered ETL, wherein a thin layer of SnO_2 was deposited upon a *c*-TiO_2 layer. [8] It was observed that after the addition of the SnO_2, the roughness of the ETL surface was decreased and it was hypothesised that the reduced roughness facilitated the growth of a high quality perovskite film, which exhibited a smoother surface, with fewer defects. The higher quality, smooth film, allowed for better contact between both the ETL and the perovskite, and also between the perovskite and the carbon. The incorporation of the SnO_2 layer was found to have a beneficial effect on the J_{SC} and the PCE. Other strategies focus on the inclusion of small molecules to passivate defects on the TiO_2 surface and perovskite surface at the interface. Defects on the surface of the TiO_2, such as Ti^{3+} trap states, oxygen vacancies, or cations on interstitial sites on the surface of the perovskite, have been reported to decrease the electron extraction ability of the TiO_2. [10] For example, Zhu *et. al.* introduced the simple small molecule, NH_4Cl, to the $TiO_2/CsPbBr_3$ interface and observed an increase in charge extraction, resulting in an increase in PCE from 6.59 % to 9.60 %. [11] It was suggested that the Cl^- anions passivated the oxygen vacancies on the TiO_2 surface, and the NH_4^+ cation bonds with uncoordinated ions in the perovskite thus also passivating defects at the surface of the perovskite. Zhu *et. al.* also employed this strategy when using 2,2'-methylenebis(4-*ter*-octyl-6-benzotriazole phenol), which is also known as UV-360, this time suggesting that the hydroxyl groups in the UV-360 would passivate the TiO_2 oxygen vacancies, whilst the triazole groups would 'combine' with the uncoordinated lead or cesium perovskite ions. However, this time it was suggested that the advantage of using UV-360 over NH_4Cl, was that it would absorb high energy UV light which would help reduce and slow photodecomposition of the PSCs. Using UV-360 a champion device, with a marginally improved PCE of 9.61 % was achieved. The UV360 devices also exhibited increased stability under continuous illumination and UV light soaking conditions, with the UV-360 modified device retaining 84 % of the initial efficiency after 300 h, whereas the control device only retained 49 %. [12]

The work in this chapter builds upon the methodology that has been previously used in the PJC group to fabricate $CsPbBr_3$ planar carbon cells, [13] and investigates a range of methods that can be employed to achieve high performing devices more consistently. The planar carbon cell architecture is shown in Figure 1. All the layers included in the $CsPbBr_3$ planar carbon devices were deposited as described in Chapter 3,

Figure 1: $CsPbBr_3$ planar carbon (FTO|TiO_2|$CsPbBr_3$|Carbon) device architecture.

4.2. $CsPbBr_3$ Thin film deposition methods

$CsPbBr_3$, is nearly always made using a two-step deposition method. [14] This is a result of solubility issues with CsBr, as it does not readily dissolve in commonly used perovskite solvents such as DMF or DMSO. [15] This solubility problem can cause morphology issues when using a one-step deposition method, with the $CsPbBr_3$ thin films often exhibiting a great number of pinholes and a large excess of CsBr on the surface. [1]

Two common, solution based, two-step methods of making $CsPbBr_3$ thin films are reported. [13, 7, 16, 17] The first method, that was originally used in the PJC lab, is the '*dipping method'*. The dipping method requires a layer of $PbBr_2$ to be deposited through spin coating and then it is annealed, before the $PbBr_2$ film is dipped in a solution of CsBr in methanol for a set amount of time. During the dipping time, the Cs^+ ions can intercalate into the $PbBr_2$ lattice and a yellow, $CsPbBr_3$ thin film is formed. However, if the film is not immersed in the CsBr solution for long enough, a Pb-rich phase of $CsPb_2Br_5$ will form. The Pb-rich phase occurs because not enough Cs^+ ions have been intercalated thus $CsPbBr_3$ cannot form stoichometrically. This phase has a tetragonal unit cell and forms a 2D structure, where the Pb^{2+} coordinates to eight Br^- ions to form elongated polyhedra of Pb_2Br_5; the Cs^+ ions are sandwiched between the $PbBr_2$ layers. [18] This phase been described in the literature as optically inactive and has been found to have an indirect band gap of 3.1 eV. [18] On the other hand, if immersed for too long, too many Cs^+ ions can intercalate and a Cs-rich phase of Cs_2PbBr_6 will form. This phase contains corner sharing $PbBr_6^{4-}$ octahedra in the Y-direction, with two Cs^+ ions spaced in between the chains of $PbBr_6$; this results in localised states which are confined to the individual

$PbBr_6^{4-}$ octahedra as there is minimal electronic overlap between the adjacent octahedra. Consequently, Cs_2PbBr_6 is also an insulating phase. [19]

In order to fully investigate the ideal dipping time required to form a pure phase of $CsPbBr_3$, $PbBr_2$ thin films were immersed in 0.08 M CsBr/MeOH solution at 50 °C for 30– 60 min. The resulting films where studied using XRD, the results are shown in Figure 2.

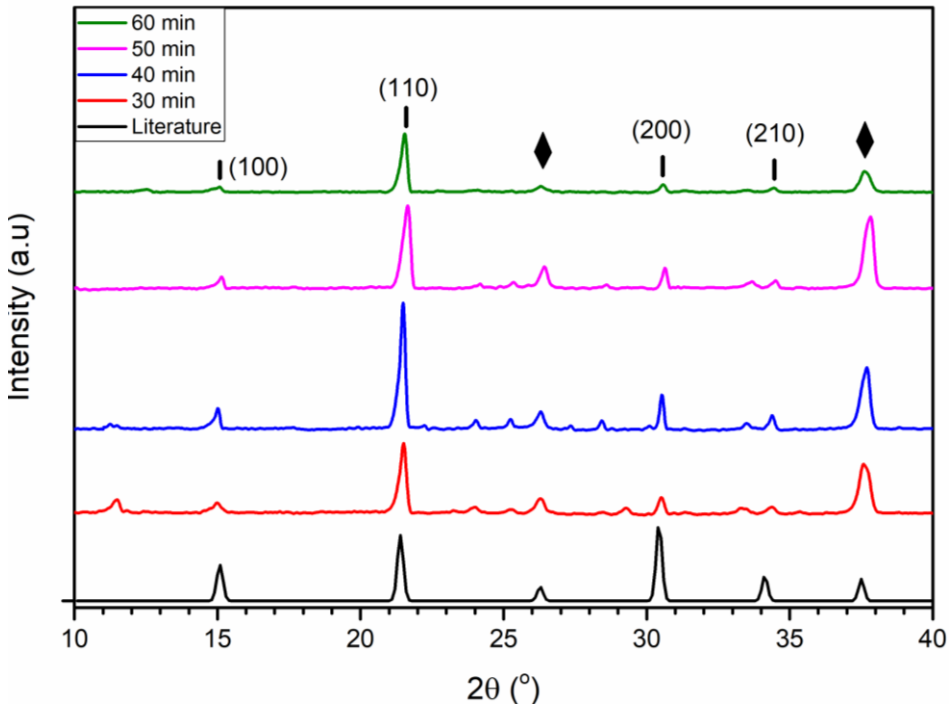

Figure 2: XRD pattern of $CsPbBr_3$ films immersed in 0.08 M CsBr/MeOH solution at 50 °C for 30, 40, 50 and 60 minutes. The black diffraction pattern is taken from the literature for initial comparison. [20] The FTO peaks are shown by the diamond marker, whilst the $CsPbBr_3$ peaks are indicated by a black dashes.

The diffraction patterns show that dipping the substrates in the CsBr/MeOH solution for a time < 50 min, results in the Pb-rich phase coexisting with $CsPbBr_3$. This is evidenced by the peak at ≈ 11 °, the peak at ≈ 24 ° and the peak at ≈ 29 °, which is present in the diffraction pattern of $CsPb_2Br_5$. [18, 21] After dipping the substrates for 50 min the peak at ≈ 11 ° is no longer visible and the diffraction pattern matches the literature diffraction pattern. However, the peak at ≈ 24 ° has been reduced in intensity, but is still present. On the other hand, when the substrates were left in the CsBr/MeOH solution for 60 min, the peak at ≈ 24 ° has now disappeared, but a small peak at ≈ 12 ° is visible; this can be attributed to the Cs-rich phase. [19] Consequently, it was determined that the optimal dipping time to achieve the best conversion to $CsPbBr_3$ was 50 min. However, trace amounts of the Pb-rich phase may still be present.

The second method for making $CsPbBr_3$ thin films, the '*spin coating*' method, involves the deposition of a $PbBr_2$ layer via spin coating with subsequent annealing. Then a solution of CsBr in MeOH is spin coated upon the $PbBr_2$ layer, multiple times, until full $CsPbBr_3$

conversion is complete. The substrate is annealed in between each consecutive spin coating step. It was observed that the sample turns yellow after first spin coating the CsBr solution onto the $PbBr_2$ surface, however, upon annealing at 250 °C, the colour fades back to grey, indicating that not much conversion to $CsPbBr_3$ has occurred and that $PbBr_2$ is still the predominant phase. After repeating this step multiple times, the sample remained yellow upon annealing; this is exhibited in Figure 3. It was also observed that the number of seconds in which the CsBr/MeOH solution was in contact with the substrate before spin coating, was an important factor for consistently observing the colour changes shown in Figure 3. As a result, the solution was left in contact with the substrate for six seconds before the spin coating started.

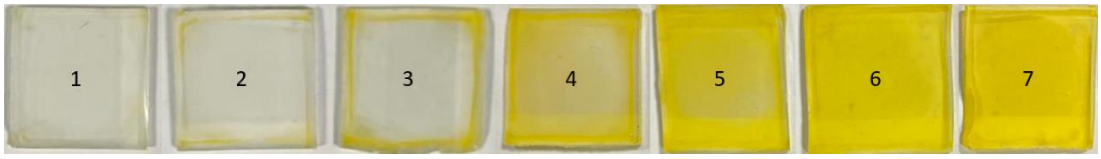

Figure 3: A photograph of $PbBr_2$ thin films after spin coating 100 µL of 0.08 M CsBr solution on the surface and annealing at 250 °C. This was repeated 1 – 7 times and the subsequent photographs are shown in order from left to right.

It was observed that the edges of the film retained the yellow colour first, before the rest of the film. Upon repeating the spin coating step 6 times, the film remained fully yellow after annealing. As $CsPbBr_3$ is reported to be a yellow in colour, XRD was only performed on samples 4 – 7 from Figure 3. The results of the XRD are shown in Figure 4.

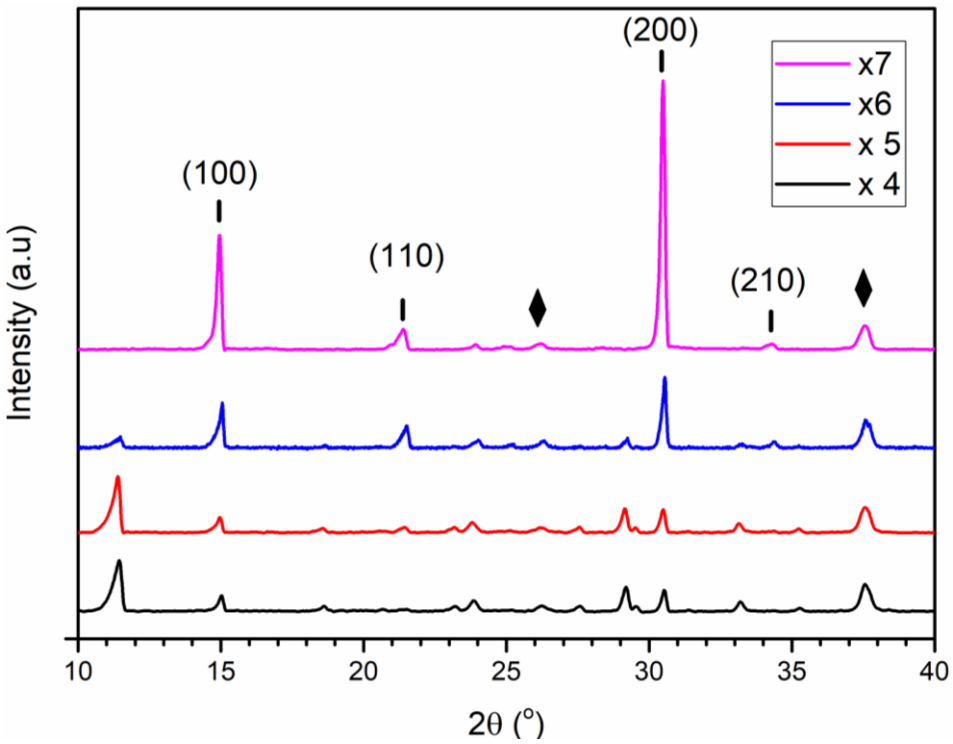

Figure 4: XRD pattern of $PbBr_2$ films spin coated with 100 µL of 0.08M CsBr solution and annealed at 250 °C. This step was repeated 4 times (black), 5 time (red), 6 times (blue) and 7 times (pink). The FTO peaks are shown by the diamond marker, whilst the $CsPbBr_3$ peaks are indicated by a black dashes.

The XRD patterns show that after repeating the process seven times, an almost pure $CsPbBr_3$ thin film was achieved, whereas repeating the process 4-6 times resulted in a Pb-rich phase. This again is demonstrated by the peak at ≈ 11, 24 and 29 ° that corresponds to $CsPb_2Br_5$. The peaks at ≈ 11 and 29 ° disappear after the seventh spin coating step has been completed, with only a weak peak at ~ 24 ° remaining. Consequently, it was decided that seven spin coating cycles of CsBr on $PbBr_2$ was the optimal number to achieve the best quality $CsPbBr_3$ film. This is in contrast to the literature, where full conversion to $CsPbBr_3$ was achieved after four cycles. [17, 22]

The XRD patterns for both of the $CsPbBr_3$ fabrication methods seem to indicate that a trace amount of the Pb-rich phase may still be present. However, literature reports indicate that the presence of small amounts of the non-perovskite $CsPb_2Br_5$ phase may be beneficial for PSC devices, as it can help to passivate grain boundaries. However, an excess of the Pb-rich phase will introduce unwanted defects, resulting in detrimental effects to the PCE of any $CsPbBr_3$ devices. [2]

It can be noted that whilst the X-ray diffraction patterns of the $CsPbBr_3$ samples, made using the two methods (Figure 2 and 4), both display peaks at the expected 2θ values for $CsPbBr_3$, the intensity ratio of the peaks in the two patterns are not the same. The diffraction pattern of

the sample made using the dipping method (Figure 2), has the (110) diffraction peak with a much higher intensity compared to the others. However, the diffraction pattern of the sample made via the spin coating method (Figure 4), has the (100) and (200) diffraction peak showing a greater intensity compared to the other peaks. Thus, it could be hypothesised that the two different methods of making $CsPbBr_3$ thin films results in a different preferred crystal orientation. These data suggest that samples made using the dipping method have a preferred crystal orientation in the (110) plane, whilst the samples made using the spin coating method, could be said to have preferred crystal orientation in the (100) plane.

To further confirm that $CsPbBr_3$ was formed in both of the methods above, the band gap of the two films was determined as shown in Figure 5.

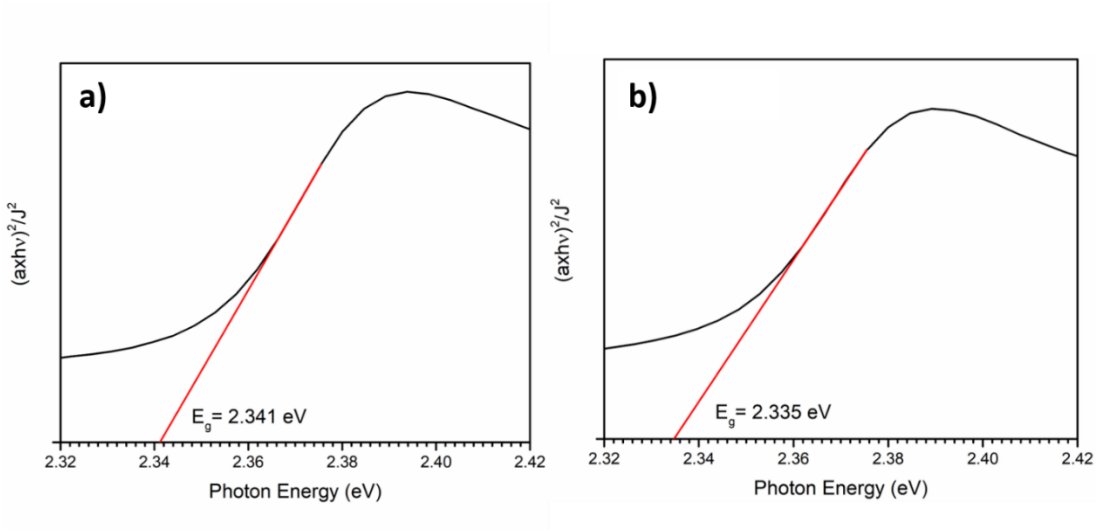

Figure 5: Tauc plots of CsPbBr3 thin films on FTO glass. a) is the sample made using the dipping method b) is the sample made using the spin coating method. Tauc plots were produced using UV/Vis transmission and reflectance data.

The Tauc plots in Figure 5 show that the two methods for producing $CsPbBr_3$, yield thin films with band gap values of 2.341 eV and 2.335 eV respectively. These values agree with the literature band gap value for $CsPbBr_3$ of ~ 2.3 eV, [23, 24, 25, 26] further evidencing that $CsPbBr_3$ can be formed through the use of both of these methods.

In order to further investigate the differences in the $CsPbBr_3$ thin film quality, produced from using the two different fabrication methods, Atomic Force Microscopy (AFM) images of the $CsPbBr_3$ thin film samples were taken. AFM images were taken on three different scales (50, 25 and 15 µm) to enable comparison of the grain size and surface morphology. The images are shown in Figure 6.

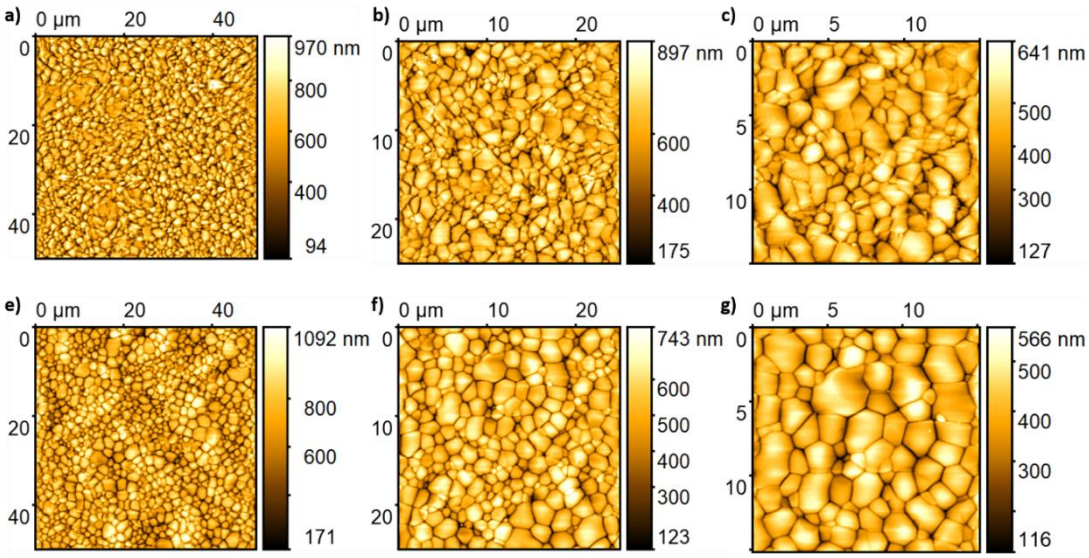

Figure 6: AFM images of $CsPbBr_3$ thin films on FTO/c-TiO_2. Images a) to c) are $CsPbBr_3$ thin films made using the dipping method, at 50 µm, 25 µm and 15 µm respectively. Images e) to g) are $CsPbBr_3$ thin films made using the spin coating method, at 50 µm, 25 µm and 15 µm respectively.

Overall, two sites from two different samples, made using the two different methods, were analysed in order to look in detail at the differences in surface roughness and grain size. To look at the surface roughness, the mean roughness (Sa) values were calculated. This was found to be 74.46 ± 5.60 nm and 102.02 ± 10.91 nm for the dipping and spin coating methods respectively, thus indicating that using the dipping method can result in films with a smoother surface. The smoother surface is beneficial for forming better surface contact between layers in the device. [27] On the other hand, the AFM images seem to suggest that using the spin coating method result in the formation of larger $CsPbBr_3$ grains than the sample made by dipping. Grain size analysis was carried out on the images by selecting 50 random grains from the images at 15 µm. The mean grain size for the dipped samples was calculated to be 1.13 ± 0.07 µm, and the mean grain size for the spin-coated samples was found to be 2.19 ± 0.08 µm. Further statistical analysis of the grain size is shown in Figure 7.

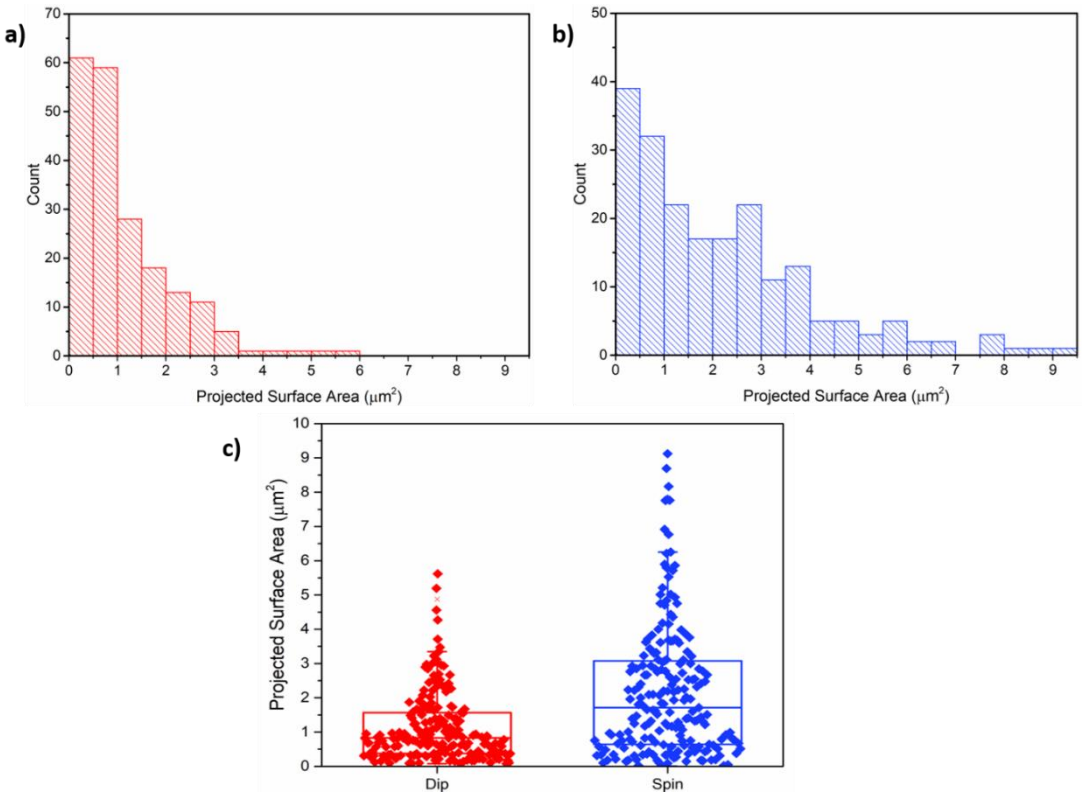

Figure 7: a) Histogram of the projected surface area of 200 grains from four different AFM images, of samples made using the dipped method. b) Histogram of the projected surface area of 200 grains from four different AFM images of samples made using the spin coating method c) Box plot comparison of the projected surface area of 200 grains from samples using the dipped method and 200 grains from samples made using the spin coating method. The median lines are shown.

The statistical analysis of the projected surface area of the grains, shows that samples made using the spin coating method, have larger grains. Whilst both methods produce a high proportion of grains with a projected surface area below 1 μm^2, the histograms in figure 5 a) and b) show that the spin coated samples have a smaller proportion of grains under 1 μm^2 and the drop off in the count of the number of grains, as the values on the x-axis grow larger, is slower. The maximum projected surface area for the spin coated samples was found to be 9.13 μm^2, whereas this was only 5.60 μm^2 for the dipped samples. Larger grain sizes are more beneficial for solar cell applications, as it results in fewer grain boundaries, which in turn, leads to improved charge transport properties, such as increased carrier mobility values and subsequently leads to improved device performance. [28, 29] Consequently, it could be hypothesised that $CsPbBr_3$ PSCs made using the spin coating method, will perform better than those made using the dipping method. However, the fact that the samples made using the spin coating method have a higher surface roughness, could cause other issues, such as reduced contact between other layers, which can be detrimental to device performance.

In order to investigate the best method for making $CsPbBr_3$ carbon PSCs, planar carbon devices, with an n-i-p architecture of FTO/c-TiO_2/$CsPbBr_3$/carbon, were made using both methods; the results are shown in Figure 8 and 9.

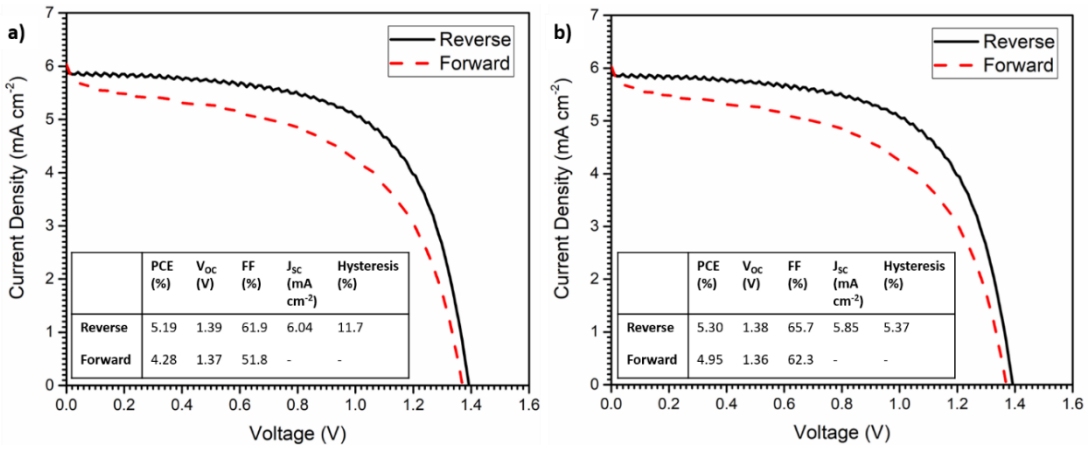

Figure 8: The J-V curves of the champion devices from a) the cells made using the dipping method and b) the cells made using the spin coating method.

Figure 8 shows the J-V curves of the champion device from each method of making $CsPbBr_3$ planar carbon cells. The champion device made using the spin coating method has a reverse PCE of 5.30 %, this is slightly higher than the champion device made using the dipping method, which has a reverse PCE of 5.19 %. The amount of hysteresis in the spin coated device is also less than half of the hysteresis in the dipped device, with a hysteresis factor of 5.37% and 11.7 % respectively. On the evidence of the champion cells alone, it would suggest that using the spin coating method to deposit $CsPbBr_3$ is superior to the dipping method. However, as the champion devices only tell us information about the very best devices and do not provide information about the reproducibility of the methods. It is therefore important to look at the full range of devices produced, in order to draw any conclusions about which method may truly yield the best PSCs. Figure 9 below compares the J-V characteristics, over 15 devices, for each of the two methods.

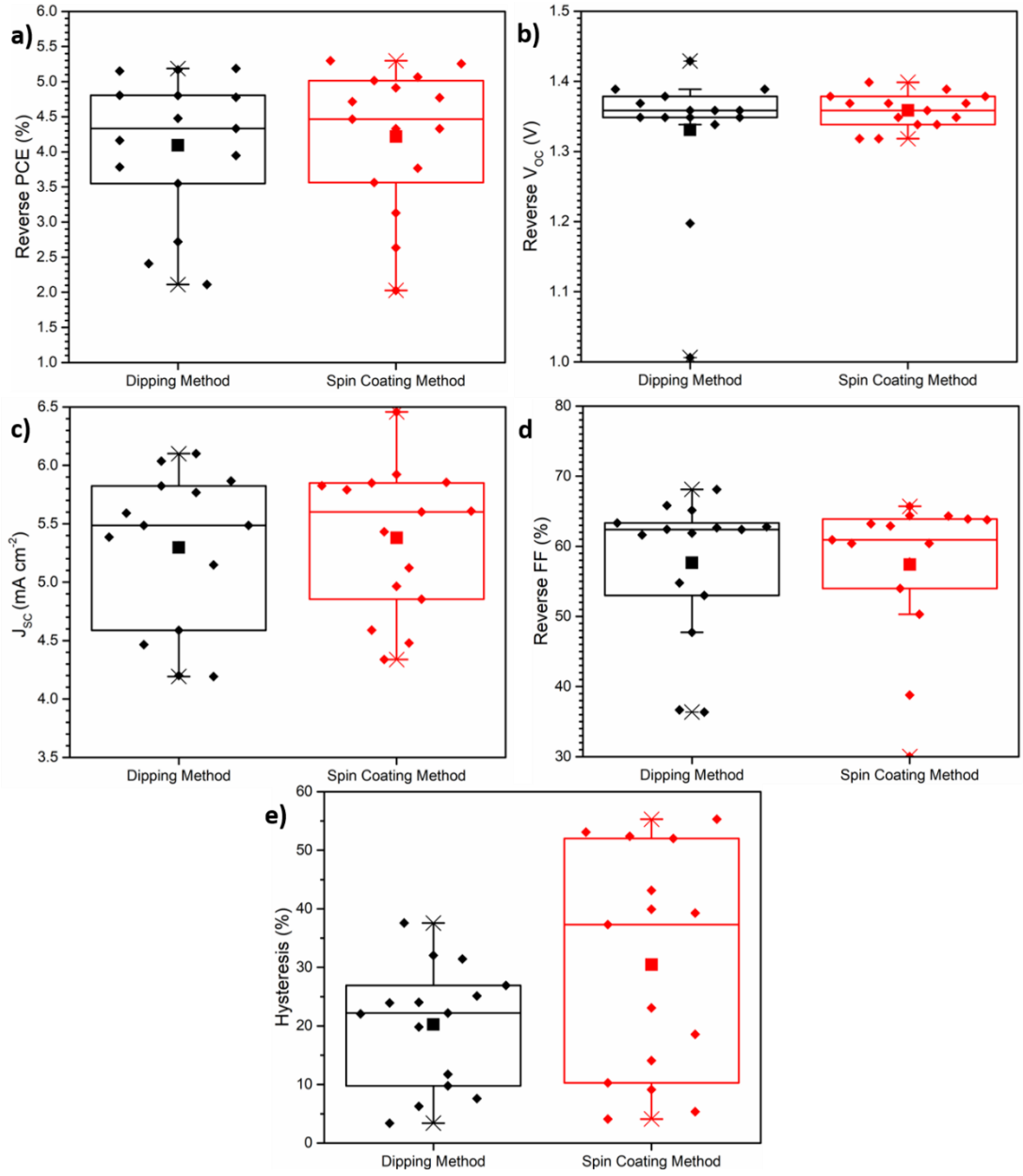

Figure 9: Box plots comparing the JV characteristics of 15 cells made using the dipping and spin coating methods. a) reverse PCE comparison, b) reverse V_{oc} comparison, c) fill factor comparison, d) J_{sc} comparision and e) hysteresis comparision. The median lines are shown, whilst the mean values are represented by the large filled squares.

The data in Figure 9 initially suggests that there is not much difference in device performance between the planar carbon $CsPbBr_3$ cells, when the perovskite layer has been deposited by either dipping or spin coating. There is not a great deal of difference in the reverse PCE, the reverse V_{OC}, the J_{SC} or the reverse FF, with the mean reverse PCE being 4.09 % ± 1.00 and 4.22 % ± 1.00 for the methods respectively. The mean and median values for the PCE and J_{SC} is marginally higher for the devices made using the spin coating method. However, the devices

made using the spin coating method also appear to be prone to more hysteresis at a scan rate of 100 mV s^{-1} than the cells made using the dipping method.

Whilst both methods are reported in the literature, the majority of the studies use the spin coating method. [30, 31, 32] The advantages of the spin coating method include; an increased level of control when making $CsPbBr_3$ thin films, as the colour changes in the film from grey to yellow can be observed more easily; the increased crystallinity of the film and an increase in grain size. There are some advantages to the dipping method, for example, the method is less time consuming and the resulting film appear to have a smoother surface. However, it was hypothesised that the longer contact time of the MeOH solvent with the substrates could cause issues in future experiments, when looking at the effects of additives to $CsPbBr_3$. Consequently, moving forward the spin coating method was chosen for making further $CsPbBr_3$ planar carbon PSCs.

4.3. Improvements to $CsPbBr_3$ Planar Carbon PSCs

In order to fully explore the use of planar carbon $CsPbBr_3$ PSCs, in the research reported throughout this thesis, it is important that a baseline set of devices can be made with a consistent PCE, J_{SC}, V_{OC} and FF. This removes variables to allow better comparisons to be made when further altering the devices, and also helps to better exhibit the capabilities of these devices in applications such as water splitting. Subsequently, a range of methods have been investigated towards improving the JV characteristics of these PSCs. These methods include, observing the effect of the different ETLs, solvent rinsing and the $PbBr_2$ annealing temperature.

4.3.1. ETL modification

Firstly, the addition of a m-TiO_2 layer or a SnO_2 layer, in tandem with the *c*-TiO_2 layer was investigated. It was expected that the inclusion of these layers would improve charge extraction, by increasing the physical contact between the ETL and the perovskite, and by providing added protection from any pinholes in the thin c-TiO_2 layer.

The preparation of the *m*-TiO_2 layer was taken from the work by Saliba *et. al.,* in which they describe methods for making various layers for use in a range of PSC architectures. [33] In order to achieve the desired effect, the *m*-TiO_2 must be doped with Li^+ to help increase the conductivity. The deposition of the SnO_2 layer was optimised by a previous PJC group member, and uses a colloidal suspension of SnO_2. Both of the layers are deposited upon *c*-

TiO_2 using spin coating. In an attempt to characterise these layers, the XRD patterns of the resulting layers on top of FTO/*c*-TiO_2 are shown in Figure 10.

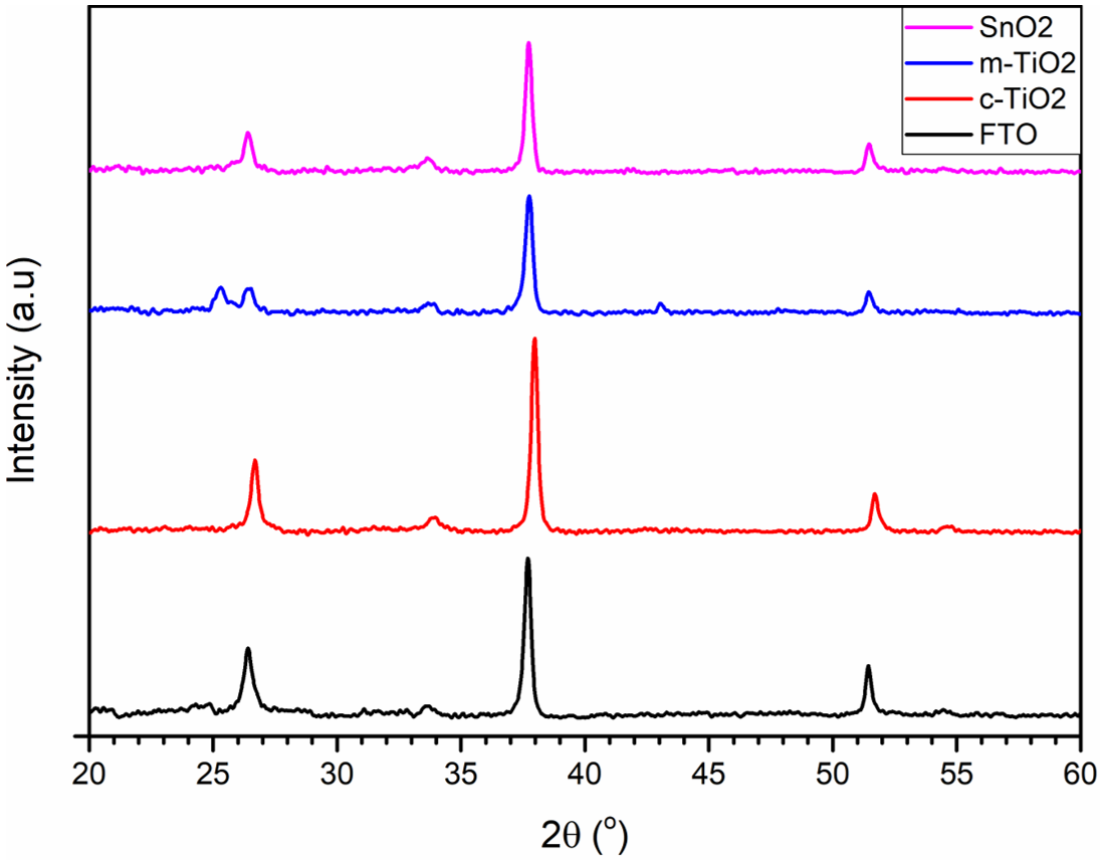

Figure 10: XRD patterns of FTO (black), c-TiO_2 on FTO (red), m-TiO_2 on c-TiO_2 and FTO (blue) and SnO_2 on c-TiO_2 and FTO (pink).

The XRD patterns of the various ETL layers, shown in Figure 10, do not reveal much about what has been deposited upon the substrates. This is because the ETL layers are very thin, for example, the optimum thickness for the *c*-TiO_2 is ≈ 50 nm. [34] The FTO layer below is much thicker; hence, the peaks from the FTO dominate the diffraction pattern. However, the XRD pattern of the m-TiO_2 layer does contain two extra weak peaks that do not correspond to the underlying FTO. There is a peak at ≈ 25 °; this peak appears in both rutile (110) and anatase (101) TiO_2 XRD patterns. The peak at ≈ 43 ° however, only appears in the rutile phase diffraction pattern. [35] This could suggest that the m-TiO_2 is crystallising in the rutile phase.

To determine which layer had the biggest effect on the devices, 10 devices containing each ETL were made. The resulting champion JV curves are shown below in Figure 11, and the resulting JV characteristics are shown in Figure 12.

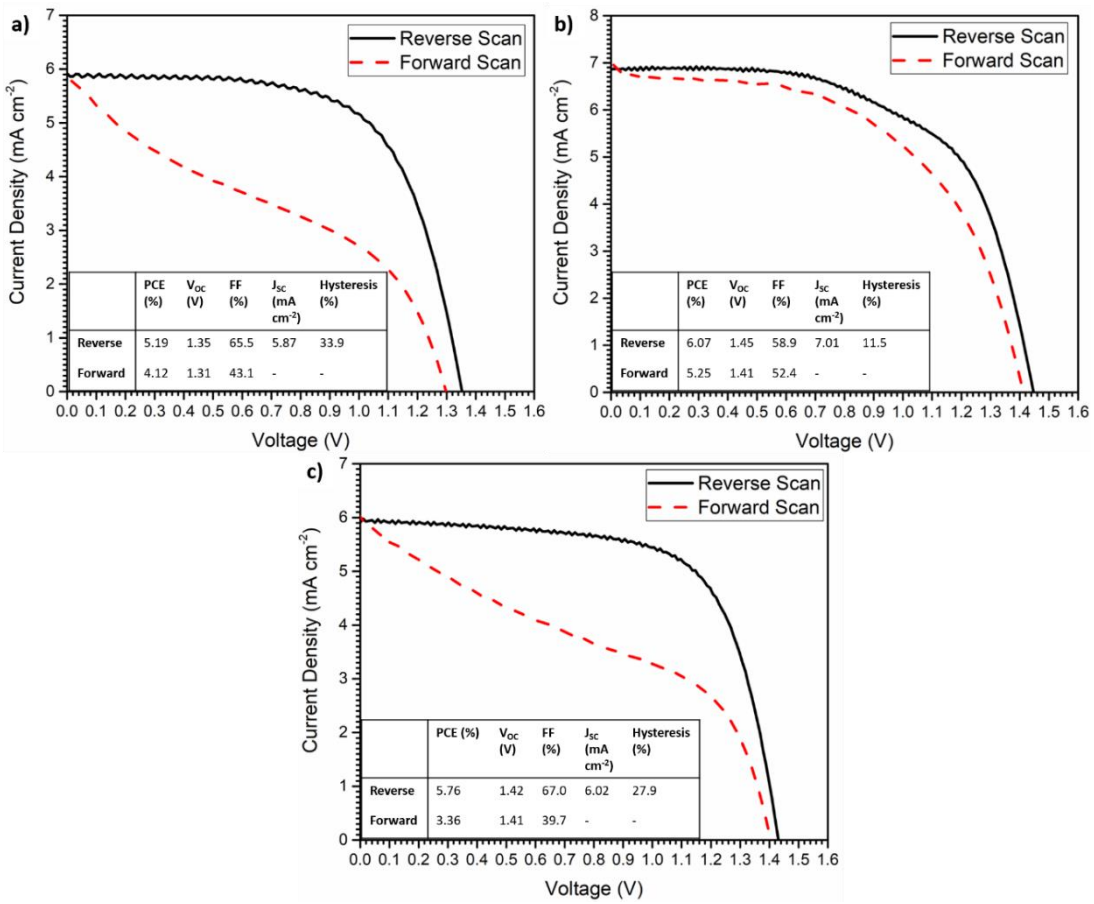

Figure 11: The J-V curves of the champion devices from a) the devices containing a c-TiO_2 layer, b) the devices containing a c-TiO_2 and m-TiO_2 layer and c) the devices containing a c-TiO_2 and SnO_2 layer.

It was observed that the best device was the PSC containing the *m*-TiO_2 layer, this champion device reached an efficiency of 6.07 %. The champion device containing the added SnO_2 layer also had an improved reverse PCE of 5.76 %, compared to 5.19 % for the control device. The reverse V_{OC} of the champion cell was also noticeably improved from 1.35 V in the control device, to 1.45 V in the *m*-TiO_2 containing device. An increase in the J_{SC} of the champion devices of both the *m*-TiO_2 and the SnO_2 containing cells, over the control, was observed, with the J_{SC} increasing from 5.87 to 7.01 and 6.02 mA cm^{-2} respectively. However, to fully see the effects of the additional layers, the distribution of results across the whole set of devices must be considered.

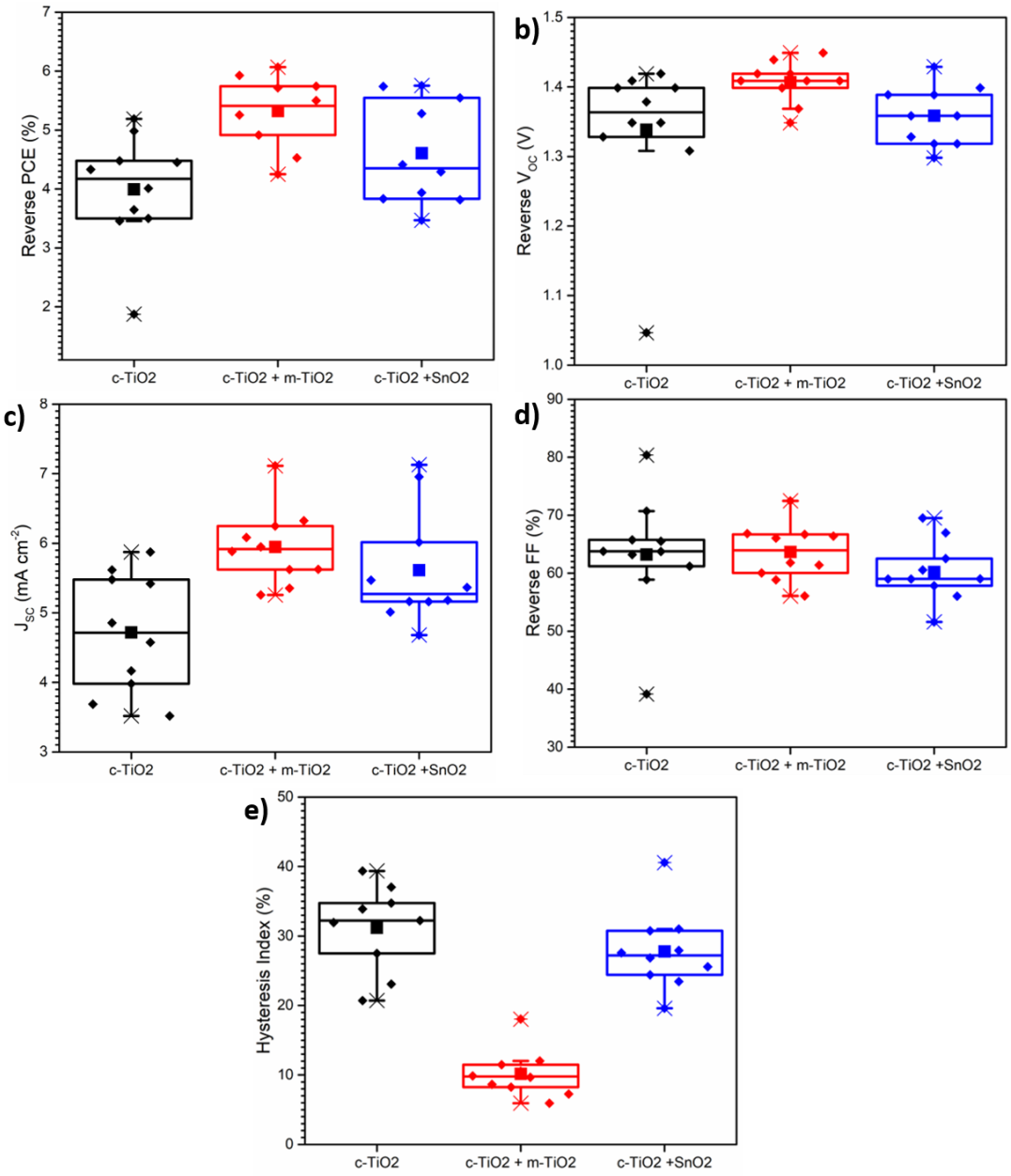

Figure 12: Box plots comparing the JV characteristics over 10 devices of each type. FTO/c-TiO_2/$CsPbBr_3$/Carbon architecture (black), FTO/c-TiO_2/m-TiO_2/$CsPbBr_3$/Carbon architecture (red) and FTO/c-TiO_2/SnO_2/$CsPbBr_3$/Carbon architecture (blue). a) reverse PCE comparison, b) reverse V_{OC} comparison, c) J_{SC} comparison d) reverse FF comparison and e) hysteresis comparison. The median lines are shown whilst the mean values are represented by the large filled squares.

It was observed that the addition of both the *m*-TiO_2 and the SnO_2 layers, in combination with the *c*-TiO_2 improved the overall performance of the $CsPbBr_3$ planar carbon cells, with increases in reverse PCE and J_{SC} observed, along with a reduction in the hysteresis factor. In particular, the average J_{SC} was increased, indicating that charge extraction was improved by the addition of the m-TiO_2 or SnO_2 layers. This could be a result of fewer pinholes in the ETL and an improved interface between the ETL and the perovskite layers. The greatest

improvements came from addition of the m-TiO_2 layer. The mean value of the reverse PCE has increased from 3.99 % ± 1.00 to 5.32 % ± 0.60. The range of the box plots was smaller for the cells with the added *m*-TiO_2, suggesting that it can help increase the consistency of the cell performance. Importantly, the addition of the *m*-TiO_2 layer has also reduced the amount of hysteresis observed in the cells at a scan rate of 100 mV s^{-1}. The mean value of the hysteresis factor has fallen from 31.2 % ± 6.2 to 10.2 % ± 3.3. The difference in hysteresis when the JV measurements are performed at a scan rate of 100 mV s^{-1-} can also be observed in Figure 11, where the champion JV curves for each type of device are displayed. Whilst it is important to remember than the observed hysteresis can be altered by changing the sweep rate at which the JV scans are conducted, it can also indicative of defects present in the device. [36, 37] The effect on the hysteresis in Figure 12 can be expected, as Xing *Et. al.* found that there is an electron transfer potential barrier between the perovskite layer and the *c*-TiO_2 layer, formed by a number of surface states in both layers, resulting in the formation of an interfacial dipole as the charges are not extracted quickly. [38] This interfacial dipole and resultant barrier can cause a large amount of hysteresis in PSCs. Furthermore, the addition of the *m*-TiO_2 layer, doped with lithium increases the efficiency of the photogenerated electron extraction due to an increase in the TiO_2/perovskite interface, which also helps reduce recombination, through a reduced number of defects at the interface, resulting in a lower interfacial barrier. [39]

Although improvements to the device were observed by the addition of the SnO_2 layer, it was not fully optimised for these devices and a wider range of thickness should be considered. However, due to the large improvements in PCE and hysteresis seen by the addition of the m-TiO_2, the optimisation of the SnO_2 layer was not investigated further in this work. Due to the observed improvements in the JV characteristics of the cells, a m-TiO_2 layer was included in the planar carbon $CsPbBr_3$ cells moving forward.

4.3.2. Rinsing Step

Next, the effect of rinsing the $CsPbBr_3$ surface with solvent, after the final conversion step, was investigated. This solvent rinsing step is commonly utilised in order to remove any excess CsBr that may be present on the surface of the film. [32] The majority of reported procedures employ IPA as the solvent of choice for this rinsing step. [8, 17] However, it has been suggested that other solvents, such as EtOH are a better choice due to the higher solubility of CsBr in EtOH and the use of IPA can lead to the formation of some of the undesirable Cs_4PbBr_6 phase. [40] Subsequently, both IPA and EtOH were investigated as rinsing solvents. After the seventh conversion step from $PbBr_2$ to $CsPbBr_3$ was complete, the resulting thin films were rinsed with 100 µl of solvent and annealed, before the carbon electrode was deposited. Sets of 10

devices were made to investigate these effects; either IPA or EtOH was employed during the rinsing step and the devices were compared to a control group featuring no rising step. The JV curves of the champion devices are displayed in Figure 13.

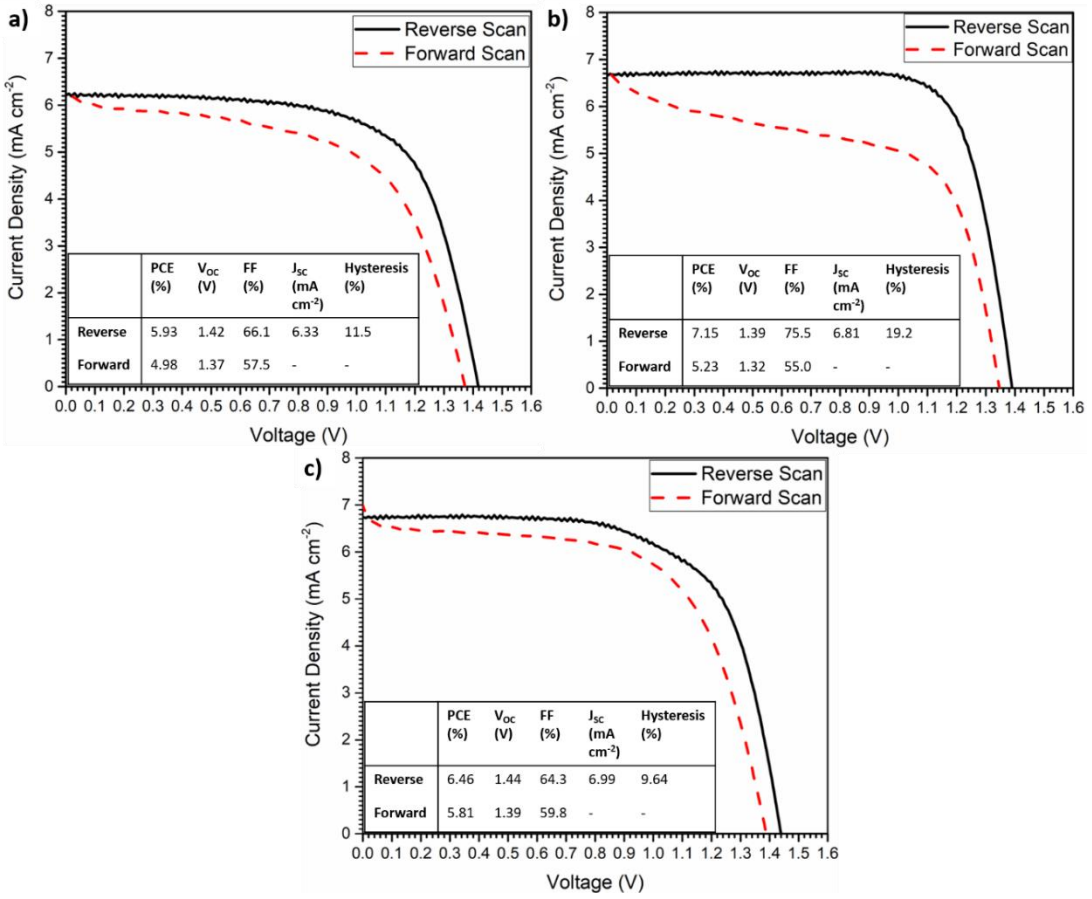

Figure 13: The J-V curves of the champion devices from a) the devices where the $CsPbBr_3$ was not rinsed with a solvent b) the devices where the $CsPbBr_3$ was rinsed with IPA and c) the devices where the $CsPbBr_3$ was rinsed with EtOH.

The best device was obtained after rinsing the $CsPbBr_3$ thin film with IPA, with the champion device reaching a PCE of 7.15 %, although, the champion EtOH rinsed device still achieved large improvement in PCE to 6.46 %, compared to 5.93 % the champion control device. This implies that adding a solvent rinsing step into the device making process can induce an increase in the efficiency of the cells. This PCE increase could be largely due to the observed increase in the J_{SC} for both of the rinsed devices. The J_{SC} has increased to 6.81 and 6.99 mA for the IPA rinsed and EtOH rinsed devices respectively, compared to 6.33 mA for the control. For further insight, a box plot comparison of all 10 devices for each set in shown in Figure 14.

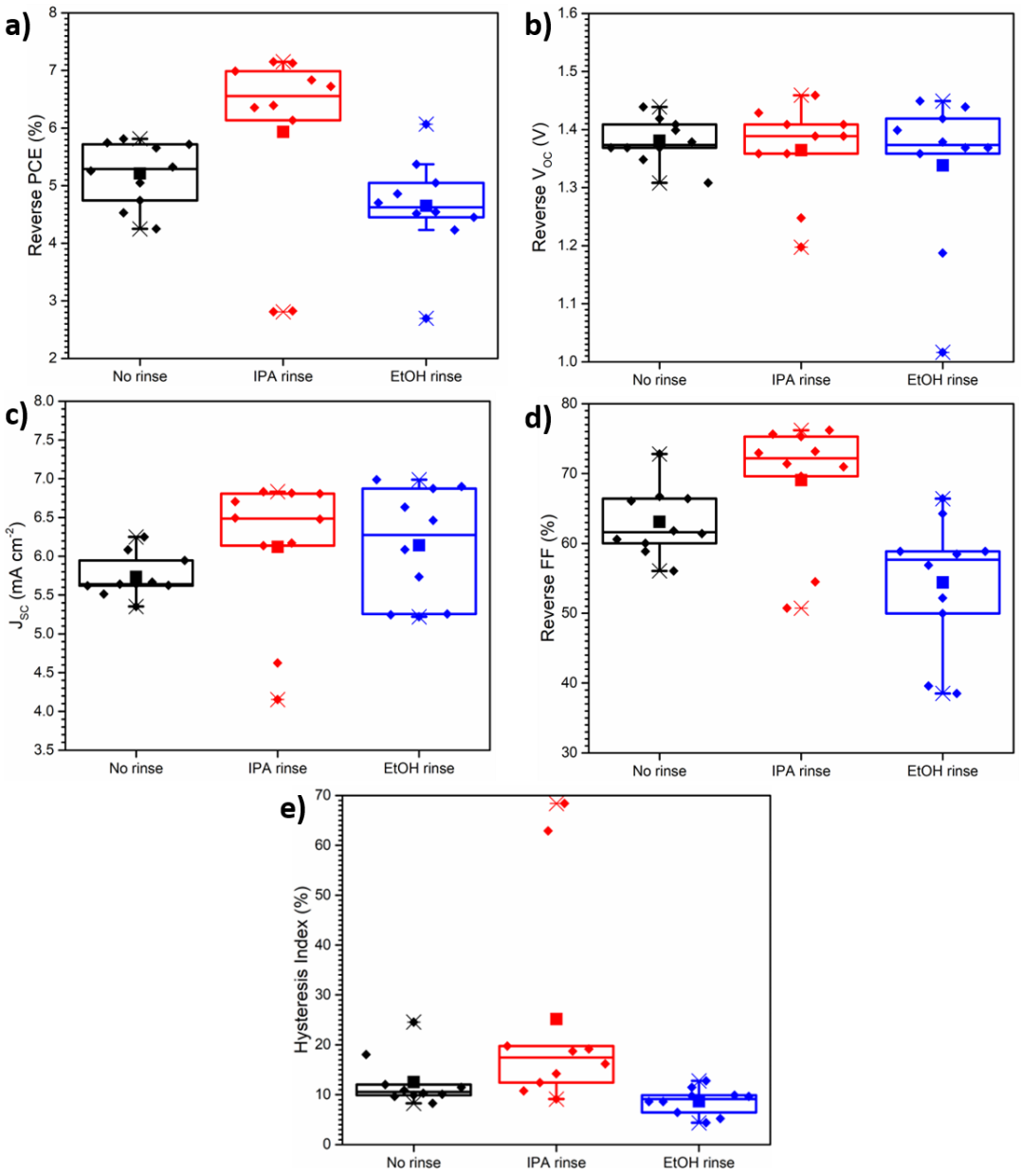

Figure 14: Box plots comparing the JV characteristics of 10 devices of each type. The devices either having no solvent rinse at all (black) or have been rinsed with IPA (red) or EtOH (blue). a) reverse PCE comparison, b) reverse Voc comparison, c) fill factor comparison, d) Jsc comparision and e) hysteresis comparision. The median lines are shown, whilst the mean values are represented by the large filled squares.

The box plots in Figure 14 compare the J-V characteristics of all the devices made, and shows that overall, rinsing the $CsPbBr_3$ film with IPA produces the best devices. Increases in reverse PCE, J_{SC} and reverse FF can be seen. The mean reverse PCE has increased from 5.21 % ± 0.60 to 5.93 % ± 1.70 after rinsing with IPA. However, there are two outlier devices for the IPA rinsed samples, which decreases the mean value; without these, the mean reverse PCE would be 6.71 % ± 0.40. This is a large increase compared to both the un-rinsed samples and the EtOH rinsed samples. There is an increase in the mean J_{SC} for the devices rinsed with both

IPA and EtOH. There has also been a large increase in the mean reverse FF of the devices rinsed with IPA, going from 63.1 % ± 4.9 to 69.1 % ± 9.0; this is an overall increase of 6%. This J_{SC} and FF increase contribute to the increased PCE seen for the IPA rinsed devices.

To examine further what could be causing the observed increase in device efficiency, the resulting $CsPbBr_3$ films were studied using XRD and AFM. Figures 15 and 16 show the results.

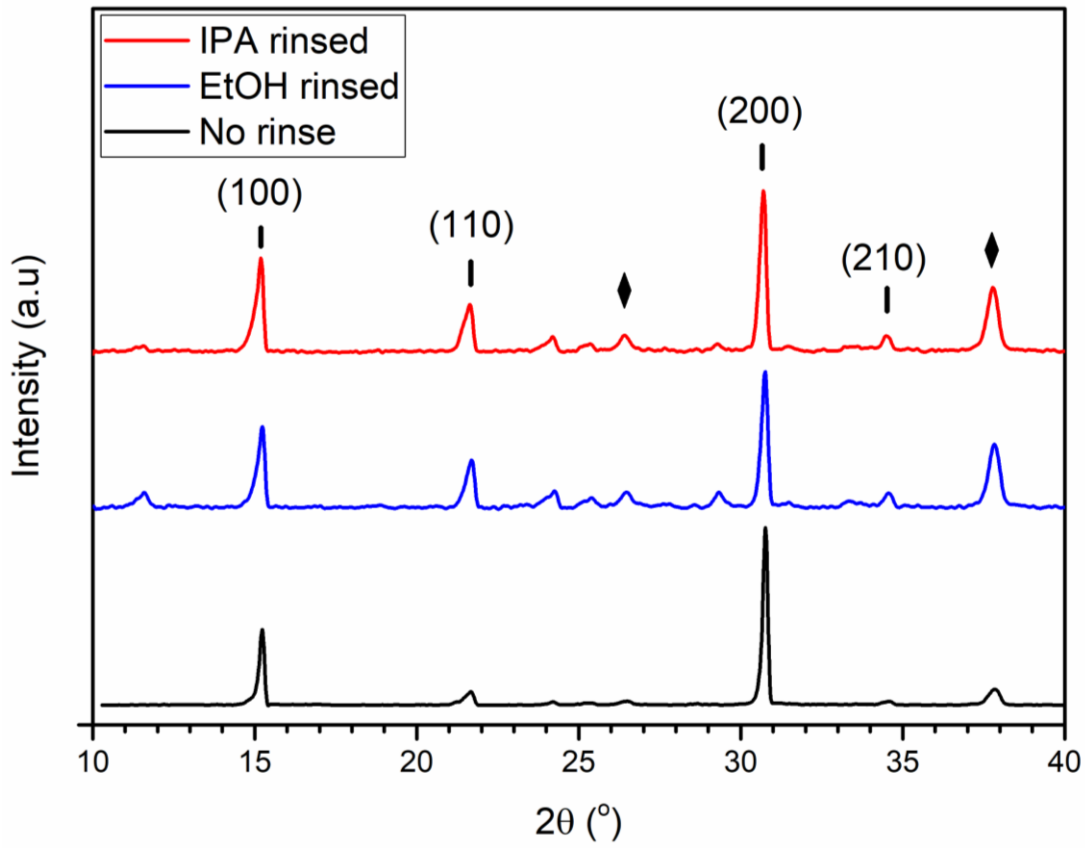

Figure 15: XRD patterns of $CsPbBr_3$ thin film on FTO with no rinse (black), $CsPbBr_3$ thin film on FTO rinsed with EtOH (red) and $CsPbBr_3$ thin film on FTO rinsed with IPA (blue).

The XRD pattern shown in Figure 15, suggests that rinsing the $CsPbBr_3$ with both IPA and EtOH leads to the formation of some of the undesirable Pb-rich $CsPb_2Br_5$ phase, evidenced by the peaks at ≈ 11, 24 and 29 °. The peak at ≈ 24 ° is also visible in the control $CsPbBr_3$ films, although it has a very weak intensity. Comparatively between the IPA and EtOH rinsed samples, the $CsPb_2Br_5$ XRD peaks appear much weaker in the cells washed with IPA. This contrasts with the report suggesting that rinsing with IPA can lead to the formation of the Cs-rich phase.

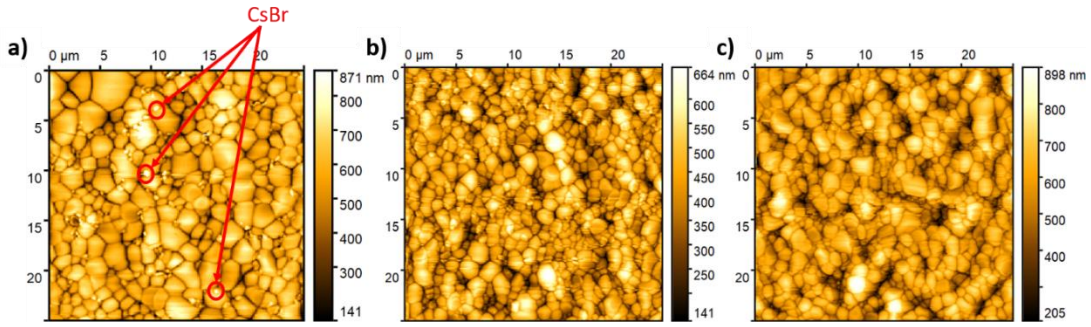

Figure 16: AFM images of $CsPbBr_3$ on FTO/TiO_2 a) with no rinsing of the thin film b) after rinsing with IPA c) after rinsing with EtOH. Images taken on a scale of 25 µm x 25 µm. Three examples of residual CsBr crystals are circled in red.

The AFM images shown in Figure 16, show that there is a reduction of residual CsBr crystals left on the surface of the two rinsed films. The CsBr can be seen as the small, bright crystals appearing most notably in the image of the un-rinsed sample. However, it does appear that rinsing with EtOH has removed more surface CsBr than the IPA. Notably, it also appears that rinsing the $CsPbBr_3$ thin films, with solvent, leads to a reduction in grain size. The largest grains displayed a diameter of ≈ 2.5 µm after rinsing with both IPA and EtOH, reduced from > 3 µm without rinsing.

This could indicate that there is a trade-off between removing the excess surface CsBr, reducing the grain size and forming the Pb-rich phase. As previously discussed, inducing a very small amount of the Pb-rich phase could be beneficial for the passivation of defects. [2] Using IPA as the rinsing solvent removes some CsBr from the surface and induces a small amount $CsPb_2Br_5$ formation. However, CsBr is more soluble in EtOH hence more surface CsBr in removed, but more $CsPb_2Br_5$ is formed. This offers an explanation for the observed trend in J-V characteristics seen in Figure 14.

With these data in mind, it was concluded that a rinsing step with IPA was beneficial for improving the performance of the $CsPbBr_3$ planar carbon devices; hence, it should be included in the fabrication process moving forward.

4.3.3. $PbBr_2$ Annealing Temperature

Next, the temperature of the $PbBr_3$ annealing was investigated. The original method used in the PJC research group, anneals the $PbBr_3$ films at 70 °C. [13] However, many literature reports anneal the $PbBr_2$ at 90 °C. [8, 16, 17] Tang and co-workers found that the porosity volume and the film thickness of the $PbBr_2$ layer increased with an increase in annealing temperature. The optimal temperature for $PbBr_2$ crystallisation and annealing was found to be 90 °C as an increase in the number of pinholes in the film was observed at annealing temperatures greater

than 90 °C. [16] An increase in porosity volume of the $PbBr_2$ is important for the diffusion of the CsBr into the lattice, as when the $PbBr_2$ and CsBr interact, the total lattice volume must expand. If the $PbBr_2$ film is too dense, not only is the number of CsBr diffusion pathways into the lattice reduced, there is also insufficient space for expansion, thus hindering crystal growth. Heating to 90 °C accelerates the evaporation of the DMF solvent, used to dissolve the $PbBr_2$. This can increase the rate of the crystallisation process. In turn, this produces a more porous $PbBr_2$ film and provides the pre-expanded volume needed for the growth of large $CsPbBr_3$ grains. [41] AFM images of the surface of the $PbBr_2$ after annealing at 70, 90 and 100 °C were taken (Figure 17), in order to look more closely at the effect of annealing temperature on the morphology of the $PbBr_2$ surface.

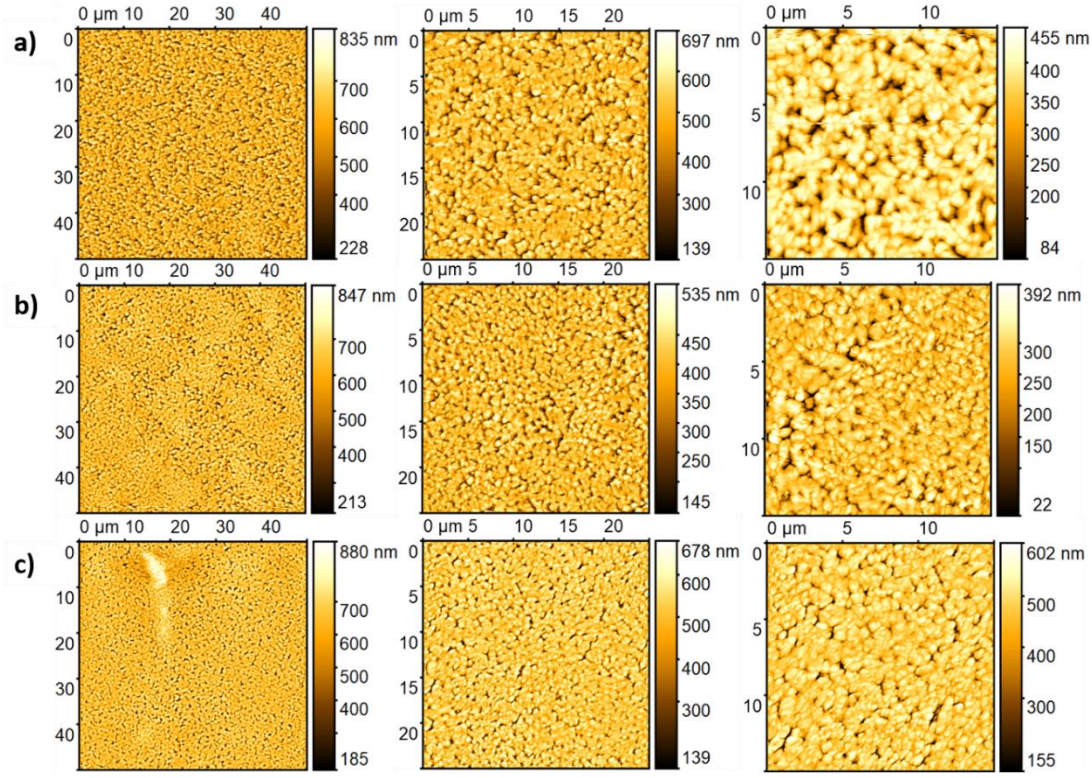

Figure 17: AFM of $PbBr_2$ thin films on FTO after being annealed at a) 100 °C b) 90 °C and c) 70 °C. AFM images taken at 50, 25 and 15 µm shown from left to right.

The AFM images appear to confirm that annealing the $PbBr_2$ at 100 °C increases the number of pinholes in the $PbBr_2$ film, however, there appears to be better surface coverage when annealing at 70 °C. Nonetheless, based on the literature, it should be expected that an increase in the annealing temperature from 70 °C to 90 °C should improve the device performance of $CsPbBr_3$ planar carbon cells.

Two sets of 12 devices, both of those with the $PbBr_2$ annealed at 70 and at 90 °C, were made and the device performances are displayed in Figures 18 and 19.

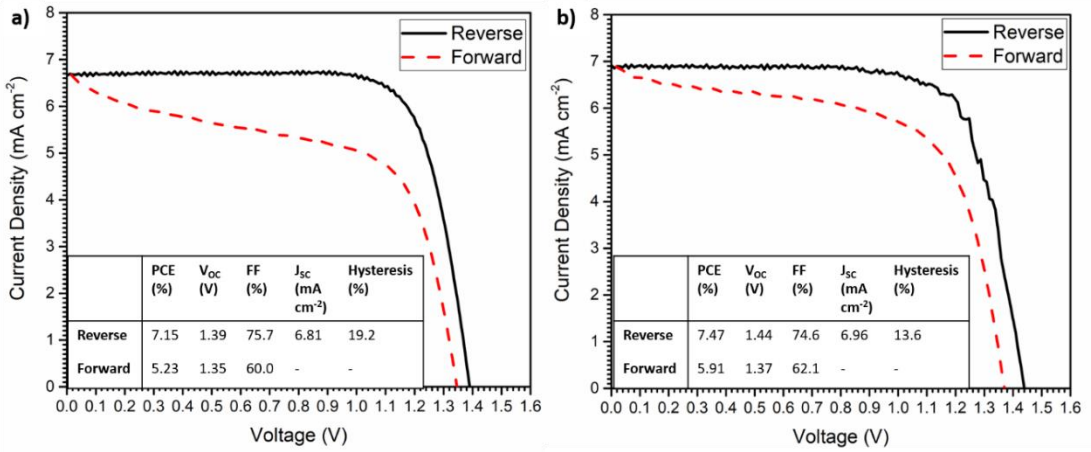

Figure 18: The J-V curves of the champion cells from a) the devices where the $PbBr_2$ layer was annealed at 70 °C b) the devices where the $PbBr_2$ layer was annealed at 90 °C.

Figure 18 shows the J-V curves of the two champion cells, one where the $PbBr_2$ was annealed at 70 °C and the other where the $PbBr_2$ was annealed at 90 ° C. The champion cell annealed at 90 °C performed the best, with an increase of 0.32 % in reverse PCE from 7.15 % to 7.47 %. As these devices become closer to the standard of those, which are reported in the literature, any increases in device performance are likely to be small. Figure 18 shows the distribution of the J-V characteristics across the set of devices and allows for further comparison.

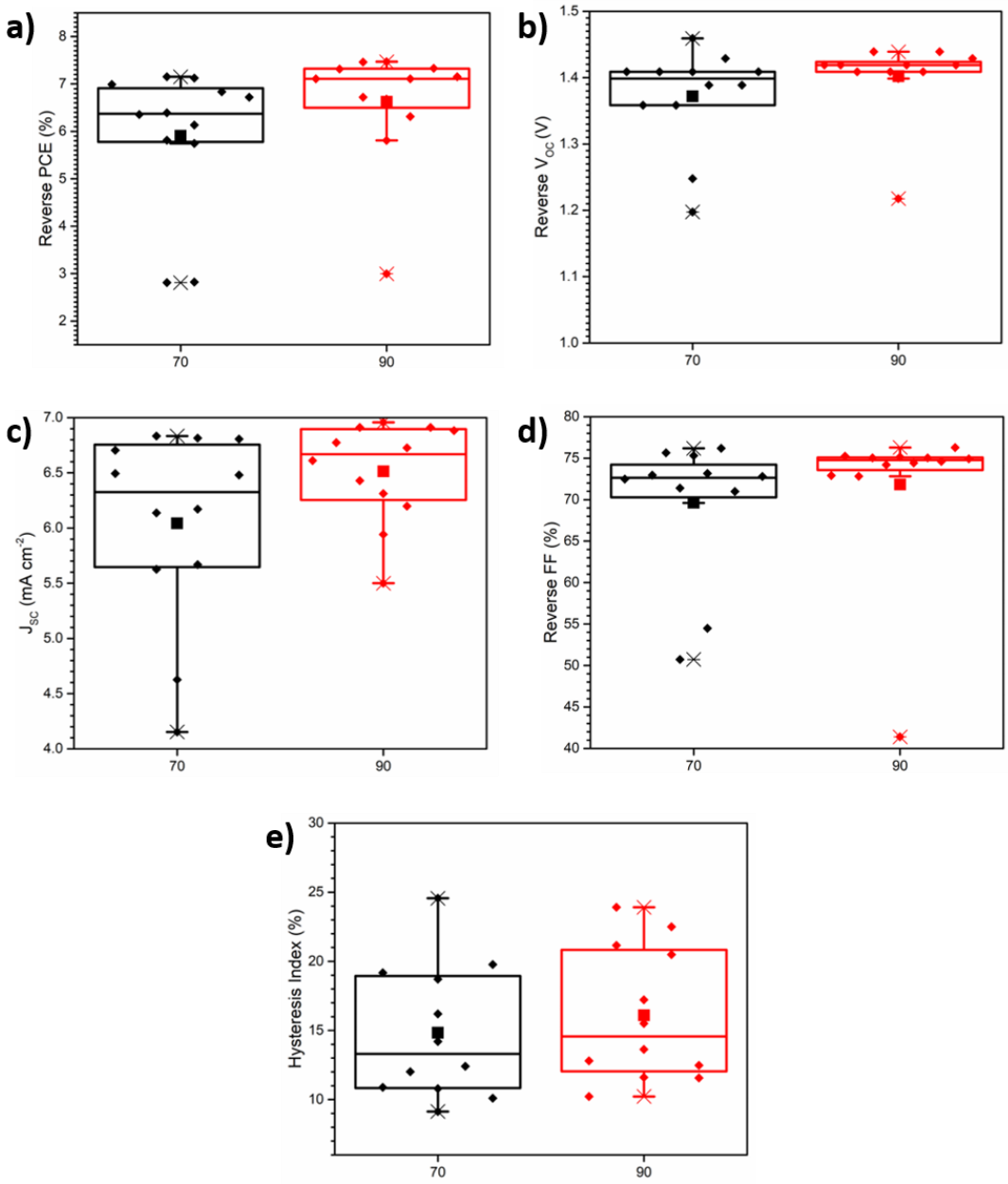

Figure 19: Box plots comparing the JV characteristics of 12 cells annealed at 70 °C (black) and 90 °C (red). a) reverse PCE comparison, b) reverse V_{OC} comparison, c) J_{SC} comparision, d) fill factor comparison and e) hysteresis comparision. The median lines are shown, whilst the mean values are represented by the large filled squares.

Overall, it appears that the increase in $PbBr_2$ annealing temperature from 70 °C to 90 °C improves $CsPbBr_3$ device performance and results in increases in the average (mean and median) reverse PCE, V_{OC}, J_{SC} and FF. The mean reverse PCE increased from 5.91 % ± 1.50 in the devices annealed at 70 °C to 6.62 % ± 1.20 in the devices annealed at 90 °C. The J_{SC} also increased from 6.04 mA cm^{-2} ± 0.90 to 6.52 mA cm^{-2} ± 0.50. However, there is not much difference in the hysteresis factor of the two types of devices. As a result, it was confirmed that annealing the $PbBr_2$ at an increased temperature of 90 °C can improve $CsPbBr_3$ planar

carbon device performance. The standard deviation is also smaller across the PCE, V_{OC}, J_{SC} and FF for the devices annealed at 90 °C, indicating that increasing the temperature of the $PbBr_2$ annealing step can lead to a set of devices, which display more consistency.

Figure 20 sums up the incremental improvements in PCE of the $CsPbBr_3$ planar carbon devices that have been achieved through making small changes to the fabrication process. Consequently, the 'standard' device that can be made in our laboratory has improved in efficiency from a mean average of 4.22 % ± 0.99 to 6.62 % ± 1.30, with the best performing cells now reaching efficiencies over 7 %. Showing that the new method for making 'standard' $CsPbBr_3$ planar carbon cells has more than doubled the mean reverse PCE value of the original 'standard' cells, yielding a 55.8 % increase compared to the original value.

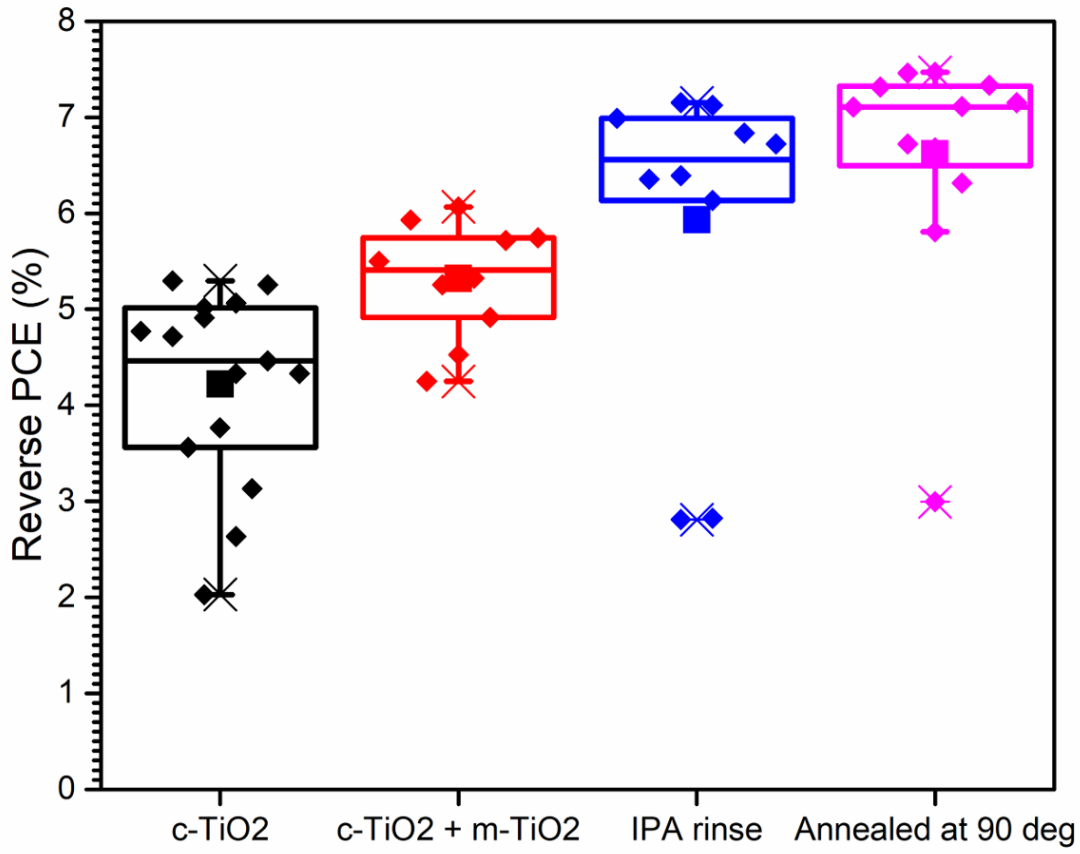

Figure 20: Box plot of the reverse PCE of $CsPbBr_3$ planar carbon devices, made using different methods. The median lines are shown, whilst the mean values are represented by the large filled squares.

Whilst the increase in the reverse PCE, traditionally considered the key parameter, is impressive, increases were also observed in the average J_{SC} and V_{OC}. The mean average J_{SC} improved from 5.29 mA cm^{-2} ± 0.70 to 6.51 mA cm^{-2} ± 0.60, whilst the mean reverse V_{OC} increased from 1.35 V ± 0.02 to 1.41 V ± 0.06. The increase in voltage is particularly of interest to enable use of these devices in water splitting applications.

To further examine the improvements that have been made in the standard planar carbon $CsPbBr_3$ devices, the IPCE of the original baseline devices and the improved baseline devices, was measured (Figure 21).

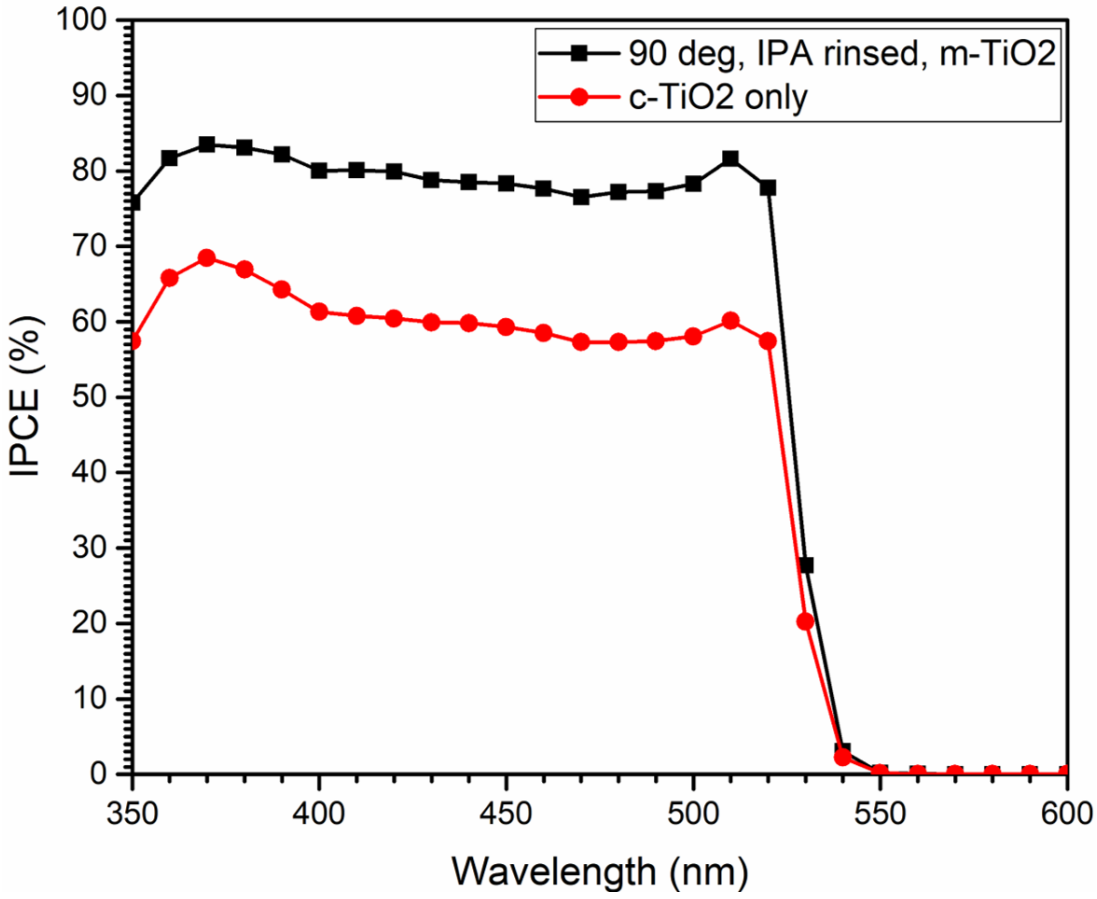

Figure 21: IPCE the champion $CsPbBr_3$ planar carbon cells made using two different methods. Cell containing a m-TiO_2 layer, the $PbBr_2$ was annealed at 90 °C and the $CsPbBr_3$ film was rinsed with IPA (Black squares). Cell containing only a c-TiO_2 layer (red circles).

Figure 21 shows the IPCE of the original FTO/c-TiO_2/$CsPbBr_3$/Carbon device Vs the FTO/c-TiO_2/m-TiO_2/$CsPbBr_3$/Carbon, where the $PbBr_2$ has been annealed at 90 °C and the surface of the $CsPbBr_3$ has been rinsed with IPA. The IPCE shows an onset at ≈ 530 nm, corresponding to the band gap of $CsPbBr_3$ at 2.3 eV and the IPCE begins to drop off as the wavelength enters the UV portion of the spectrum at 350 nm. The improved device shows an IPCE between 75 – 84 %, whereas the original device displays an IPCE between 59 – 69 %. This demonstrates further that the changes in the device fabrication process have improved the electron generation and extraction in $CsPbBr_3$ cells and thus has improved the ability of the device to efficiently convert photons into energy.

4.4. Conclusions and future work

Overall, the work in this chapter has been successful in improving the standard $CsPbBr_3$ planar carbon cell that will be used as a baseline for future work carried out in this thesis. All of the standard J-V characteristics of the device were improved, with the top PCE reaching 7.47 %, the top V_{OC} that was achieved was 1.46 V and the highest J_{SC} achieved reached 7.1 mA cm^2. Furthermore, at the scan rate of 100 mVS^{-1}, the extent of hysteresis in the devices has been considerably reduced. Notably it was found that adding a *m*-TiO_2 layer upon the *c*-TiO_2 layer helped increase the average J_{SC} of the device and resulted in a large reduction in hysteresis at the scan rate used. Rinsing the $CsPbBr_3$ layer with IPA was also beneficial and lead to further increases in the J_{SC} and improvements to the FF. Finally, an increase in the annealing temperature of the $PbBr_2$ layer led to small improvements in all of the parameters used to characterise the devices.

However, there are many opportunities for future work. On a small scale, investigations into the optimal layer thickness of the added ETL layers could be carried out to see if charge extraction could be further improved. Furthermore, methods to increase the average grain size of the $CsPbBr_3$ again, after the solvent rinsing step has decreased it, could be investigated. This could include observing the effect of solvent annealing, using a common perovskite solvent such as DMF or DMSO.

The impact of adding small molecules or other additives into the device could be explored further. Whilst there was no observed improvement after adding either NH_4Cl^- or UV360, a range of other small molecules, which are able to passivate defects in either the TiO_2 or the $CsPbBr_3$ layer, could be added at the interface, to observe the effect this also has on charge extraction. The effect of adding small molecules has been shown to not only increase the PCE of a device, but also increase the V_{OC}. [11] With the aim of increasing the V_{OC} of the devices, the use of transition metal additives could also be explored. Transition metal in the 2^+ state have been shown to help increase the quality of perovskite films by inducing larger growth, which can result in large V_{OC} values. [30] An increased $V_{OC,}$ above the 1.46 V that has been achieved in this chapter, would be beneficial for the use of these cells as photoanodes for water oxidation. The use of transition metal ions is investigated in detail in Chapter 5.

4.5. References

1 M. Kulbak, D. Cahen and G. Hodes, *J. Phys. Chem. Lett*, 2015, **6**, 42.

2 H. Li, G. Tong, T. Chen, H. Zhu, G. Li, Y. Chang, L. Wang and Y. Jiang, *J. Mater. Chem. A*, 2018, **6**, 14255–14261.

3 Q. Zhou, J. Duan, J. Du, Q. Guo, Q. Zhang, X. Yang, Y. Duan and Q. Tang, *Adv. Sci.*, 2021, **8**, 2101418.

4 G. Tong, T. Chen, H. Li, L. Qiu, Z. Liu, Y. Dang, W. Song, L. K. Ono, Y. Jiang and Y. Qi, *Nano Energy*, 2019, **65**, 104015.

5 N. Kumar, J. Rani and R. Kurchania, *Sol. Energy*, 2021, **221**, 197–205.

6 I. Poli, J. Baker, J. Mcgettrick, F. De Rossi, S. Eslava, T. Watson and P. J. Cameron, *J. Mater. Chem. A*, 2018, **6**, 18677–18686.

7 X. Chang, W. Li, L. Zhu, H. Liu, H. Geng, S. Xiang, J. Liu and H. Chen, *Appl. Mater. Intefaces*, 2016, **8**, 33649–33655.

8 X. Liu, X. Tan, Z. Liu, H. Ye, B. Sun, T. Shi, Z. Tang and G. Liao, *Nano Energy*, 2019, **56**, 184–195.

9 K. Wang, Z. Jin, L. Liang, H. Bian, D. Bai, H. Wang, J. Zhang, Q. Wang and L. Shengzhong, *Nat. Commun.*, 2018, **9**, 1–8.

10 Y. C. Ho, M. N. F. Hoque, E. Stoneham, J. Warzywoda, T. Dallas and Z. Fan, *J. Phys. Chem. C*, 2017, **121**, 23939–23946.

11 J. Zhu, M. Tang, B. He, W. Zhang, X. Li, Z. Gong, H. Chen, Y. Duan and Q. Tang, *J. Mater. Chem. A*, 2020, **8**, 20987–20997.

12 J. Zhu, M. Tang, B. He, K. Shen, W. Zhang, X. Sun, M. Sun, H. Chen, Y. Duan and Q. Tang, *Chem. Eng. J.*, 2021, **404**, 126548.

13 I. Poli, U. Hintermair, M. Regue, S. Kumar, E. V. Sackville, J. Baker, T. M. Watson,

S. Eslava and P. J. Cameron, *Nat. Commun.*, 2019, **10**, 2097.

14 S. Ullah, J. Wang, P. Yang, L. Liu, S. E. Yang, T. Xia, H. Guo and Y. Chen, *Mater. Adv.*, 2021, **2**, 646–683.

15 W. Wang, Y. Wu, D. Wang and T. Zhang, *ACS Omega*, 2019, **4**, 41.

16 Y. Zhao, J. Duan, Y. Wang, X. Yang and Q. Tang, *Nano Energy*, 2020, **67**, 104286.

17 C. Wang, Y. Long, X. Liu, S. Fu, J. Wang, J. Zhang, Z. Hu and Y. Zhu, *J. Mater. Chem. C*, 2020, **8**, 17211.

18 I. Dursun, M. De Bastiani, B. Turedi, B. Alamer, A. Shkurenko, J. Yin, A. M. El-Zohry, I. Gereige, A. AlSaggaf, O. F. Mohammed, M. Eddaoudi and O. M. Bakr, *ChemSusChem*, 2017, **10**, 3746–3749.

19 M. I. Saidaminov, J. Almutlaq, S. Sarmah, I. Dursun, A. A. Zhumekenov, R. Begum, J. Pan, N. Cho, O. F. Mohammed and O. M. Bakr, *ACS Energy Lett.*, 2016, **1**, 840–845.

20 M. Rodová, J. Brooek, K. Knííek and K. Nitsch, *J. Therm. Anal. Calorim.*, 2003, **71**, 667–673.

21 C. Tenailleau, S. Aharon, B. El Cohen and L. Etgar, *Nanoscale Adv.*, 2019, **1**, 147–153.

22 J. Duan, Y. Zhao, B. He and Q. Tang, *Angew. Chemie Int. Ed.*, 2018, **57**, 3787–3791.

23 C. C. Stoumpos, C. D. Malliakas, J. A. Peters, Z. Liu, M. Sebastian, J. Im, T. C. Chasapis, A. C. Wibowo, D. Young Chung, A. J. Freeman, B. W. Wessels and M. G. Kanatzidis, *Cryst. Growth Des*, 2013, **13**, 2722–2727.

24 M. Ezzeldien, S. Al-Qaisi, Z. A. Alrowaili, M. Alzaid, E. Maskar, A. Es-Smairi, T. V. Vu and D. P. Rai, *Sci. Reports 2021 111*, 2021, **11**, 1–12.

25 P. Maji, P. Sadhukhan and S. Das, *J. Mater. Sci. Mater. Electron.*, 2020, **31**, 17100–

17109.

26 J. Liang, C. Wang, Y. Wang, Z. Xu, Z. Lu, Y. Ma, H. Zhu, Y. Hu, C. Xiao, X. Yi, G. Zhu, H. Lv, L. Ma, T. Chen, Z. Tie, Z. Jin and J. Liu, *J. Am. Chem. Soc.*, 2016, **138**, 15829–15832.

27 F. Meng, A. Liu, L. Gao, J. Cao, Y. Yan, N. Wang, M. Fan, G. Wei and T. Ma, *J. Mater. Chem. A*, 2019, **7**, 8690–8699.

28 N. Giesbrecht, J. Schlipf, I. Grill, P. Rieder, V. Dyakonov, T. Bein, A. Hartschuh, P. Müller-Buschbaum and P. Docampo, *J. Mater. Chem. A*, 2018, **6**, 4822–4828.

29 O. G. Reid, M. Yang, N. Kopidakis, K. Zhu and G. Rumbles, *ACS Energy Lett.*, 2016, **1**, 561–565.

30 Y. Zhao, Y. Wang, J. Duan, X. Yang and Q. Tang, *J. Mater. Chem. A*, 2019, **7**, 6877–6882.

31 X. Yang, M. Li, J. Jiang, L. Ma, W. Tang, C. Xu, H. L. Cai, F. M. Zhang and X. S. Wu, *J. Phys. D. Appl. Phys.*, 2021, **54**, 154001.

32 X. Cao, G. Zhang, Y. Cai, L. Jiang, Y. Chen, X. He, Q. Zeng, Y. Jia, G. Xing and J. Wei, *Appl. Surf. Sci.*, 2020, **529**, 147119.

33 M. Saliba, J. P. Correa-Baena, C. M. Wolff, M. Stolterfoht, N. Phung, S. Albrecht, D. Neher and A. Abate, *Chem. Mater.*, 2018, **30**, 4193–4201.

34 L. Gouda, K. J. Rietwyk, J. Hu, A. Kama, A. Ginsburg, M. Priel, D. A. Keller, S. Tirosh, S. Meir, R. Gottesman and A. Zaban, *ACS Energy Lett.*, 2017, **2**, 2356–2361.

35 K. Thamaphat, P. Limsuwan and B. Ngotawornchai, *Kasetsart J. (Nat. Sci.)*, 2008, **42**, 357–361.

36 W. Tress, N. Marinova, T. Moehl, S. M. Zakeeruddin, M. K. Nazeeruddin and M. Grätzel, *Energy Environ. Sci.*, 2015, **8**, 995–1004.

37 A. Kumar, A. Rana, N. Vashistha, K. K. Garg and R. K. Singh, *Sol. Energy*, 2020, **211**, 345–353.

38 G. Xing, B. Wu, S. Chen, J. Chua, N. Yantara, S. Mhaisalkar, N. Mathews and T. C. Sum, *Small*, 2015, **11**, 3606–3613.

39 J. Zhou, X. Wei, J. Zhu, X. Yang, H. Niu, L. Wan, P. Jiang, J. Xu, R. Zhou and G. Cao, *Sci. China Mater.*, 2020, **63**, 1151–1162.

40 J. Ryu, S. Yoon, S. Lee, D. Lee, B. Parida, H. W. Kwak and D. W. Kang, *Electrochim. Acta*, 2021, **368**, 137539.

41 T. Liu, Q. Hu, J. Wu, K. Chen, L. Zhao, F. Liu, C. Wang, H. Lu, S. Jia, T. Russell, R. Zhu, Q. T. Gong Liu, Q. Hu, J. Wu, K. Chen, L. Zhao, R. Zhu, Q. Gong, F. Liu, T. Russell, C. Wang, H. Lu and S. Jia, *Adv. Energy Mater.*, 2016, **6**, 1501890.

Chapter 5 Investigation into the Effects of Transition Metal Ions in $CsPbBr_3$ Planar Carbon Devices

5. Introduction

As discussed in Chapter 2, the large bandgap of ≈ 2.3 eV for $CsPbBr_3$ results in large V_{OC} values. The mean average V_{OC} value that has been obtained in this thesis from $CsPbBr_3$ cells with an architecture of FTO/*c*-TiO_2/*m*-TiO_2/$CsPbBr_3$/Carbon is ≈ 1.4 V; this value is above the theoretical required potential for water oxidation of 1.23 V. As seen in chapter 4, $CsPbBr_3$ is a good choice of semiconductor for performing photoelectrochemical water oxidation, however, due to the required overpotential, the voltage across the $CsPbBr_3$ device is still not enough to drive the water splitting reaction alone and extra potential from the potentiostat is required in order to reach the onset potential for water oxidation. Thus, it has been theorised that by increasing the V_{OC} of these devices to high enough values, less applied potential may be needed and it could even be possible to perform unassisted water splitting. However, a potential of ≈ 1.8 V is often quoted as the minimum amount of energy needed for unassisted water splitting, [1] and increasing the V_{OC}s by as much as 0.4 V may difficult. Nonetheless, there are a range of available methods that can help increase the V_{OC} of a device.

There are a number of strategies that can be employed in order to increase the V_{OC} of $CsPbBr_3$ planar carbon devices. It is important to minimise any losses to the V_{OC}. It is understood that voltage loss can be related to charge recombination. Perovskites films are polycrystalline solution processed materials and hence there are a number of defects present both on the surface of the material and at the grain boundaries. These defects can act as trap sites and provide potential route for recombination in perovskite devices and can lead to losses in the V_{OC} of the device. [2]

Past reports have shown that the addition of small amounts of transition metals or rare earth metals, substituted in at the Pb^{2+} site, can lead to overall device improvements. In 2017 Zhao *et al.* found that substituting small amounts of the divalent Zn^{2+} ion into the B site in $MAPbI_3$ improved the quality of the resulting perovskite thin film and increased the grain size, therefore non-radiative recombination in the device was reduced. The biggest increases in PCE and V_{OC} were seen when 5 % Zn^{2+} was used, with the V_{OC} increasing from 1.10 V to 1.14 V. [3] Divalent zinc was also used to substitute the Pb^{2+} in $CsPbI_2Br$. It was found that Zn^{2+} slows the crystal growth and results in larger grains. This reduces the number of grain boundaries present, the excess Zn^{2+} was also shown to passivate trap states at the grain

boundaries. As a result, both the PCE and V_{OC} of the device improved from 11 % to 13.6 % and from 1.1 V to 1.18 V respectively, when 10 % Zn^{2+} was used. [4]

These studies inspired later work to investigate the effects of substituting Pb^{2+} in planar carbon $CsPbBr_3$ devices. Tang and co-workers reported that divalent transition metal (TM) ions such as Mn^{2+}, $Ni^{2+,}$ Cu^{2+} and Zn^{2+}, when substituted in to $CsPbBr_3$ at a 0.5 % of the original Pb^{2+} content to form $CsPb_{0.995}TM_{0.005}Br_3$, showed increases PCE, J_{SC}, V_{OC} and FF. The biggest increase was seen when Zn^{2+} was substituted in at 5 %, with the PCE increasing from 6.37 % in the pristine $CsPbBr_3$ device, to 9.18 %; the V_{OC} increased from 1.43 V to 1.56 V. Improvements over the control $CsPbBr_3$ devices, without ion substitution, were still observed when increasing the ratio of the TM ions to 1 %, but these improvements were not as large as those observed using 0.5 %. However, upon increasing the ratio of the TMs to 3 %, the PCE and V_{OC} were drastically reduced. [5]

Whilst all the TM ion substitution has involved divalent 2+ ions, Duan *et. al.* found that that the substitution of rare earth metals, in the 3+ oxidation state, could also induce increases in the V_{OC} of $CsPbBr_3$ devices. All the rare earth metals ions used in the study (Yb^{3+}, Er^{3+}, Ho^{3+}, Tb^{3+} and Sm^{3+}) showed improvements. The device with architecture FTO/*c*-TiO_2/*m*-TiO_2/$CsPb_{0.97}Sm_{0.03}Br_3$/carbon achieved an efficiency of 10.14 % and an 'ultrahigh' V_{OC} of 1.59 V. [6]

There have been plenty of studies that centre on the effects of TM and rare earth ions in $CsPbBr_3$ nanocrystals, [7, 8, 9, 10] however, the range of studies observing the effect of these ions in $CsPbBr_3$ devices is limited; these studies have been summed up in Table 1. From the table it is clear to see that the inclusion of small amounts of TM/rare earth ions could be used to improve the V_{OC} of $CsPbBr_3$ devices for water splitting applications. However, the majority of the studies, very small changes in the XRD and XPS spectra are given as proof for the Pb^{2+} substitution, [3, 5, 6] and it could be possible that substitution is not occurring but the presence of the metal ions in the solution is influencing the crystallisation process, resulting in larger grains.

Table 1: Summary of planar carbon $CsPb_{1-x}M_xBr_3$ champion devices with metals substituted at the B site.

Composition	PCE (%)	V_{OC} (V)	J_{SC} (mA cm^{-2})	FF (%)
$CsPb_{0.995}Mn_{0.005}Br_3$ [5]	6.98	1.443	6.10	79.29
$CsPb_{0.995}Ni_{0.005}Br_3$ [5]	8.03	1.479	6.80	79.49
$CsPb_{0.995}Cu_{0.005}Br_3$ [5]	8.23	1.530	6.97	79.22
$CsPb_{0.995}Zn_{0.005}Br_3$ [5]	9.18	1.560	7.30	80.61
$CsPb_{0.998}Co_{0.002}Br_3$ [11]	8.57	1.357	7.45	84.84
$CsPb_{0.998}Co_{0.002}Br$ [12]	8.67	1.38	7.48	84
$CsPb_{0.97}Yb_{0.03}Br_3$ [6]	9.20	1.536	7.45	80.2
$CsPb_{0.97}Er_{0.03}Br_3$ [6]	9.66	1.563	7.46	82.8
$CsPb_{0.97}Ho_{0.03}Br_3$ [6]	9.75	1.572	7.45	83.2
$CsPb_{0.97}Tb_{0.03}Br_3$ [6]	10.06	1.588	7.47	84.8
$CsPb_{0.97}Sm_{0.03}Br_3$ [6]	10.14	1.59	7.48	85.1

Additionally, a range of computational studies have also been done to study the effect of divalent TM substitution in $CsPbBr_3$. Kanoun and Goumri-Said found that doping $CsPbBr_3$ with Mn^{2+} up to 12.5 % should result in stable structures. This doping substantially modifies the electronic structure of the material and thus leads to a reduced band gap and an increase in the carrier effective masses. [13] These effects could in fact be detrimental to achieving a high V_{OC} as instead both larger band gaps and lower effective masses are known to produce high V_{OC}s. [14] In reality, achieving 12.5 % Pb^{2+} substitution with Mn^{2+} would be difficult, due to the low solubility of $MnBr_2$ in DMF preventing its use in device fabrication. Further computational studies have shown that substitution of the Pb^{2+} with Zn^{2+} and Mn^{2+} could also improve the optoelectronic properties of $CsPbBr_3$ by reducing structural disorder, lowering the band gap and enhancing optical absorption in the visible region. [15] It was suggested that the Pb^{2+} content could be reduced by 50 %, which is beneficial for producing less toxic perovskites. Nonetheless, the study was purely theoretical and the majority of the Pb^{2+} devices that have been fabricated in the literature suggest that small amounts of substitution give the best results. [5, 6] Furthermore, a large reduction in the band gap is not favourable for achieving V_{OC} values.

This chapter explores the effect of substituting transition metal ions (Zn^{2+}, Cu^{2+}, Ni^{2+}, Co^{2+}, Fe^{2+} and Mn^{2+}) and the lanthanide Tb^{3+} at the Pb^{2+} site in $CsPbBr_3$ in planar carbon devices. The aim of this chapter is to explore substitution as a method for achieving V_{OC} increases in $CsPbBr_3$ devices, with the end goal of using them as photoanodes for water oxidation.

5.2. Partial Pb^{2+} Site Substitution with Metal Ions

In order to incorporate metal ions into the $CsPbBr_3$ lattice, a solution of $Pb_{1-X}M_xBr_2$ in DMF was made, where M is a metal ion. Figure 1 shows photographs of the solutions containing copper, nickel, cobalt and iron ions. Note that only four out of seven ions investigated are pictured, this is because these were the only ions that produced significantly coloured solutions. The colours show that the transition metal ions are present in the initial solution. This solution is used in the first part of the two-step $CsPbBr_3$ deposition process. Whilst the ions were originally added in the MBr_2, 2+ oxidation state form, the orange colour of the iron solutions, suggests that it has been oxidised in solution to the 3+ oxidation state form. The solutions containing $NiBr_2$, $MnBr_2$ and $FeBr_2$ required multiple rounds of sonication and heating to dissolve the powder in full.

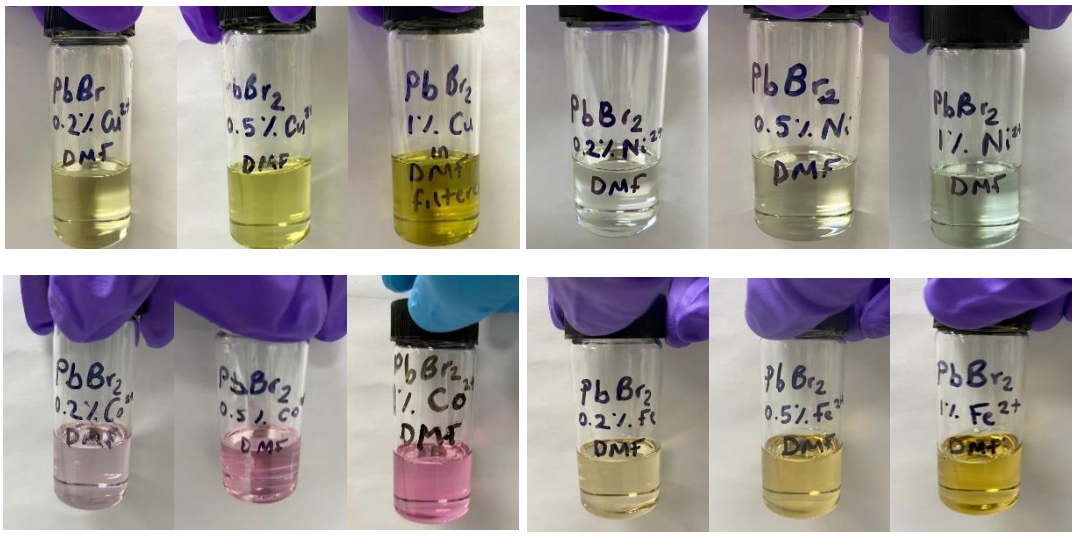

Figure 1: Photographs of $Pb_{1-x}M_xBr_2$ DMF solutions, with 0.2, 0.5 and 1 % copper (top left), 0.2, 0.5, 1 % nickel (top right), 0.2, 0.5, and 1 % cobalt (bottom left), 0.2, 0.5 and 1 % iron (bottom right).

To attempt to replicate the results shown in Table 1 the methods used for Pb^{2+} substitution were followed from the literature. Tang *et al*. stated that transition metal ions doped $CsPbBr_3$ perovskite was fabricated by adding a certain proportion of TMX_2 to the $PbBr_2$ solution.

5.2.1. UV/Vis Analysis

The $Pb_{1-X}M_xBr_2$ solutions were spin coated onto the substrate and annealed. The resulting thin films were light grey, with no discernible colour difference. $CsPb_{1-X}M_xBr_2$ was then formed using the two-step method, described in detail in Chapter 4. The resulting thin films were yellow. The thin films, with 1 % of the Pb^{2+} substituted for TM ions (3 % for Tb^{3+}) were analysed using UV/Vis to see if the substitution has an effect on the band gap. Tauc plots were constructed (Appendix 1.1 and 1.2), and the resulting band gap energies calculated. Three films containing each of the different ions. were measured in order to get a mean average value for the band gap. The results are shown in Figure 2.

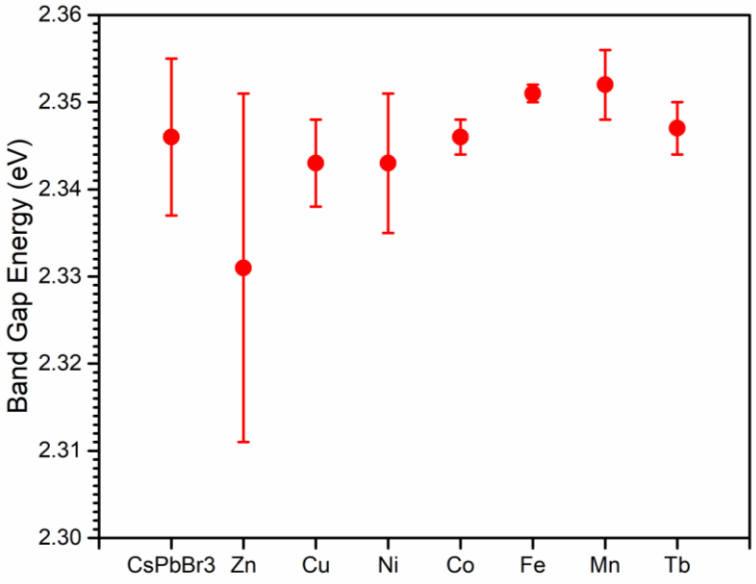

Figure 2: The mean band gap energies of $CsPb_{1-x}M_xBr_2$ thin films on an FTO substrate, with error bars to indicate the standard deviation.

The range in the band gap energies in Figure 2 is small, with overlap in the standard deviation between all samples. Whilst the band gap energy values are given to three decimal places, it is unlikely that this is accurate. Issue can arise due to noise in the measurement and the decision on where to fit the linear part of the Tauc plot. Overall, it appears that the inclusion of metal ions in to the $CsPbBr_3$ has no effect on the bandgap of the sample. It has been reported in the literature that alloying of the B site can be an effective way to the tune the band gap of $CsPbBr_3$. [16] The literature suggests that addition of TM ions, such as Zn^{2+} decreases the optical band gap of $CsPbBr_3$ due to a change in the electron density. [5] The mean band gap value of the Zn^{2+} containing samples in Figure 2, was 2.33 compared to 2.35 for the pristine sample, although there is largest amount of standard deviation around the Zn^{2+} containing

samples. However, the band gap of the resulting Pb^{2+} substituted $CsPbBr_3$ films is not routinely examined in the literatures. Although it was noted that Zhu *et al.* did not observe a change in the band gap in $CsPb_{0.99}Co_{0.01}Br_3$ thin film, suggesting any proposed changes in band gap may not be detectable. [12] Whilst the mean value of the optical band gap, for $CsPb_{0.99}Zn_{0.01}Br_3$, $CsPb_{0.99}Cu_{0.01}Br_3$ and $CsPb_{0.99}Ni_{0.01}Br_3$ are smaller than that of the pristine $CsPbBr_3$, the large overlap in standard deviation, suggest that the true values could lie anywhere in that range.

5.2.2. Analysis Using X-rays

5.2.2.1. XRD Analysis

The XRD patterns of the resulting $CsPb_{0.99}M_{0.01}Br_3$ thin films were also analysed, to ensure that the expected perovskite structure was formed and to look for evidence of the presence of the substituted metal ions. It was hypothesised that as TM ions have a smaller ionic radius than Pb^{2+}, the peaks in the diffraction pattern should be shifted to larger 2θ values, due to shrinkage in the perovskite crystal lattice. The ions have ionic radii, as determined by Imperial College (Materials Department), of Pb^{2+} = 1.19 Å, Zn^{2+} = 0.74 Å, Cu^{2+} = 0.77 Å, Ni^{2+} = 0.69 Å, Co^{2+} = 0.65 Å, Fe^{2+} = 0.61, Mn^{2+} = 0.67 Å and Tb^{3+} = 0.92 Å. [17] Upon first inspection, the 1 % Zn, 1% Ni, 1 % Fe and 3 % Tb diffraction patterns all had peaks at ≈ 11 °, indicating that the Pb rich phase of $CsPbBr_3$ was present (see Appendix 1.3). To remedy this, an extra spin coating cycling with the CsBr/MeOH solution was performed. Figure 3 displays the resulting XRD patterns. The diffraction patterns were normalised around the FTO peaks, allowing comparison of $CsPbBr_3$ peak position.

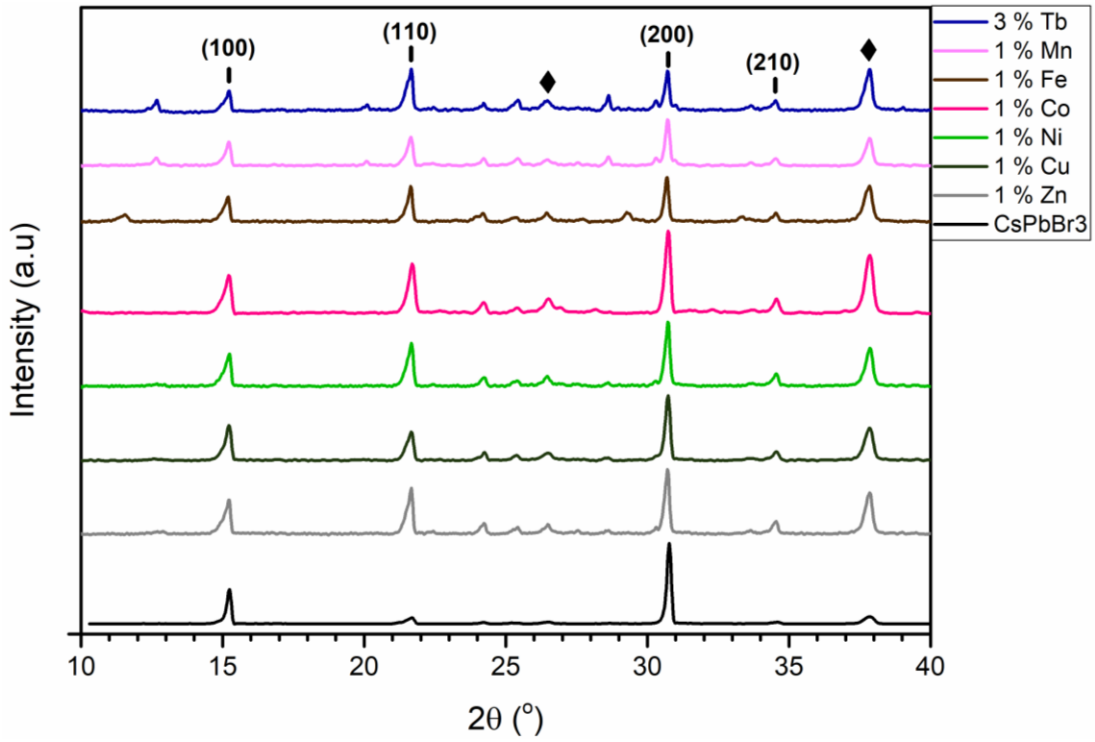

Figure 3: XRD patterns of the $CsPb_{1-x}M_xBr_3$ thin films on FTO. The expected $CsPbBr_3$ peaks are indicated by the black dashes, the FTO peaks are indicated by the black diamonds. The XRD patterns have been normalised to the FTO peaks.

The XRD patterns show that the majority of the metal ion containing films now have a small peak at ≈ 12°. This indicates that the Cs rich phase is now present, this is consistent with the majority of the other impurity peaks present. [18] The full diffraction patterns published in the supporting information by Tang *et al.* also exhibited large peaks at ≈ 12°, including the pristine $CsPbBr_3$ sample, [5] suggesting that the Cs rich phase was present in the literature work and does not negatively impact $CsPbBr_3$ device performance. It was also observed in Figure 3 that the (110) peak intensity increased with respect to the (100) and (200) peaks in the substituted samples, this could indicate an increase in the number of grains with orientation in (110) direction. Although, overall it appears that the addition of the metal ions does not affect the $CsPbBr_3$ perovskite structure. The 2θ peak positions are analysed in Table 2.

Table 2: The 2θ values of the (100), (110), (200) and (210) $CsPbBr_3$ XRD peaks for $CsPb_{1-x}M_xBr_3$, where X = 0.01 for Zn^{2+}, Cu^{2+}, Ni^{2+}, Co^{2+}, Fe^{2+} and Mn^{2+}, and X= 0.03 for Tb^{3+}.

	(100) (°)	**(110) (°)**	**(200) (°)**	**(210) (°)**
$CsPbBr_3$	15.24	21.68	30.77	34.62
$CsPb_{0.99}Zn_{0.01}Br_3$	15.24	21.67	30.72	34.53
$CsPb_{0.99}Cu_{0.01}Br_3$	15.23	21.67	30.74	34.55
$CsPb_{0.99}Ni_{0.01}Br_3$	15.24	21.67	30.74	34.55
$CsPb_{0.99}Co_{0.01}Br_3$	15.22	21.70	30.74	34.56
$CsPb_{0.99}Fe_{0.01}Br_3$	15.22	21.66	30.72	34.54
$CsPb_{0.99}Mn_{0.01}Br_3$	15.22	21.66	30.72	34.54
$CsPb_{0.97}Tb_{0.03}Br_3$	15.22	21.67	30.72	34.53

Table 2 clearly shows that there is no obvious shift to higher 2θ values for the ions with a smaller ionic radius than Pb^{2+}. Work by Tang *et al.* exhibited very minor shifts (< 0.05 °) in some peaks of the XRD patterns of $CsPb_{0.995}X_{0.005}Br_3$ thin film samples. [5] As a result, it is not clear whether the added ions have been integrated into the lattice onto the B site. However, as such small amounts of the substituted ions were added, any change in peak positions could be difficult to detect, perhaps the expected shift would be visible if larger substitution concentrations were used.

5.2.2.2. XPS analysis

Next, the XPS spectra of the thin films were obtained and normalised. The Pb4f, Br3d and Cs4d peak positions were analysed to look for changes in the binding energies. Work by Tang *et al.* suggests that the addition of smaller ions onto the B site of the perovskite lattice shifts the peaks to higher binding energy values. [5] Figure 4 shows the positions of the Pb4f peak, the Br 3d and the Cs 4d peaks.

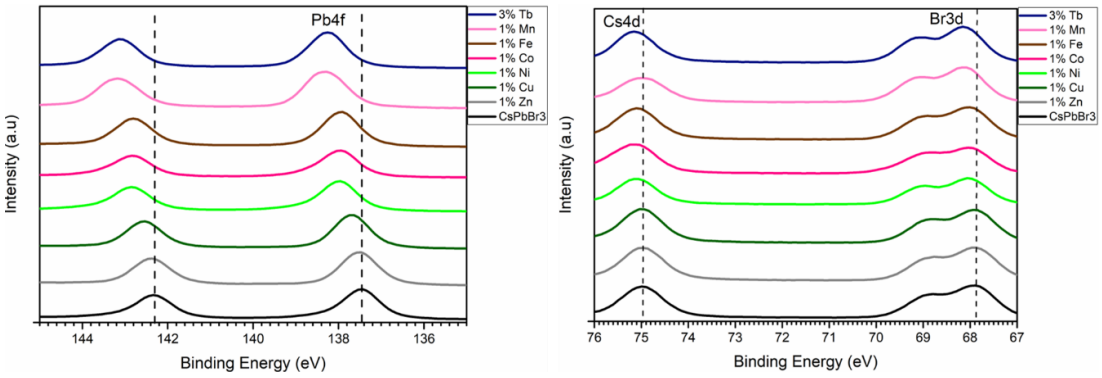

Figure 4: XPS spectra of the Pb4f (left) and Cs4d/Br3d (right) for the $CsPb_{1-x}M_xBr_3$ thin films.

It is clear that there is some change in the binding energy peak positions for the samples containing metal ions. Both the Pb4f, Cs4d and Br3d have been shifted to higher values, as was expected. However, they do not necessarily follow the expected trend. Tb^{3+} is the ion closest in size to Pb^{2+}, so a smaller shift would have been expected, however, it appears that the substitution of Tb^{3+} for Pb^{2+} has caused the largest shift in binding energy of the Pb4f, Cs4d and Br3d peaks. Similarly, the sample containing Mn^{2+} also shows a larger shift in the Pb4f and Br3d than the samples containing Co^{2+} and Fe^{2+}. Whilst the shift in the position of these peaks could indicate the presence of the metal ions within the perovskite lattice, the shifting could also be a result of poor calibration. The XPS spectra are calibrated to a C1s peak.

XPS was also used to investigate the metal 2p binding energies of the TM ions and the 3d binding energy of Tb^{3+}. The presence of the expected binding energies would help confirm the presence of the expected metal ions. The resulting spectra are shown in Figure 5.

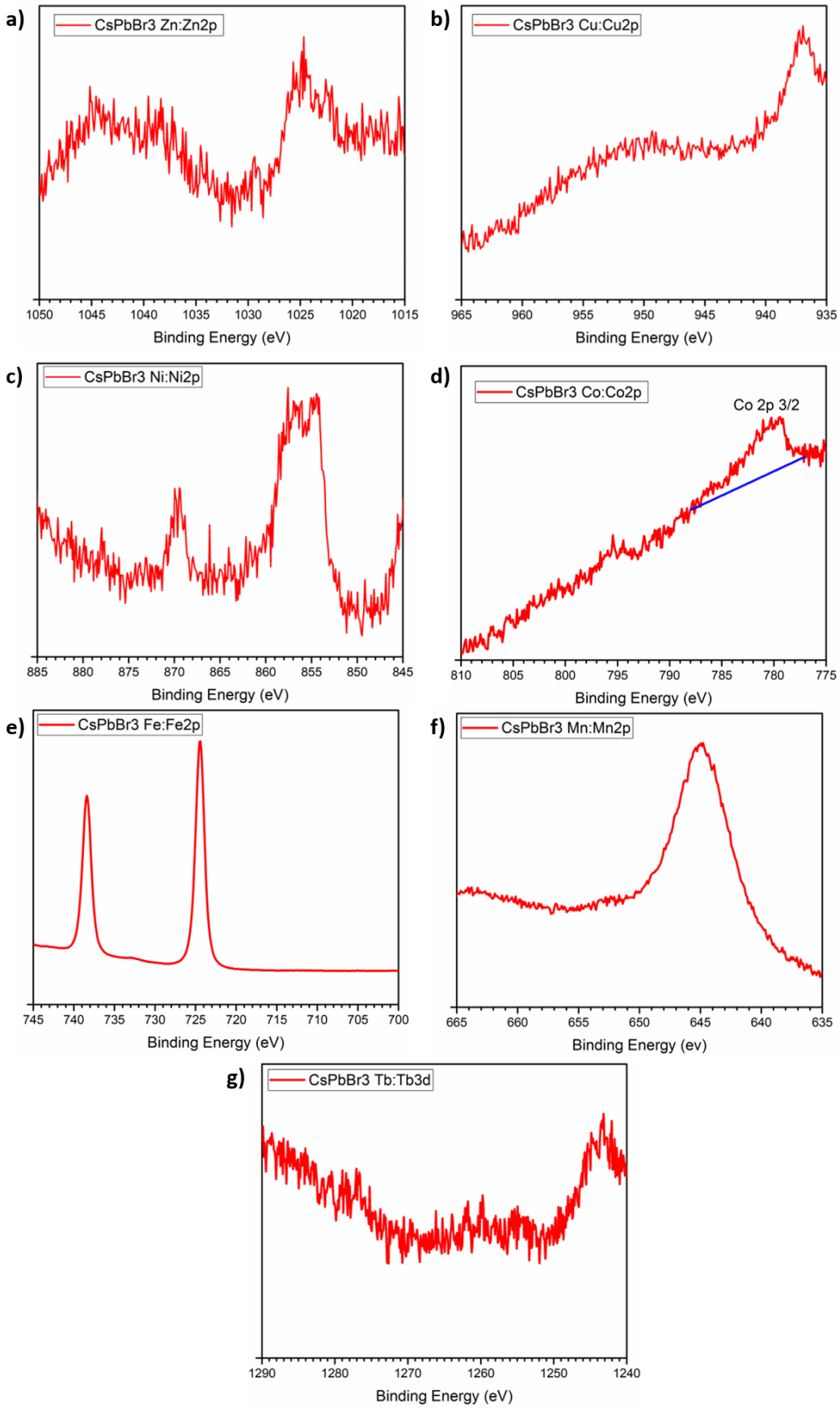

Figure 5: XPS spectra of the a) Zn^{2+} b) Cu^{2+} c) Ni^{2+} d) Co^{2+} e) Fe^{2+} f) Mn^{2+} 2p binding energies and g) Tb^{3+} 3d binding energy.

A compositional analysis failed to identify the expected metal ions in all samples, apart from the sample containing Co^{2+}. This is shown in Figure 5 (d) where a peak between ≈ 785 – 780 is observed, corresponding to a Co^{2+} spin S= 3/2 peak. However, whilst similar expected peaks were not observed in the samples containing the other metal ions, it does not necessarily mean that they are not present. Identifying the presence of and quantifying small amounts of metal ions is difficult, especially if there is overlap with other peaks, such as Auger peaks. This is the case here, as many of the expected metal ion 2p peaks are expected where there is already a peak, or the spectra is noisy. For example, Zn^{2+} 2p peaks can be expected at ≈ 1021 eV for S=3/2 or 1044 eV for S=1/2, [19] and Cu^{2+} peaks can be expected at ≈ 935 eV for S =2/3 or 950 eV for S = 1/2. [20] However, there are small peaks and noise present in the spectra at these positions making it difficult to accurately determine whether the ions are present. Potentially if the metal ions had been present in a greater concentration (> 3 %) they may have been detected more easily with a stronger signal in the expected regions. Other reasons the metal ions may not have been identified include the fact that the metal ions may be distributed better within the bulk of the thin film, than the surface. Nonetheless, the identification of Co^{2+} in the $CsPb_{0.99}Co_{0.01}Br_3$ sample, indicates that the other ions could indeed be present in the other respective samples.

5.2.2.3. EDX Analysis

In an attempt to further investigate the thin films, to find evidence of the metal ions, SEM EDX analysis was undertaken on the films containing 1 % of the substituted metal ions. Both surface and cross-sectional measurements were taken. Nonetheless, neither analysis of the surface or of the bulk gave indication that the expected ions were present in the films. See Appendix 1.4 – 1.10 for the SEM/EDX analysis. It was suggested that such small amounts of the ions would be difficult to detect using EDX. The EDX detection limit is considered to be ≥ 0.1% for atoms with atomic numbers greater than 4, however, for standardless quantative EDX, the error can be as large as ± 5 %. [21] The error also increases when the surface is rough, as the topography of the sample can block the emitted X-rays preventing them from reaching the detector; [21] this is likely to be the case for the thin film surfaces of the perovskite sample. Nonetheless, it was unexpected to not observe some evidence of the metal ions in the film, as SEM/EDX images reportedly showing the presence of transition metal ions in smaller amounts, have been published in the literature. [5, 6, 12] However, further analysis of the images in the literature provided some cause for disagreement. The images in the literature showed images of TM ions in $CsPbBr_3$ down to concentrations as small as 0.2 %, with the images appearing to show a larger than expected concentration of the ions present. Using the EDX software, it is possible to predefine a list of elements that would be expected in the sample.

Whilst this can be useful for including elements that are definitely present e.g. Cs, Pb and Br and for excluding other elements that should not be present, this feature can cause issues. When selecting a particular element, the software will look for any peaks in the spectra that could correspond to the selected element. However, if the expected peak positions of the chosen element overlap with those of another element that is definitely present in the sample, or other small background peaks, it can mistake these peaks for the selected element, even if it is not actually present. Therefore, whilst the EDX mapping images may suggest the presence of the metal ions in the samples, it is possible that they are not present or not identifiable.

5.2.3. AFM Analysis

AFM images of the surface of the thin films were taken to analyse the effect of the metal ions on the morphology and grain size of the samples. An increase in the perovskite grain size results in the reduction of grain boundaries within the sample, thus leading to reduced charge carrier combination; [22] this would be beneficial for $CsPbBr_3$ device performance. The literature suggests that the inclusion of metal ions increases the perovskite crystal grain size. [3, 5, 6] In the $PbBr_2$ solution, each Pb^{2+} can form Lewis base adducts with the oxygen atom in one DMF molecule. [23] However, transition metal $^{2+}$ ions are stronger Lewis acids than Pb^{2+} due to their smaller ionic radii; Tb^{3+} is also a stronger Lewis acid than Pb^{2+} due to the increased level of charge. As a result, the added ions can coordinate to the DMF solvent molecules more strongly than the Pb^{2+} ions, which slows down the solvent evaporation in the device fabrication process. In turn, this slows down the crystallisation of the thin film, reducing the number of nucleation sites and yielding larger grain sizes. [24] Thus, it was expected that the partially substituted $CsPbBr_3$ thin films would exhibit larger grain sizes than the control. Thin films where the Pb^{2+} site had been substituted with 0.5 % and 1 % of the transition metal ions were investigated. However, in the case of Tb^{3+} 3 % substitution was investigated as larger concentrations of lanthanide ions within $CsPbBr_3$ have been reported to yield larger grain sizes and better device performance. [6] The AFM images are shown below in Figures 6 and 7.

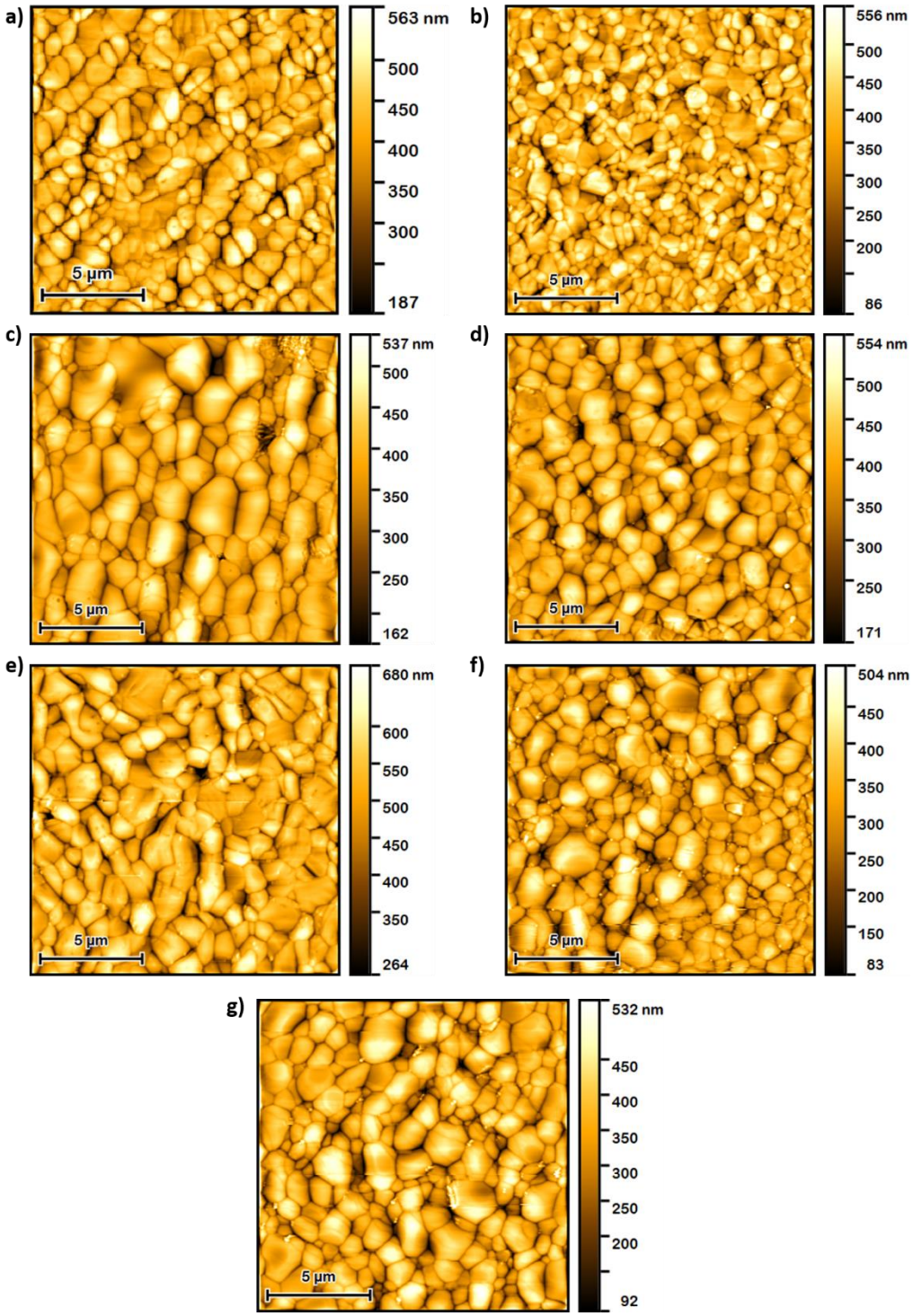

Figure 6: AFM images of 0.5% TM metal substituted $CsPbBr_3$. a) pristine $CsPbBr_3$ b) 0.5 % Zn c) 0.5% Cu d) 0.5 % Ni e) 0.5% Co f) 0.5% Fe and g) 0.5% Mn, taken at 15 x 15 μm^2. The scale bar represents 5 µm.

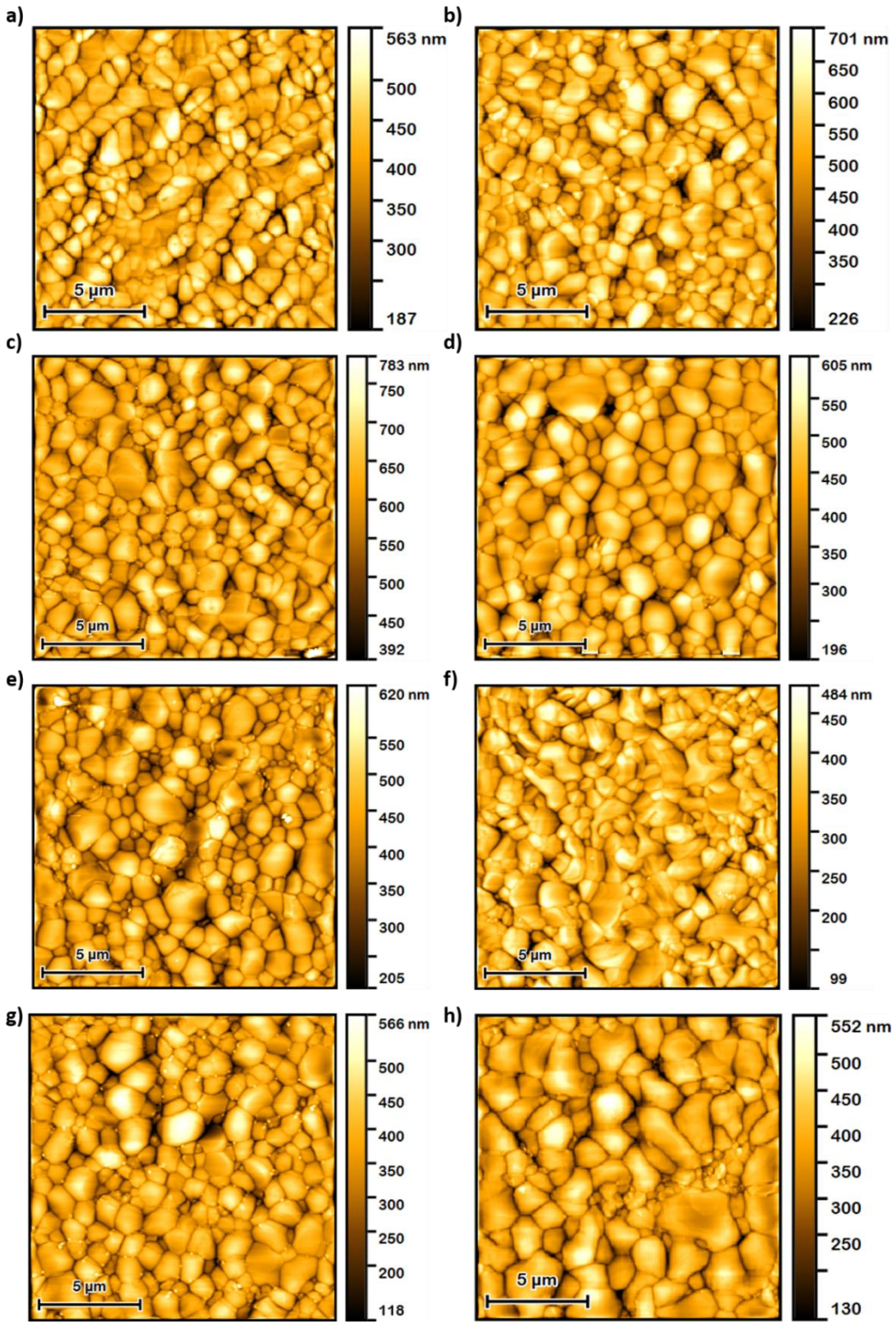

Figure 7: AFM images of the 1 % TM metal and 3 % Tb^{3+} substituted $CsPbBr_3$. a) pristine $CsPbBr_3$ b) 1 % Zn c) 1 % Cu d) 1 % Ni e) 1 % Co f) 1 % Fe g) 1 % Mn, and f) 3 % Tb taken at 15 x 15 μm^2. The scale bar represents 5 µm.

At first glance it does appear that the incorporation of metal ions into the perovskite crystal lattice can increase the size of the grains. Excluding the samples containing Zn^{2+}, all of the metal ion substituted samples included some grains that were much larger than those seen in

the AFM images of the pristine sample. Grains with a diameter greater than 3 µm observed in the Cu^{2+} and Tb^{3+} containing films. However, to truly assess whether certain conditions or additives give rise to larger grain sizes, it is important to consider the range in grain size over multiple samples. As a result, AFM images were taken from four samples and various parameters were investigated. The mean roughness (S_a), the mean grain size and the mean grain area were examined across the four samples. Figures 8 and 9 show the results.

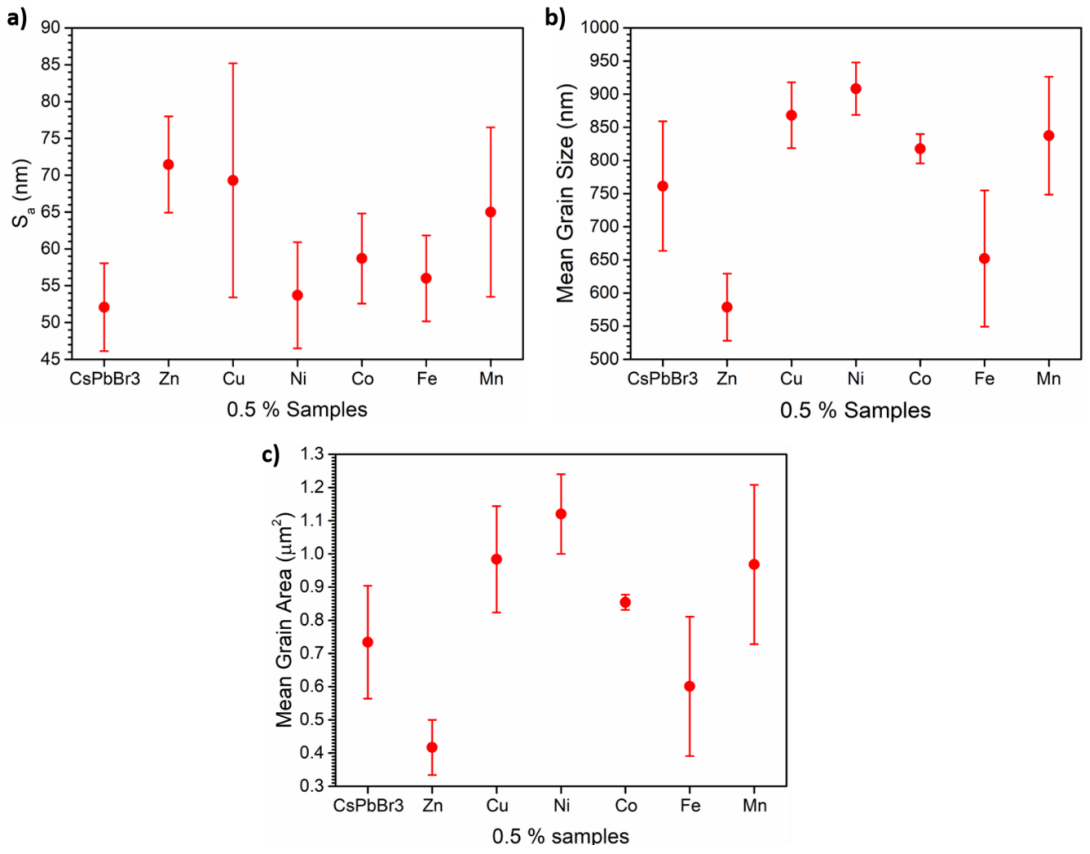

Figure 8: AFM grain size comparison of the 0.5 % substituted $CsPbBr_3$ samples showing a) the mean roughness (S_a) of the thin films b) the mean grain size and c) the mean grain area. The error bars show the standard deviation.

Figure 8 shows that the substitution of the TM ions into the Pb^{2+} site at a concentration of 0.5 % can produce some large grains, with Ni^{2+} giving rise to a mean grain size of over 900 nm and a mean grain area of over 1.1 µm^2, compared to 761 nm and 0.73 µm^2 respectively for the pristine $CsPbBr_3$. However, there is a large amount of variation around the mean values, shown by the large error bars. Thus, whilst the Cu^{2+}, Ni^{2+}, Co^{2+} and Mn^{2+} samples all have mean grain sizes and areas larger than the pristine sample, the fact that the grain sizes and areas vary so much within and across the samples mean that potentially a much larger population of samples would be more useful to fully determine the effect of substitution on the grain size of $CsPbBr_3$ thin films. Unexpectedly, 0.5 % Zn^{2+} resulted in a smaller grains than the pristine sample; this contrasts what was found by Tang and co-workers. [5] It was also

noted that the pristine $CsPbBr_3$ had the lowest mean roughness value of 52 nm, compared to the values for the 0.5 % substituted samples. Smoother perovskite thin film layers are associated with higher PCE values in devices as contact between the ETL and HTL is improved, with reduced surface defects facilitating charge transfer between the layers. [25]

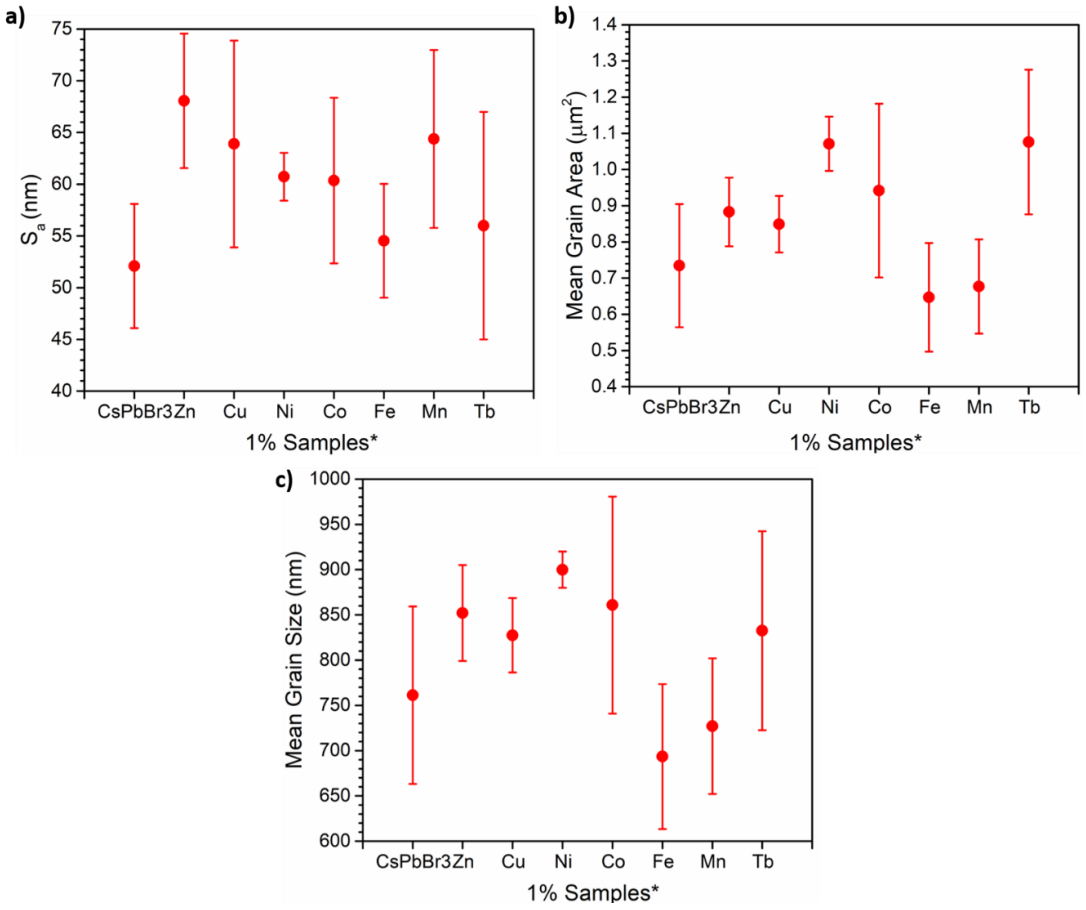

*Figure 9: AFM grain size comparison of the 1 % substituted $CsPbBr_3$ samples showing a) the mean roughness (S_a) of the thin films b) the mean grain size and c) the mean grain area. The error bars show the standard deviation * Tb^{3+} samples are substituted at a concentration of 3 %.*

Figure 9 also shows that the substitution of the Pb^{2+} site in larger concentrations can give rise to the presence of some large grains, with Ni^{2+} again providing the largest mean grain size of 900 nm and largest mean grain area of just below 1.1 µm^2. Despite this, the grains were not as large as those seen in the 0.5 % samples. Again, there is a large amount of variation around the mean values.

Whilst the AFM images and analysis give some indication that the substitution of Pb^{2+} in $CsPbBr_3$ for ions such as Ni^{2+} or Tb^{3+} can result in larger perovskite crystal grain, more samples are needed to definitively determine this. In fact, work by K O'Grady *et. Al.* concluded that over 500 thin film samples of data would be required to be able to accurately determine the average grain size. [26] Due to the sheer number of samples and time this would

require, the suggested number of samples was not met, and it is unlikely that detailed grain sizes analyses are carried out regularly throughout the literature. As a result, a larger sample size and further statistical analysis, both within this work and throughout the literature would be useful to determine whether the difference in the mean grain sizes and areas are statistically significant.

5.2.4. Device Performance

$CsPbBr_3$ devices with an FTO|c-TiO_2/m-TiO_2|$CsPb_{1-x}M_xBr_3$|Carbon|Ag architecture were fabricated in ambient conditions to investigate the effects of Pb^{2+} substitution on device performance. Based on previous literature findings, it was expected that substitution of the Pb^{2+} site for transition metal ions would enhance the device performance and lead to large increases in the V_{OC} for some of the ions. [5, 6] However, this was not necessarily the case. Table 3 shows the champion device for each substitution condition investigated.

Table 3: Champion $CsPb_{1-x}M_xBr_3$ carbon devices.

	Reverse PCE (%)	**Reverse V_{OC} (V)**	**J_{SC} (mA cm^{-2})**	**Reverse FF (%)**
$CsPbBr_3$	8.99	1.48	8.53	71.3
$CsPb_{0.998}Zn_{0.002}Br_3$	6.88	1.40	6.73	72.5
$CsPb_{0.995}Zn_{0.005}Br_3$	7.81	1.45	7.18	75.0
$CsPb_{0.99}Zn_{0.01}Br_3$	7.97	1.48	7.04	76.5
$CsPb_{0.998}Cu_{0.002}Br_3$	6.37	1.42	6.22	71.6
$CsPb_{0.995}Cu_{0.005}Br_3$	7.55	1.44	6.99	75.1
$CsPb_{0.99}Cu_{0.01}Br_3$	8.25	1.44	7.83	73.3
$CsPb_{0.998}Ni_{0.002}Br_3$	7.68	1.46	6.63	79.4
$CsPb_{0.995}Ni_{0.005}Br_3$	8.61	1.47	7.52	77.9
$CsPb_{0.99}Ni_{0.01}Br_3$	6.94	1.46	5.91	80.4
$CsPb_{0.998}Co_{0.002}Br_3$	7.35	1.45	6.59	76.9
$CsPb_{0.995}Co_{0.005}Br_3$	6.82	1.41	6.40	75.7
$CsPb_{0.99}Co_{0.01}Br_3$	6.70	1.39	6.83	70.6
$CsPb_{0.998}Fe_{0.002}Br_3$	1.92	1.18	3.15	51.6
$CsPb_{0.995}Fe_{0.005}Br_3$	1.05	1.19	1.75	50.4
$CsPb_{0.99}Fe_{0.01}Br_3$	0.77	1.14	1.28	52.5
$CsPb_{0.998}Mn_{0.002}Br_3$	5.84	1.37	5.93	71.9
$CsPb_{0.995}Mn_{0.005}Br_3$	2.74	1.25	4.15	52.9
$CsPb_{0.99}Mn_{0.01}Br_3$	1.27	1.16	3.29	33.3
$CsPb_{0.995}Tb_{0.005}Br_3$	6.86	1.44	6.36	75.0
$CsPb_{0.99}Tb_{0.01}Br_3$	6.64	1.45	6.27	73.1
$CsPb_{0.97}Tb_{0.03}Br_3$	6.26	1.45	5.91	73.1

Overall, the champion cell with the highest PCE was the pristine $CsPbBr_3$, with a reverse PCE of 8.99 % and a V_{OC} of 1.48 V. This was unexpected as PCE values greater than 9.0 % have been achieved by Pb^{2+} substitution with transition metal ions, reaching over 10 % when lanthanide ions are used, as reported by Tang *et al.* [5, 6] The data in Table 3 is visulised in Figure 10, which displays the JV curves of the champion cells at each substitution concentration.

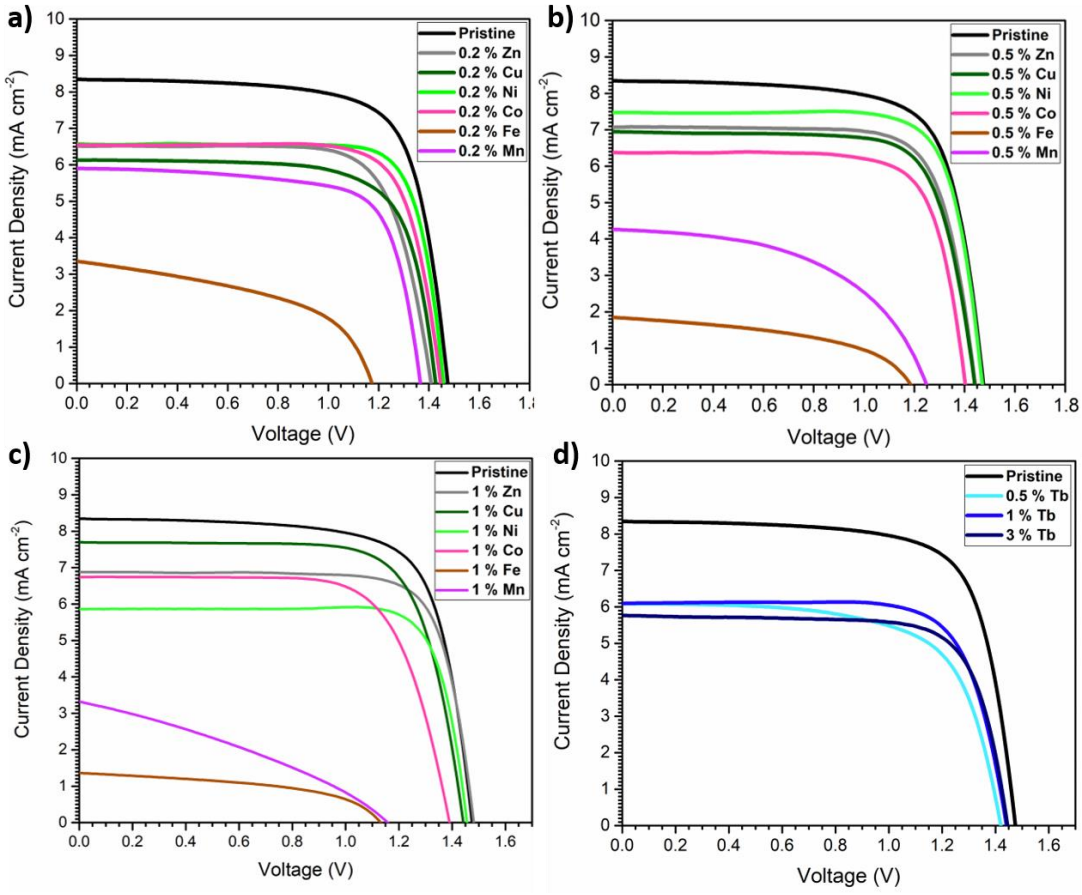

Figure 10: JV curves a) champion $CsPb_{0.998}M_{0.002}Br_3$ devices, b) champion $CsPb_{0.995}M_{0.005}Br_3$ devices c) champion $CsPb_{0.99}M_{0.01}Br_3$ devices and c) $CsPb_{1-x}Tb_xBr_3$ devices.

Figure 10 clearly shows that the pristine champion cell out performs the substituted devices, this is likely due to the large current density value of 8.53 mA cm^{-2}, which is the largest value of all the champion devices, with the substituted devices all having current densities below 8 mA cm^{-2}. However, the champion device has a worse FF value than some of the substituted devices. Despite the unchanged $CsPbBr_3$ champion device displaying the best JV characteristics, it is important to look at the spread of values across a number of devices to determine whether the Pb^{2+} site substitution has a positve effect. As a result, a set of 12 devices were made for each substituion condition and compared to the set of the pristine devices. Student t-tests were carried out to determine whether there was a significant statistical difference between the pristine $CsPbBr_3$ and substituted $CsPbBr_3$planar carbon devices. The null hypothesis was defined as '*there is no significant difference between the control $CsPbBr_3$ devices and the $CsPb_{1-x}M_xBr_3$ devices'.* A value of $p < 0.05$ was taken as the threshold to reject the null hypothesis and therefore it would infer that there was a significant statistical difference between the two sets of devices that were being tested.

5.2.4.1. Zn^{2+} Substituted Devices

The divalent zinc ion was substituted for Pb^{2+} on the B-site of the perovskite at concentrations of 0.2, 0.5 and 1.0 %. It was expected that all three substitution concentrations would improve the JV characteristics of the devices as Tang *et al.* found that Zn^{2+} was the transition metal ion that yields greatest improvements in the devices. [5] Consequently, large PCE and V_{OC} values were anticipated. The box plots in Figure 11 compares the reverse PCE, the reverse V_{OC}, the J_{SC}, the reverse FF and the hysteresis factor of the devices.

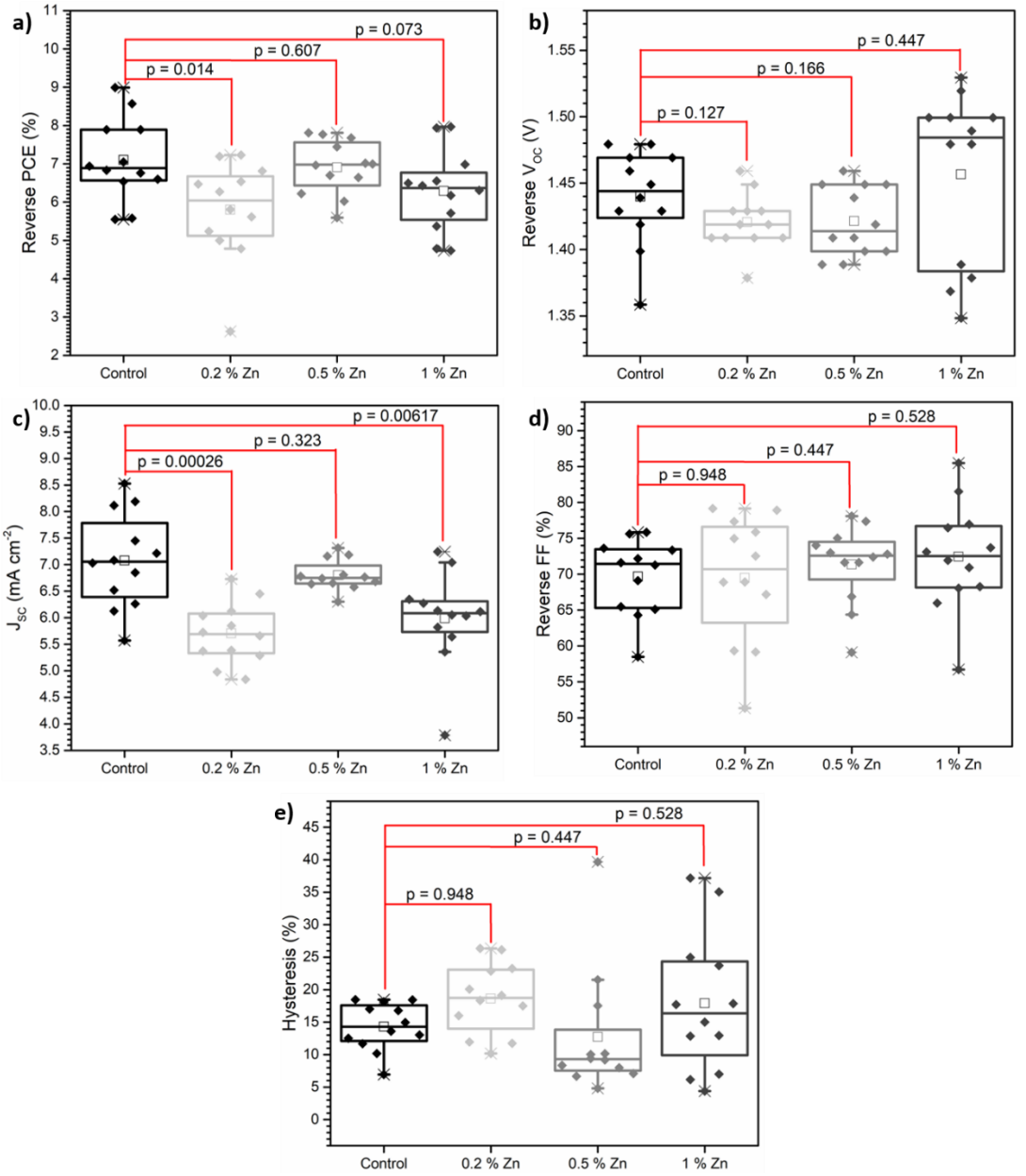

Figure 11: Box plots comparing a) the reverse PCE, b) the reverse V_{OC} c) the J_{SC} d) the reverse FF and e) the hysteresis factor of $CsPbBr_3$, $CsPb_{0.998}Zn_{0.002}Br_3$, $CsPb_{0.995}Zn_{0.005}Br_3$ and $CsPb_{0.99}Zn_{0.01}Br_3$ planar carbon devices. The mean values are represented by the square symbol.

The pristine $CsPbBr_3$ devices has the highest mean reverse PCE value of 7.09 %, compared to 5.81, 6.89 and 6.27 % respectivley, for the 0.2, 0.5 and 1 % substitued devices. Nonetheless, no significantly statiscial difference was observed between the PCE of the pristine $CsPbBr_3$ and the 0.5 and 1 % substituted devices. Furthermore, there was a statisical difference between the reverse PCE values of the pristine and the 0.2 % substituted devices, with the Zn substited devices performing worse in this case.

The 1 % Zn substittued devices did achieve the largest reverse V_{OC} values, with two of these devices reaching V_{OC}s above 1.5 V and five devices reaching V_{OC} values greater than any of the pristine devices. The top V_{OC} of 1.53 V, achieved by one device with a substituion concentration of 1 % Zn, was the largest V_{OC} value achieved by any device in this thesis, perhaps demonstrating that in some cases, the use of Zn^{2+} can be used to achiev high V_{OC} values. However, it is impossible to attribute this increase soley on the addition of the Zn^{2+}. Despite this, there was no significant statistical difference between the pristine devices and any of the Zn substituted devices, so it cannot be concluded that Zn^{2+} has an overall benefical effect on the V_{OC} of $CsPbBr_3$ planar carbon devices. The PCE and V_{OC} values shown in Figure 11, were also much lower than the values of 9.18 % and 1.56 V for the champion $CsPb_{0.995}Zn_{0.005}Br_3$ cell that was achieved in the literature. [5]

The very small p values of 0.0026 and 0.00617 show that J_{SC} of the 0.2 % and 1 % substitued devices were significantly worse than the standard devices. However, there was no statisical difference in either the reverse FF values or the hysteresis factor values. Overall it was concluded that were was no substanital beneficial effect of substituting Pb^{2+} for Zn^{2+}.

5.2.4.2. Cu^{2+} Substituted Devices

The divalent copper ion was substituted for Pb^{2+} on the B-site of the perovskite at concentrations of 0.2, 0.5 and 1.0 %. Improvements in the PCE and V_{OC} were once again expected. The box plots in Figure 12 compares the reverse PCE, the reverse V_{OC}, the J_{SC}, the reverse FF and the hysteresis factor of the devices.

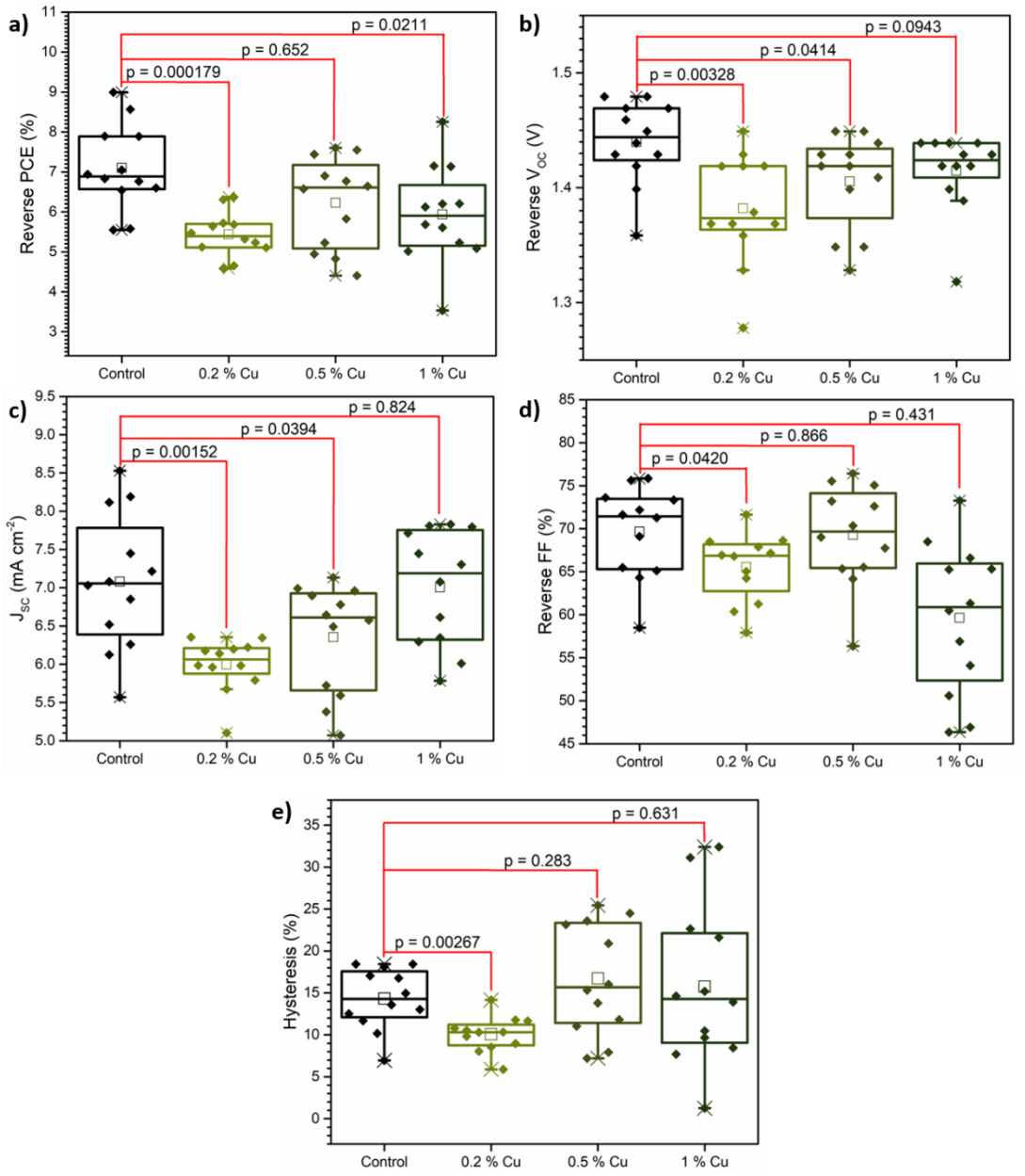

Figure 12: Box plots comparing a) the reverse PCE, b) the reverse V_{OC} c) the J_{SC} d) the reverse FF and e) the hysteresis factor of $CsPbBr_3$, $CsPb_{0.998}Cu_{0.002}Br_3$, $CsPb_{0.995}Cu_{0.005}Br_3$ and $CsPb_{0.99}Cu_{0.01}Br_3$ planar carbon devices. The mean values are represented by the square symbol.

Statistical differences were found between the reverse PCE of the pristine $CsPbBr_3$ devices and the Cu^{2+} substituted devices; however, these differences are not in favour of the Cu^{2+} substitution. The P values between the PCE of pristine and the 0.2 % devices and the pristine and the 1 % substituted devices were 0.000179 and 0.0211 respectively. The mean reverse PCE values were 7.09, 5.43 and 5.89 % respectively. However, the P value between the PCE of the pristine devices and the 0.5 % substituted devices showed no significant difference to the performance of the device. Overall, this indicates that Pb^{2+} substitution for small amounts of Cu^{2+} is not beneficial for $CsPbBr_3$ planar carbon devices

Additionally, there is no obvious benefit to the V_{OC} of these devices, with the p values showing that the devices containing Cu^{2+} are either no different (1 % Cu^{2+}) or statistically worse (0.2 and 0.5 % Cu^{2+}) than the control. There was also no statistically significant improvement in the J_{SC} or the reverse FF. However, the results in Figure 12 do suggest that a small amount of copper (0.2 %) may be able to reduce hysteresis within the devices under the measurement conditions used, although overall the performance of the 0.2 % Cu^{2+} substituted devices was worse than the control. As a result, a small reduction in the hysteresis factor is not necessarily beneficial compared to the loss in performance.

5.2.4.3. Ni^{2+} Substituted Devices

The divalent nickel ion was substituted for Pb^{2+} on the B-site of the perovskite at concentrations of 0.2, 0.5 and 1.0 %. Although the literature results for Ni^{2+} substitution did not yield improvements as great as those for Zn^{2+} and Cu^{2+}, [5] improvements in the PCE and V_{OC} were still expected to be observed. The box plots in Figure 13 compares the reverse PCE, the reverse V_{OC}, the J_{SC}, the reverse FF and the hysteresis factor of the devices.

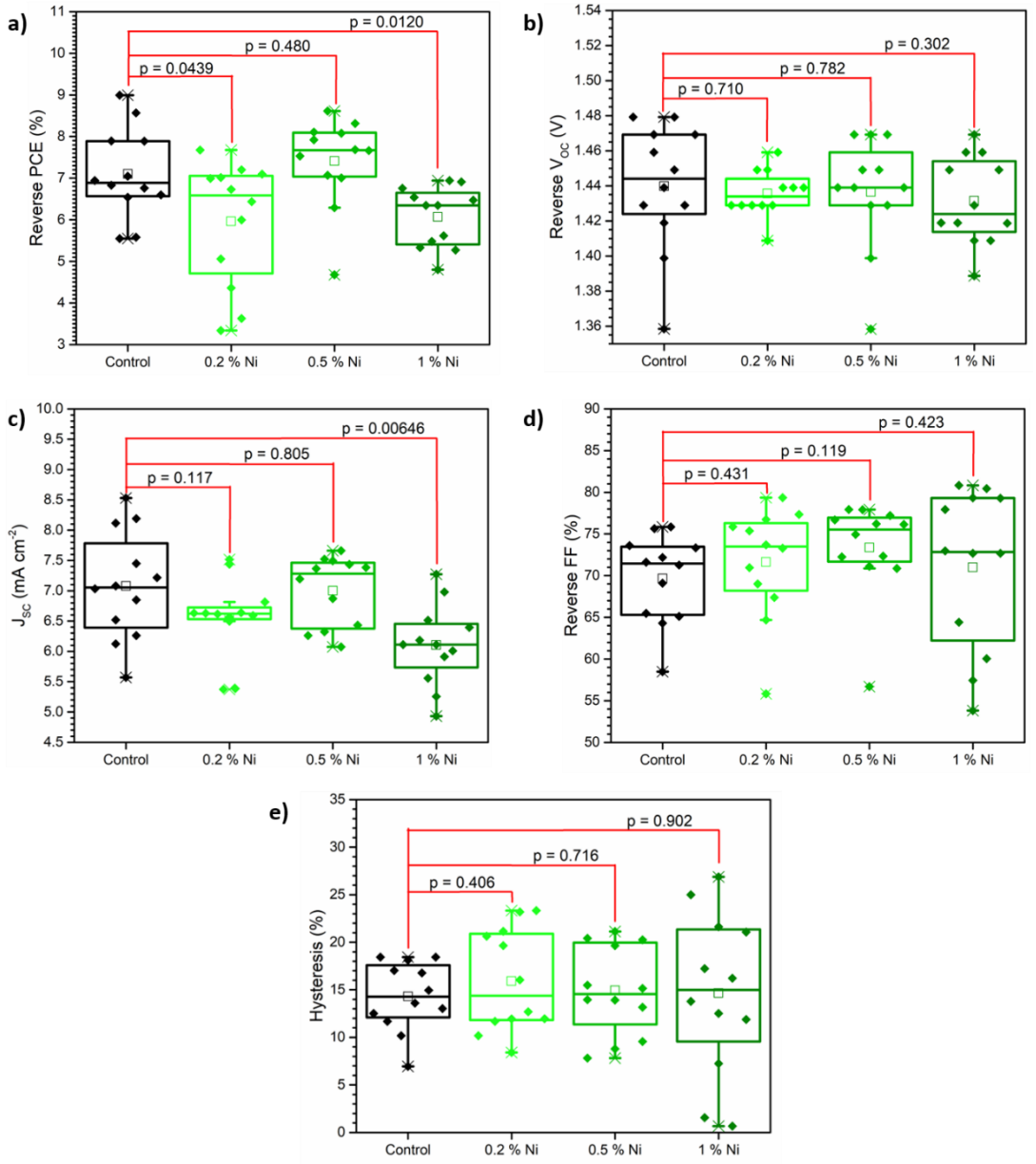

Figure 13: Box plots comparing a) the reverse PCE, b) the reverse V_{OC} c) the J_{SC} d) the reverse FF and e) the hysteresis factor of $CsPbBr_3$, $CsPb_{0.998}Ni_{0.002}Br_3$, $CsPb_{0.995}Ni_{0.005}Br_3$ and $CsPb_{0.99}Ni_{0.01}Br_3$ planar carbon devices. The mean values are represented by the square symbol.

The data in Figure 13, shows that the mean reverse PCE value for 0.5 % substituted Ni^{2+} samples is 7.41 %, compared to 7.09 % for the pristine devices, initially suggesting that a small amount of Ni^{2+} could help improve the efficiency of $CsPbBr_3$ planar carbon devices. Despite this, once again, the p values demonstrate that there was no statistically significant improvement in any of the JV characteristics for the devices where Ni^{2+} was substituted in at the Pb^{2+} site. However, the values of the champion PCE and V_{OC} for $CsPb_{0.995}Ni_{0.005}Br_3$ was comparable to that of the literature Ni^{2+} containing champion device. [5]

5.2.4.4. Co^{2+} Substituted Devices

The divalent cobalt ion was substituted for Pb^{2+} on the B-site of the perovskite at concentrations of 0.2, 0.5 and 1.0 %. Although the literature results for Co^{2+} substitution did not yield V_{OC} values greater than the average V_{OC} values achieved for the pristine devices in this thesis, [11, 12] improvements in the PCE were still expected to be observed. The box plots in Figure 14 compares the reverse PCE, the reverse V_{OC}, the J_{SC}, the reverse FF and the hysteresis factor of the devices.

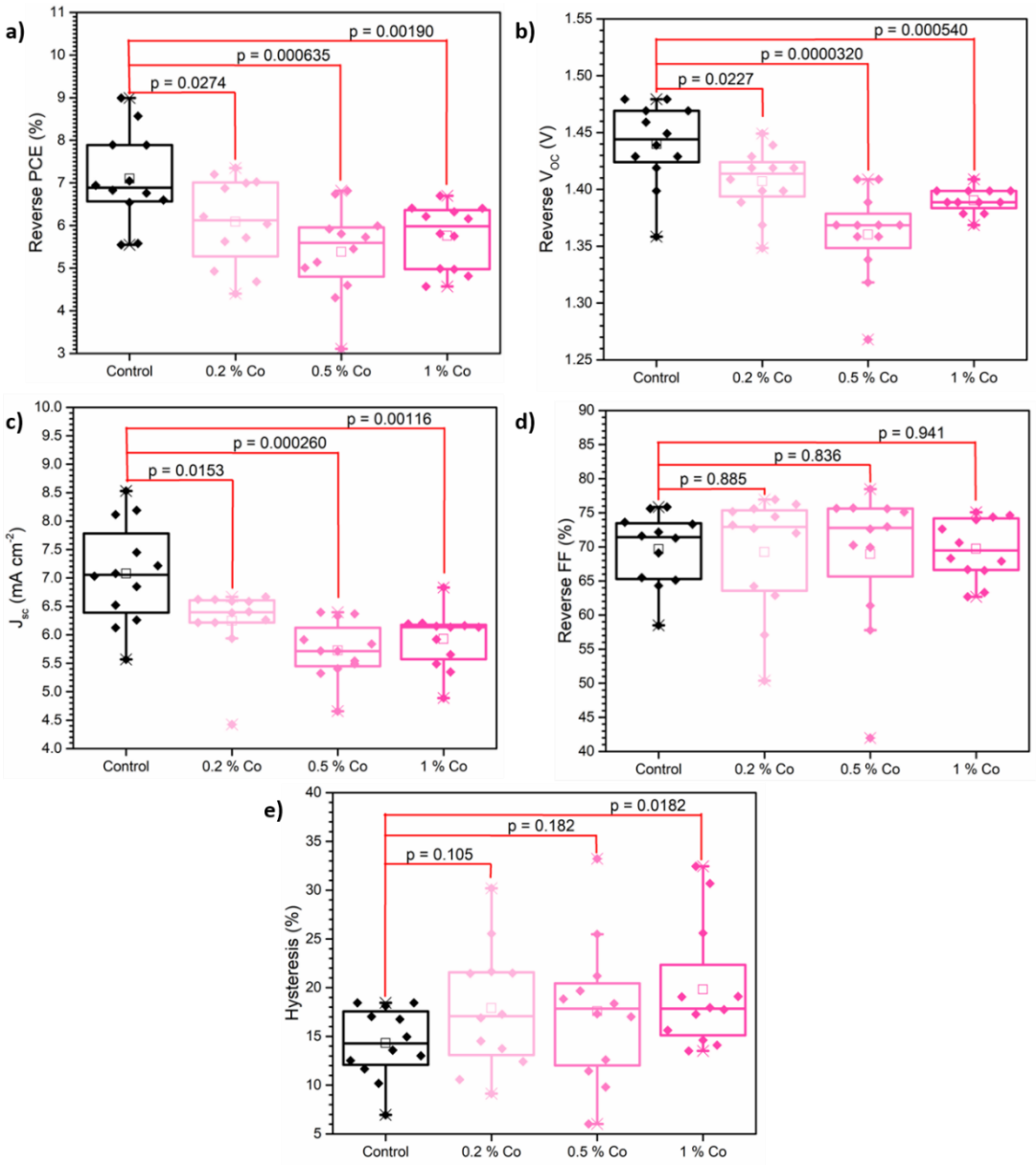

Figure 14: Box plots comparing a) the reverse PCE, b) the reverse V_{OC} c) the J_{SC} d) the reverse FF and e) the hysteresis factor of $CsPbBr_3$, $CsPb_{0.998}Co_{0.002}Br_3$, $CsPb_{0.995}Co_{0.005}Br_3$ and $CsPb_{0.99}Co_{0.01}Br_3$ planar carbon devices. The mean values are represented by the square symbol.

The substitution of Pb^{2+} for Co^{2+} resulted in statistically significantly worse device performance, with the 0.2, 0.5 and 1% Co^{2+} devices exhibiting poorer PCE, V_{OC} and J_{SC} values than the control devices. The champion PCE for the 0.2 % substituted devices in the literature was 8.67 %, [12] which was not reached by any of the Co^{2+} containing devices shown in Figure 14. However, the champion V_{OC} for $CsPb_{0.998}Co_{0.02}Br_3$ achieved by Wang and co-workers, was 1.38 V, [12] whereas the same devices in Figure 14 reached an average V_{OC} of 1.41 V. In Figure 14, the average value of 1.41 V for the 0.2 % substituted devices, is less than the average V_{OC} of 1.44 V for the pristine devices. It is therefore clear that the use of Co^{2+} in $CsPbBr_3$ devices is not advantageous. Additionally, it appears that increasing the substitution concentration to 1 % could increase the hysteresis factor of the devices measured under these conditions.

5.2.4.5. Fe^{2+} Substituted Devices

The divalent iron ion was substituted for Pb^{2+} on the B-site of the perovskite at concentrations of 0.2, 0.5 and 1.0 %. Whilst Fe^{2+} has been shown to be beneficial when doped in $CsPbBr_3$ quantum dots, [27] there is not much work in the literature that incorporates Fe^{2+} into $CsPbBr_3$ planar carbon devices. As a result, this was investigated and the box plots in Figure 15 compares the reverse PCE, the reverse V_{OC}, the J_{SC}, the reverse FF and the hysteresis factor of the devices.

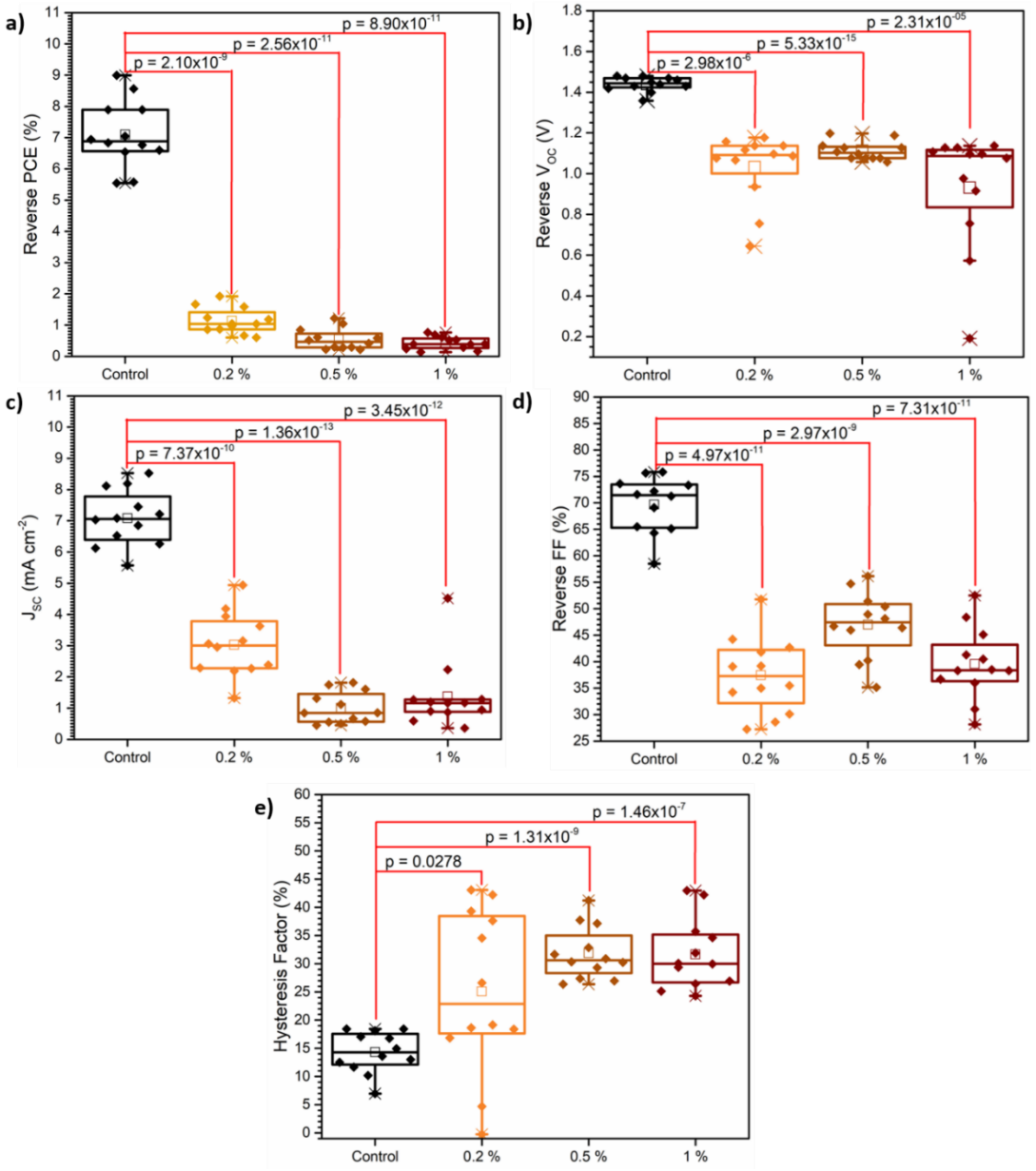

Figure 16: Box plots comparing a) the reverse PCE, b) the reverse V_{OC} c) the J_{SC} d) the reverse FF and e) the hysteresis factor of $CsPbBr_3$, $CsPb_{0.998}Fe_{0.002}Br_3$, $CsPb_{0.995}Fe_{0.005}Br_3$ and $CsPb_{0.99}Fe_{0.01}Br_3$ planar carbon devices. The mean values are represented by the square symbol.

It is clear from the five box plots in Figure 15, that substituting Fe^{2+} into the B-site in $CsPbBr_3$ negatively affects $CsPbBr_3$ planar carbon device performance. The p values calculated between the pristine devices and the Fe^{2+} containing devices are very small, indicating that the decreases in the device performances are statistically significant. The mean reverse PCE for the three substitution concentrations are 1.11, 0.53 and 0.34 % with p values of 2.10×10^{-9}, 2.56×10^{-11} and 8.90×10^{-11} respectively, compared to 7.09 % for the control devices. This shows that even small amounts of Fe^{2+} can cause a large drop in PCE and increasing the iron concentration results in the PCE decreasing further. Furthermore, a large decrease in the V_{OC},

the J_{SC} and the FF were observed upon the addition of Fe^{2+}. All of the sets of devices containing Fe^{2+}, had a mean reverse V_{OC} below 1.23 V (the theoretical requirement for water oxidation), with V_{OC} values of 1.03, 1.11 and 0.93 V respectively. This shows that substituting Pb^{2+} for Fe^{2+} is not beneficial in the use of $CsPbBr_3$ devices for water oxidation.

5.2.4.6. Mn^{2+} Substituted Devices

The divalent manganese ion was substituted for Pb^{2+} on the B-site of the perovskite at concentrations of 0.2, 0.5 and 1.0 %. Again, Mn^{2+} has been shown to be beneficial when doped in $CsPbBr_3$ quantum dots, [9] and work by Qi *et al.* demonstrates that small quantities on Mn^{2+} (0.5 % substitution concentration) can improve $CsPbI_{1.01}Br_{1.99}$ carbon devices. [28] It was expected that these benefits could also apply to $CsPbBr_3$ carbon devices, thus this was investigated. The box plots in Figure 16 compares the reverse PCE, the reverse V_{OC}, the J_{SC}, the reverse FF and the hysteresis factor of the devices.

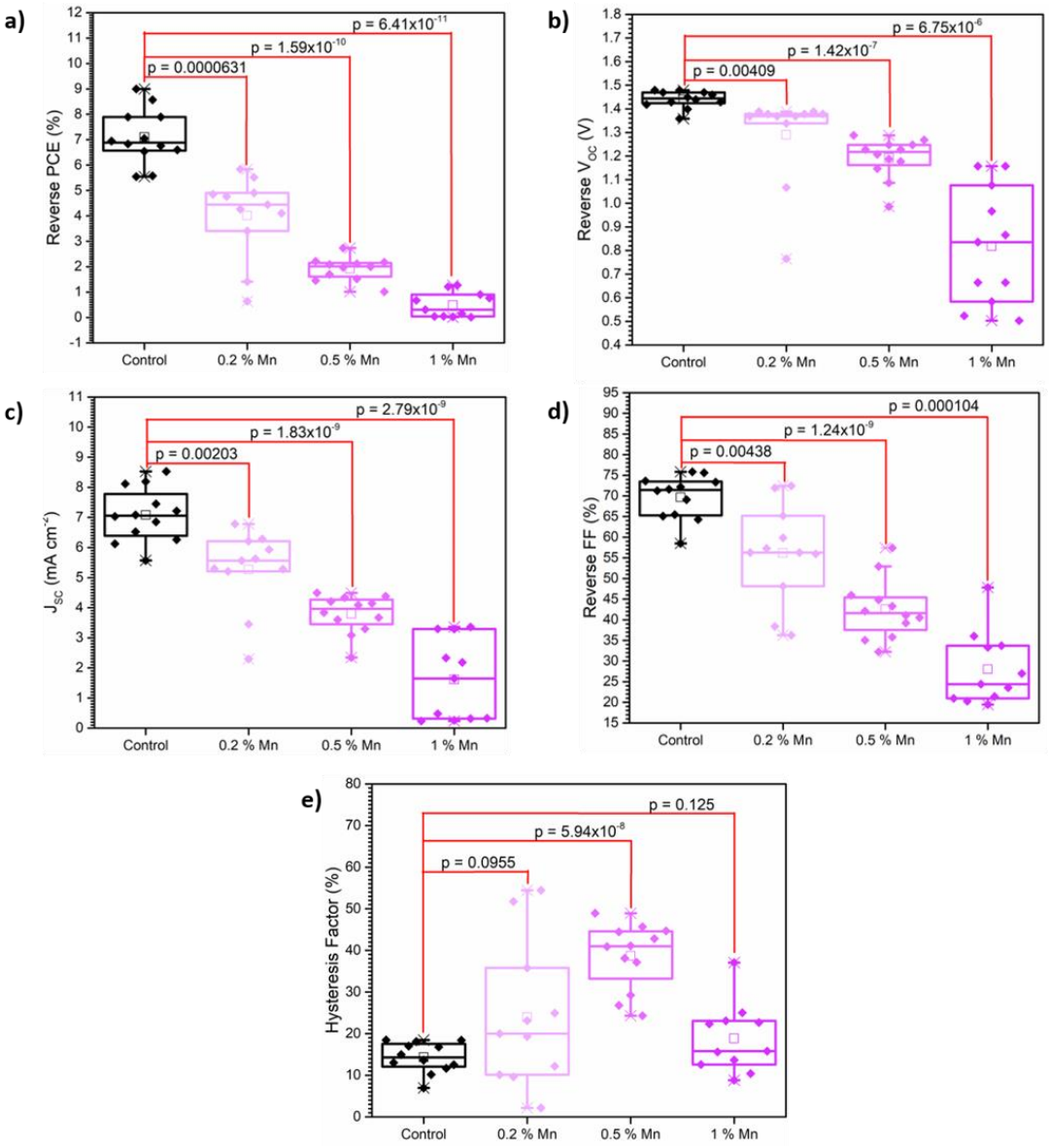

Figure 17: Box plots comparing a) the reverse PCE, b) the reverse V_{OC} c) the J_{SC} d) the reverse FF and e) the hysteresis factor of $CsPbBr_3$, $CsPb_{0.998}Mn_{0.002}Br_3$, $CsPb_{0.995}Mn_{0.005}Br_3$ and $CsPb_{0.99}Mn_{0.01}Br_3$ planar carbon devices. The mean values are represented by the square symbol.

Once more, is clear from the five box plots in Figure 15, that substituting Mn^{2+} into the B-site in $CsPbBr_3$ negatively affects $CsPbBr_3$ planar carbon device performance. The p values calculated between the pristine devices and the Mn^{2+} containing devices are very small, indicating that the observed decreases in the device performances are statistically significant. Similarly to Fe^{2+}, as the concentration of Mn^{2+} in the $CsPbBr_3$ crystal lattice increases, the device performance decreases. For example, the average reverse PCE of the devices containing 0.2 % Mn^{2+} is 3.99 %, decreasing to 1.88 % for 0.5 % Mn^{2+} and dropping again to 0.50 % for 1 % Mn^{2+}. The same trend is observed in the reverse V_{OC} values, where the mean values are 1.29 V, 1.19 V and 0.82 V respectively. The J_{SC} and reverse FF values also follow

the same pattern with increasing Mn^{2+} concentration. Once again, all of the sets of devices containing Mn^{2+}, had a mean reverse V_{OC} below 1.23 V (the theoretical requirement for water oxidation), demonstrating that substituting Pb^{2+} for Mn^{2+} is not favourable for the use of $CsPbBr_3$ devices for water oxidation.

The results in Figure 16 contrast those published by Tang *et. al.* where small amounts of Mn^{2+} increased $CsPbBr_3$ device performance. [5] However, it is clear from the box plots in Figure 16 that Mn^{2+} can negatively affect these devices.

5.2.4.7. Tb^{3+} Substituted Devices

This time the trivalent terbium ion was substituted for Pb^{2+} on the B-site of the perovskite at concentrations of 0.5, 1.0 and 3.0 %. Higher substitution concentrations were chosen as work by Tang *et al.* demonstrated that larger amounts of lanthanide ions could improve $CsPbBr_3$ planar carbon device performance, with a substitution concentration of 3 % producing the best outcomes. [6] Whilst Sm^{3+} was shown to produce the devices with the highest PCEs and V_{OC}s, $SmBr_3$ was difficult to obtain, so the lanthanide ion producing the second-best results, Tb^{3+}, was used instead. Consequently, large PCE above 10 % and V_{OC} values greater than 1.5 V were anticipated. The box plots in Figure 17 compares the reverse PCE, the reverse V_{OC}, the J_{SC}, the reverse FF and the hysteresis factor of the devices.

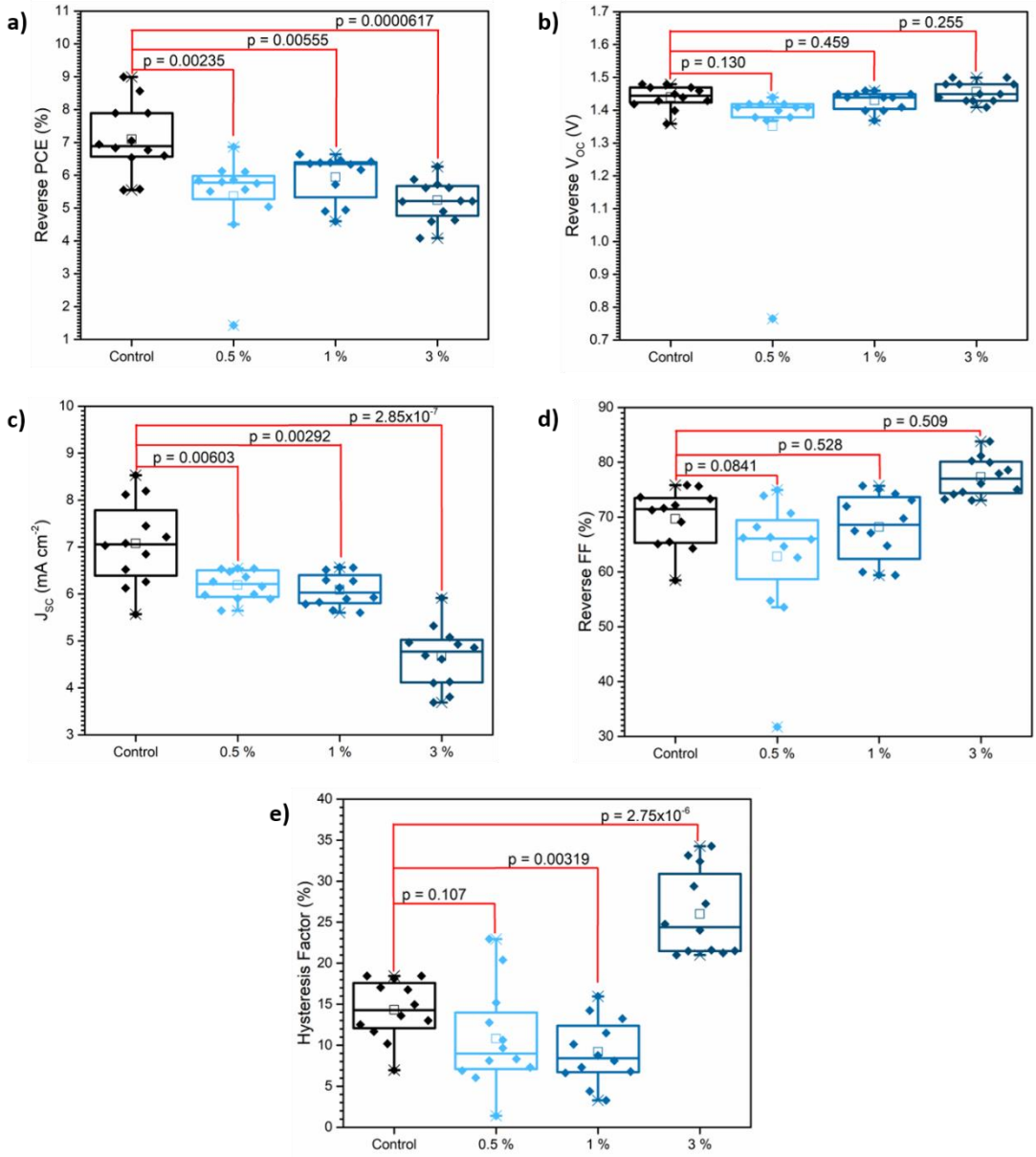

Figure 18: Box plots comparing a) the reverse PCE, b) the reverse V_{OC} c) the J_{SC} d) the reverse FF and e) the hysteresis factor of $CsPbBr_3$, $CsPb_{0.995}Tb_{0.005}Br_3$, $CsPb_{0.99}Tb_{0.01}Br_3$ and $CsPb_{0.97}Tb_{0.03}Br_3$ planar carbon devices. The mean values are represented by the square symbol.

The results shown in Figure 17 were disappointing. The inclusion of Tb^{3+} resulted in significantly poorer device performance compared to the pristine devices, with small p values demonstrating this. The mean reverse PCE values were 5.36, 5.94 and 5.23 % respectively, compared to 7.09 % for the control. The champion Tb^{3+} containing devices did not even reach efficiencies above 7 %, illustrating that Pb^{2+} substitution for Tb^{3+} does not improve device performance.

The V_{OC} values produced by the Tb^{3+} containing devices were also not statistically better than the control devices. Mean reverse V_{OC} values of 1.35, 1.43 and 1.46 V were achieved

compared to 1.44 for the pristine devices. Whilst the 3 % substituted set produced two devices with a V_{OC} of 1.50 V, the expected V_{OC} values greater than 1.50 V were not observed. The results did not achieve the super high V_{OC} values of 1.59 V nor the large efficiencies of 10 % reported by Tang *et al.* [6] Thus, Tb^{3+} containing $CsPbBr_3$ devices do not yield the properties required to achieve water splitting using reduced applied overpotentials.

5.3. Conclusion and Future Work

In summary, this chapter investigated the effect that substituting Pb^{2+} in $CsPbBr_3$ with small amounts of a range of metal ions had on band gap, grain size and planar carbon device performance. However, finding evidence to determine the presence of the added ions within the thin films proved difficult. No obvious effect on band gap was observed, and small variations within the band gap are difficult to detect and error may occur during the extrapolation process. [29] Therefore, if the ion substitution did have a minor effect on the band gap, it may not have been detected. XRD was used to confirm that the thin films with the substituted ions still formed the perovskite structure. Whilst the expected $CsPbBr_3$ peaks were observed, additional peaks, corresponding to the Cs rich phase were also present. However, the expected shift to higher 2θ values was not observed. Furthermore, XPS analysis failed to detect and quantify the presence of the metal ions, except for Co^{2+}, in the surface of the thin films, although a shift in the Pb 4f and the Br 3d peaks was observed. However, the observed peak shift could be down to poor calibration. The EDX data also did not provide any evidence for the presence of the metal ions, as the specified ions were not detected, although this may have been due to the detection limits of the instrument. Nonetheless, the ions could still be present within the film and the concentration within the surface of the films may have been too low to detect accurately with the techniques available. The methods used for metal ion detection in the $CsPbBr_3$ thin films, were the same methods used to confirm the metal ions presence in the literature, [5, 6] yet the analysis of the result may need further examination. Firstly, the literature XRD results show minimal shifting of the peaks and the magnitude of the shifting does not correlate to the ion size. [5, 6] Furthermore the EDX data in the literature raises questions about the data collection methods used, thus they may not accurately depict the true concentration of the metal ions in the thin films. [5, 6, 12]

The grain size of the thin films was also analysed. Whilst there is some evidence that substituting Pb^{2+} for metal ions such as Cu^{2+} and Ni^{2+}can help to increase $CsPbBr_3$ grain size, a larger number of samples would be required to determine this definitively. However, the number of samples required to fully investigate this is very large, thus, that number was not met in this thesis, nor is it routinely met in literature work. [5, 6] As a result, it is difficult to truly

establish the effect of the metal ion's presence on the surface morphology of the perovskite in both the work in this chapter and the results in the literature.

The investigation into $CsPbBr_3$ planar carbon device performance, clearly demonstrated that no metal ion investigated for substation had the desired positive effect. Statistical analysis of the devices in section 5.2.4 of this chapter concluded that the substitution had either no effect, with no difference observed from the pristine devices, or had a negative impact on device performance. The V_{OC} of the devices was of particular interest, as large V_{OC}s could be useful in reducing the amount of over potential required to perform water splitting, or even allow for unassisted water splitting. It was concluded that the use of metal ions could not increase the V_{OC} of the devices to values appropriate for unassisted water oxidation. However, the method for the substitution of metal ions into the $CsPbBr_3$ lattice was followed as described in the literature by Tang *e. al.* [5, 6] where large improvements in device performance was reported. This is contradictory to the findings of this chapter and thus further information as to the methods used by Tang *et al.* would be beneficial. However, performing statistical analysis on the data sets from the literature would provide further insight into the proposed improvements achieved by substituting Pb^{2+} in $CsPbBr_3$ for metal ions. Furthermore, 12 devices were included in each set of data in section 5.2.4, which consisted of two separate set of cells that were made on different days. However, for some of the substitution conditions, more than two sets of devices were made for various reasons, such as wanting to confirm results. As a result, this led to having to choose which dataset to include in this study. Datasets were used in their entirety and the best devices were not cherry picked, which may contribute to these discrepancies. However, the pristine $CsPbBr_3$ control devices that were made in this chapter out-perform those made by Tang *et al.* where the champion pristine device has a PCE of 6.37 % and a V_{OC} of 1.43 V. [5] If a set of control devices that had a poorer performance were chosen, in line with the literature devices, the substitution of Pb^{2+} for a range of metal ions would have appeared to improve the $CsPbBr_3$ devices. Thus, whilst, using the data in this chapter, it is not possible to state that Pb^{2+} substitution had a beneficial effect on $CsPbBr_3$ device performance, the data used in the literature may need further examination. Statistical analysis of data sets should be routinely used to show that any changes to device performance are significant. An increased number of devices measured in each data set to provide a wider range of data points would also be beneficial.

Further work could be carried out to observe the stability effect of the substituted $CsPbBr_3$ devices under water oxidation conditions. Future work in this field could also extend to the investigation of other ions to partially replace Pb^{2+} to determine whether the substitution improves planar carbon $CsPbBr_3$ devices enough to be suitable for water splitting applications. For example, group 2 elements have also been investigated by Tang *et al.* and have also shown

improvements in PCE and $V_{OC.}$ [30] The effects of doping in small amounts, instead of substitution, of metal ions could also be investigated. Furthermore, the addition of metal ions to the layer interfaces could be explored to determine whether there is any defect passivation effect.

5.4. References

1 H. C. Fu, P. Varadhan, C. H. Lin and J. H. He, *Nat. Commun. 2020 111*, 2020, **11**, 1–9.

2 A. Buin, P. Pietsch, J. Xu, O. Voznyy, A. H. Ip, R. Comin and E. H. Sargent, *Nano Lett.*, 2014, **14**, 6281–6286.

3 W. Zhao, D. Yang, Z. Yang and S. (Frank) Liu, *Mater. Today Energy*, 2017, **5**, 205–213.

4 H. Sun, J. Zhang, X. Gan, L. Yu, H. Yuan, M. Shang, C. Lu, D. Hou, Z. Hu, Y. Zhu and L. Han, *Adv. Energy Mater.*, 2019, **9**, 190896.

5 M. Tang, B. He, D. Dou, Y. Liu, J. Duan, Y. Zhao, H. Chen and Q. Tang, *Chem. Eng. J.*, 2019, **375**, 121930.

6 J. Duan, Y. Zhao, X. Yang, Y. Wang, B. He and Q. Tang, *Adv. Energy Mater.*, 2018, **8**, 1802346.

7 H. Kim, S. R. Bae, T. H. Lee, H. Lee, H. Kang, S. Park, H. W. Jang and S. Y. Kim, *Adv. Funct. Mater.*, 2021, **31**, 2102770.

8 B. Wang, L. Liu, B. Liu, J. Li, B. Cao, Z. Zhao and Z. Liu, *Phys. B Condens. Matter*, 2020, **599**, 412488.

9 D. Parobek, Y. Dong, T. Qiao and D. H. Son, *Chem. Mater.*, 2018, **30**, 2939–2944.

10 Q. Hu, Z. Li, Z. Tan, H. Song, C. Ge, G. Niu, J. Han, J. Tang, Q. Hu, Z. Li, Z. Tan, H. Song, C. Ge, G. Niu, J. Tang and J. Han, *Adv. Opt. Mater*, 2018, **6**, 1700864.

11 D. Wang, W. Li, Z. Du, G. Li, W. Sun, J. Wu and Z. Lan, *J. Mater. Chem. C*, 2020, **8**, 1649.

12 C. Wang, Y. Long, X. Liu, S. Fu, J. Wang, J. Zhang, Z. Hu and Y. Zhu, *J. Mater. Chem. C*, 2020, **8**, 17211.

13 M. B. Kanoun and S. Goumri-Said, *Mater. Today Energy*, 2021, **21**, 100796.

14 T. Kirchartz and U. Rau, *Sustain. Energy Fuels*, 2018, **2**, 1550–1560.

15 Y. J. Guo, J. Su, L. Wang, Z. Lin, Y. Hao and J. Chang, *J. Phys. Chem. Lett.*, 2021, **12**, 3393–3400.

16 D. B. Straus and R. J. Cava, *Cite This ACS Appl. Mater. Interfaces*, 2022, **14**, 34890.

17 Database of Ionic Radii, http://abulafia.mt.ic.ac.uk/shannon/ptable.php, (accessed 4 October 2022).

18 Y. Li, W. Shao, L. Chen, J. Wang, J. Nie, H. Zhang, S. Zhang, R. Gao, X. Ouyang, X. Ouyang and Q. Xu, *NPG Asia Mater.*, 2021, **13**, 308.

19 M. C. Biesinger, L. W. M. Lau, A. R. Gerson and R. S. C. Smart, *Appl. Surf. Sci.*, 2010, **257**, 887–898.

20 A. Waskowska, L. Gerward, J. S. Olsen, S. Steenstrup and E. Talik, *J. Phys. Condens. Matter*, 2001, **13**, 2549.

21 Electron Optic Documents, https://www.jeolusa.com/RESOURCES/Electron-Optics/Documents-Downloads/can-i-trust-my-quantitative-eds-data, (accessed 5 December 2022).

22 M. Nukunudompanich, G. Budiutama, K. Suzuki, K. Hasegawa and M. Ihara, *CrystEngComm*, 2020, **22**, 2718–2727.

23 M. Liu, J. Zhao, Z. Luo, Z. Sun, N. Pan, H. Ding and X. Wang, *Chem. Mater.*, 2018, **30**, 5846–5852.

24 Q. Cai, C. Liang, Z. Lin, W. Zhang, G. Shen, H. Dong, X. Xu, H. Wang, C. Mu and G. Xing, *Sustain. Energy Fuels*, 2022, **6**, 2955–2961.

25 J. F. Wang, L. Zhu, B. G. Zhao, Y. L. Zhao, J. Song, X. Q. Gu and Y. H. Qiang, *Sci. Reports 2017 71*, 2017, **7**, 1–9.

26 G. . Jones, M. Jackson and K. O'Grady, *J. Magn. Magn. Mater.*, 1999, **193**, 75–78.

27 S. Shyamal, S. K. Dutta and N. Pradhan, *J. Phys. Chem. Lett.*, 2019, **10**, 7965–7969.

28 J. Liang, Z. Liu, L. Qiu, Z. Hawash, L. Meng, Z. Wu, Y. Jiang, L. K. Ono and Y. Qi, *Adv. Energy Mater.*, 2018, **8**, 1800504.

29 G. (Associate professor of mechanical and nuclear engineering) Singh, A. Bhalla, M. M. Mahmoud, R. H. R. Castro, N. P. Bansal, D. Zhu, J. P. Singh, Y. Wu and O. Materials Science & Technology Conference (2015 : Columbus, *Processing, Properties, and Design of Advanced Ceramics and Composites II*, Wiley, 2016.

30 Y. Zhao, Y. Wang, J. Duan, X. Yang and Q. Tang, *J. Mater. Chem. A*, 2019, **7**, 6877–6882.

Chapter 6. Ir-Based Water Oxidation Catalyst Interactions with Graphite Surfaces

6.1. Introduction

Due to the slow kinetics of the water oxidation reaction, discussed in Chapter 2, water oxidation catalysts (WOCs) are often used to help overcome this kinetic barrier and allow water oxidation reactions to be carried out at lower potentials. The slow water oxidation kinetics are often accredited to the intermediates that are formed during the four electron transfer step of the oxidation of water to $O_{2(g)}$. An effective WOC is able to stabilise these intermediates, therefore lowering the kinetic energy barrier for water oxidation and thus increasing the rate of oxygen production. [1] Developing effective WOCs can be challenging; a good WOC must allow the water oxidation to occur at a fast rate; must be capable of water oxidation at potentials above 1.23 eV and must be stable to air, water and heat. There are two main types of synthetic WOCs: oxides and molecular complexes. Metal oxides, such as those containing ruthenium and iridium, have been shown to be some of the most active and stable WOCs. [2, 3, 4, 5] Iridium oxides, such as IrO_2, are popular due to their high catalytic activities, high turnover frequencies and good longevity. [6] However, some oxide materials have high dissolution rates and hence have short catalytic life times; this can be improved by using more robust oxide materials such as IrO_x nanoparticles or $SrIO_3$. [7, 8]

The first molecular WOC was discovered when it was found that upon adding $[(bpy)_3Ru^{III}]^{3+}$ to water, a blue coloured, *cis*-$[(H_2O)Ru^{III}(bpy)_2(\mu\text{-}O)Ru^{III}(bpy)_2(OH_2)]^{4+}$ dimer was formed and oxygen evolution resulted. [9] In the last 10 years, organometallic Cp^*Ir^{III} complexes (where Cp^* = pentamethyl-cyclopentadienyl) have become popular as pre-catalysts for water oxidation, and it has been observed that active homogenous WOCs can be formed through the oxidative removal of the Cp^* group. These compounds must possess a bidentate chelating ligand to help stabilise the complexes after the oxidative Cp removal. [10] In the absence of a chelating ligand, a layer of amorphous IrO_x is instead deposited onto the anode, creating a heterogenous WOC layer. However, the homogeneous WOCs, formed in the presence of the chelating ligands, can be heterogenized to form surface bound, iridium based electrocatalysts for water oxidation, which operate in acidic conditions and have higher catalytic activity and a lower onset potential than IrO_x. [11, 12] Brudvig *et al.* used dynamic light scattering (DLS) to confirm that the iridium complexes containing chelating ligands did not produce nanoparticles, thus it could be concluded that the Ir complexes themselves where behaving as water oxidation catalysts instead of IrO_x nanoparticles. [1] Cp^*Ir^{III} precatalyst complexes can be

oxidised and dimerised, with the use of a oxidising agent such as $NaIO_4$ or Ceric Ammonium Nitrate (CAN), to form a homogenous WOC (hom-WOC). The hom-WOC can then bind to the surface of metal oxides to form a heterogeneous WOC layer (het-WOC). [11] Figure 1 shows the transformation of the [Cp*Ir(pyalc)Cl] precatalyst into the het-WOC using $NaIO_4$.

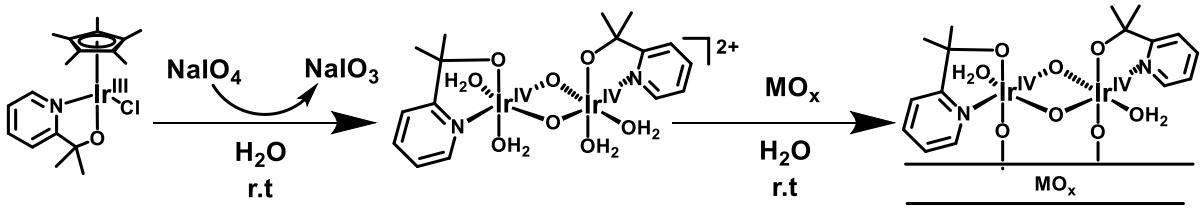

*Figure 1: Formation of the hom-WOC and then subsequent formation of the het-WOC. Oxidation of [Cp*Ir(pyalc)Cl] using $NaIO_4$ to form the hom-WOC ($[Ir(pyalc)(H_2O)_2(\mu\text{-}O)]^{2+}{}_2$). Further heterogenization of the hom-WOC is shown at room temperature with a metal oxide surface.*

The hom-WOC, formed after the oxidation of the precatalyst, exhibits a deep blue colour which absorbs light close to 600 nm. Dynamic Light Scattering (DLS) was used to show that despite the fact that the deep blue colour is similar to that shown by IrO_x in solution, the chelating ligands, prevented IrO_x nanoparticle formation. [13] Hintermair *et. al.* proposed the water oxidation catalytic cycle of the hom-WOC ($[Ir(pyalc)(H_2O)_2(\mu\text{-}O)]^{2+}{}_2$), in acidic conditions shown in Figure 2, [14] the heterogeneous, surface bound catalyst is expected to behave in a similar manner. The cleavage of the O-H bond, depicted in the second step in, Figure 2, is the proposed rate determining step (RDS) for the oxidation of water, using the hom-WOC.

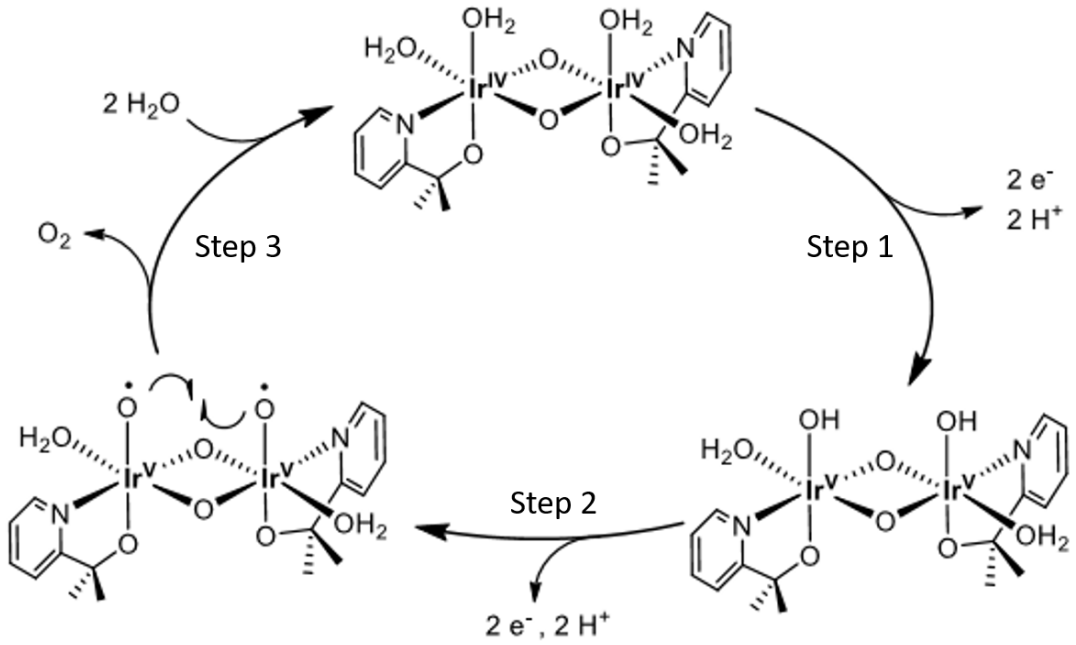

Figure 2: Proposed catalytic cycle for the oxidation of water with the dimeric hom-WOC ($[Ir(pyalc)(H_2O)_2(\mu\text{-}O)]^{2+}{}_2$) complex in aqueous solution with $NaIO_4$. [14]

Whilst, the mechanism above shows step 2 as the RDS for the hom-WOC, a kinetic study of the het-WOC, found that the rate-determining step for the het-WOC, may be electron transfer from the Ir catalyst centres to the oxygen functional group containing scaffold. [11]

As discussed in Chapter 2, the high V_{OC} values that are produced by $CsPbBr_3$ devices, as a result of its large bandgap, give these solar cells applications in water splitting. In previous work by Poli and co-workers, planar carbon $CsPbBr_3$ devices were encapsulated using a commercially available graphite sheet (GS) with the iridium based het-WOC grafted to the surface. The devices were then used as photoanodes for water oxidation. [15] The π electrons in the layers of graphite mean that it is a good electrical conductor, thus it can conduct the photogenerated holes that are produced in the $CsPbBr_3$ layer, bringing them to the surface where they can be used to oxidise water. The surface defects found in a sheet of graphite often consist of oxygen containing functional groups, [16] thus, after soaking the GS in the blue dimeric hom-WOC solution, the catalyst was able to bind to the GS at oxidised sites on the surface. The catalyst was able to lower the overpotential needed for the water oxidation reaction to occur on the surface of the photoanode and produce high water oxidation currents. [15] This chapter further investigates the interactions between the GS and the ($[Ir(pyalc)(H_2O)_2(\mu\text{-}O)]^{2+}{}_2$) WOC (Figure 1) and discusses the methods to increase the loading of the WOC onto the surface of GS to further increase the water oxidation capabilities of the GS-WOC anode.

6.2. WOC On Untreated 70 µm Thickness GS

A commercially available GS, with a thickness of 70 µm was used and soaking the GS in the hom-WOC/$NaIO_4$ aqueous solution for 48 h was the suggested method for adhering the WOC to the GS. [15] After soaking, the GS was rinsed thoroughly with deionised water to remove any loosely bound or non-covalently adsorbed catalyst. It was first ensured that the presence of the aq. $NaIO_4$, which is an oxidant, did not cause any changes to the GS, nor was it electrochemically active on the surface of the GS. A cyclic voltammogram (CV) of the blank GS was compared with the CV of the GS after soaking in $NaIO_4$ solution for 48 h; this is shown in Figure 3, to establish that the $NaIO_4$ does not possess any catalytic properties for water oxidation. Figure 3 also compares the CV of the GS-WOC to that of the blank GS

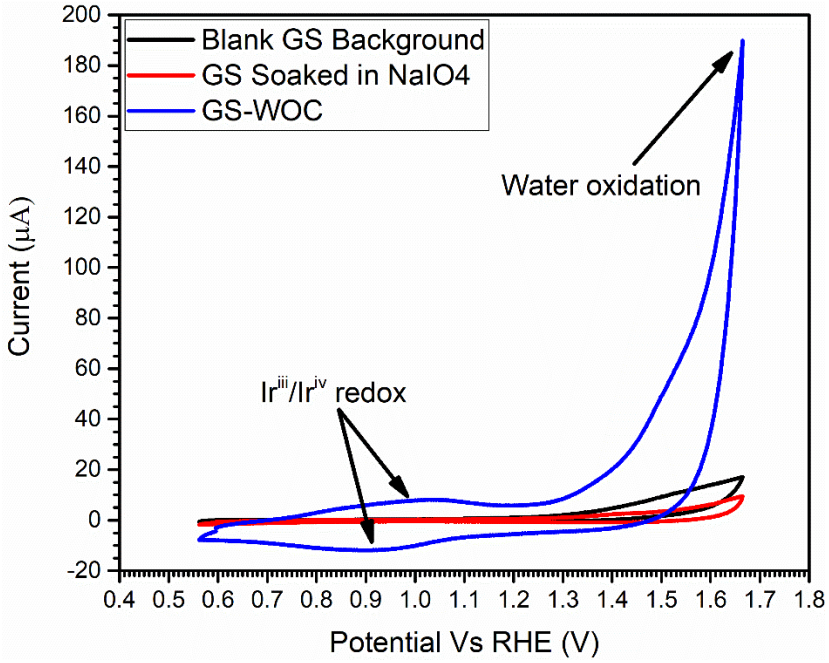

Figure 3: Cyclic voltammogram (one scan) of the blank 1 cm^2 GS (black), the GS soaked in 0.125 mM $NaIO_4$ for 48 h (red) and the GS soaked in the hom-WOC solution (blue). Measured in 0.1 M KNO_3 at pH 2.5, at a scan rate of 50 mV s^{-1}.

Figure 3 shows that the changes to the CV of the GS are minimal before and after soaking with $NaIO_4$, the oxidation current at 1.63 V for the blank GS is slightly larger before soaking. However, the changes are small and insignificant compared to the changes after soaking in the hom-WOC solution. This shows that the $NaIO_4$ has no effect on the water oxidation reaction. The GS that has been soaked in the hom-WOC shows noticeable differences compared the GS without any WOC. The oxidation and reduction peaks that are centred on ≈ 0.95 V correspond to the $Ir^{iii/iv}$ redox couple as the iridium centre is oxidised and reduced on the surface of the GS. The small oxidation peak at ≈ 1.5 V V is often referred to as the '*pre-*

peak' and could correspond to the $Ir^{iv/v}$ oxidation that occurs during the water oxidation process, however this is unconfirmed and the peak is largely obscured by the onset of the water oxidation catalytic wave. The current value at 1.66 V gives the water oxidation current. However, if the potential was raised past 1.66 V (vs RHE), the current would also increase further. It is clear that the presence of the WOC on the GS surface, causes the water oxidation current to greatly increase. The water oxidation onset potential is also greatly decreased by the WOC. The onset potential, for the purposes of this thesis, can be defined as the value of the potential when the current begins to rise sharply. In Figure 3, the CV of the GS-WOC begins to rise sharply at ≈ 1.3 V (vs RHE), compared to the blank GS which begins to increase sharply at ≈ 1.4 V. This demonstrates that the WOC can lower the overpotential required to achieve water splitting.

The optimal hom-WOC soaking time, for the GS, was investigated to observe when the maximum amount of catalyst had adhered to the surface of the GS. Thus, the GS was soaked in the WOC solution and a CV was taken every 4 hours from 0 – 72 h. The anodic peak current for the $Ir^{iii} \rightarrow Ir^{iv}$ oxidation was recorded and the water oxidation current at 1.66 V was also recorded; these results are shown in Figure 4. However, due to unexpected shifting in the anodic $Ir^{iii/iv}$ peak current, a potential for defining the anodic current could not be specified.

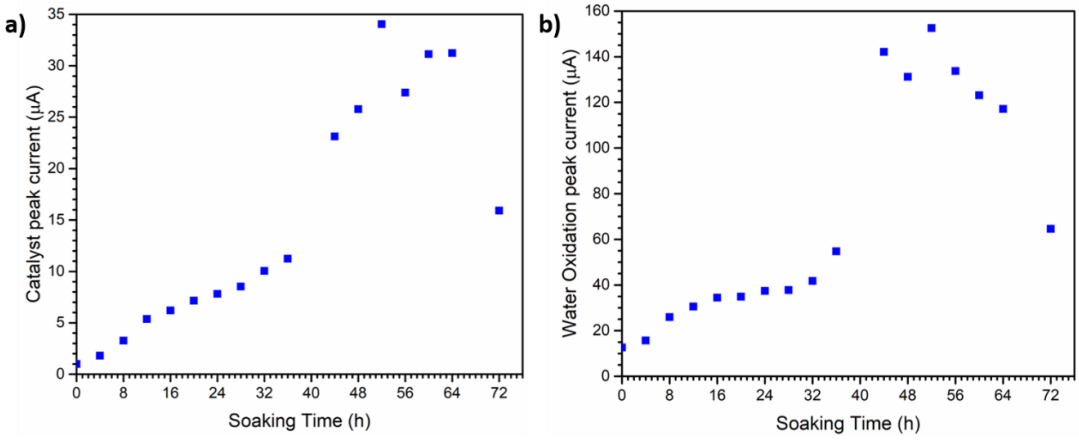

Figure 4: a) anodic peak current for the $Ir^{iii/iv}$ redox couple and b) water oxidation peak current at 1.66 V (vs RHE) after soaking the 1 cm^2 GS in the hom-WOC for 0 – 72 h.

From the plots in Figure 4, it is clear that the both the anodic peak current and the water oxidation current, increase with the catalyst soaking time, peaking at 52 h, with an anodic current of 34 µA and a water oxidation current of 153 µA. At soaking times greater than 52 h, both of the recorded current values decrease. This indicates that a soaking time of 48 – 52 h is optimal. It should be noted that there is variation in the currents that are achieved across different samples of GS, however, the observed trend still stands (see Appendix 2.1). The WOC forms a monolayer on surfaces with oxidised sites, such as ITO, [11] however, the typical

Langmuir shaped curve that would be expected, is not observed in Figure 4, with the current increase appearing to slow and even flatten out at ≈ 16 h of soaking, before beginning to sharply increase again after 32 h of soaking. Figure 5 shows how the CV of the GS-WOC changes with WOC soaking time up to 52 h clearly demonstrating the current increases in the anodic peak current and the water oxidation current.

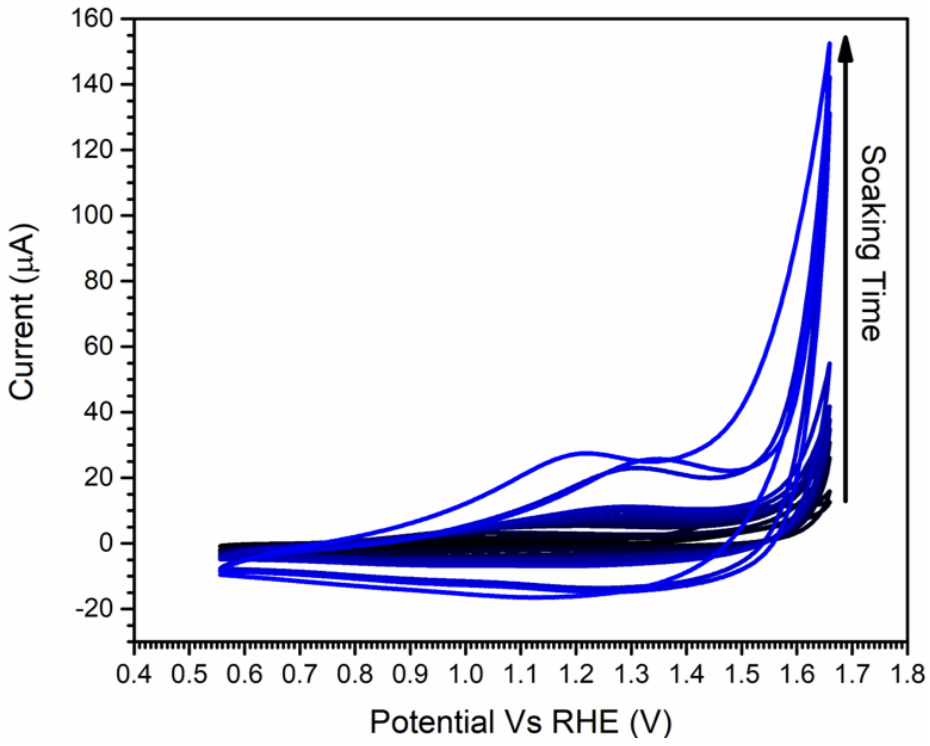

Figure 5: Cyclic Voltammograms of the 1 cm^2 GS-WOC recorded after 0 – 52 h of soaking), the colour gradient goes dark to light as the soaking time is increased. Measured in 0.1 M KNO_3 at pH 2.5, at a scan rate of 50 mV s^{-1}.

Figure 5 demonstrates the effect that soaking time has on the anodic and water oxidation current. Despite the scan rate remaining the same at 50 mV s^{-1}, for all of the scans, the $Ir^{iii/iv}$ anodic peak has shifted to slightly higher potentials as the soaking time increases. However, this effect is only observed after cumulative soaking and CV measurement rounds to reach the 52 h mark and is not observed when the GS is soaked directly for 52 h without interruption. The anodic peak currents observed after more than 40 cumulative hours of soaking are greater than that observed in Figure 3, however, after 48 h of continuous soaking, the water oxidation peak current achieved is similar and peaks at 52 h. The onset of the water oxidation catalytic wave is decreased by the longer soaking times, this time from ≈1.55 V to 1.40 V. The evidence in Figure 5 suggests that the anodic peak current, the water oxidation current and the water oxidation onset potential, may be good indicators of the amount of the WOC bound to the surface of the GS. The pre-peak however, is difficult to use as an indicator for the amount of

WOC present as it is often not visible after multiple CV cycles have been ran, it is also difficult to define the peak as it gets lost in the current increase caused by the water oxidation.

Next, the stability of WOC on the surface of the GS was investigated by running multiple CV scan cycles. This would reduce any surface catalyst residue that is not bound to the GS and provide a true picture of the GS-WOC interaction. The result is shown in Figure 6.

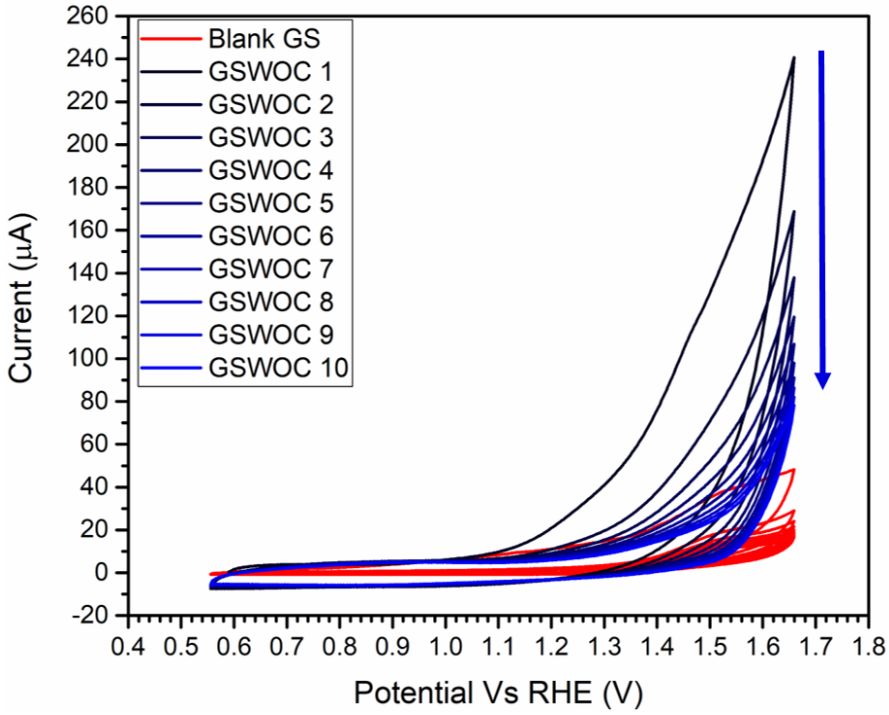

Figure 6: Cyclic voltammogram of the blank 1 cm^2 GS (red) and the GS soaked in the Ir-based WOC for 52 h (blue). Ten scans were measured, the colour gradient get lighter as the scan number increases. Measured in 0.1 M KNO_3 at pH 2.5, at a scan rate of 50 mV s^{-1}.

After 10 CV cycles, the CV shape is more stable and the anodic peak current and the water oxidation current do not change noticeably. However, the water oxidation current has drastically decreased from 240 µA to 78 µA. This indicates that despite rinsing the GS thoroughly with DI water, there is potentially loose WOC on the GS surface. It is important to remove this to get a true idea of relative amount of catalyst bound to the GS and to observe the true performance effect of the surface bound WOC. Under operating conditions, any loose WOC would detach from the surface over time, thus reducing the water oxidation capabilities of the photoanode. It was also noted that whilst the $Ir^{iv/v}$ feature is visible at ≈ 1.45 V (vs RHE) in the first scan, the peak is not visible in subsequent scans and is fully obscured by the water oxidation onset; this was similar to the results observed by Schumuttenmaer *et al.* when the WOC was bound to an ITO surface. [11]

It was observed that the CVs of the ≈ 1 cm^2 blank GS and GS-WOC varied from piece to piece, despite all being cut from the same larger sheet. To account for variation in the GS whilst assessing the performance of the WOC on the GS surface, three samples were taken (See Appendix 2.2). Table 1 shows the outcome across three different ≈ 1 cm^2 70 µm thickness GS anodes before and after soaking in the hom-WOC solution and gives the mean average currents.

Table 1: Water oxidation current at 1.66 V on the 10th CV scan, taken of GS soaked in the Ir-based WOC for 52 h. Measured in 0.1 M KNO_3 at pH 2.5, at a scan rate of 50 mV s^{-1}.

	GS Blank (µA)	**GS-WOC (µA)**	**Current Difference after WOC (µA)**
GS 1	17.6	76.5	59.0
GS 2	39.5	68.3	28.8
GS 3	16.30	78.3	62.0
Mean Average	**24.5 ± 13.0**	**74.4 ± 5.0**	**49.9 ± 18.0**

From the data in Table 1, it is clear that even the blank GS samples hugely vary from piece to piece. The average increase in the water oxidation current, between the blank GS and the GS-WOC was 49.9 ± 18 µA. Whilst the small increase in the water oxidation current is beneficial, the main advantage of using the WOC, is the increase in the water oxidation onset potential. This is shown by the earlier onset of the catalytic water oxidation wave; whereby the current of the GS-WOC begins to increase sooner than the blank GS to reach the maximum water oxidation current. This effect can be observed in Figures 3, 5 and 6.

In order to improve the function of GS-WOC in the $CsPbBr_3$ based photoanodes, it is proposed that a higher catalyst loading on the GS surface would increase the amount of water oxidation that is able to take place on the surface of the anode. As the WOC binds to the oxygen containing functional groups on the surface of the GS, it appears logical that further oxidation of the GS surface would increase the number of catalyst binding sites available, which in turn may increase the catalyst concentration. Graphite consists of a multiple layers of graphene, which can be oxidised to form graphene oxide (GO). When forming graphene oxide, it has been shown that epoxy and hydroxyl groups can form on the basal planes, whilst ketone, carboxyl and hydroxyl groups can form at the edges. [17, 18] Figure 7 demonstrates the oxygen containing functional groups found in oxidised graphite.

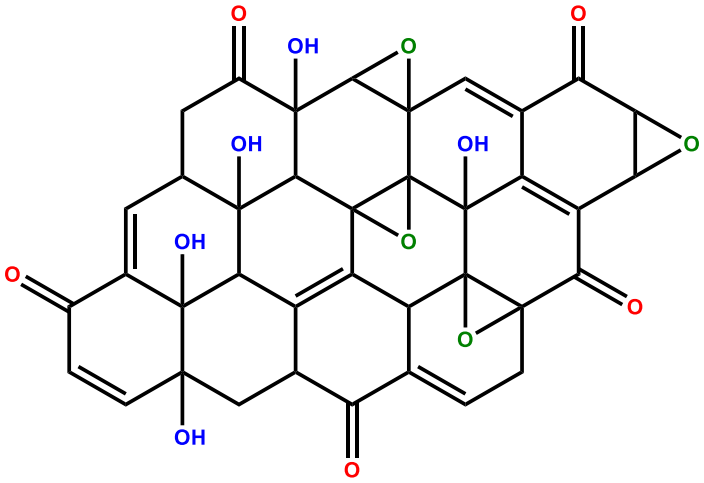

Figure 7: Proposed structure of oxidised graphene, reproduced from work by Barnes et al. [17]

Thus, within this chapter, a number of strategies are proposed to further oxidise the GS and introduce a higher concentration of oxygen containing functional groups at the surface.

6.2.1. UV/Ozone treated GS (70 µm)

UV/ozone exposure is often used to clean a variety of substrates by removing a wide array of surface contaminants. [19] Prudkovskiy and co-workers demonstrated that UV/Ozone treatment of graphene could remove any hydrocarbon surface contaminants, which lead to improvements in the charge-carrier mobility of the graphene. [20] This alone provides a reason to investigate the effect of UV/ozone on the water oxidation abilities of the GS. However, it is also well known that exposing graphite to ozone can lead to the formation of epoxy functional groups on the surface. [20, 21, 22] Mulyana and co-workers found that a layer of graphene could be oxidised into chemically homogeneous graphene oxide (GO), with epoxide groups forming on the graphene surface, after UV/ozone treatment. Epoxide groups are reactive electrophiles due to high ring strain, hence increasing the concentration of epoxide functional groups that are present on the GS surface could provide additional catalyst binding sites and lead to an increase in the quantity of WOC binding. [23] However, as epoxides are a reactive functional group, upon contact with the aqueous hom-WOC solution, the epoxide ring may spontaneously open to form hydroxyl groups instead, [24] although this may still be beneficial for increasing the WOC loading.

Consequently, 1 cm^2 GS pieces were placed into a UV/ozone cleaner for 2 and 24 h before being soaked in the hom-WOC solution. Figure 8 shows the CV scans of the UV/ozone treated GS-WOC and compares the UV/ozone treated GSWOC to the untreated GSWOC.

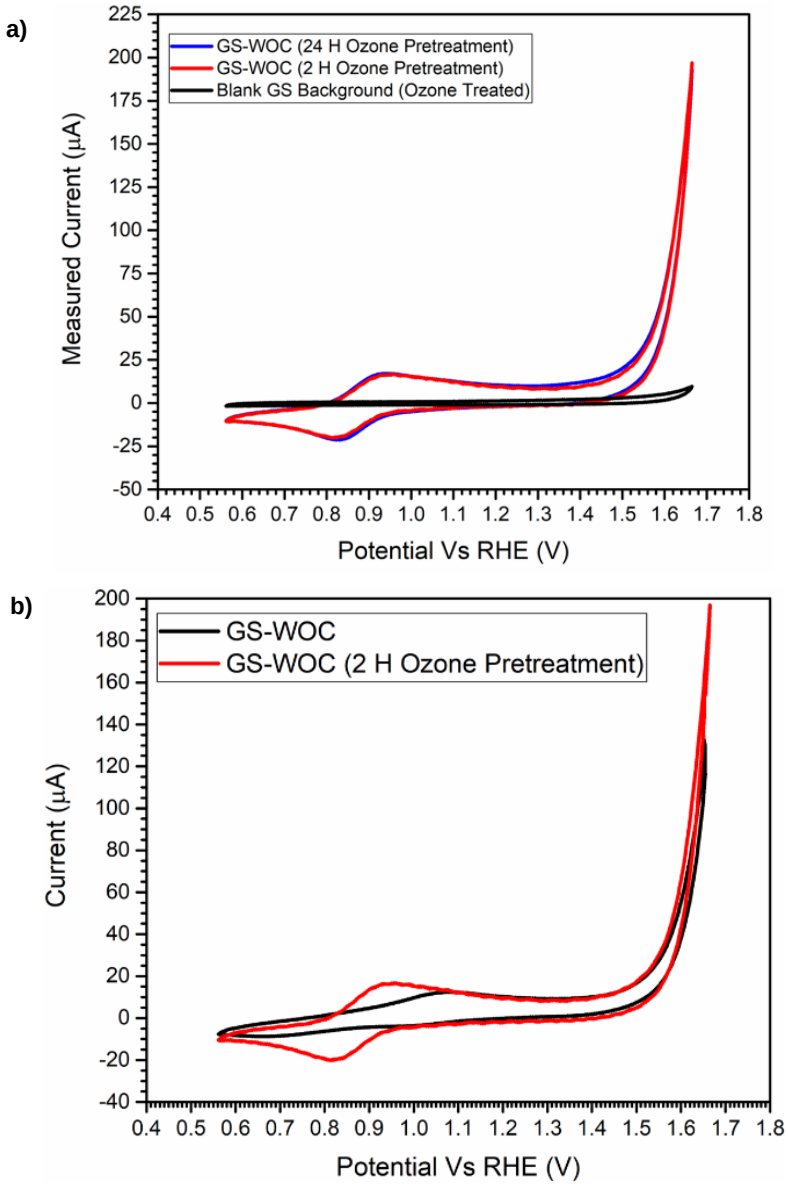

Figure 8: a) Cyclic voltammogram of the 1 cm^2 blank GS (black), the 1 cm^2 GS-WOC treated with UV/ozone for 2 h (red) and the 1 cm^2 GS-WOC treated with UV/Ozone for 24 h (blue), b) cyclic voltammogram of the 1 cm^2 untreated GS-WOC (black) and the 1 cm^2 GS-WOC treated with UV/Ozone for 2 h (red). Measured in 0.1 M KNO3 at pH 2.5, at a scan rate of 50 mV s^{-1}. Ten scans were run; the tenth scan is shown.

The cyclic voltammograms in Figure 8(a), show that pre-treating the GS with UV/ozone does not cause a change the water oxidation properties of the blank GS without the WOC, as the water oxidation peak current remains low at below 10 µA. There is no discernible difference between the CV of the GS-WOC treated for 2 h and 24 h, suggesting that after 2 h, no further change to the GS occurs. Figure 8(b) compares the UV/ozone treated GS-WOC to the untreated GS-WOC. It was observed that the water oxidation current of the UV/ozone treated GS-WOC was greater than that of the untreated GS-WOC. The anodic peak current from the $Ir^{iii/iv}$ redox couple also appears higher in the UV/ozone treated sample, this could indicate that there is a higher concentration of Ir centres on the surface of the GS, thus indicating a higher

WOC concentration. The $Ir^{iii/iv}$ anodic and cathodic peaks also have been shifted to a lower potential than those in the GS-WO without pre-treatment, although the size of the shift varies from sample to sample (see Appendix 2.3). However, the cathodic peak is more pronounced in the CV of the UV/Ozone treated GS-WOC, even after 10 scans have been run, perhaps suggesting that the WOC has been bound in a way that it is more stable on the GS surface and thus can be easily reduced and oxidised multiple times. This could provide potential improvements to the stability and lifetime of the WOC on the GS surface. Table 2 shows the outcome across three different ≈ 1 cm^2 70 µm thickness GS anodes that have been pre-treated with UV/ozone exposure before being soaked in the hom-WOC solution for 52 h.

Table 2: Water oxidation current at 1.66 V on the 10th CV scan, taken of GS cleaned with UV/ozone, then soaked in the Ir-based WOC for 52 h. Measured in 0.1 M KNO_3 at pH 2.5, at a scan rate of 50 mV s^{-1}.

	GS Blank (µA)	**GS Blank (UV/ozone Treated) (µA)**	**GS-WOC (UV/ozone treated) (µA)**	**Current Difference after WOC (µA)**
GS 1	4.3	10.1	112.5	108.2
GS 2	5.0	10.5	93.8	88.8
GS 3	4.8	12.0	99.1	94.3
Mean Average	**4.7 ± 0.4**	**10.9 ± 1.0**	**102 ± 10**	**97.1 ± 10.0**

It is apparent from Table 2 that exposing the GS to UV/ozone increases the water oxidation current of the blank GS, without the WOC, by a factor of ≈ 2. This could be a result of the removal of surface contaminants that may have been blocking the surface causing an increase in the charge-carrier mobility of graphite. [20] It is also apparent that the water oxidation current of the UV/ozone treated GS-WOC samples are larger than those of the untreated GS-WOC samples. This could further indicate that there is a higher concentration of the WOC bound to the surface of the GS, with the mean average current increase at 1.6 V, after the WOC addition, reaching 97.1 µA ±10. See Table 7 for a full comparison.

6.2.2. Electrochemical GS (70 µm) Oxidation

Graphite can be electrochemically oxidised using strong acids such as H_2SO_4 or HNO_3.[25, 26] The graphite oxidation process occurs via intercalation of the acid between the graphene layers. HNO_3 is able to spontaneously intercalate into the graphite once a certain electrochemical potential has been reached, whilst other acids cannot intercalate without the presence of a strong oxidant. [26] When HNO_3 is used, both the HNO_3 and the NO_3^- species intercalate into the layers within the graphite, but it is the nitronium ion that is responsible for

oxidising the graphite, forming oxygen containing functional groups within the graphite and the NO_2^+ ion. However, for electrochemical HNO_3 oxidation, typically highly concentrated HNO_3 is used at 15 M or above, [26, 27] this is not suitable for the GS anode with the self-adhesive back layer, nor for the Ag/AgCl dri-ref electrode used. Consequently, other methods of electrochemically oxidising the graphite were considered.

In 2017 Kohakade and co-workers presented a method of preparing a stable oxidised graphite electrode, formed through the anodic oxidation of graphite in 0.5 M KH_2PO_4 at 2 V (Vs Ag/AgCl). [28] They found that KH_2PO_4 is a mild oxidising agent that does not exfoliate the graphite and only causes surface modification. The proposed mechanism involves intercalation of the PO_4^{3-} anions along with H_2O molecules and subsequent graphite oxidation. [28] Thus, it was investigated whether KH_2PO_4 was a suitable oxidising agent for the GS and whether treatment of the GS with KH_2PO_4 could help increase the concentration of surface bound WOC molecules.

The GS was placed in an aqueous 0.5 M KH_2PO_4 solution and held at a potential of 2 V (Vs Ag/AgCl) for 20, 40 and 60 min. Figure 9 shows the subsequent CV scans of both the blank GS and the GS-WOC as the oxidation time is increased.

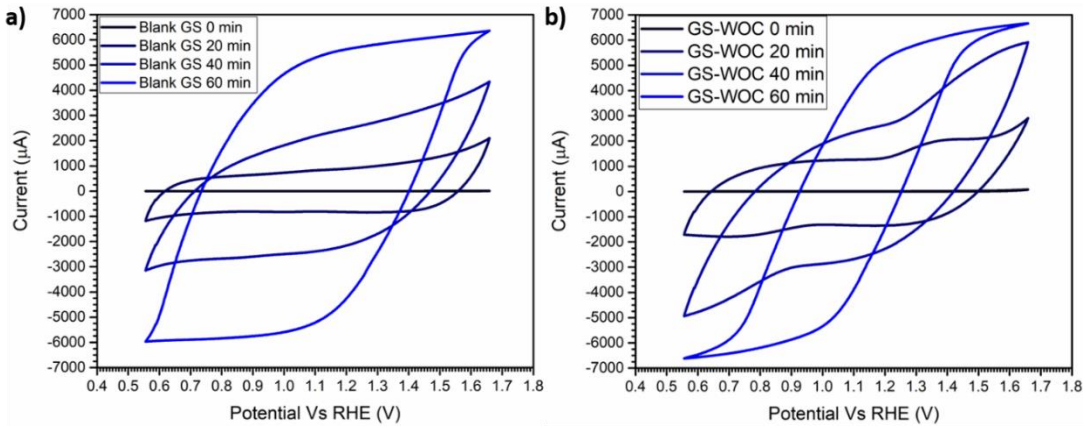

Figure 9: a) Cyclic voltammograms of the 1 cm² blank GS after electrochemical oxidation with KH_2PO_4 for 0, 20, 40 and 60 min b) cycling voltammograms of the 1 cm² GS-WOC after electrochemical oxidation with KH_2PO_4 for 0, 20, 40 and 60 min. Measured in 0.1 M KNO3 at pH 2.5, at a scan rate of 50 mV s^{-1}. Ten scans were run; the tenth scan is shown.

Figure 9 shows that as the KH_2PO_4 oxidation time increases so does the capacitance of the GS. Eq. 1 shows gives the equation for capacitance (C), where Q is the charge and V is the voltage.

$$C = \frac{Q}{\Delta V} \quad (1)$$

The charge can be calculated from the integrated area under a peak in a CV, [29, 30] and after 60 min of oxidation, the integrated area of the blank GS CV is over 3500 times greater than the unoxidised blank GS. (See Appendix 2.4). Thus, it can be inferred that the capacitance is greater. This also suggests that the surface area of the GS may have increased. [31] This would also indicate that the GS surface has been oxidised, as graphene oxide exhibits higher capacitance than graphene, which can be attributed to a pseudo-capacitive effect of the newly attached oxygen containing functional groups. [32] After electrochemical oxidation with KH_2PO_4, the surface of the GS that was submerged within the KH_2PO_4, became black and flaky in appearance, this is shown in Figure 10.

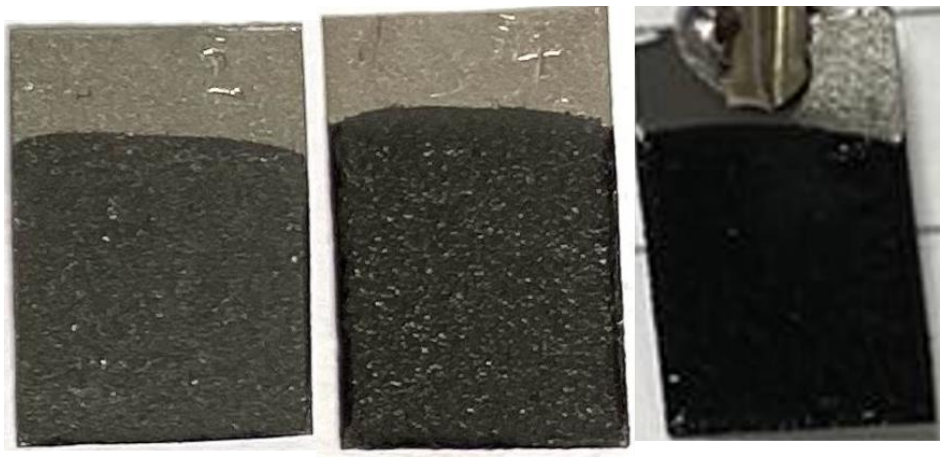

Figure 10: Photographs of the GS electrode after electrochemical oxidation in 0.5 M KH_2PO_4 aqueous solution at 2 V for 20, 40 and 60 min as shown from left to right. The tops of the samples were not immersed in the solution, thus are unchanged.

The images in Figure 10 demonstrate that as the oxidation progresses, the GS surface darkens and becomes more textured. This can be compared to the untreated GS, shown within the top portion of the GS in the three images, where the tops of the GS where not submerged in the solution. The untreated GS is grey in colour and smooth. Figure 11 shows SEM images of the GS before and after electrochemical oxidation.

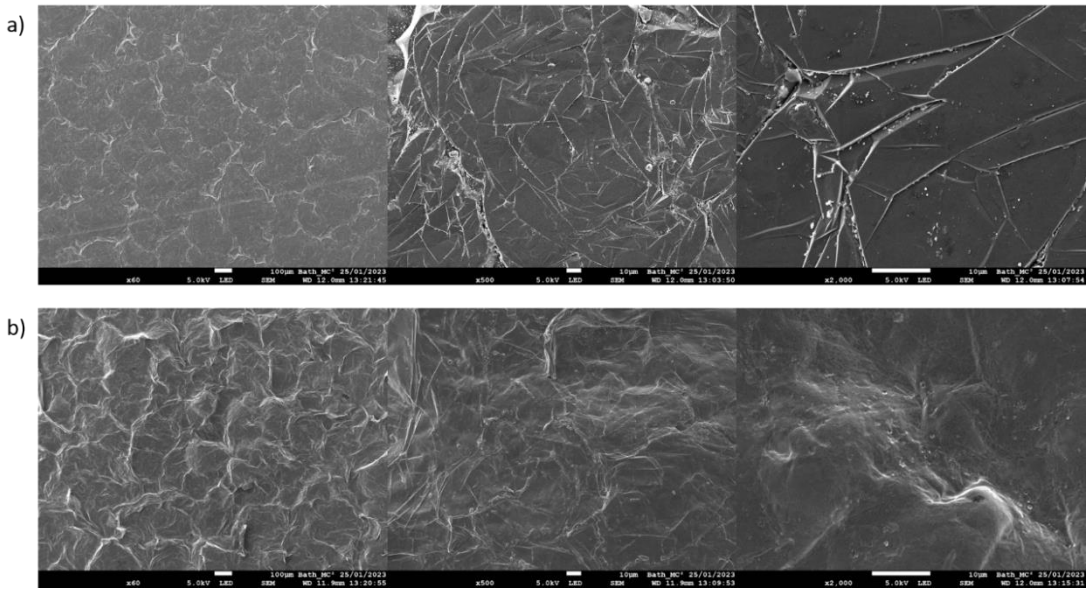

Figure 11: SEM images of the untreated GS (top) and the electrochemically oxidised with 0.5 KH_2PO_4 at 2 V for 60 min (bottom). Images shown a magnification of 60, 500 and 2000 from left to right.

From the SEM images in Figure 10 it is clear that the surface texture of the GS has changed after the oxidation. The surface of the GS appears more textures and this is consistent with the flaky texture observed by Kohakade *et al.* after electrochemical oxidation of a graphite electrode with KH_2PO_4. [28] The textured surface likely arises from the intercalation of the KH_2PO_4 and the fact that graphene oxide cannot π stack as effectively as graphene can, due to the degradation of some of its carbon sp^2 centres to sp^3 centres with the introduction of oxygen containing functional groups. [32]

Despite the above evidence suggesting that the GS surface may have been oxidised, the FTIR analysis of the GS before and after electrochemical oxidation, did not demonstrate any differences (Appendix 2.5 and 2.6). However, both exhibit a sharp peak centred around 1713 cm^{-1}, without the presence of a broad O-H stretching peak in the region above 2500 cm^{-1}, possibly suggesting the presence of ketone functional groups. Whilst there was no discernible difference between the FTIR spectra of the two samples, the other evidence suggests that the GS has been oxidised to some degree.

As a result, it would be expected that a larger amount of the WOC can bind to the electrochemically oxidised samples. Despite the fact that the area under the curve of the background scans increases with the oxidation time, the water oxidation current at 1.6 V is still larger in Figure 9(b) is larger than the current at 1.6 V in Figure 9(a). This is shown in Table 3.

Table 3: The water oxidation current at 1.6 V (Vs RHE) of the blanks GS after electrochemical oxidation with KH_2PO_4 at 2 V for 0, 20, 40 and 60 min and the resulting GS-WOC. Data taken from the CVs in Figure 9.

Oxidation Time (min)	**Blank GS Current at 1.6 V (µA)**	**GS-WOC current at 1.6 V (µA)**
0	7.900	83.20
20	2099	2907
40	4341	5914
60	6366	6671

From Table 3, it is clear that the presence of the WOC increases the water oxidation current, the current increase on addition of the WOC, is larger after electrochemically oxidising the GS, as the current value at 0 min is 7.9 µA, however this increases to 6366.2 µA, after 60 min of oxidation. The $Ir^{iii/iv}$ redox peaks are still clear in CV of the sample that was oxidised for up to 40 min, whilst they are not observable in the CV of the sample that was oxidised for 60 min. As a result, it was decided that 40 min was the optimal oxidation time for the GS. Table 4 shows the outcome across three different ≈ 1 cm^2 70 µm thickness GS anodes that have been electrochemically oxidised with KH_2PO_4 at 2 V for 40 min.

Table 4: Water oxidation current at 1.66 V on the 10^{th} CV scan, taken of GS, electrochemically oxidised in 0.5 M aqueous KH_2HPO_4 at 2 V for 40 min, then soaked in the Ir-based WOC for 52 h. Measured in 0.1 M KNO_3 at pH 2.5, at a scan rate of 50 mV s^{-1}.

	GS Blank (µA)	**KH_2PO_4 Oxidised GS Blank (µA)**	**GS-WOC (µA)**	**Current Difference After WOC (µA)**
GS 1	1.314	4316	5575	1258
GS 2	4.162	1359	5917	4558
GS 3	2.350	2008	2849	840.4
Mean Average	**2.61 ± 1.40**	**2562 ± 1500**	**4781 ± 1700**	**2219 ± 2000**

Whilst the impressive water oxidation currents that can be achieved using the pre-oxidised GS-WOC are shown in Table 4, it is also clear that again, there is a large amount of variation in the currents that are produced. Despite the variation, the water oxidation currents are larger than those of both the un-treated GS-WOC and the UV/Ozone treated GS-WOC (see Table 7), which again suggests that there may be a higher concentration of the WOC present.

6.2.3. Electrochemical and UV/Ozone GS (70 µm) Oxidation

In an attempt to further increase the number of oxidised sites on the surface of the GS, the GS was first electrochemically oxidised in 0.5 M aqueous KH_2PO_4 at 2 V for 40 min, before being placed under a UV/ozone cleaner for 2 h. Figure 12 shows the difference in the appearance of the electrochemically oxidised GS, before and after UV/ozone exposure.

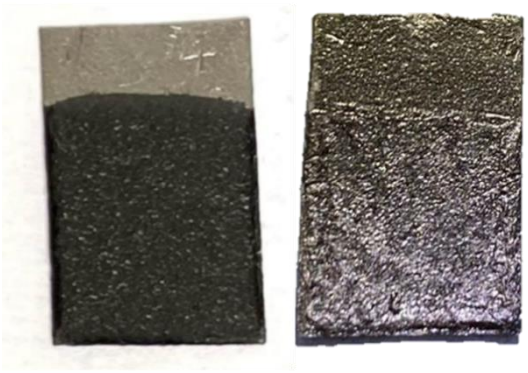

Figure 12: Photographs of the GS electrode after electrochemical oxidation in 0.5 M KH_2PO_4 aqueous solution at 2 V for 40 min before (left) and after (right) being placed under a UV/ozone cleaner for 2 h.

After electrochemical oxidation, the surface of the GS is black and textured with bubbles. If the sample is then exposed to UV/ozone, the surface keeps the texture that is obtained from the electrochemical oxidation, but the colour returns to grey. It is possible that the colour change is due to the removal of contaminants left on the surface from the $KHPO_4$ electrochemical oxidation processes. However, Mulyana and co-workers found that treating GO with UV radiation could reduce GO back to graphite. [23] Hence, it is also possible that the UV component is reducing the oxidising graphite, whilst the O_3 component is re-oxidising the GS surface forming mostly epoxide groups.

To observe the properties of the electrochemically and UV/Ozone oxidised GS as an anode for water oxidation, it was soaked in the Ir-based WOC for 52 h, in the hope that a greater concentration of the catalyst would bind to the surface. Again, cyclic voltammetry was used to investigate this. Figure 13 shows the CV of the modified blank GS and GS-WOC.

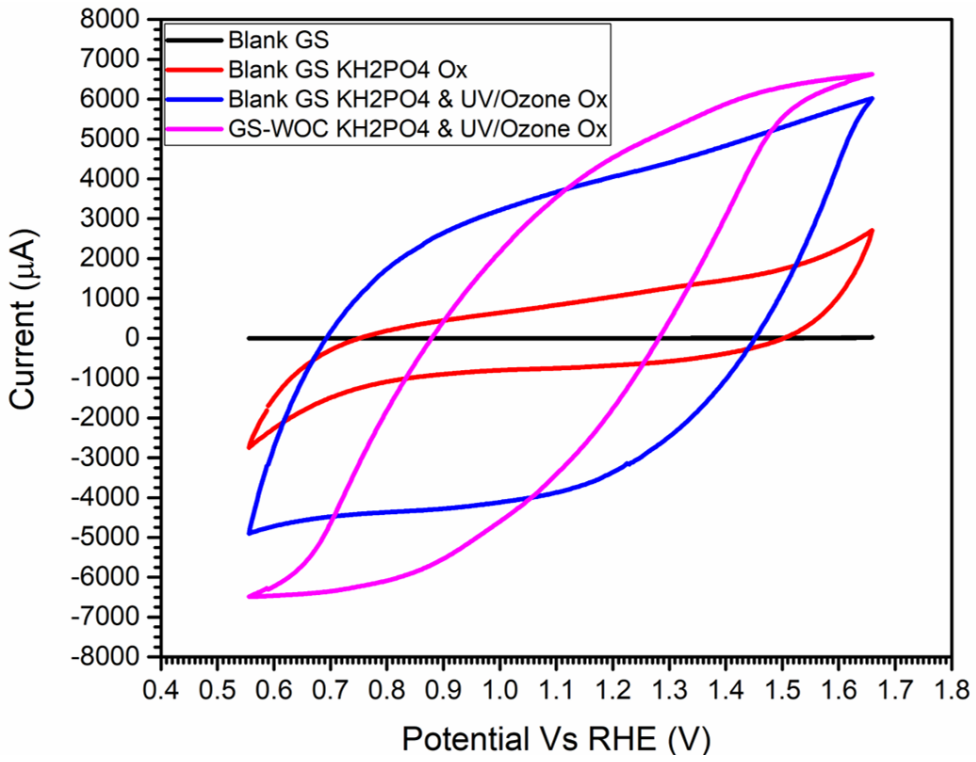

Figure 13: Cyclic voltammograms of the 1 cm^2 blank GS before and after electrochemical oxidation with KH_2PO_4 for 40 min, the electrochemically oxidised blank GS after UV/ozone treatment and the subsequent GS-WOC. Measured in 0.1 M KNO_3 at pH 2.5, at a scan rate of 50 mV s^{-1}. Ten scans were run; the tenth scan is shown.

From Figure 13, it is clear that the current at 1.66 V of the background scan increases further after treating the electrochemically oxidised GS with UV/ozone. The current is subsequently increased again after the addition of the WOC. Whilst the CV of the GS-WOC after electrochemical and UV/ozone oxidation appears stretched, the $Ir^{iii/iv}$ anodic peak is still just visible at ≈ 1.15 V, demonstrating the fact that the WOC is still able to bind. However, due to the increased capacitance, it is not possible to determine if the onset potential has been decreased by the use of this GS-WOC surface modification. Table 5 shows the outcome across three different ≈ 1 cm^2 70 µm thickness GS anodes that have been electrochemically oxidised with KH_2PO_4 at 2 V for 40 min and then treated with UV/ozone for 2 h.

Table 5: Water oxidation current at 1.66 V on the 10th CV scan, taken of GS, electrochemically oxidised in 0.5 M aqueous KH_2HPO_4 at 2 V for 40 min, placed under a UV/ozone cleaner for 2 h, then soaked in the Ir-based WOC for 52 h. Measured in 0.1 M KNO_3 at pH 2.5, at a scan rate of 50 mV s^{-1}.

	GS Blank (µA)	**KH_2PO_4 Oxidised GS Blank (µA)**	**KH_2PO_4 + UV/Ozone Oxidised GS Blank (µA)**	**GS-WOC (µA)**	**Current Difference After WOC (µA)**
GS 1	22.64	2707	6026	6632	606.7
GS 2	18.10	1738	4319	6592	2272
GS 3	9.051	4314	5183	6705	1521
Mean Average	**16.6 ± 6.9**	**2935 ± 1300**	**5176 ± 900**	**6643 ± 60**	**1466 ± 800**

Again, there is large variation in the currents produced by the GS anode; however, it is clear that the addition of the WOC still leads to a large increase in the water oxidation current. The water oxidation currents that have been achieved are the largest out of all the GS treatment methods, this is shown in Table 7.

6.2.4. TiO_2 modified GS (70 µm) Surface

As the Ir-based WOC has been shown to bind well to metal oxide surfaces such as those coated with ITO, TiO_2 and WO_3, [11] it was thought that a thin metal oxide coating, on top of the GS may lead to an increased concentration of the WOC that is bound to the GS surface. It was also considered that a thin metal oxide layer may reduce the amount of any graphite oxidation that may occur under working conditions in the photoanode.

TiO_2 is a well-known metal oxide semiconductor. [33, 34, 35] In order to investigate the effect of a thin TiO_2 coating on the water oxidation properties of the GS-WOC, TiO_2 was deposited onto the GS via a spray coating method. However, as TiO_2 requires high deposition and annealing temperatures (500 °C), a GS sample, without the self-adhesive layer was used. This may cause issues later when assembling the $CsPbBr_3$ based photoanode. The TiO_2 precursor solution was sprayed between 4 and 12 times, before annealing and soaking in the hom-WOC solution for 52 h. Figure 14 displays the resulting CVs.

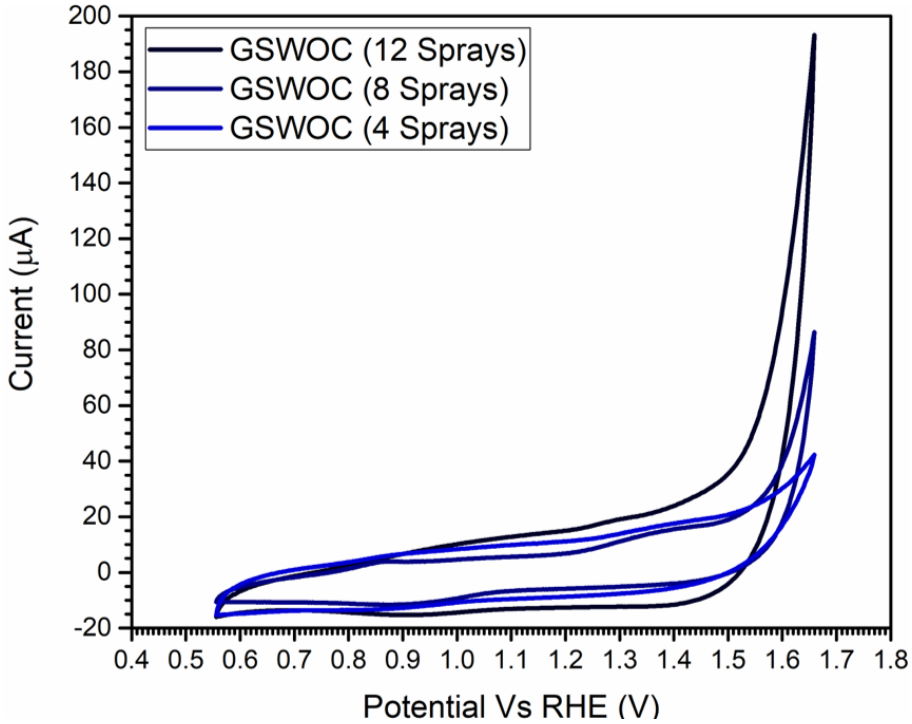

Figure 14: Cyclic voltammograms of the 1 cm^2 TiO_2 modified GS-WOC after 4, 8 and 12 sprays of the TiO_2 precursor. Measured in 0.1 M KNO3 at pH 2.5, at a scan rate of 50 mV s^{-1}. Ten scans were run; the tenth scan is shown.

After modifying the surface of the GS with TiO_2, the $Ir^{iii/iv}$ redox peaks are clearly visible, and the anodic current slightly increases as the amount of deposited TiO_2 increases, demonstrating that the WOC is able to bind to the TiO_2 and the GS. Figure 14 also shows that the water oxidation current increases as the amount of TiO_2 that is deposited on the surface of the GS increases, hence implying that the TiO_2 is providing an increased number of oxidised sites for the WOC to bind. This trend is confirmed by the data in Table 6 which shows the outcome across three different ≈ 1 cm^2 70 µm thickness TiO_2 GS anodes for each number of TiO_2 sprays.

Table 6: Water oxidation current at 1.66 V on the 10th CV scan, taken of TiO_2 modified GS anodes, after 4, 8 and 12 sprays of the TiO_2 precursor and the resulting GS-WOC. Measured in 0.1 M KNO_3 at pH 2.5, at a scan rate of 50 mV s^{-1}.

	GS Blank (µA)	**TiO_2 modified GS Blank (µA)**	**TiO_2 modified GS-WOC (µA)**	**Current Difference After WOC (µA)**
GS 1 (4 Sprays)	20.1	33.6	42.3	8.70
GS 2 (4 Sprays)	9.70	9.10	33.4	23.7
GS 3 (4 Sprays)	8.70	11.3	57.5	48.8
Mean Average	**12.8 ± 6.3**	**17.1 ± 14.0**	**44.4± 12.0**	**27.1 ± 20.0**
GS 1 (8 Sprays)	9.70	14.5	86.4	76.7
GS 2 (8 Sprays)	9.60	21.9	43.3	33.8
GS 3 (8 Sprays)	9.60	13.5	61.9	52.3
Mean Average	**9.6 ± 0.1**	**16.6 ± 4.6**	**63.9 ± 20.0**	**54.3 ± 20.0**
GS 1 (12 Sprays)	10.8	14.3	193	182
GS 2 (12 Sprays)	10.3	21.9	85.7	75.4
GS 3 (12 Sprays)	11.5	14.4	75.7	64.2
Mean Average	**10.9 ± 0.6**	**16.9 ± 4.0**	**118 ± 70**	**107 ± 70**

From Table 6, it can clearly be seen that as the as the amount of TiO_2 deposited is increased, the water oxidation current, as a result of the WOC addition, also increases. Spraying the GS with the TiO_2 4 – 8 times, does not appear to yield much benefit, as the water oxidation currents achieved after applying the WOC are similar or less than those achieved with the unmodified GS (see Table 7). However, after 12 sprays with TiO_2, the water oxidation current has increased significantly. This suggests that a thicker layer of TiO_2 could be more beneficial for increasing the WOC concentration and thus the water oxidation properties of the GS-WOC anode. However, Due to the roughness of the GS surface, quantifying the thickness of a thin layer of TiO_2 layer is difficult. Whilst it is estimated that on FTO glass 8 sprays would result in a layer of c- TiO_2 with a thickness ≈ 50 nm, this may not be the case when deposited onto the GS surface. Furthermore, whilst Schmuttenmaer and co-workers demonstrated the binding of the Ir-based WOC to TiO_2 that was deposited on FTO substrates at a thickness of 21 nm, [11] it is not possible to directly compare this to the TiO_2 film deposited on the GS in this work. Schumuttenmaer and co-workers used a TiO_2 nanoparticle paste deposited through doctor blading, whilst in this work the TiO_2 was deposited using spray pyrolysis with titanium diisopropoxide bis(acetylacetonate) in EtOH as the precursor, thus resulting in TiO_2 films with different morphology.

6.2.5. Summary and Comparison of the GS (70 µm) Modification Methods

To allow for clear comparison, Table 7 sums up the data that has been discussed throughout section 6.2

Table 7: Summary of the data in Table 1,2,3,4,5 and 6. Shows the average current at 1.66 V and the average current increase at 1.66 V before and after addition of the WOC across GS-WOC samples that have been modified using different methods.

Sample Type	**Mean Average Water Oxidation Current of the GS-WOC (µA)**	**Mean Average Increase in the Water Oxidation Current on addition of the WOC (µA)**
GS-WOC	74.4 ± 5.0	49.9 ± 18
GS-WOC (UV/ozone)	101 ± 10	97.1 ± 10
GS-WOC (KH_2PO_4)	4780 ± 1700	2220 ± 2000
GS-WOC (KH_2PO_4 & UV/ozone)	6640 ± 60	1470 ± 800
GS-WOC (12 Sprays TiO_2)	118 ± 70	107 ± 70

The data in Table 7 clearly demonstrates how modifying the GS-WOC in a number of different ways, can increase the water oxidation current that is produced. All the modification methods investigated lead to increased differences in the water oxidation current before and after the WOC was applied. This indicates the modification methods may result in a higher concentration of the WOC on the surface of the GS. The electrochemically oxidised samples gave the largest increases in the water oxidation current upon addition of the WOC, perhaps suggesting that this method is the most effective at introducing oxygen containing functional groups to the GS surface, thus providing the most binding sites of the WOC. However, whilst UV/ozone treatment and TiO_2 modification show smaller increases in the water oxidation current, there may be other benefits such as an increased stability of the WOC on the GS surface.

6.2.5.1. XPS Analysis of the GS-WOC (70 µm)

Inductively coupled plasma mass spectrometry (ICP-MS) and X-ray photoelectron spectroscopy (XPS) were considered as quantitative methods to confirm that modification of the GS surface could increase the WOC loading. ICP-MS is a sensitive trace analysis technique that can be used to detect metals at a sensitivity level of parts per trillion (at the

lower detection limit). [36] ICP-MS can be carried out using laser ablation or though digestion of the sample. However, the sample area that is covered using laser ablation is relatively small and would not allow for analysis of the whole 1 cm^2 sample, [37] thus, it was decided that digestion of the sample would be more suitable for analysing the GS anodes. Unfortunately, the GS samples proved difficult to digest in acid using microwave digestion (see Appendix 2.12) without the use of HF; therefore, it was not possible to perform ICP-MS analysis of the GS-WOC samples with the facilities provided. As a result, XPS analysis of the GS-WOC samples was carried out. The amount of Ir present in the samples was of the most interest as this would allow us to compare the relative concentrations of the WOC in each sample, however, the oxygen concentration and the type of function groups present was also examined. The amount of carbon sp^3 hybridisation can also be investigated as it corresponds to functionalisation of the formerly sp^2 graphitic carbon. Table 8 and 9 display the data from the quantitative XPS analysis. The corresponding XPS plots can be found in Appendix 2.13 – 2.17.

Table 8: XPS Elemental Quantification of the 1 cm^2 GS-WOC surface, the error in the quantification of the XPS spectra is taken as 5 %.

Sample	**C 1s (%)**	**Ir 4f (%)**	**O 1s (%)**	**Ti 2p (%)**
GS-WOC	87.5 ± 4.0	0.42 ± 0.02	12.1 ± 0.6	0
GS-WOC (Uv/ozone)	90.1 ± 5.0	0.29 ± 0.01	9.58 ± 0.50	0
GS-WOC (KH_2PO_4)	64.3 ± 3.0	0.39 ± 0.02	35.4 ± 2.0	0
GS-WOC (KH_2PO_4 & UV/ozone)	79.9 ± 4.0	0.31 ± 0.02	19.8 ± 1.0	0
GS-WOC (12 Sprays TiO_2)	50.6 ± 3.0	0.25 ± 0.01	34.6 ± 2.0	14.5 ± 0.7

Table 9: XPS Quantification of the carbon – oxygen and carbon – carbon bonds present on the 1 cm^2 GS-WOC surface, the error in the quantification of the XPS spectra is taken as 5 %.

Sample	**C sp^3 (%)**	**C-O (%)**	**C=O (%)**	**Graphitic Carbon (%)**	**O-C=O (%)**
GS-WOC	18.7 ± 1.0	9.90 ± 0.50	1.07 ± 0.05	69.8 ± 4.0	0.4690 ± 0.020
GS-WOC (UV/ozone)	12.9 ± 0.6	9.00 ± 0.50	0.24 ±0.01	75.5 ± 4.0	0.9200 ± 0.050
GS-WOC (KH_2PO_4)	21.1 ± 1.0	33.0 ± 2.0	7.77 ± 0.30	36.7 ± 2.0	1.890 ± 0.100
GS-WOC (KH_2PO_4 & UV/ozone)	26.9 ± 1.0	16.3 ± 0.8	5.36 ± 0.30	49.1 ± 3.0	2.340 ± 0.100
GS-WOC (12 Sprays TiO_2)	31.9 ± 2.0	6.11 ± 0.30	1.06 ± 0.05	60.4 ± 3.0	0.5170 ± 0.030

The data in Table 8 shows that the amount of iridium, therefore the amount of the WOC, present on the surface of the GS-WOC is very small (< 0.5 %). It also shows that, contrary to previous thought, the GS modification methods do not lead to an increase in the concentration of the WOC on the surface, as the unmodified GS-WOC sample has the highest concentration of iridium. It appears as through the UV/Ozone treatment of the GS reduces the amount of the WOC that is able to bind by approximately a third. The number of sp3 carbons and oxygen contacting functional groups has also been reduced for the UV/ozone treated sample, suggesting that the treatment has had the opposite effect to the desired effect and reduced some of the oxidised sites on the surface of the GS. Mulyana and co-workers showed that UV radiation can reduce oxidised sites in GO, [23] hence it is possible that the UV component in the UV/ozone cleaner had more of an effect than the ozone, causing overall reduction. It is therefore possible that the increased currents seen in the CV of the UV/ozone sample could have been a result of the increased electron mobility. [23] However, the O-C=O relative concentration did increase after UV/ozone treatment, suggesting the introduction of some carboxyl groups at the edges of the GS; however, this was not sufficient enough to increase the WOC loading on the GS surface.

Despite the iridium concentration being lower for the electrochemically oxidised samples, the relative concentration of oxygen containing functional groups was higher, with the C-O concentration increasing from ≈ 10 % to ≈ 33 %; this could indicate an increase in the number of hydroxyl groups present within the sample. The C=O and O-C=O concentrations were also

increased by the KH_2PO_4 electrochemical oxidation, suggesting that the GS surface was successfully oxidised. Nonetheless, unexpectedly this did not lead to an increase in the WOC present on the surface. It was also observed that after treating the electrochemically oxidised sample with UV/ozone, the number of C-O and C=O functional groups was decreased and the concentration of graphitic carbon increased, which is consistent with the observation discussed in the paragraph above.

Ti is detected in the TiO_2 modified samples and the oxygen concentration is also increased, implying that the TiO_2 has been successfully deposited on the GS surface. The number of sp^3 carbon centres has increased the most in the TiO_2 modified samples, which may be because thermal treatment of graphite can cause mild oxidation at temperatures between 400 – 600 °C. [38] However, the iridium concentration in the TiO_2 modified sample, was the lowest of all the samples, suggesting that the TiO_2 addition did not providing additional WOC binding sites.

Despite the data above showing that the methods used to modify the GS were not successful in providing more binding sites for the iridium based WOC, only one sample for each of the modification methods was analysed. As shown throughout this chapter, there is huge variation in the properties of GS, hence submitting multiple samples of the GS-WOC for XPS quantification may have offered greater insight. However, due to time and material constraints, this was not possible.

6.3. WOC On Untreated 25 µm Thickness GS

Graphite is a good electrical conductor in the plane of the graphene sheets, however, is less conductive across layers of stacked graphene sheets, [16] thus a thinner GS could be more beneficial for hole transport in the $CsPbBr_3$ based photoanode. The self-adhesive GS is commercially available at a range of different thicknesses, hence the water oxidation properties of the GS and GS-WOC with a thickness of 25 µm were investigated. Figure 15 shows the CV of the GS-WOC (25 µm) compared to the GS-WOC (70 µm).

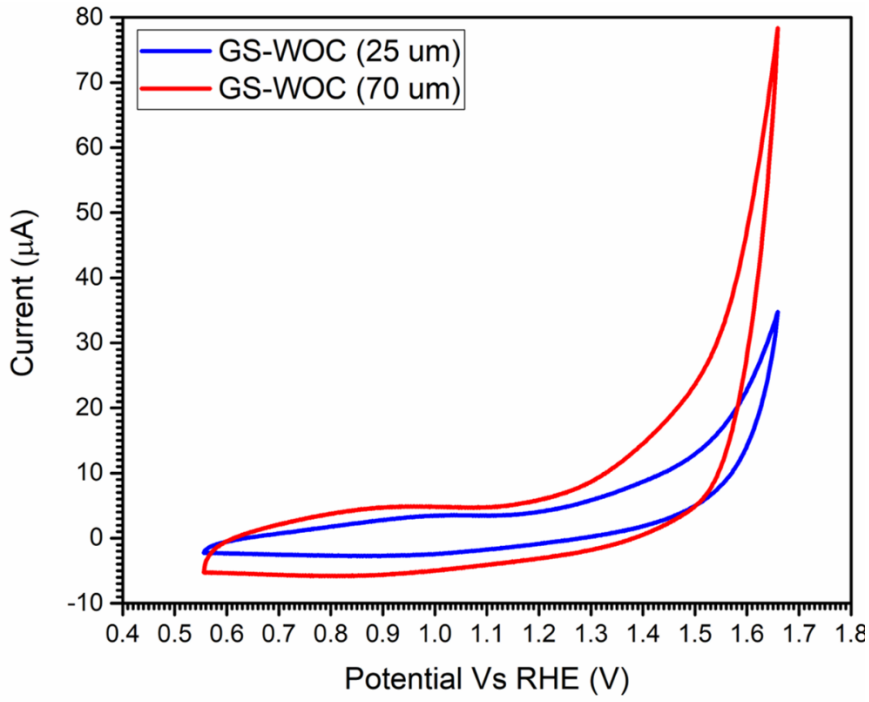

Figure 15: Cyclic voltammograms of the 1 cm^2 GS-WOC (25 µm) and the GS-WOC (70 µm). Measured in 0.1 M KNO3 at pH 2.5, at a scan rate of 50 mV s-1. Ten scans were run; the tenth scan is shown.

Figure 15 shows that the water oxidation current reached by the thinner GS (25 µm), is not as great as the currents reached by the thicker (70 µm) GS. The $Ir^{iii/iv}$ redox peaks are still visible in the CV of the thinner GS-WOC, however, the anodic and cathodic peak currents are reduced compared to those of the thicker GS. Table 10 shows the outcome across three different ≈ 1 cm^2 25 µm thickness GS anodes to allow for comparison of the mean average water oxidation currents between the thinner and the thicker GS.

Table 10: Water oxidation current at 1.66 V on the 10th CV scan, taken of GS (25 µm) soaked in the Ir-based WOC for 52 h (blue). Measured in 0.1 M KNO_3 at pH 2.5, at a scan rate of 50 mV s^{-1}.

	GS Blank (µA)	**GS-WOC (µA)**	**Current Difference After WOC (µA)**
GS 1	3.1	29	26
GS 2	3.1	32	27
GS 3	3.4	35	31
Mean Average	**3.2 ± 0.2**	**32 ± 3.0**	**28 ± 3.0**

The mean average current increase after the WOC addition for the thinner GS was 28.3 µA ± 2.7, compared to 49.9 µA ± 18 for the thicker 70 µm GS. This might suggest that more of the WOC is able to bind to the surface of the thicker GS likely due to an increased surface area.

6.4. WOC On Untreated 160 µm Thickness GS

As it appears that greater water oxidation currents can be achieved by the GS with greater thickness, the water oxidation properties of the GS-WOC using a GS with a thickness of 160 µm was investigated. Figure 16 shows the CV of the GS-WOC (160 µm) compared to the GS-WOC (70 µm) and the GS-WOC (25µm).

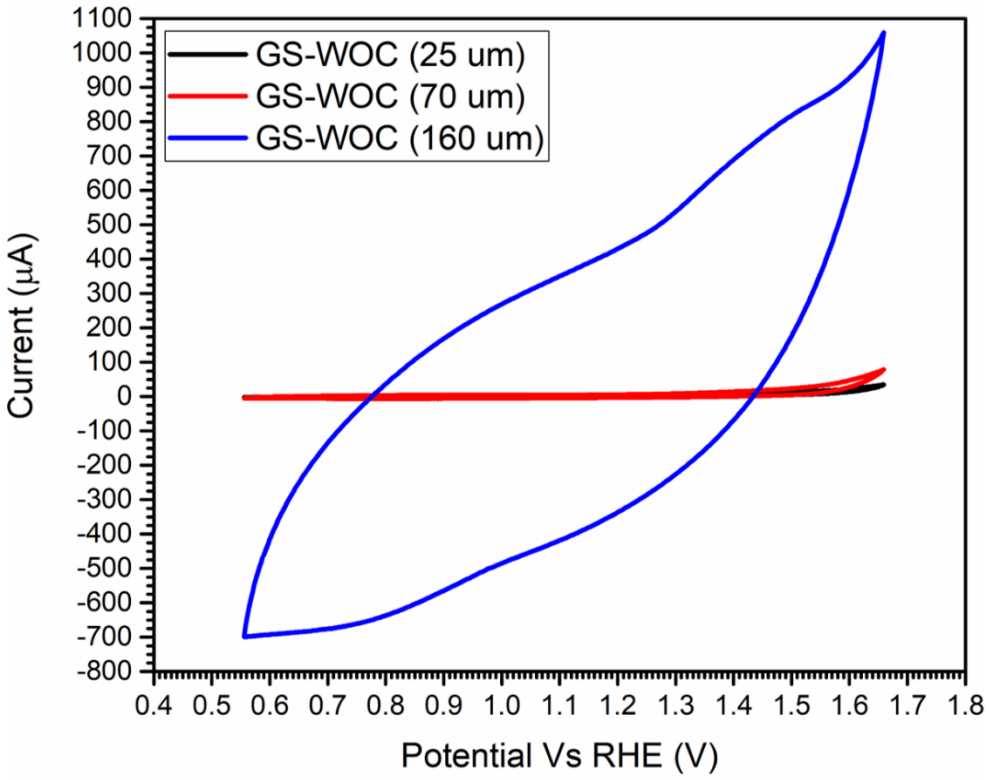

Figure 16: Cyclic voltammograms of the 1 cm^2 GS-WOC (160 µm), the GS-WOC (70 µm) and the GS-WOC (25 µm). Measured in 0.1 M KNO3 at pH 2.5, at a scan rate of 50 mV s-1. Ten scans were run; the tenth scan is shown.

The currents produced by the 160 µm thickness GS-WOC dwarf those produced by the 70 and 25 µm thickness samples. The $Ir^{iii/iv}$ redox peaks are still clearly visible, centred around ≈ 0.9 V, however, the anodic peak at ≈ 1.45 V is also clearly visible, even after 10 cycles of the CV scans has been completed. This can be assigned to the $Ir^{iv/v}$ redox couple that occur during the catalytic water oxidation reaction. [11] Normally, this feature is obscured by the early onset of the water oxidation catalytic wave; however, this is not the case for the 160 µm thickness GS-WOC. The background scan of the blank GS also produces higher currents and shows a large integrated area under the curve (see Appendix 2.20) when compared to the background scan of the blank 25 and 70 µm GS samples. Therefore, the onset of the water oxidation curve is difficult to observe in Figure 16. Table 11 shows the outcome across three different ≈ 1 cm^2

160 µm thickness GS anodes to allow for comparison of the mean average water oxidation currents between the thinner and the thicker GS.

Table 11: Water oxidation current at 1.66 V on the 10th CV scan, taken of GS (160 µm thickness) soaked in the Ir-based WOC for 52 h (blue). Measured in 0.1 M KNO_3 at pH 2.5, at a scan rate of 50 mV s^{-1}.

	GS Blank (µA)	**GS-WOC (µA)**	**Current Difference After WOC (µA)**
GS 1	833.1	1059	193.4
GS 2	647.1	925.9	278.8
GS 3	817.0	900.3	83.30
Mean Average	**765.8 ± 100.0**	**961.9 ± 86.0**	**185.2 ± 98.0**

The average increase of the water oxidation current after the WOC was added was much larger for the thicker (160 µm) GS, showing a mean average increase of 185.2 µA ± 98, compared to 49.9 µA ± 18 for the 70 µm GS. The large background scans of the blank GS may suggest a larger surface area. The larger surface area may provide an increased number of WOC binding sites, resulting in the larger increases in the water oxidation current observed. However, in this study, the 160 µm thickness GS is produced by a different manufacturer from the 70 and 25 µm thickness GSs. As a result, the amount of surface oxidation could vary between manufacturers which would also increase the number of WOC binding sites.

6.5. Summary and Conclusion

A range of methods were investigated in an attempt to increase the WOC loading on the GS anode. The methods mostly aimed to increase the number of oxidised sites on the surface of the GS to provide a greater number of binding sites for the iridium based WOC. Methods investigated included the use of UV/ozone exposure, electrochemical oxidation using KH_2PO_4, a combination of UV/ozone with KH_2PO_4 oxidation, and the use of a TiO_2 coating. However, it appeared that whilst the use of KH_2PO_4 and TiO_2 were successful in introducing a higher amount of oxygen containing sites to the sample, the concentration of iridium detected did not increase. Hence implying that the WOC loading, on the surface of the GS, had not been increased. However, the error in the XPS analysis is large suggesting that perhaps it was not the best method for quantification.

Despite no observable increase in the WOC concentration, the water oxidation currents that were achieved showed an increase after all four GS modification processes. Whilst this does not correspond to an increase in WOC concentration, it may still be beneficial for use in the $CsPbBr_3$ photoanodes and allow a higher photocurrent to be achieved. Some of the modification methods, for example the UV/Ozone treatment, may have also improved the

stability of the WOC on the GS, which may lead to high photocurrents being achieved for longer periods of time.

A deeper analysis of the GS surface modification would be beneficial. A larger range of UV/ozone exposure times could have been examined. A shorter exposure time may have been more beneficial for epoxide group introduction. [23] Investigating thicker TiO_2 layers could have also been useful to see if the water oxidation current would increase any further.

The thickness of the GS also appeared to have an effect on the water oxidation current that can be achieved by the photoanode, with a thicker GS giving the largest increase. This is probably a result of an increased GS surface area. The thicker GS may also provide greater protection against the water for the $CsPbBr_3$ device within the photoanode. This would allow the photoanode to function for longer.

Future work involves examining the various GS-WOC modification methods within the $CsPbBr_3$ photoanodes for water splitting uses. This investigation is carried out in Chapter X of this thesis. However, further work could investigate additional ways to modify the GS. Other oxidation methods, such as acid oxidation, could be used. Other metal oxide coatings for the GS could also be examined. Hole transporting metal oxide layers such as NiO_x or ZnO could be beneficial as they would provide additional oxygen sites for WOC binding, whilst also facilitating hole transport. However, it is worth noting that graphene oxide is more hydrophilic than graphene/graphite, which may cause problems when using the GS to protect the $CsPbBr_3$ from water in the photoanode.

Additionally, other carbon materials, such as glassy carbon, could be explored to see whether they are able to bind more of the WOC. Finally, other known water oxidation catalysts could be investigated to see whether they are more effective or whether a greater concentration of the other catalysts are able to be applied to the carbon electrode.

6.6. References

1 J. D. Blakemore, R. H. Crabtree and G. W. Brudvig, *Chem. Rev.*, 2015, **115**, 12974–13005.

2 M. Yagi, E. Tomita, S. Sakita, A. Takayuki Kuwabara and N. Keiji, *J. Phys. Chem. B*, 2005, **109**, 21489–21491.

3 Andrew Mills, P. A. Duckmanton and John Reglinski, *Chem. Commun.*, 2010, **46**, 2397–2398.

4 D. Galizzioli, F. Tantardini and S. Trasatti, *J. Appl. Electrochem.*, 1975, **5**, 203–214.

5 J. Horkans and M. W. Shafer, *J. Electrochem. Soc.*, 1977, **124**, 1202–1207.

6 A. Mills and T. Russell, *J. Chem. Soc. Faraday Trans.*, 1991, **87**, 1245–1250.

7 T. Naito, T. Shinagawa, T. Nishimoto and K. Takanabe, *Inorg. Chem. Front*, 2021, **8**, 2900.

8 D. Lebedev, M. Povia, K. Waltar, P. M. Abdala, I. E. Castelli, E. Fabbri, M. V. Blanco, A. Fedorov, C. Copéret, N. Marzari and T. J. Schmidt, *Chem. Mater.*, 2017, **29**, 5182–5191.

9 J. A. Gilbert, D. S. Eggleston, W. R. M. Jr., D. A. Geselowitz, S. W. Gersten, D. J. Hodgson and T. J. Meyer, *J. Am. Chem. Soc.*, 2002, **107**, 3855–3864.

10 U. Hintermair, S. W. Sheehan, A. R. Parent, D. H. Ess, D. T. Richens, P. H. Vaccaro, G. W. Brudvig and R. H. Crabtree, *J. Am. Chem. Soc.*, 2013, **135**, 10837–10851.

11 S. W. Sheehan, J. M. Thomsen, U. Hintermair, R. H. Crabtree, G. W. Brudvig and C. A. Schmuttenmaer, *Nat. Commun.*, 2015, **6**, 1–9.

12 J. M. Thomsen, D. L. Huang, R. H. Crabtree and G. W. Brudvig, *Dalt. Trans.*, 2015, **44**, 12452.

13 U. Hintermair, S. M. Hashmi, M. Elimelech and R. H. Crabtree, *J. Am. Chem. Soc.*, 2012, **134**, 9785–9795.

14 E. V. Sackville, F. Marken and U. Hintermair, *ChemCatChem*, 2018, **10**, 4280–4291.

15 I. Poli, U. Hintermair, M. Regue, S. Kumar, E. V. Sackville, J. Baker, T. M. Watson, S. Eslava and P. J. Cameron, *Nat. Commun.*, 2019, **10**, 2097.

16 A. Ambrosi, C. K. Chua, A. Bonanni and M. Pumera, *Chem. Rev.*, 2014, **114**, 7150–

7188.

17 D. W. Lee, L. De Los Santos V., J. W. Seo, L. L. Felix, A. Bustamante D., J. M. Cole and C. H. W. Barnes, *J. Phys. Chem. B*, 2010, **114**, 5723–5728.

18 C. Li, X. Chen, L. Shen and N. Bao, *ACS Omega*, 2020, **5**, 3397–3404.

19 J. R. Vig, *J. Vac. Sci. Technol. A Vacuum, Surfaces, Film.*, 1998, **3**, 1027.

20 V. S. Prudkovskiy, K. P. Katin, M. M. Maslov, P. Puech, R. Yakimova and G. Deligeorgis, *Carbon N. Y.*, 2016, **109**, 221–226.

21 S. Groveman, J. Peng, B. Itin, I. Diallo, L. M. Pratt, A. Greer, E. J. Biddinger, S. G. Greenbaum, C. M. Drain, L. Francesconi and M. Vittadello, *Carbon N. Y.*, 2017, **122**, 411–421.

22 P. Magne and N. Dupont-Pavlovsky, *Carbon N. Y.*, 1988, **26**, 249–255.

23 Y. Mulyana, M. Uenuma, Y. Ishikawa and Y. Uraoka, *J. Phys. Chem. C*, 2014, **118**, 27372–27381.

24 R. David, A. Tuladhar, L. Zhang, C. Arges and R. Kumar, *J. Phys. Chem*, 2020, **2020**, 8178.

25 J. O. Besenhard, E. Wudy, H. Möhwald, J. J. Nickl, W. Biberacher and W. Foag, *Synth. Met.*, 1983, **7**, 185–192.

26 N. E. Sorokina, L. A. Monyakina, N. V Maksimova, I. V Nikol'skaya and V. . Avdeev, *Inorg. Mater.*, 2002, **38**, 482–489.

27 W. C. Forsman, F. L. Vogel, D. E. Carl and J. Hoffman, *Carbon N. Y.*, 1978, **16**, 269–271.

28 R. B. Kohakade, E. Senthil Kumar, R. W. Gaikwad, S. Raghu and R. A. Kalaivani, *Rasayan J. Chem*, **10**, 1151–1158.

29 F. Marken, A. Neudeck and A. M. Bond, in *Electroanalytical Methods*, 2010, pp. 57–106.

30 W. R. Browne, *Electrochemistry*, Oxford University Press, 2018.

31 E. Taer, A. Agustino, R. Farma, R. Taslim, Awitdrus, M. Paiszal, A. Ira, S. D. Yardi, Y. P. Sari, H. Yusra, S. Nurjanah, S. D. Hartati, Z. Aini and R. N. Setiadi, *J. Phys. Conf. Ser.*, 2018, **1116**, 32040.

32 B. Xu, S. Yue, Z. Sui, X. Zhang, S. Hou, G. Cao and Y. Yang, *Energy Environ. Sci.*,

2011, **4**, 2826–2830.

33 A. Hernández-Granados, A. N. Corpus-Mendoza, P. M. Moreno-Romero, C. A. Rodríguez-Castañeda, J. E. Pascoe-Sussoni, O. A. Castelo-González, E. C. Menchaca-Campos, J. Escorcia-García and H. Hu, *Opt. Mater. (Amst).*, 2019, **88**, 695–703.

34 L. Gouda, K. J. Rietwyk, J. Hu, A. Kama, A. Ginsburg, M. Priel, D. A. Keller, S. Tirosh, S. Meir, R. Gottesman and A. Zaban, *ACS Energy Lett.*, 2017, **2**, 2356–2361.

35 L. Kavan, *Catal. Today*, 2019, **328**, 50–56.

36 Comparison of ICP-OES and ICP-MS for Trace Element Analysis - UK, https://www.thermofisher.com/uk/en/home/industrial/environmental/environmental-learning-center/contaminant-analysis-information/metal-analysis/comparison-icp-oes-icp-ms-trace-element-analysis.html, (accessed 12 January 2023).

37 J. Koch and D. Günther, *Encyclopedia of Spectroscopy and Spectrometry*, Academic Press, Third Edition., 2017.

38 S. S. Nair, T. Saha, P. Dey and S. Bhadra, *J. Mater. Sci.*, 2021, **56**, 3675–3691.

Chapter 7. New and Improved CsPbBr3 Photoanodes

7.1. Introduction

Photelectrochemical (PEC) water splitting is widely considered to be a promising approach for producing chemical energy directly from sunlight; the products are often referred to as solar fuels. Interest in the topic of hydrogen production using semiconductors has grown immensely since 1972, when Fujishima and Honda first demonstrated water oxidation, using a TiO_2 anode and a platinum cathode under UV irradiation with the application of an external bias, [1]. [2, 3, 4, 5] Fujishima and Honda demonstrated that electromagnetic radiation can be used to provide the theoretical 1.23 V of energy required for water splitting. Nonetheless, the development of an adequately efficient and stable solar to hydrogen energy conversion device remains a considerable challenge.

The majority of photoanodes that were first developed for water splitting applications use wide bandgap metal oxides such as TiO_2 [6] or ZnO. [7] However, this wide bandgap means that these materials only absorb photons in the UV portion of the AM 1.5 spectrum, resulting in these photoanodes only absorbing a small portion of sunlight. Hence wide bandgap semiconductors photoanodes have low solar to hydrogen conversion efficiencies. [8] Other metal oxide-based semiconductors, with slightly smaller band gaps that reach into the visible region of the electromagnetic spectrum, such as WO_3, [9] or $BiVO_4$ are also popular. [10] However, despite having a more suitable bandgap, many of these materials suffer from poor surface water oxidation kinetics and carrier recombination at the semiconductor/electrolyte interface, thus reducing their solar to hydrogen efficiency to values far below the theoretical values. [11] Many of these photoanodes function by placing the thin film of the chosen material directly in contact with the electrolyte, however often fast recombination will occur. The use of solar cell devices, such as PSCs, rather than a single semiconductor thin film, can help to supress carrier recombination during the water oxidation process, due to the hole and electron separation that occurs within the devices, thus overall improving solar to hydrogen efficiencies. [12] The tuneable bandgaps and high PCEs of PSCs make them a suitable choice for use as photoanodes, however the instability of PSCS to water remains a significant issue. As a result, a number of encapsulation methods to help PSCs withstand submersion in aqueous solutions have been developed.

In 2014, Grätzel *et al*. used $MAPbI_3$ based devices, with a band gap of 1.5 eV and a PCE of 17.3 %, in combination with NiFe based electrodes, to achieve a solar to hydrogen efficiency of 12.3 % and produce stable photocurrents above 10 mA cm^{-2}. [13] However, this was not an integrated system, and the PSCs were placed outside of the electrolyte and were wired to the NiFe electrodes. Using this non-integrated approach can be beneficial as the PSC acts as a means for simply producing energy to drive the water splitting reaction and the strict requirements for direct semiconductor water splitting can be relaxed. However, the integrated system, wherein the solar cell device is submerged in the electrolyte, can provide other benefits, such as saved space and reduced wiring which can also prevent some ohmic losses. [14]

In 2015 Da and co-workers, used a thin nickel surface as a protection layer for a $MAPbI_3$ based device, The Ni surface also functioned as a hole-transferring catalyst to aid the water oxidation reaction. [15] The Ni layer was deposited by sputtering and the photoanode was able to briefly reach a photocurrent of 10 mA cm^{-2} in a Na_2S solution (pH 12.8) when connected to a Pt electrode and a Ag/AgCl reference electrode at 0 V. Despite the Ni layer, the photoanode was not stable for long, the 10 mA cm^{-2} photocurrent rapidly dropped to ≈ 2 mA cm^{-2} and this was only maintained for 20 min before water degraded the perovskite absorber layer. [15] However, the Ni encapsulation showed promise for protecting PSC based photoelectrodes. As a result, other metal encapsulation layers have also been developed as a means to prevent water degrading lead halide perovskite based photoelectrodes. Reisner *et al.* chose a InBiSn alloy (known as Field's metal) to encapsulate their $MaPbI_3$ based photocathodes. [16] The use of Field's metal allowed the device to function for 1 h 45 min before water ingress occurred and the perovskite layer was degraded. Nam and co-workers also later employed Field's metal with an additional Ni catalyst film to encapsulate a $MAPbI_3$ based photoanode, that was able to survive in alkaline conditions for 5.5 h. [17] This again showed that whilst lead halide perovskites are not stable in water, with suitable encapsulation they can be used as photoelectrodes for direct solar fuel production.

Carbon materials are also popular encapsulation materials for PSCs based photoelectrodes. In 2019, Xu *et al*. encapsulated a $MAPbI_3$ based photoanode using conductive carbon paste and silver conductive paint, followed by a second carbon paste layer. [18] This allowed the photoanode to be stable for 48 h in the dark, however, under 1 sun illumination, the device was able to produce a photocurrent above 8 mA cm^{-2} for 12 h with an applied bias of 1.23 V (Vs RHE). [18] Improving upon this, Poli and co-workers, encapsulated a $CsPbBr_3$ planar carbon device using a commercially available GS layer, with a thickness of 70 µm, and epoxy resin to seal the edges. [4] The device operated under 1 sun illumination, in H_2O (pH = 2.5),

continuously for 30 h, however eventually catastrophic failure of the glue allowed water ingress, thus degrading the perovskite layer.

In 2022, Park *et al*. employed both a PSC based photocathode and photoanode to achieve unbiased water splitting under alkaline conditions. [19] A mixed cation $(FAPbI_3)_{0.85}(MAPbBr_3)_{0.15}$ perovskite was used as the two absorber layers, and the devices were protected using a nickel foil coated in NiPCoP and NiFe, then sealed using epoxy resin. A photocurrent of above 8 mA cm^{-2} was achieved, however, this value halved over 20 h. [19]

The longest reported operating time for a lead halide perovskite photoelectrode is 120 h, which was achieved by Choi *et al.* who developed a $MAPbI_3$ based photocathode, encapsulated an In-Ga alloy with MoS_2 coated Ti foil. [20] The lifetime of this PSC based photoelectrode showed that lead halide perovskite devices could operate in aqueous conditions for an extended period of time. A summary of the photoelectrode and operating times, from a range of lead halide perovskite-based devices in the literature, is shown in Table 1, as are the stability issues faced by lead halide based photoelectrodes. The devices must be stable enough to withstand the operating conditions for a substantial amount of time for direct solar-to-fuel conversion technology to be viable.

Table 1: A comparison of lead halide perovksite based photoelectrodes

Photoelectrode System	**Electrolyte**	**Photocurrent**	**Stability**
FTO/TiO_2/$MAPbI_3$/Spiro-MeOTAD/Au/Ni Photoanode [15]	0.1 M NaS, pH 12.8	12 – 2 mA cm^{-2} (0 V vs Ag/AgCl)	20 min
FTO/PEDOT:PSS/$MAPbI_3$/PCBM/Au/InBiSn Photocathode [16]	0.1 M BBS, pH 8.5	- 7 mA cm^{-2} (0 V Vs RHE)	1.5 h
FTO/TiO_2/$MAPbI_3$/Spiro-OMeTAD/Au/InBiSn/Ni	0.1 M KOH, pH 14	> 13 mA cm^{-2} (1.23 V Vs RHE)	5.5 h
FTO/TiO_2/ZnO_2/Carbon/$MAPbI_3$/Carbon/Ag/Carbon Photoanode [18]	1 M KOH	> 9 mA cm^{-2} (1.23 V Vs RHE)	12 h
FTO/TiO_2/$CsPbBr_3$/Carbon/Ag/GS Photoanode [4]	0.1 M KNO_3, pH 7	> 2 mA cm^{-2} (1.23 V Vs RHE)	30 h
ITO/PTAA/ $(FAPbI_3)_{0.85}(MAPbBr_3)_{0.15}$ /PCBM/Au/Ni Foil/NiPCoP Photocathode [19]	0.1 M KOH	- 20 - - 10 mA cm^{-2} (0 V Vs RHE)	40 h
ITO/SnO_2/ $(FAPbI_3)_{0.85}(MAPbBr_3)_{0.15}$ /Spiro-OMeTAD/Au/Ni Foil/NiFe Photoanode [19]	0.1 M KOH	< 23 mA cm^{-2} (1.23 V Vs RHE)	20 h
ITO/PTAA/$MAPbI_3$:Proline/PCBM/Cu/GaIn/Ti foil/MoS_2 Photocathode [20]	0.5 M H_2SO_4	-22 - - 12 mA cm^{-2} (0V Vs RHE)	120 h

This chapter follows work done by Poli *et al*. using the self-adhesive GS-WOC, which was discussed in detail throughout Chapter 6, to encapsulate planar carbon $CsPbBr_3$ solar cells. The aim was to increase the operating stability of these photoanodes to times above 30 h.

7.2. Improved $CsPbBr_3$ Photoanode Encapsulation for Water Oxidation

Poli *et al.* used epoxy resin to seal around the edges of the GS, to protect the $CsPbBr_3$ device. However, after approximately 30 h, the sealant failed and water ingress occurred, which in turn lead to catastrophic failure of the device. [4] Thus, an encapsulation method that would avoid the need for the epoxy resin sealant was sought. In this work, the $CsPbBr_3$ devices were encapsulated using the GS (70 µm) and a well-designed flow system to ensure that water was only in contact with the GS. A small Teflon cell, with a hole cut through the middle was designed. The hole had a diameter of 0.75 cm. Grooves around the hole on either side of the cell were added to allow O-rings to encompass the hole. An inlet and an outlet were added at the top and bottom of the cell, and two holes were also cut out to allow for insertion of the reference and counter electrodes. The Teflon cell is pictured below in Figure 1.

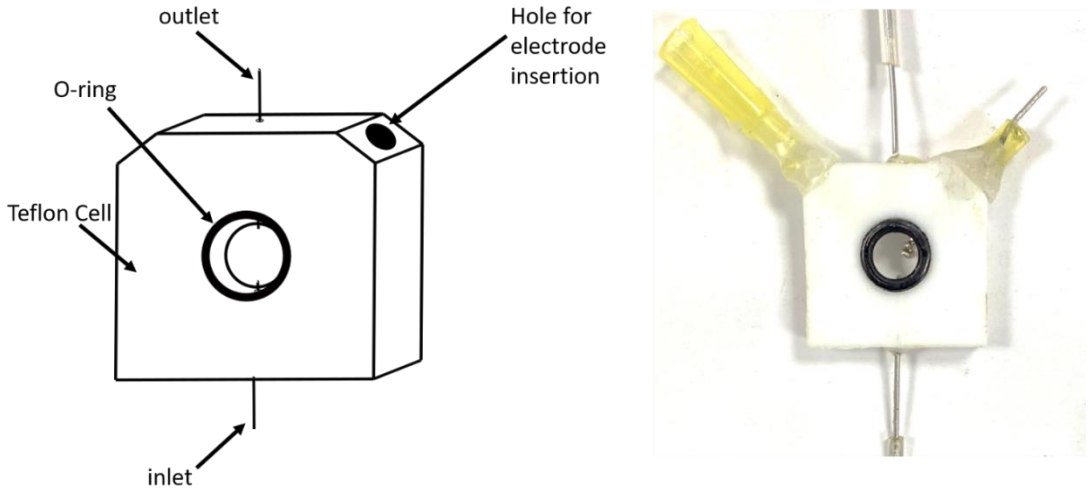

Figure 1: Schematic diagram of Teflon cell (left). Photograph of Teflon cell (right)

The Teflon cell was sandwiched between the TiO_2/$CsPbBr_3$/Carbon/GSWOC device and a thin sheet of glass. This was clamped together in a frame to allow the O-rings to provide a seal and create a circular chamber. This resulted in an area of the GS exposed to the solution, thus the active area of the photoanode, of 0.44 cm^2. It was important to ensure that the O-ring was positioned fully within the area of the GS to fully seal the device. An aqueous 0.1 M KNO_3 solution, adjusted to a pH of 2.5 using HNO_3 was then flowed into the chamber at the bottom of the Teflon cell, and out through the top at a flow rate of 2 mL min^{-1}. Figure 2 demonstrates the new encapsulation and operating method.

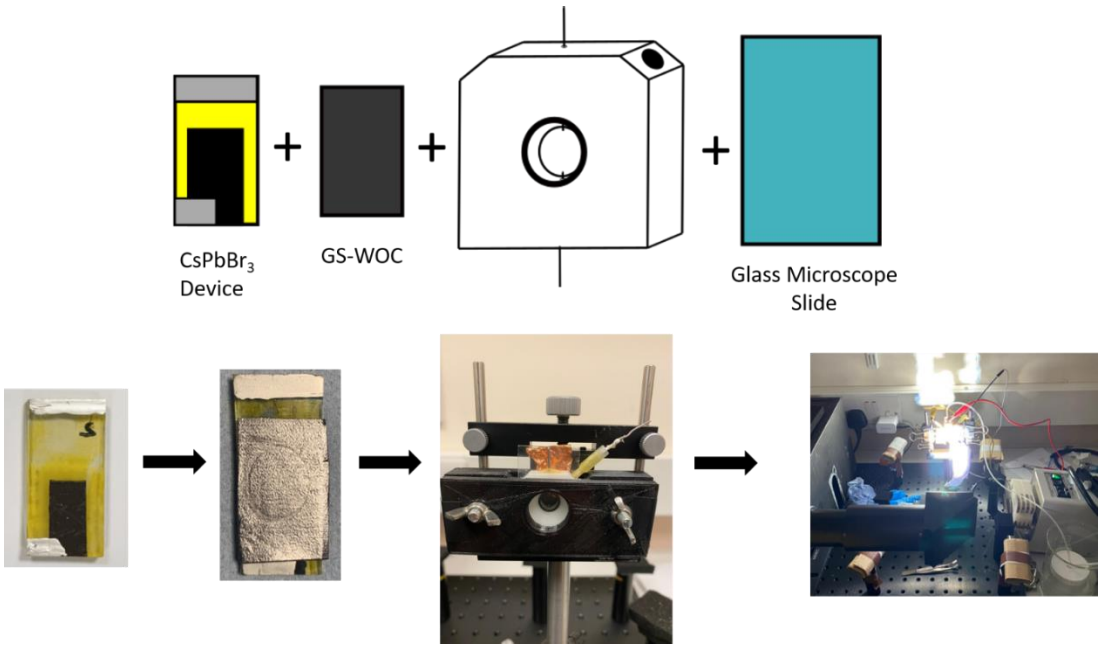

Figure 2: Schematic diagram of $CsPbBr_3$ photoanode encapsulation (top), photograph of water splitting set up (bottom).

The set up pictured in Figure 2 meant that the system is now free from epoxy resin, hence water oxidation should be able to continue past 30 h without failure. A peristaltic pump was used, set to a flow rate of 2 mL/min, to continuously fill the chamber with fresh electrolyte solution. This also allowed gas bubbles to be easily removed from the chamber, thus the electrodes could always remain in contact with the solution.

To further improve this operation, planar carbon $CsPbBr_3$ devices with V_{OC} values ≤ 1.4 V were selected for use in measurements. These voltages values are larger than those that were achieved by Poli *et al.* which may also lead to the need for less externally applied potential. The reverse PCE values of the devices chosen were also ≤ 5.5 % and J_{SC} values were ≤ 5.5 mA cm^{-2}, which again are greater than values achieved by Poli *et al.*, which may also lead to improved water oxidation photocurrents.

7.2.1. Water oxidation setup tests

The $CsPbBr_3$ devices were chosen for their high V_{OC} values. As a result, when the TiO_2/$CsPbBr_3$/Carbon/GS-WOC photoanode was placed under 1 sun illumination, large photovoltages were observed. Figure 3 shows the voltage difference between a set of TiO_2/$CsPbBr_3$/Carbon/GS-WOC photoanodes in the dark and under illumination.

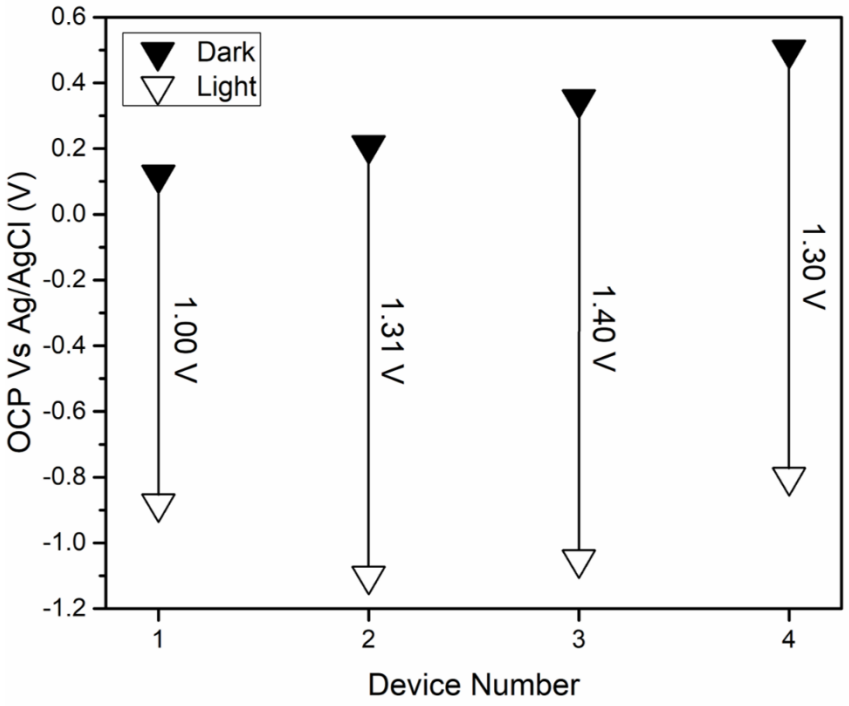

Figure 3: The open circuit potential (OCP) of four TiO_2/$CsPbBr_3$/Carbon/GS-WOC anodes measured in 0.1 M KNO_3 at pH 2.5. Measurements performed in the dark are represented with solid black triangles, whereas the measurements performed under 1 sun illumination are represented with open triangles.

The open circuit potential values, given in Figure 3, show that large photovoltages, close to the expected V_{OC} values, can be achieved with these devices. Across four photoanodes, the average photovoltage was 1.25 V, although photovoltages as large as 1.40 V are achievable. These values are above the theoretical required potential for water splitting of 1.23 V thus theoretically could drive the water splitting reaction. However, in practice the application of an external bias is required to reach the necessary overpotential values. Poli *et al*. clearly demonstrated that use of the Ir-based WOC, applied to the surface of the GS, reduces the extent of the overpotential required. [4] To investigate the performance of the photoanodes and to observe the amount of overpotential that is required for water splitting to be observed, chronoamperometry measurements were run. The applied voltage was increased every 5 min from 0.36 V to 1.56 V (vs RHE). The 5 min period at each voltage stage, allowed the current to stabilise so that a true idea of the water oxidation current could be observed.

First, a test was run using 0.1 M CF_3KO_3S in dry acetonitrile. This was used to measure the oxidation current in the absence of water and to observe any electrode oxidation effects under 1 sun illumination. The potential was stepped from 0 -1.4 V (vs Ag/AgCl) and 1 mL of water was spiked into the electrolyte reservoir at 40 min. The result is shown in Figure 4.

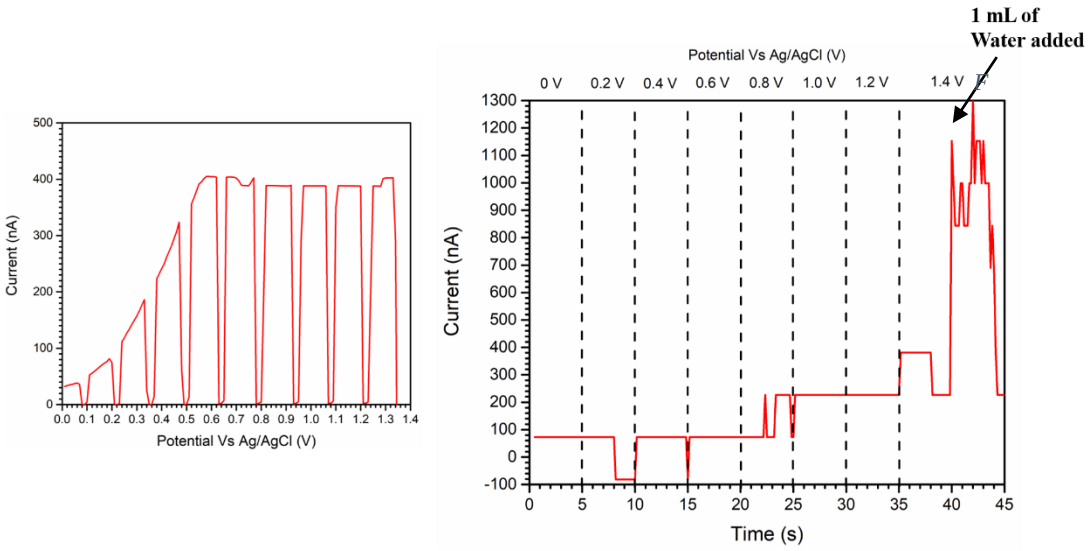

Figure 4: a) Chopped light (1 sun) linear sweep between 0 – 1.4 V (vs Ag/AgCl) 50 mV s^{-1} in 0.1 M CF_3KO_3S in MeCN b) Chronoamperometry under 1 sun illumination, in 0.1 M CF_3KOS in MeCN,. The voltage was stepped up 0.2 V every 5 min, from 0. V to 1.4 V (vs Ag/AgCl). At 40 min, 1 mL of H_2O was spiked into the solution reservoir

Figure 4 demonstrates that there is minimal current without the presence of water, and that light and an applied potential alone are not enough to produce a substantial current. Figure 4(a) shows that the current is light responsive, with the signal increasing to a maximum of ≈ 400 nA at potentials greater than 0.5 V (vs Ag/AgCl) when the light is on. The reason for the photocurrent could be a small amount of water present in the MeCN solvent as the experiment was carried out in ambient air. Figure 4(b) again shows that in MeCN currents below 400 nA are achieved, until 1 ml of water is spiked into the system, after which the current increases to reach a maximum of 1300 nA. This would suggest water oxidation is the main cause for the current that is produced under illumination. However, as acetonitrile is an aprotic solvent, adjusting and measuring the pH is difficult and converting the potential in line with the Reversible Hydrogen Electrode (RHE) is not possible. Thus, this measurement cannot be directly compared to the other measurements in the chapter that are performed in 0.1 M KNO_3 at pH 2.5 at potentials between 0.36 – 0.56 V (vs RHE).

A similar measurement was then performed in aqueous 0.1 M KNO_3 (pH 2.5), both in the dark and under illumination, to observe the effect of light on the current when water is present. This is shown in Figure 5.

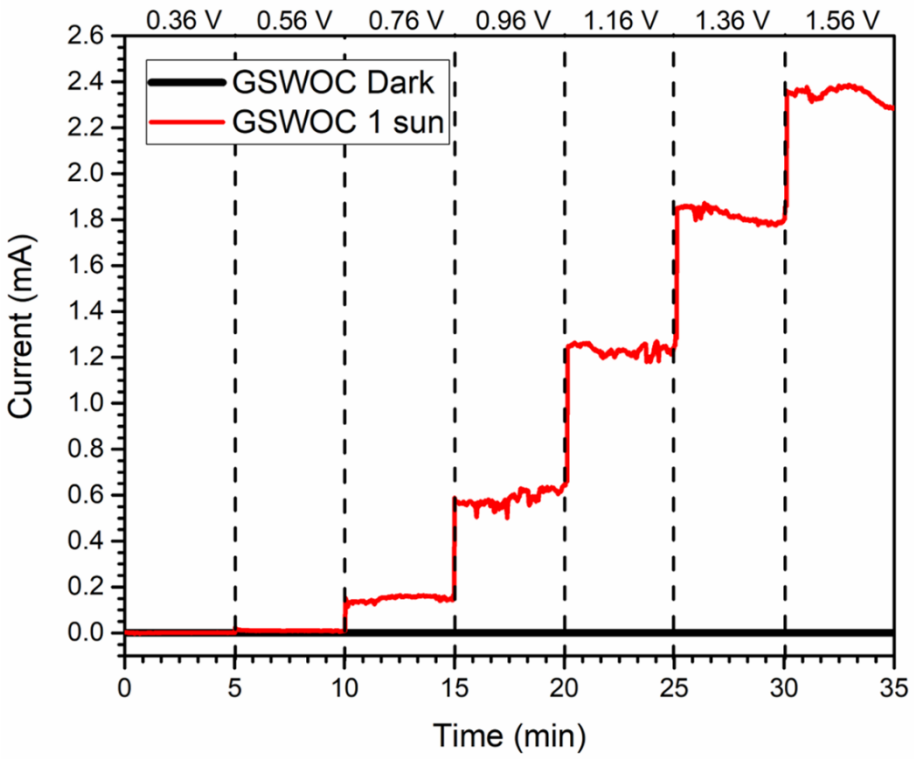

Figure 5: Chronoamperometry measurements of the TiO_2/$CsPbBr_3$/Carbon/GSWOC based photoanode in 0.1 M KNO_3, pH 2.5, in the dark (black) and under 1 sun illumination (red). The voltage was stepped up 0.2 V every 5 min from 0.36 V – 1.56 V (vs RHE).

Figure 5 clearly shows that the current is a result of the light. When the measurement is performed in the dark, the photocurrent appears flat, and reaches a maximum of 400 nA at 1.56 V (vs RHE). On the other hand, under illumination, the photocurrent begins to increase when the potential is stepped to 0.76 V (vs RHE) and reaches a maximum photocurrent of ≈ 2.4 mA at 1.56 V (vs RHE), this corresponds to 5.5 mA cm^{-2} when adjusted for the area of the exposed photoanode.

To further investigate the effect of light on the photocurrent, the light intensity was increased from 0.3 to 1 sun and the average photocurrent measured. The photocurrent was expected to increase linearly as the intensity of light increased. Figure 5 confirms this trend.

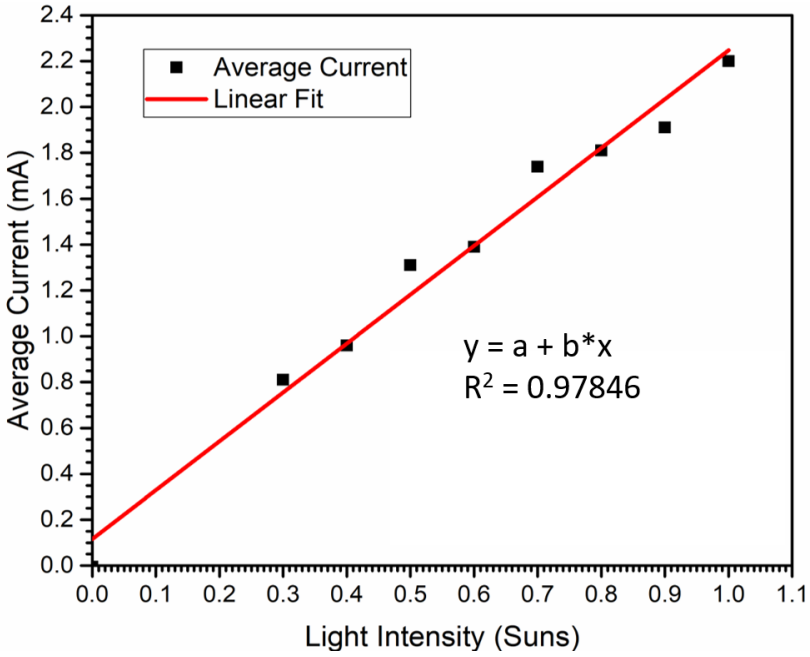

Figure 6: Plot of the average photocurrent value over 5 min at light intensities between 0.3 and 1 sun. The measurements were performed at 1.23 V (vs RHE) in 0.1 M KNO_3 pH 2.5.

There was a strong corelation between the light intensity and the current measured in Figure 6, further showcasing the dependence of the current on the light.

7.2.2. Water Oxidation Long Term Performance Tests

Table 1 in section 7.1 shows that many water oxidation tests using photoanodes are performed with an external bias of 1.23 V vs RHE thus, this was taken as a suitable potential to apply. The stepped voltage chronoamperometry measurements and a chopped light linear sweep measurement of the photoanode (Appendix 3.1) determined that a suitable current could be producing at an applied external potential of 1.23 V (vs RHE). During the long-term performance tests a potential of 1.23 V vs RHE was applied to the TiO_2/$CsPbBr_3$/Carbon/GS-WOC based photoanodes. Figure 7 shows the resulting chronoamperometry trace. Whilst an applied potential of 1.23 V (vs RHE) would result in a STH efficiency of 0 %, this value was chosen to allow direct comparison to the literature.

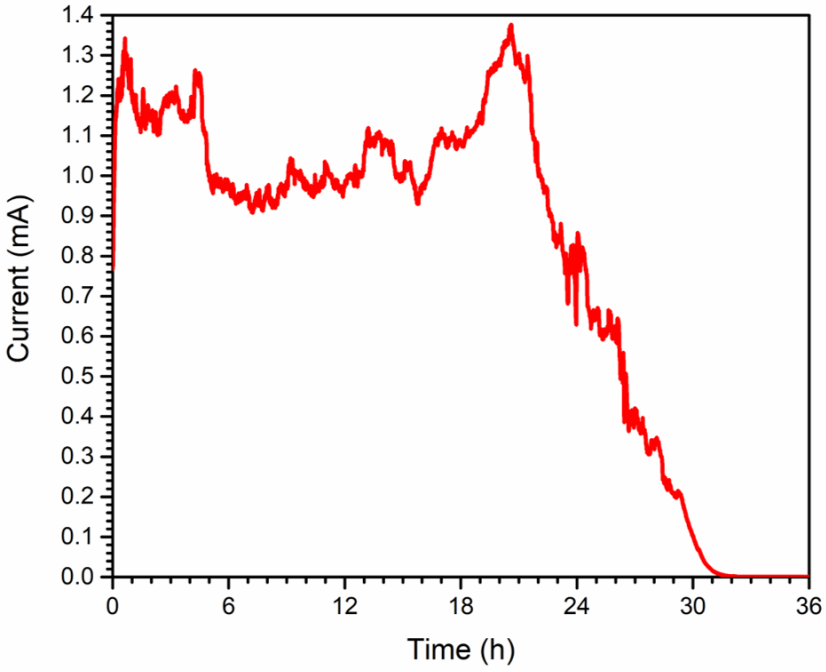

Figure 7: Chronoamperometric trace of TiO_2 /$CsPbBr_3$/m-c/GS/ WOC recorded at an applied potential of 1.23 V (vs RHE), in 0.1M KNO_3, pH 2.5, under continuous 1 sun illumination.

It was predicted that the improved encapsulation technique would increase the lifetime of the device under operating conditions, however, the results in Figure 7 show that the device began to fail at ≈ 23 h. This is a shorter lifetime than the photoanodes tested by Poli *et al.*, which reached 30 h of operation before failure. [4] The current produced was also lower than expected, despite the planar carbon $CsPbBr_3$ device demonstrating good JV characteristics. The current peaked at a value of ≈ 1.3 mA (2.95 mA cm^{-2}) but dropped below 1.0 mA (2.3 mA cm^{-2}) for the majority of the measurement. After failure, the device was removed from the encapsulation cell and inspected. A JV curve of the failed device was also measured to compare the performance of the PSC before and after water oxidation. Figure 8 shows the results.

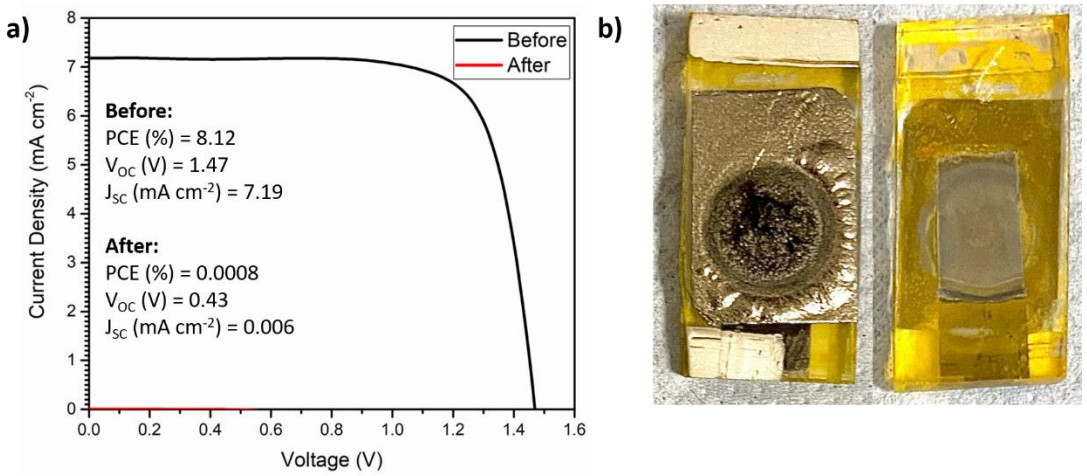

Figure 8: a) J-V curves of the $CsPbBr_3$ device before (black) and after (red) operating under 1 sun illumination at an applied potential of 1.23 V (vs RHE), in 0.1M KNO_3, pH 2.5. b) Photographs of the front and back of the device after operating under 1 sun illumination at an applied potential of 1.23 V (vs RHE), in 0.1M KNO_3, pH 2.5 for 23 h.

From Figure 8 it is clear that the PSC has been degraded severely. The photographs show that the $CsPbBr_3$ layer within the O-ring has been degraded to $PbBr_2$, evidenced by the loss of the yellow colour in the middle of the device, in the photoanode active area. The PCE of the device has fallen from 8.12 % to 0.00 % after operation. The fact that the yellow colour remains surrounding the O-ring area, shows that water ingress has occurred through the GS within the active area of the electrode. The GS active area has turned black and textured, and this area looks similar to the GS after the electrochemical oxidation treatment discussed in Chapter 6. This may suggest that throughout the measurement the GS has also been oxidised and this has weakened the structure of the carbon and formed pores within the GS. However, this is not a direct effect of either the applied potential or the light, as minimal currents are observed both under illumination without water, and in the dark in aqueous conditions. The oxidation could occur as a result of the oxygen that is formed at the surface of the photoanode, which can encourage oxidation reactions to occur at the surface of the graphite electrode, causing corrosion. [21] As a result, it was theorised that a lower applied potential may slow some of the oxidation effects and allow the photoanode to function for longer. Thus, a lower external bias of 1.06 V (vs RHE) was chosen as it is after the onset potential, as shown above in Figure 5, but a photocurrent greater than 1 mA is still achievable. The applied voltage is also less than the theoretical required voltage for water oxidation, meaning that a greater STH efficiency can be obtained. The resulting chronoamperometric trace is shown in Figure 9.

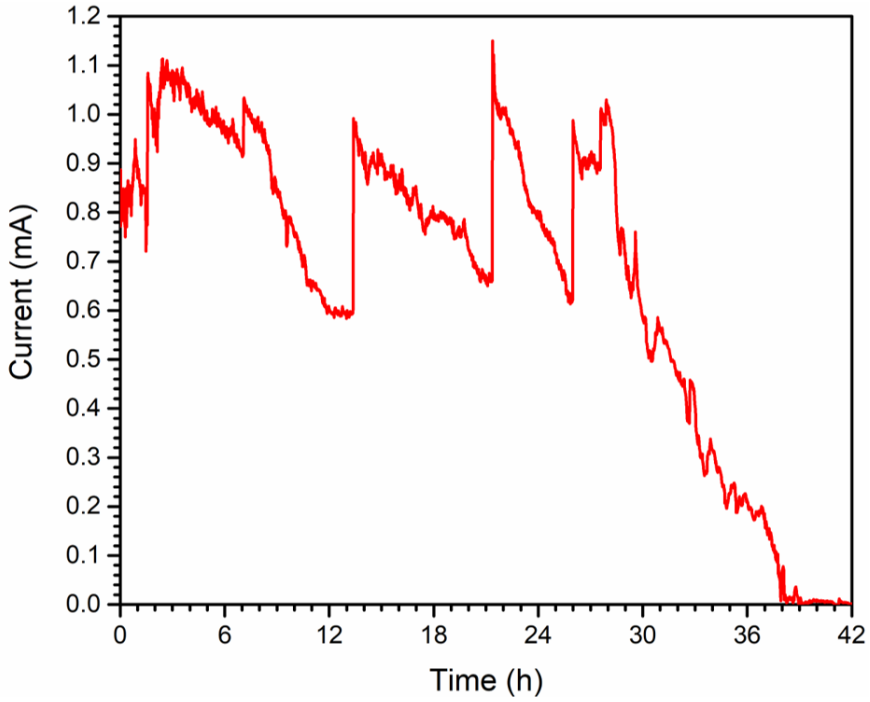

Figure 9: Chronoamperometric trace of TiO2/CsPbBr3/m-c/GS/ WOC recorded at an applied potential of 1.06 V (vs RHE), in 0.1M KNO_3, pH 2.5, under continuous 1 sun illumination.

Figure 9 shows that reducing the external applied potential did briefly extend the lifetime of the TiO_2/$CsPbBr_3$/Carbon/GS-WOC photoanode from ≈ 23 to 29 h. However, this is still below the operation lifetime achieved by Poli *et al*. [4] The sequential drops in the photocurrent can be attributed to a build of gas bubbles on the electrodes, thus causing a drop in photocurrent until they are removed. After the failure of the photoanode the device was inspected again. The results are shown in Figure 10.

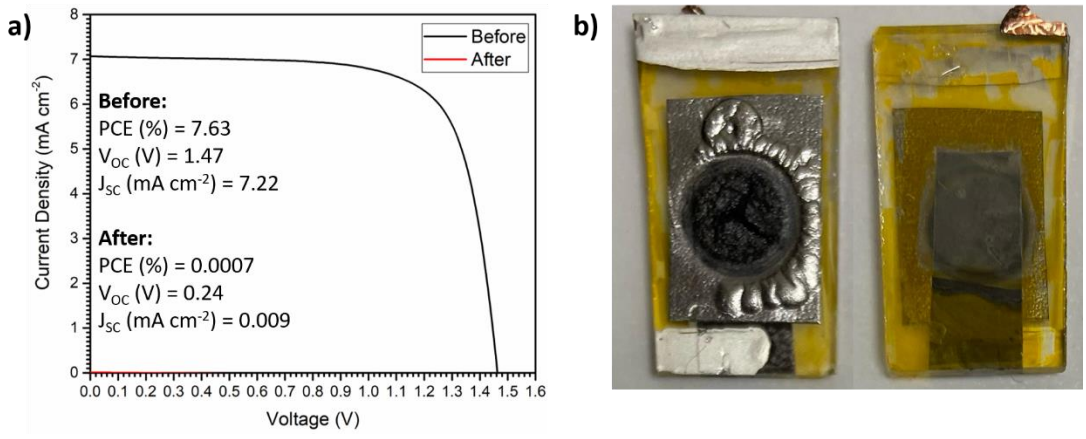

Figure 10: a) J-V curves of the $CsPbBr_3$ device before (black) and after (red) operating under 1 sun illumination at an applied potential of 1.06 V (vs RHE), in 0.1M KNO_3, pH 2.5. b) Photographs of the front and back of the device after operating under 1 sun illumination at an applied potential of 1.06 V (vs RHE), in 0.1M KNO_3, pH 2.5 for 23 h.

Again, it is clear from Figure 10, that the device was degraded after 29 h of continuous operation. Once more, the $CsPbBr_3$ within the encapsulated area has been degraded to $PbBr_2$ due to the ingress of water into the device. The GS within the active area of the electrode also turned black and textured again.

Poli *et al.* reported similar symptoms after the use of a thinner GS, with a thickness of 25 µm, however, the lifetime of the device was extended by increasing the thickness of the GS to 70 µm. As a result, in an attempt to slow the GS oxidation and prolong the lifetime of the device in water, the use of a thicker (160 µm) GSWOC was investigated. It was theorised that a thicker the GS would mean that there were more layers of carbon to oxidise and corrode before the $CsPbBr_3$ underneath was reached. To observe the behaviour of the photoanode with the 160 µm thickness GS-WOC, a stepped voltage chronoamperometry measurement was carried out, both in the dark and under 1 sun illumination. Figure 11 shows the stepped chronoamperometric trace of a TiO_2/$CsPbBr_3$/Carbon/GS-WOC photoanode, using the 160 µm thickness GS instead of the 70 µm.

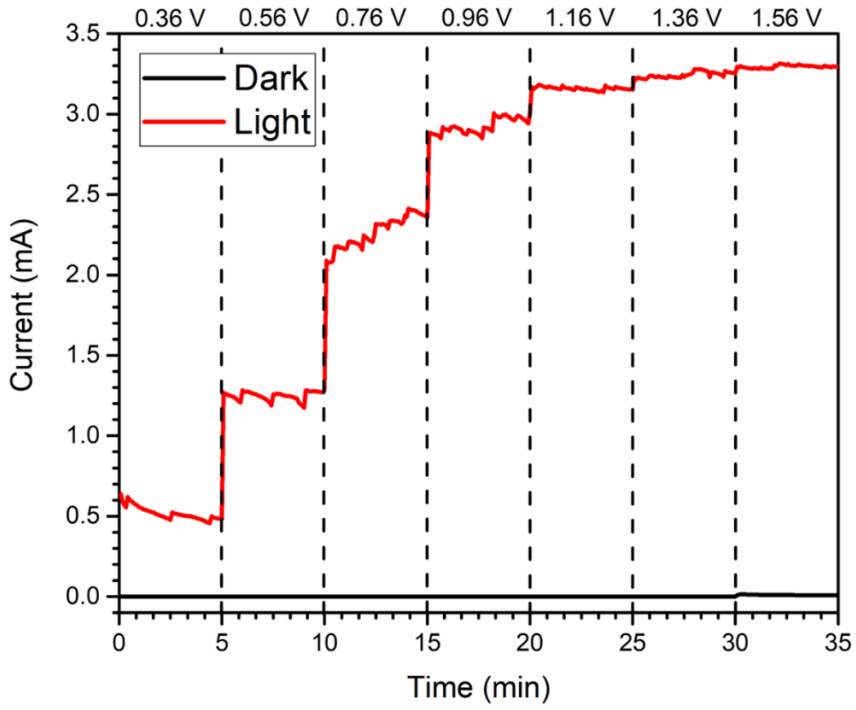

Figure 11: Chronoamperometry measurements of the TiO_2/$CsPbBr_3$/Carbon/GSWOC, using the 160 µm thickness GS, based photoanode in 0.1 M KNO_3, pH 2.5, in the dark (black) and under 1 sun illumination (red). The voltage was stepped up 0.2 V every 5 min from 0.36 V – 1.56 V (vs RHE).

Figure 11 shows that larger currents can be produced by the photoanode with the 160 µm thickness GSWOC at lower potentials, compared to the 70 µm thickness GSWOC in Figure 5. The photoanode with the 70 µm thickness GS-WOC does not exceed a photocurrent of 1 mA (2.3 mA cm^{-2}) until an external potential of 1.16 V has been applied, whereas the

photoanode with the 160 µm thickness GS-WOC achieves a photocurrent of 1 mA (2.3 mA cm^{-2}) with an external applied bias of only 0.56 V. However, the dark current is still low and stays below 1 µA until the applied potential reaches 1.56 V, at which point the current spikes to 15 µA. This demonstrates that the light is having a large effect on current. To investigate whether the increased thickness of the GS-WOC can improve the lifetime of the photoanode, a chronoamperometry measurement was run at an applied potential of both 1.23 V and 1.06 V. Figure 12 shows the results.

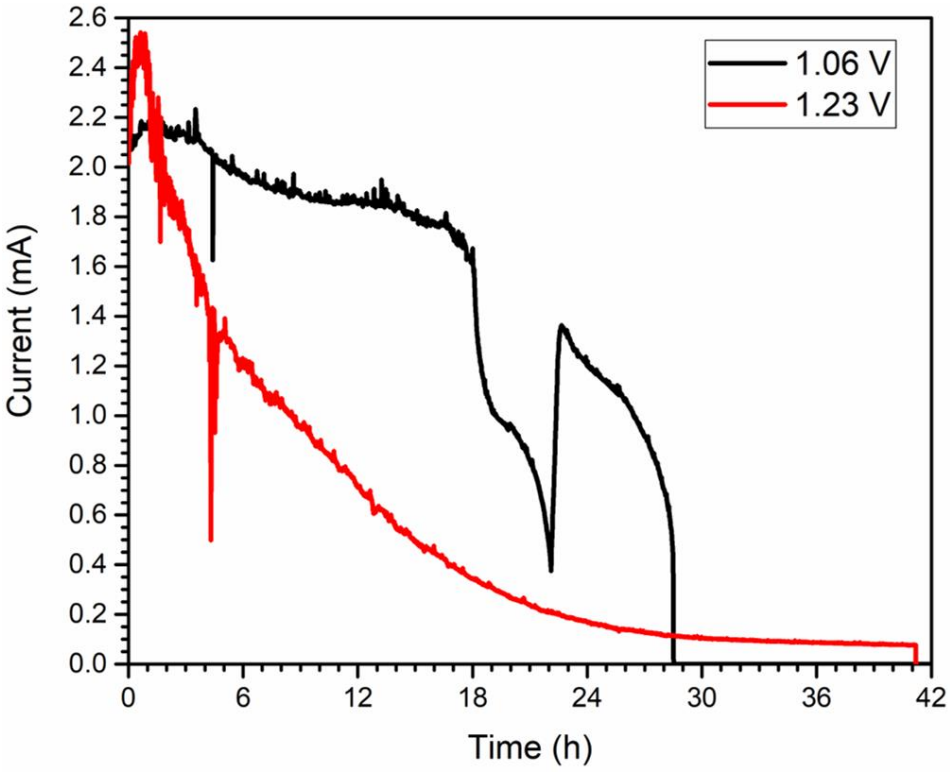

Figure 12: Chronoamperometric trace of TiO_2/$CsPbBr_3$/m-c/GS/ WOC recorded at an applied potential of 1.06 V (black) and an applied potential of 1.23 V (red) (vs RHE), in 0.1M KNO_3, pH 2.5, under continuous 1 sun illumination.

Figure 12 shows that despite the increased GS-WOC thickness, the lifetime of the photoanode was not increased. When the applied potential was 1.23 V, the photocurrent peaked at ≈ 2.5 mA (5.7 mA cm^{-2}), within the first two hours of the measurement, before declining slowly. The photocurrent reached below 0.2 mA (0.5 mA cm^{-2}) at 26 h. When the applied potential was 1.06 V (vs RHE), the device failed at 28 h. The maximum lifetime of the photoanode using the 70 µm thickness GS-WOC was 29 h, thus the use of the thicker GS was not beneficial for extending the lifetime of the photoanodes. Figure 13 shows the photoanode (with the 1.06 V (vs RHE) applied potential) after the measurement.

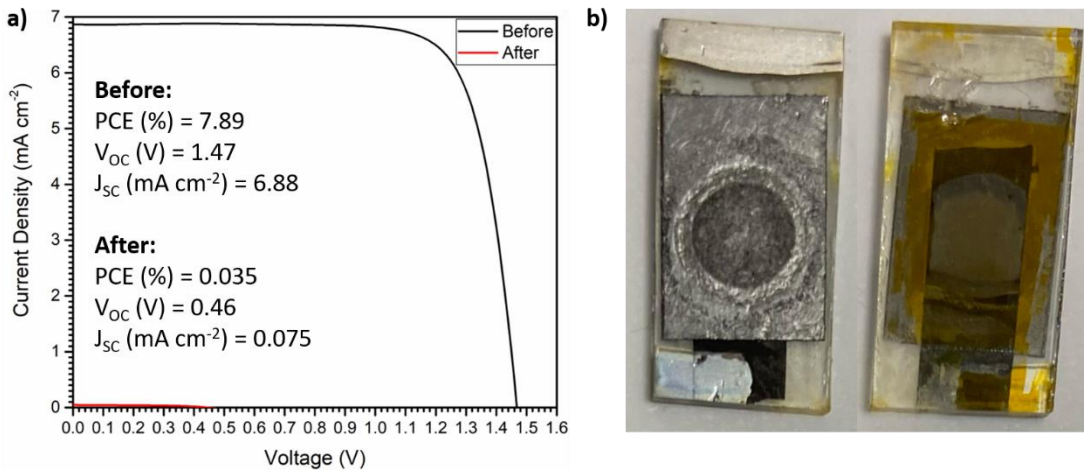

Figure 13: a) J-V curves of the $CsPbBr_3$ device before (black) and after (red) operating under 1 sun illumination at an applied potential of 1.06 V (vs RHE), in 0.1M KNO_3, pH 2.5. b) Photographs of the front and back of the device with the 160 µm GS-WOC after operating under 1 sun illumination at an applied potential of 1.06 V (vs RHE), in 0.1M KNO_3, pH 2.5 for 28 h.

Once more it is clear, from Figure 13, that the photoanode was degraded after operation for 28 h. The GS in the active area of the electrode is black and textured again. The GS, around the outside of the O-ring in all three photographs of the devices (Figures 13, 10 and 8) shows signs of bubbling and delamination away from the PSC below. It was thought that the due to the small active area of the electrode, and the high photovoltages produced, a lot of charge was passing through a small area. This was placing stress on the surrounding GS, causing it to delaminate. There are also reports that intercalation of anions (such as NO_3^-) into graphene can also aid the delamination from the surface below. [22] The proposed solution was to ensure the O-ring was almost flush with the surface of the Teflon block. Then clamping the components together more tightly meant that the Teflon block was pressing against the surface of the GS, thus, allowing no space for the GS to delaminate from the PSC beneath.

A TiO_2/$CsPbBr_3$/Carbon/GSWOC, with the standard 70 µm thickness GS was tested to see whether the hypothesis was correct. An external bias of 1.06 V (vs RHE) was applied to the photoanode. Figure 14 shows the long-term measurement.

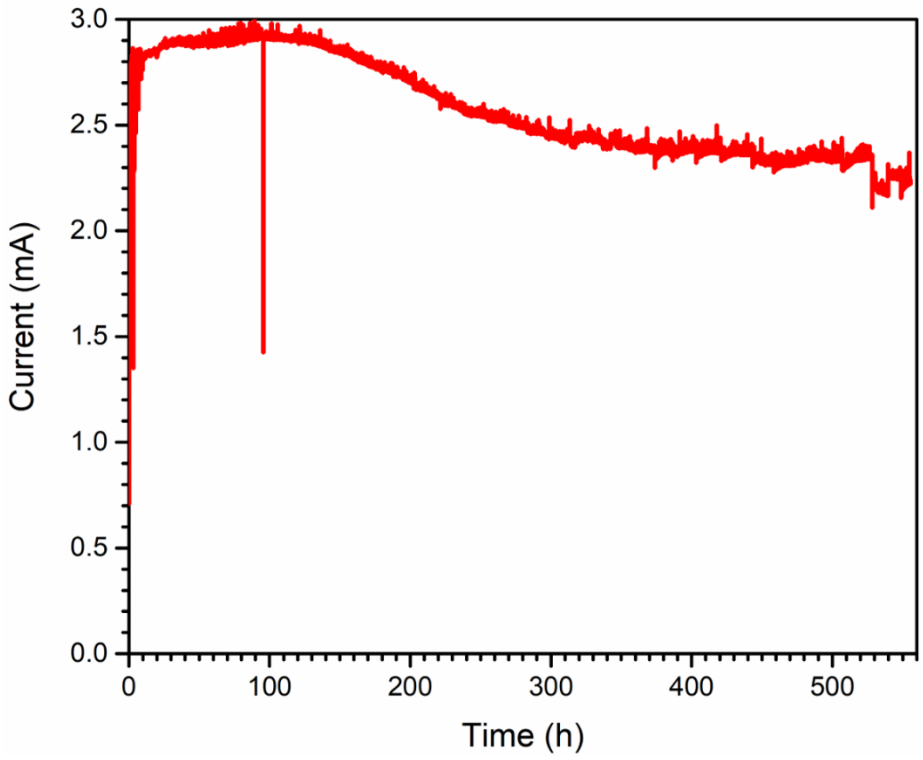

Figure 14: Chronoamperometric trace of TiO2/CsPbBr3/m-c/GSWOC (70 µm thickness GS) recorded at an applied potential of 1.06 V (vs RHE), in 0.1M KNO_3, pH 2.5, under continuous 1 sun illumination.

As a result of the changes, Figure 14 shows that the photoanode was able to produce currents above 2 mA for an impressive 555 h. This equates to just over 23 days of continuous water oxidation. After this time the computer software was unable to record anymore data, yet the device remained stable under operating conditions for an additional 12 days before it was removed (see Appendix 3.2). This represents the longest lifetime of a lead halide perovskite based photoelectrode in direct contact with an aqueous solution ever published. The increase in the photocurrent from ≈ 0.7 mA to ≈ 2.9 mA is likely a result of the light soaking effect on the $CsPbBr_3$ device, whereby after a period of sustained illumination, improvements to the PSC are observed. [4, 23] However, whilst the current peaked at ≈ 2.9 mA at 100 h, the current remained stable above 2 mA for the remainder of the duration of the measurement. When the area of the electrode is considered, this equates to a sustained current above 4.6 mA cm^{-2}. This demonstrates that the new and improved $CsPbBr_3$ encapsulation technique is promising for future use of lead halide perovskites for the generation of solar fuels such as hydrogen gas.

After 35 days under operating conditions, the photoanode was removed from its encapsulation and the planar carbon $CsPbBr_3$ device was examined. Figure 15 shows the photoanode after 840 h of operation under 1 sun illumination with an applied bias of 1.06 V (vs RHE).

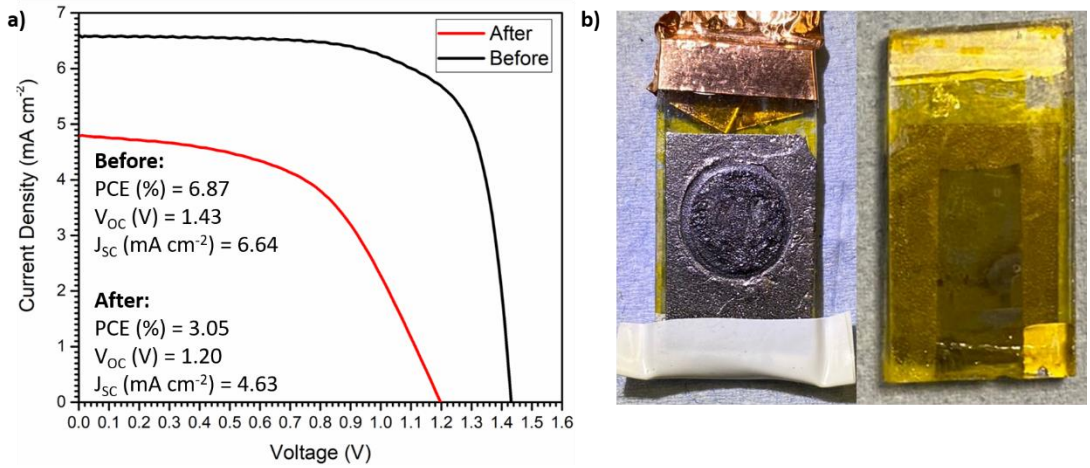

Figure 15: a) J-V curves of the $CsPbBr_3$ device before (black) and after (red) operating under 1 sun illumination at an applied potential of 1.06 V (vs RHE), in 0.1M KNO_3, pH 2.5. b) Photographs of the front and back of the device with the 160 µm GS-WOC after operating under 1 sun illumination at an applied potential of 1.06 V (vs RHE), in 0.1M KNO_3, pH 2.5 for 840 h.

Figure 15 shows that after 840 h under operation conditions, the $CsPbBr_3$ device performance has decreased, however, it is still functioning. The PCE value of the device has halved but the V_{OC} of the device has been reduced to 1.2 V. The photographs show minimal $CsPbBr_3$ degradation within the active area. However, the photographs suggest that the GS may have been beginning to fail and very small amounts of water may be able to reach the PSC as there is a small patch of $CsPbBr_3$ that has been discoloured. The GS within the electrode area has also become textured and flaky, suggesting that some oxidation of the GS has occurred. This implies that the photoanode was reaching the end of its lifetime.

Whilst measurements to confirm that oxygen was being produced by the photoanodes are required, previous research carried out by Poli *et al.* found that the Faradaic efficiency of the TiO_2/$CsPbBr_3$/Carbon/GSWOC photoanodes was 80 %. [4] The some of the additional current observed could be a result of the GS oxidation that occurs due to the presence of the O_2 gas produced. However, further experiments are required to confirm this, as discussed in more detail within section 7.4.

7.3. Water Oxidation using GS with Surface modification

After demonstrating that the improved encapsulation of the TiO_2/$CsPbBr_3$/Carbon/GSWOC photoanodes can increase the lifetime of the device, in aqueous conditions, for 18 times longer than the previously reported encapsulation method, it was investigated whether there was any benefit to modifying the surface of the GSWOC (as discussed in Chapter 6). It was predicted that modification of the GSWOC may lead to increased and more stable photocurrents and

may even lead to improved lifetimes of the devices. The investigated surface treatments include, exposing to UV/ozone for two hours before the WOC was applied to the surface; electrochemical oxidation of the GS with KH_2PO_4 and electrochemical oxidation of the GS with KH_2PO_4 followed by UV/ozone exposure. The resulting stepped chronoamperometry measurements of the resulting photoanodes are displayed in Figure 16.

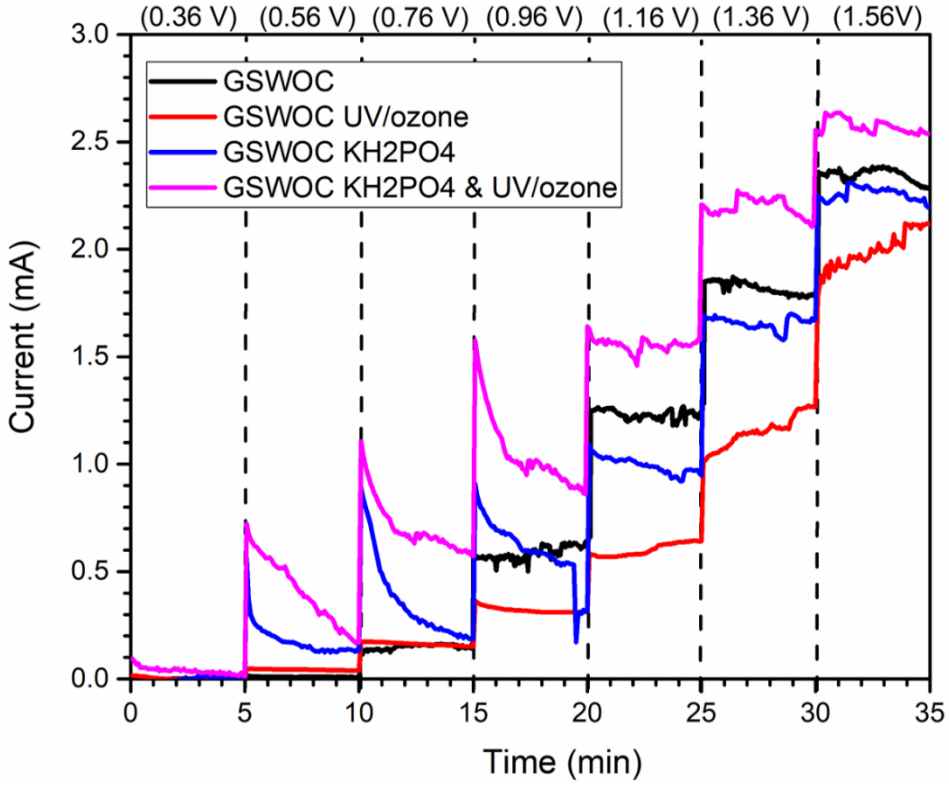

Figure 16: Chronoamperometry measurements of the TiO_2/$CsPbBr_3$/Carbon/GSWOC, using the 70 µm thickness GS, based photoanode in 0.1 M KNO_3, pH 2.5, under 1 sun illumination. The voltage was stepped up 0.2 V every 5 min from 0.36 V – 1.56 V (vs RHE). The photoanode using the untreated GSWOC is shown in black, the photoanode using the UV/ozone treated GSWOC is shown in red, the photoanode using KH_2PO_4 treated GSWOC is shown in blue and the photoanode using the KH_2PO_4 and UV/ozone GSWOC is shown in pink.

Figure 16 displays the stepped voltage chronoamperometric traces of the TiO_2|$CsPbBr_3$|Carbon|GSWOC photoanodes after three different surface treatment methods have been performed on the GS, to allow for comparison between the treatments. The UV/ozone treated GSWOC did not yield any obvious benefits when compared to the untreated GSWOC. It was anticipated that the UV/ozone treated GSWOC may have led to an earlier onset of the water oxidation photocurrent, however this is not apparent, as was further confirmed by the chopped light linear sweep measurements (Appendix 3.3). The two KH_2PO_4 electrochemically treated GSWOC samples showed unusual behaviour. At low applied potentials, the current spiked, before decaying to a more stable photocurrent value. This

behaviour was not seen at potentials above 1.16 V (vs RHE). It is possible that the observed behaviour was a result of the increased capacitance of the GS after surface treatment, as discussed in Chapter 6. Whilst it is difficult to directly compare the photocurrent values of the photoanodes, due to the differences in both $CsPbBr_3$ device performances and variation in the GS surface, it appears as though the combined K_2HPO_4 and UV/ozone treated GSWOC may lead to increased photocurrent values, particularly at lower applied potentials. To further evaluate the properties of the TiO_2/$CsPbBr_3$/Carbon/GSWOC photoanodes with surface modified GSWOC, longer measurements of the photocurrent were taken at an external applied bias of 1.23 V (vs RHE). The chronoamperometric traces at an applied potential of 1.23 V are shown in Figure 17.

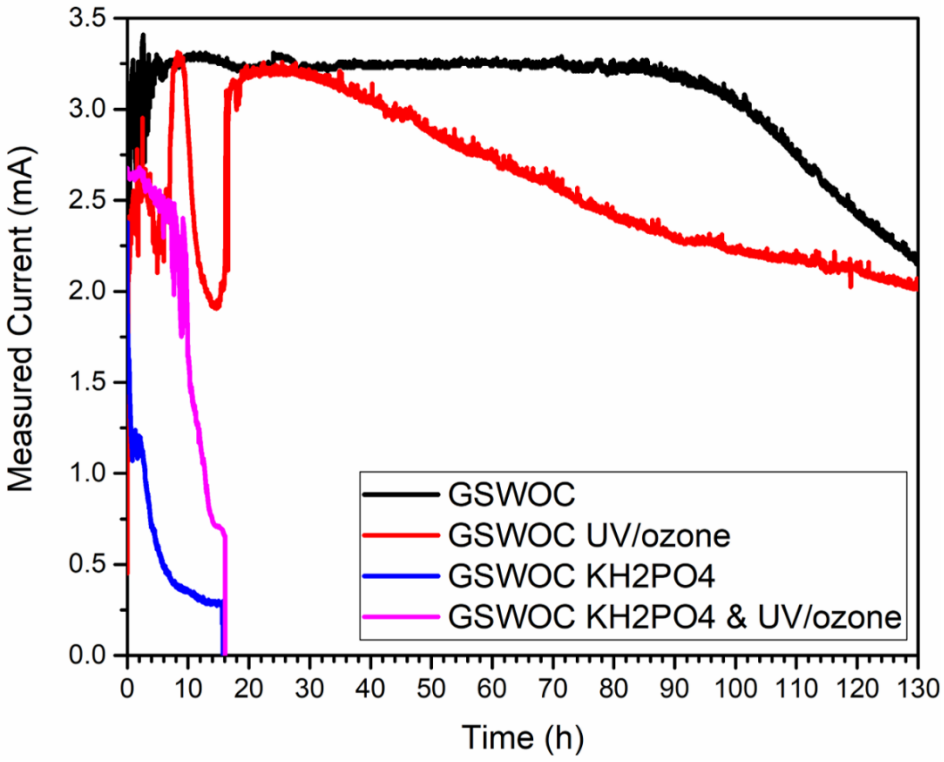

Figure 17: Chronoamperometric trace of TiO2/CsPbBr3/m-c/GSWOC (70 µm thickness GS) recorded at an applied potential of 1.23 V (vs RHE), in 0.1M KNO_3, pH 2.5, under continuous 1 sun illumination. The photoanode using the untreated GSWOC is shown in black, the photoanode using the UV/ozone treated GSWOC is shown in red, the photoanode using KH_2PO_4 treated GSWOC is shown in blue and the photoanode using the KH_2PO_4 and UV/ozone GSWOC is shown in pink.

It is clear from Figure 17, that the modification of the GS (discussed in Chapter 6), used for encapsulated TiO_2/$CsPbBr_3$/Carbon/GSWOC photoanodes, is not beneficial for either prolonging the lifetime of the devices or for increasing the photocurrent. The device using the standard GSWOC sustains the highest current above, above 3 mA (6.8 mA cm^{-2}), for 100 h, which is the longest amount of time out of any of the tested photoanodes. The short lifetime of the two GS samples, electrochemically oxidised with KH_2PO_4, shows that the pre-oxidation

of the GS weakens the structure of the GS, making it more porous and more hydrophilic. This again, may also further suggest that the blackening of the GS that is observed is a result of the GS being oxidised throughout the duration of the measurements.

7.3.1. GS Without a Self-Adhesive Layer

The GSWOC used in this chapter thus far has been applied to the $CsPbBr_3$ device using a self-adhesive layer. However, GS surface modification methods, such as those with metal oxides applied to the surface, cannot be used on the GS with the self-adhesive layer, due to the high temperatures required for deposition. As a result, methods to attach the GS without any adhesive were investigated. A GS with no adhesive layer is also commercially available. It was also theorised that the removal of the adhesive layer may increase the photocurrent as a result of the removal of any resistance arising from the glue.

To fabricate the TiO_2/$CsPbBr_3$/Carbon/GS photoanodes without the self-adhesive layer, the conductive carbon paste that was used to make the planar carbon $CsPbBr_3$ PSCs, was used. The carbon paste was first applied on top of the $CsPbBr_3$ layer before being dried on a hot plate at 100 °C for 5 min. A second thin layer of carbon paste was then spread on the back surface of GS before that was placed on top of the carbon contact of the $CsPbBr_3$ cell. The GS was pressed on to the device using a microscope slide, before being annealed in the oven at 360 °C. A small weight was placed on top of the GS during the annealing step to keep it in place. Figure 18 shows the JV characteristics of the $CsPbBr_3$ devices Vs the $CsPbBr_3$ devices with the non-adhesive GS.

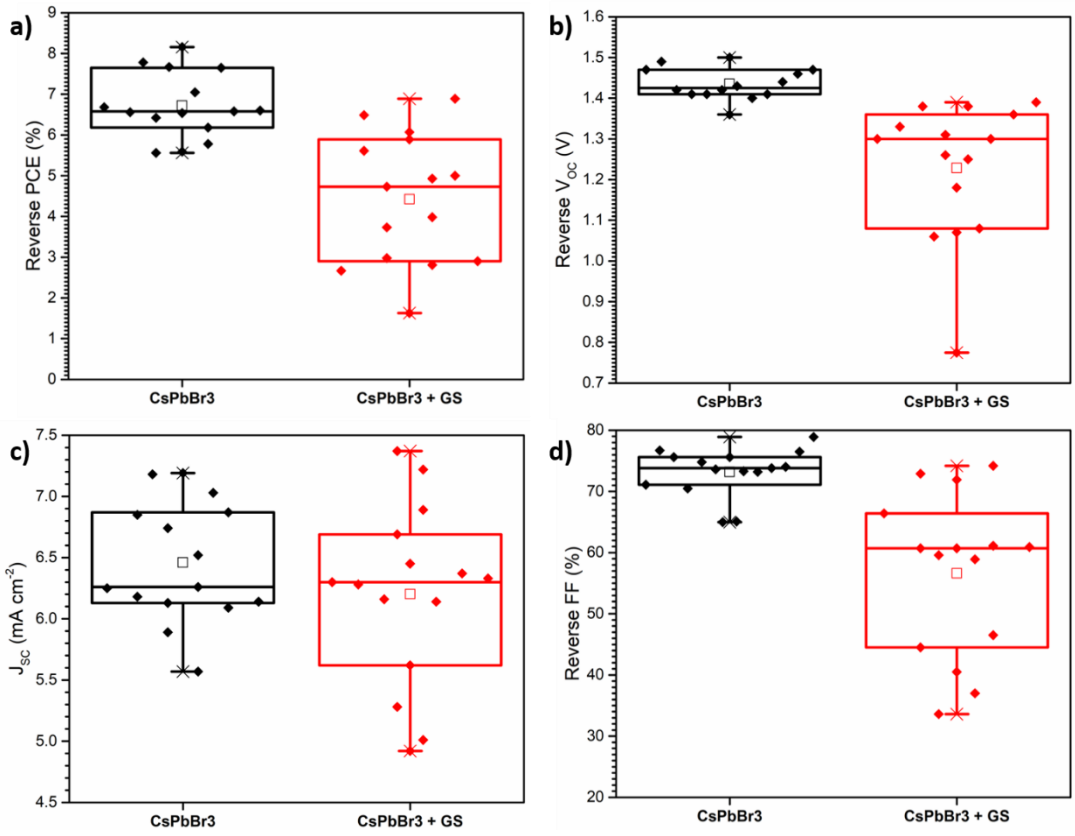

Figure 18: Box plots showing the performance of the planar carbon $CsPbBr_3$ devices, with and without the non-adhesive GS.

The data in Figure 18 shows that whilst the devices with the non-adhesive GS do still work the performance is often severely reduced. There is large in variation in the PCE and V_{OC} values that can be achieved in the devices where the GS has been stuck onto the surface using the carbon paste. This is likely to be a result of defects within the carbon layer causes by the pressing on of the GS. However, V_{OC} values above 1.23 V can still be achieved and hence are acceptable for use, thus, it was decided to test these devices as photoanodes.

After the annealing step at 360 °C, the carbon becomes soft because of the solvent and binder removal. As a result, encapsulating the photoanode within the Teflon block cell, without disturbing the placement of the GS, was difficult. It was found that a small amount of Kapton tape, placed around the edges of the GS, was sufficient to hold the GS in place. Figure 19 shows the stepped voltage chronoamperometric trace of a TiO_2/$CsPbBr_3$/Carbon/GS photoanode where the GS has been stuck onto the device without the self-adhesive layer.

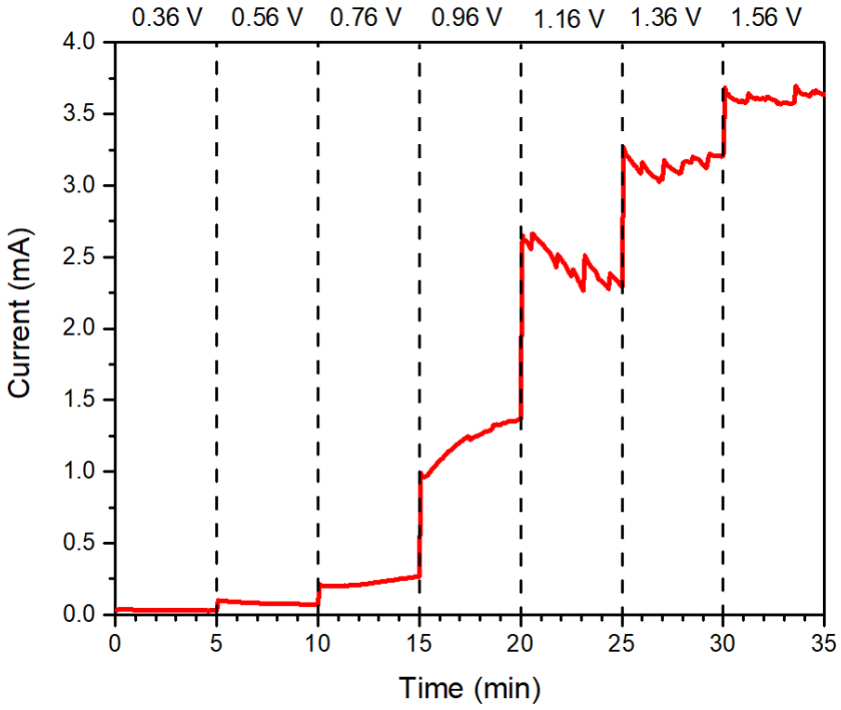

Figure 19: Chronoamperometry measurements of the TiO_2/$CsPbBr_3$/Carbon/GS, using the 70 µm thickness GS without the self-adhesive layer, based photoanode in 0.1 M KNO_3, pH 2.5, under 1 sun illumination. The voltage was stepped up 0.2 V every 5 min from 0.36 V – 1.56 V (vs RHE).

Figure 19 shows that the device without the self –adhesive can function well as a photoanode. It also may suggest that without the self-adhesive glue present, larger photocurrent values can be achieved. For example, at an applied bias of 1.16 V (vs RHE), the photoanode using self-adhesive GSWOC was producing a photocurrent of ≈ 1.2 mA (Figure 5), but the photoanode using the GS without the self-adhesive layer was able to double this and reach a photocurrent of ≈ 2.5 mA. This could be due to the fact that the conductive carbon paste may be more conductive than the adhesive.

However, applying the WOC to the GS surface was now a challenge. The WOC must be applied after the annealing step, thus it must be applied whilst the GS is stuck to the $CsPbBr_3$ device. Consequently, the method of floating the GS in the aqueous het-WOC solution is no longer a viable option. Attempts were made to apply the WOC using a second Teflon cell and clamp system, however, due to various leaks in the experimental set-up, none of the attempts were successful.

7.4. Conclusions and Further Work

The aim of this chapter was to tie together the work done in the previous chapters to showcase new and improved $CsPbBr_3$ based photoanodes for water splitting. This work has improved

upon the work done previously by Poli *et. al.* [4] and lead to improvements in the lifetime of the devices. The Photoanodes can now operate for ≈ 18 times longer in aqueous conditions, than those in the previous work.

Overall, the encapsulation of TiO_2/$CsPbBr_2$/Carbon/GSWOC based photoanodes was improved by removing the need to seal the device with epoxy resin, which was a previous weak point. Instead, the device was made watertight using a Teflon based cell with O-rings. When tightened correctly, this prevents water ingress into the PSC device and hence prevented early failure of the photoanode due to degradation of the perovskite absorber film. As a result, the lifetime of the device was extended to over 555 h, which is the longest reported lifetime of a PSC based photoelectrode that is in direct contact with an aqueous solution. This paves the way for future use of PSCs in the production of solar fuels, through either water oxidation or carbon dioxide reduction.

This work should be continued to measure the oxygen production and calculate the resulting Faradaic efficiency of these devices. Whilst it was calculated to be 82 % at an applied bias of 1.23 V (vs RHE) by Poli *et al.* [4] the PSC devices used in this chapter have higher efficiencies and V_{OC} values and the photoelectrode has a smaller active area. The photocurrent achieved by the TiO_2|$CsPbBr_3$|Carbon|GSWOC photoanodes in this work are also greater than the photocurrents achieved by Poli *et al.* (>4.6 mA cm^{-2} and > 3.0 mA cm^{-2} respectively). The oxygen concentration should also be measured to further ensure that oxygen is being produced at the applied potential of 1.06 V (Vs RHE). However, the current encapsulation technique meant that it was difficult to insert and oxygen electrode into the chamber without damaging the crucial membrane. This measurement could become easier with the use of a differently designed oxygen electrode or a better designed flow system.

Further work could also focus on use of the photoanode without the self-adhesive GS. To ensure that the WOC can be applied to the GS easily, another identical Teflon block, should be made. When the photoanode is clamped in place, the chamber can then be filled with the aqueous het-WOC solution. An identical block would help prevent any leakage of the solution and thus prevent degradation of the perovskite. It would also prevent contamination of the system with residual WOC, which may affect the results. Once these issues have been resolved, the effect of surface modification of the GS surface with metal oxides such as TiO_2 on the photocurrent and lifetime of the photoanode can be investigated. The application of a metal oxides such as TiO_2, onto the surface of the GS, may reduce the surface oxidation of the GS. This would therefore allow the photoanode to function for longer.

7.5. References

1 A. Fujishima and K. Honda, *Nature*, 1972, **238**, 37–38.

2 J. R. Bolton, S. J. Stricklert and J. Connolly, *Nature*, 1985, **316**, 495-500

3 R. Solarska, R. Jurczakowski and J. Augustynski, *Nanoscale*, 2012, **4**, 1553–1556.

4 I. Poli, U. Hintermair, M. Regue, S. Kumar, E. V. Sackville, J. Baker, T. M. Watson, S. Eslava and P. J. Cameron, *Nat. Commun.*, 2019, **10**, 2097.

5 V. Andrei, R. L. Z. Hoye, M. Crespo-Quesada, M. Bajada, S. Ahmad, M. De Volder, R. Friend and E. Reisner, *Adv. Energy Mater.*, 2018, **8**, 1801403.

6 X. Zhang, S. Zhang, X. Cui, W. Zhou, W. Cao, D. Cheng and Y. Sun, *Chem. Asian J.*, 2022, **17**, 668.

7 H. R. Khan, B. Akram, M. Aamir, M. A. Malik, A. A. Tahir, M. A. Choudhary and J. Akhtar, *Sci. Reports 2020 101*, 2020, **10**, 1–10.

8 M. Ni, M. K. H. Leung, D. Y. C. Leung and K. Sumathy, *Renew. Sustain. Energy Rev.*, 2007, **11**, 401–425.

9 J. Knöppel, A. Kormányos, B. Mayerhöfer, A. Hofer, M. Bierling, J. Bachmann, S. Thiele and S. Cherevko, *ACS Phys. Chem. Au*, 2021, **1**, 6–13.

10 J. Zhang, Y. Huang, X. Lu, J. Yang and Y. Tong, *ACS Sustain. Chem. Eng.*, 2021, **9**, 8306–8314.

11 K. Song, H. Hou, C. Gong, F. Gao, D. Zhang, F. Zhi, W. Yang and F. He, *J. Mater. Chem. A*, 2022, **10**, 22561–22570.

12 X. Liu, Y. Wang, X. Cui, M. Zhang, B. Wang, M. Rager, Z. Shu, Y. Yang, Z. Li and Z. Lin, *J. Mater. Chem. A*, 2018, **7**, 165–171.

13 J. Luo, J. H. Im, M. T. Mayer, M. Schreier, M. K. Nazeeruddin, N. G. Park, S. D. Tilley, H. J. Fan and M. Grätzel, *Science.*, 2014, **345**, 1593–1596.

14 C. Moon and B. Shin, *Discov. Mater. 2022 21*, 2022, **2**, 1–16.

15 P. Da, M. Cha, L. Sun, Y. Wu, Z. S. Wang and G. Zheng, *Nano Lett.*, 2015, **15**, 3452–3457.

16 M. Crespo-Quesada, L. M. Pazos-Outón, J. Warnan, M. F. Kuehnel, R. H. Friend and E. Reisner, *Nat. Commun.*, 2016, **7**, 12555.

17 S. Nam, C. T. K. Mai and I. Oh, *ACS Appl. Mater. Interfaces*, 2018, **10**, 14659–14664.

18 R. Tao, Z. Sun, F. Li, W. Fang and L. Xu, *ACS Appl. Energy Mater.*, 2019, **2**, 1969–1976.

19 R. Rhee, T. G. Kim, G. Y. Jang, G. Bae, J. H. Lee, S. Lee, S. Kim, S. Jeon and J. H. Park, *Carbon Energy*, 2022, **5**, 1–10.

20 H. Choi, S. Seo, J. H. Kim, J. H. Lee, S. Kim, G. Piao, H. Park, K. Lee and S. Lee, *J. Mater. Chem. A*, 2021, **9**, 22291–22300.

21 M. X. Qiao, Y. Zhang, L. F. Zhai and M. Sun, *Chem. Eng. J.*, 2018, **344**, 410–418.

22 K. Verguts, J. Coroa, C. Huyghebaert, S. De Gendt and S. Brems, *Nanoscale*, 2018, **10**, 5515–5521.

23 I. Poli, J. Baker, J. Mcgettrick, F. De Rossi, S. Eslava, T. Watson and P. J. Cameron, *J. Mater. Chem. A*, 2018, **6**, 18677–18686.

Chapter 8. Conclusion

The overall aim of the research in this thesis was to find methods to improve TiO_2|$CsPbBr_3$|Carbon|GSWOC photoanodes for water oxidation. Three areas for improvement were identified and investigated.

i) Improvement of the V_{OC} produced by the planar carbon $CsPbBr_3$ devices. This would increase the photovoltage of the photoanodes and reduce the amount of external bias that is required to achieve water oxidation. If the V_{OC} was increased to high enough values, the requirement for an external bias could be removed and unassisted water splitting could proceed.

ii) Increase the loading of the Ir-based WOC that binds to the surface of the GS. This would increase the amount of water oxidation than occurs at the surface of the GS, thus increasing the photocurrent and the amount of O_2 and H_2 gas produced.

iii) Improvement of the device lifetime under operating conditions. The leading PSC based photoelectrodes in the literature fail after 120 hours. Substantially increasing the lifetime of these devices would improve their prospects of being scaled up and used for solar fuel production.

Chapter 4 of this thesis discussed methods for making an improved baseline carbon based $CsPbBr_3$ device with consistent performance. The PCE of the devices were improved from a mean average of 4.09 % to 7.47 % and the V_{OC} increased from a mean average of 1.33 V to 1.46 V. This was achieved through incremental changes to the original baseline devices. The two-step deposition method was altered from a spin coated $PbBr_2$ layer, which was then immersed in a CsBr/MeOH solution to form a $CsPbBr_3$ thin film. Instead, to a method where the $PbBr_2$ layer was spin coated onto the substrate, then the CsBr/MeOH solution was sequentially spin coated onto the $PbBr_2$ layer until a sufficient $CsPbBr_3$ thin film was achieved. A m-TiO_2 layer was also included on top of the c-TiO_2 layer to help aid charge extraction. Furthermore, the $PbBr_2$ annealing temperature was increased from 70 ˚C to 90 ˚C to help increase the $PbBr_2$ surface coverage. These methods helped increase the baseline average PCE of the devices and the IPCE improved from 65 % to 84 % at a wavelength of 530 nm. Overall, this work ensured that there was a consistent standard of $CsPbBr_3$ devices produced, this allowed further research using the planar carbon $CsPbBr_3$ devices to progress and allowed meaningful comparison of modified devices.

Chapter 5 of this thesis aimed to increase the performance, particularly the V_{OC}, of the planar carbon $CsPbBr_3$ devices, by partially substituting the lead (B) site for a range of other metal

ions. In total seven ions were investigated, Zn^{2+}, Cu^{2+}, Ni^{2+}, Co^{2+}, Fe^{2+}, Mn^{2+} and Tb^{3+} and these were substituted at amounts ranging from 0.2 % - 3 %. Ideally, the ions would have caused an increase in the $CsPbBr_3$ grain size, consequently leading to improved JV characteristics. However, this was not the case. Statistical analysis was performed on the data acquired using the different sets of devices and it appeared that substitution either had no significant improvement on the device performance, or in some cases, device performance was worsened. The anticipated increase in V_{OC} values was not observed. Nonetheless, the methods used to fabricate the $CsPb_{1-X}M_XBr_3$ thin films were the same as those described throughout the literature, yet the same conclusions were not achieved. Further investigation into the literature data provided issues surrounding the analysis methods used to prove that the added metal ions were present. For example, the XRD data displayed minute shifts in the 2θ ˚ values and the extent of the shift was not consistent with the size of the ionic radii. The EDX data presented also raised questions around the data acquisition methods used for these measurements in the literature. Furthermore, it was concluded that the grain size analysis methods used both in the literature and in this work were not extensive enough to deduce a definite increase in grain size in the samples containing metal ions.

Chapter 6 explored the interactions between the commercially available GS, used for $CsPbBr_3$ photoanode encapsulation, and the WOC. The goal was to modify the GS surface, increasing the number of oxidised sites, which would in theory lead to an increase in the WOC bound to the surface. A number of surface modification methods were investigated: i) the use of UV/ozone exposure ii) electrochemical oxidation using KH_2PO_4 iii) the combination of electrochemical oxidation using KH_2PO_4 followed by UV/ozone exposure and iv) the deposition of metal oxides such as TiO_2 onto the GS surface. Whilst electrochemical studies of the GS-WOC after surface modification implied that more of the WOC was present, due to increased water oxidation currents, XPS analysis did not confirm this. However, the error for the XPS results was given as approximately 5 %, thus, XPS was possibly not the most suitable method for quantification.

Finally, chapter 7 tied together the research carried out in the previous chapters and used the improved $CsPbBr_3$ planar carbon devices, encapsulated with the GSWOC, as photoanodes for water oxidation. The encapsulation of the device was improved through use of a clamped Teflon chamber/O-ring and flow system to seal the area around the GS, instead of epoxy resin as previously reported. Initially there were issues arising from GS oxidation and GS delamination, however, these were solved by ensuring better contact between the Teflon chamber/O-ring and $CsPbBr_3$ photoanode. Overall, the lifetime of the photoanode under operation conditions was increased from 30 h to over 550 h. To the best of the authors knowledge available, this is the longest operating lifetime of a lead halide perovskite based

photoelectrode in aqueous conditions. However, no suggested benefits to the photoanode, from using surface modification methods (discussed in Chapter 6) for the GS, were discovered. In fact, pre-oxidation of the GS surface drastically shortened the lifetime of the photoanodes under operating conditions.

To further conclude, making high performing $CsPbBr_3$ devices consistently is difficult. Figure 1 demonstrates the PCE of all of the devices made throughout this project. Figure 1 further highlights the sheer number of devices that were made, over a time period of four years, in order to complete this work done in this thesis. A total of 1656 devices were made and measured.

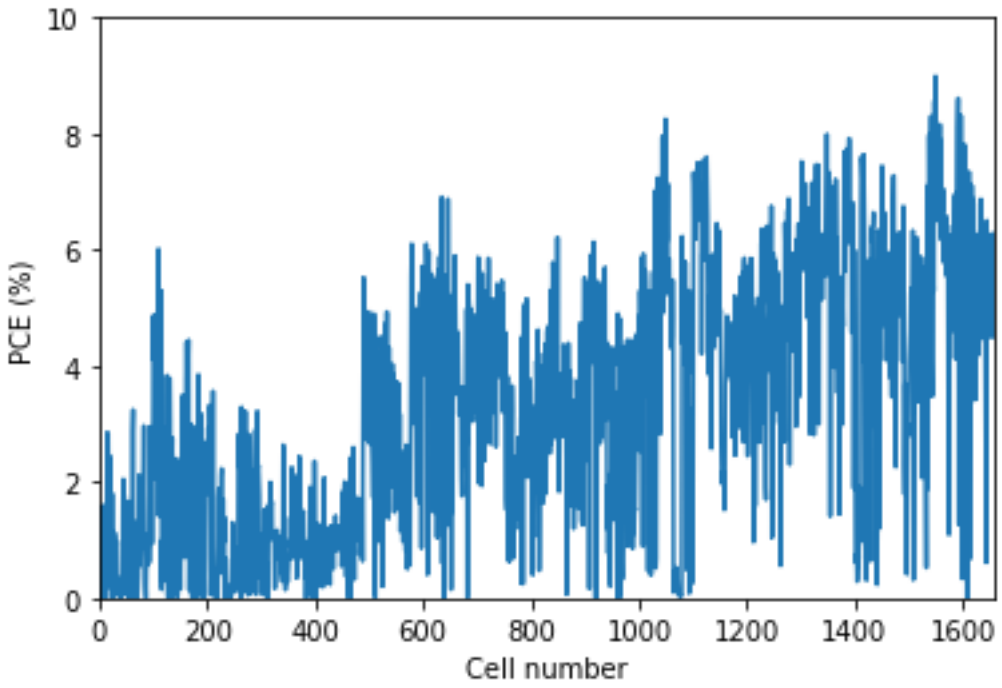

Figure 1: A line chart demonstrating the reverse PCE value of the 1656 $CsPbBr_3$ planar carbon devices that were made throughout the course of this work.

To begin, the processes used to deposit the individual layers in the devices were not yet optimised, thus the PCE values are low and often PCE values above 4 % were not achieved. However, even after optimisation, the PCE values are variable. More regularly high PCE values 6-8 % are achieved but still many devices do not perform well. Overall, this made comparison between sets of devices difficult. A larger number of devices made in the sets would help improve this. However, the more devices that were made, the more efficient the process became. Some deposition techniques required '*a knack*' hence, this meant that as more devices were made, the more the devices improved.

Further work could focus on further investigation into the $CsPbBr_3$ photoanodes. More work is required to understand the processes happening during operation. Several experiments should be completed to characterise the STH efficiency of the devices, in particular oxygen measurements. These should be carried out at a range of applied external biases to determine the point when oxygen production begins. Further long-term studies should be carried out to determine the failure point of the photoanode. Then methods to extend the lifetime, such as the metal oxide deposition, should also be investigated. The use of $CsPbBr_3$ in photocathodes is also further avenue for exploration.

Furthermore, whilst the substitution methods used Chapter 5, were not successful in increasing the V_{OC} of the $CsPbBr_3$ planar carbon device, a range of other methods could be investigated to improve the V_{OC}. Including, different ions for Pb^{2+} substitution and methods of passivating defects in all layers.

In conclusion, the work in this thesis demonstrates that $CsPbBr_3$ based PSCs can be used to produce stable lead halide perovskite-based electrodes for photoelectrochemical fuel generation. The use of lead halide PSCs, in combination with other '*green*' methods of producing energy, offers a potential route towards a future free from dependence on fossil fuels.

Appendix 1.

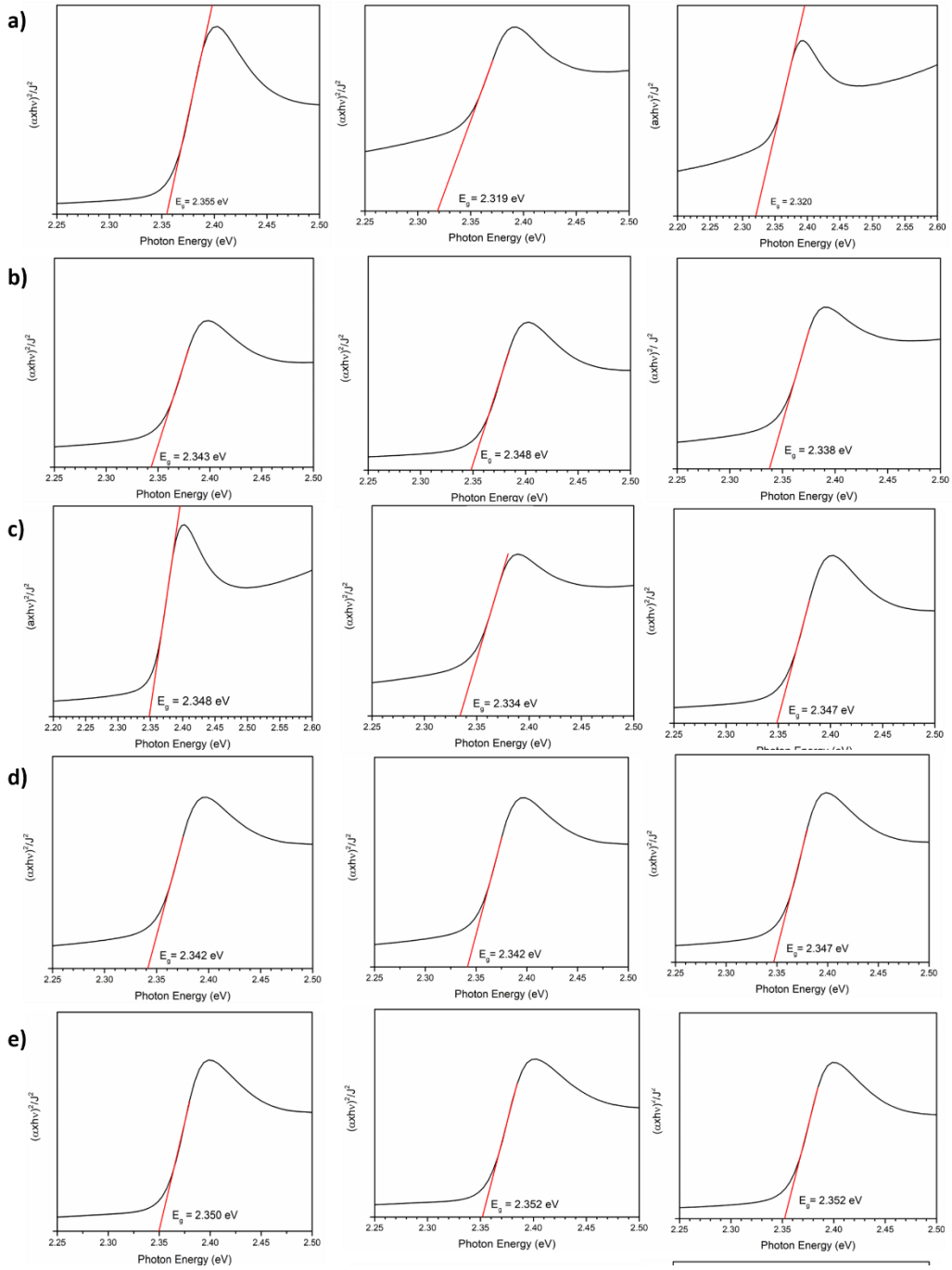
a)
b)
c)
d)
e)
Photon Energy (eV)
E_g = 2.355 eV
E_g = 2.319 eV
E_g = 2.320
E_g = 2.343 eV
E_g = 2.348 eV
E_g = 2.338 eV
E_g = 2.348 eV
E_g = 2.334 eV
E_g = 2.347 eV
E_g = 2.342 eV
E_g = 2.342 eV
E_g = 2.347 eV
E_g = 2.350 eV
E_g = 2.352 eV
E_g = 2.352 eV

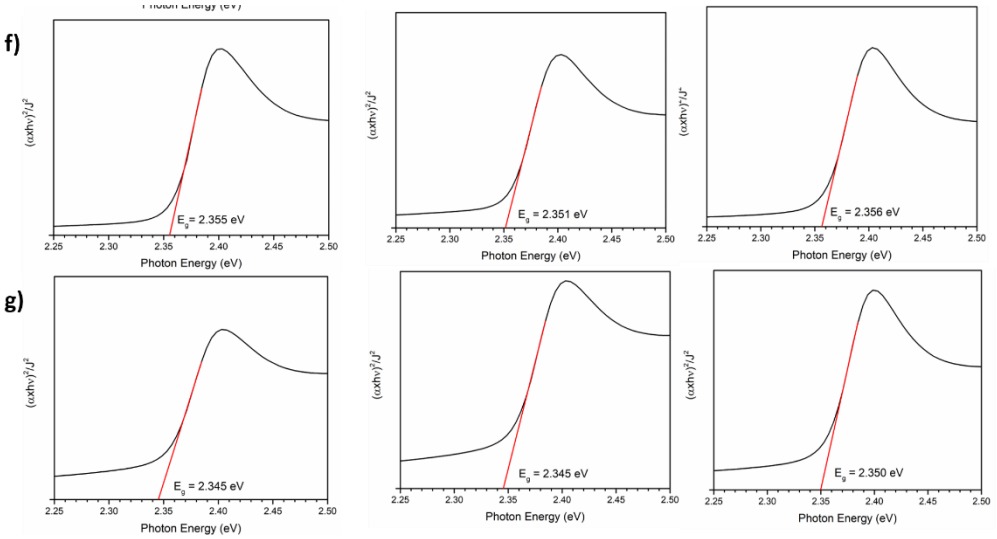

Appendix 1.1: Tauc plots of $CsPb_{1-x}M_xBr_3$ where M = a) Zn^{2+} b) Cu^{2+} c) Ni^{2+} d) Co^{2+} e) Fe^{2+} f) Mn^{2+} g) Tb^{3+}

Appendix 1.2: Table showing the mean band gap values for the $CsPb_{1-x}M_xBr_3$ thin films

$CsPb_{1-x}TM_xBr_3$	**Band Gap (eV)**
$CsPbBr_3$	2.346 ± 0.009
$CsPb_{0.99}Zn_{0.01}Br_3$	2.331 ± 0.02
$CsPb_{0.99}Cu_{0.01}Br_3$	2.343 ± 0.005
$CsPb_{0.99}Ni_{0.01}Br_3$	2.343 ± 0.008
$CsPb_{0.99}Co_{0.01}Br_3$	2.346 ± 0.002
$CsPb_{0.99}Fe_{0.01}Br_3$	2.351 ± 0.001
$CsPb_{0.99}Mn_{0.01}Br_3$	2.352 ± 0.004
$CsPb_{0.97}Tb_{0.03}Br_3$	2.347 ± 0.003

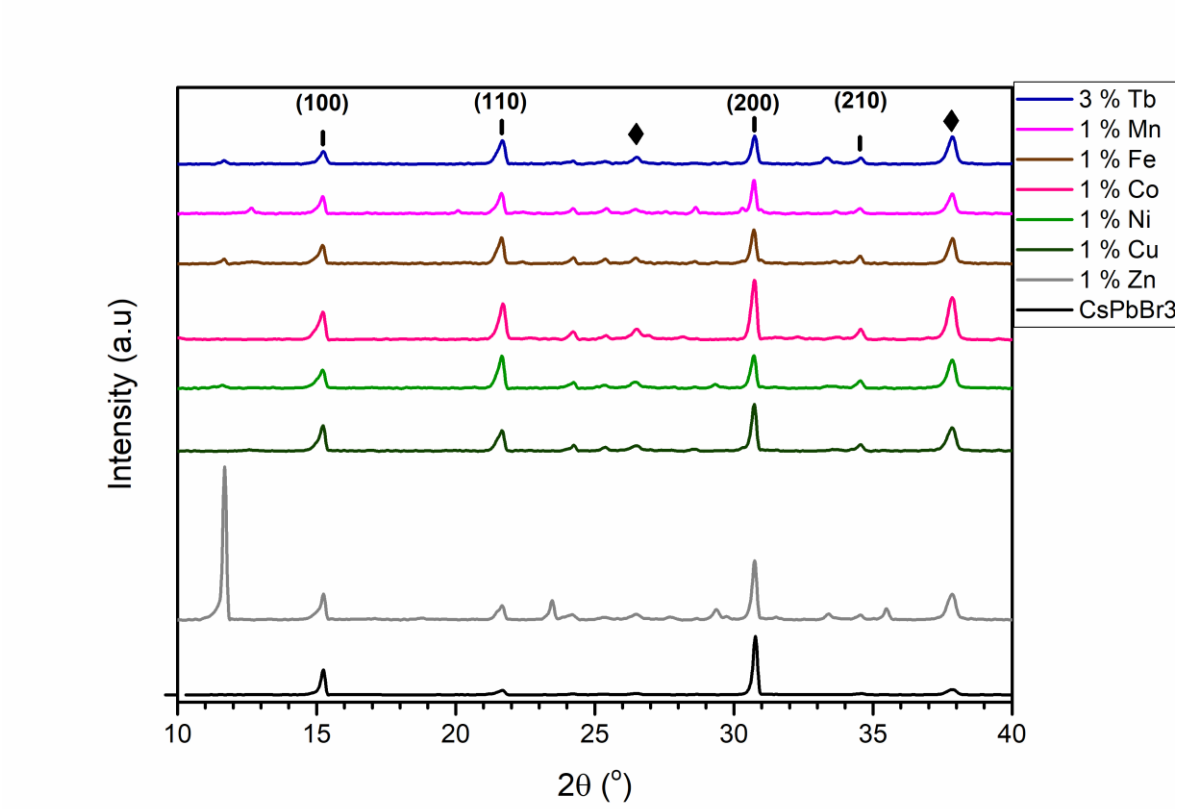

Appendix 1.3: XRD patterns of the $CsPb_{1-x}M_xBr_3$ thin films on FTO. First attempt with the CsBr process repeated only 7 times. The expected $CsPbBr_3$ peaks are indicated by the black dashes, the FTO peaks are indicated by the black diamonds. The XRD patterns have been normalised to the FTO peaks.

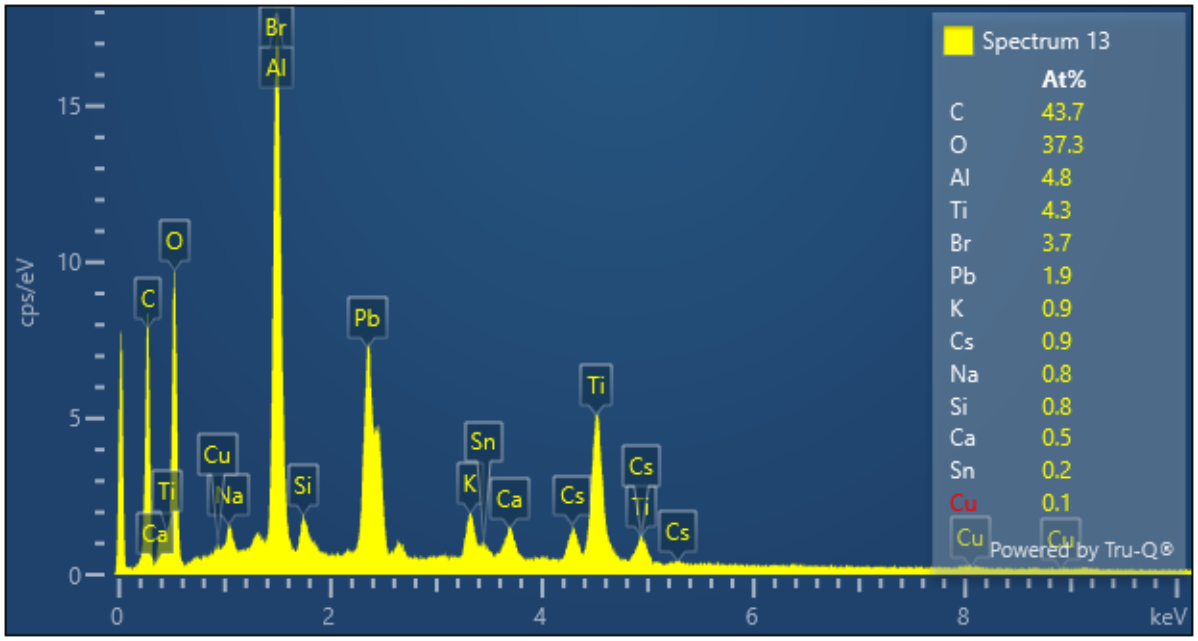

Appendix 1.4: EDX spectrum of the $CsPb_{0.99}Zn_{0.01}Br_3$ thin film cross section.

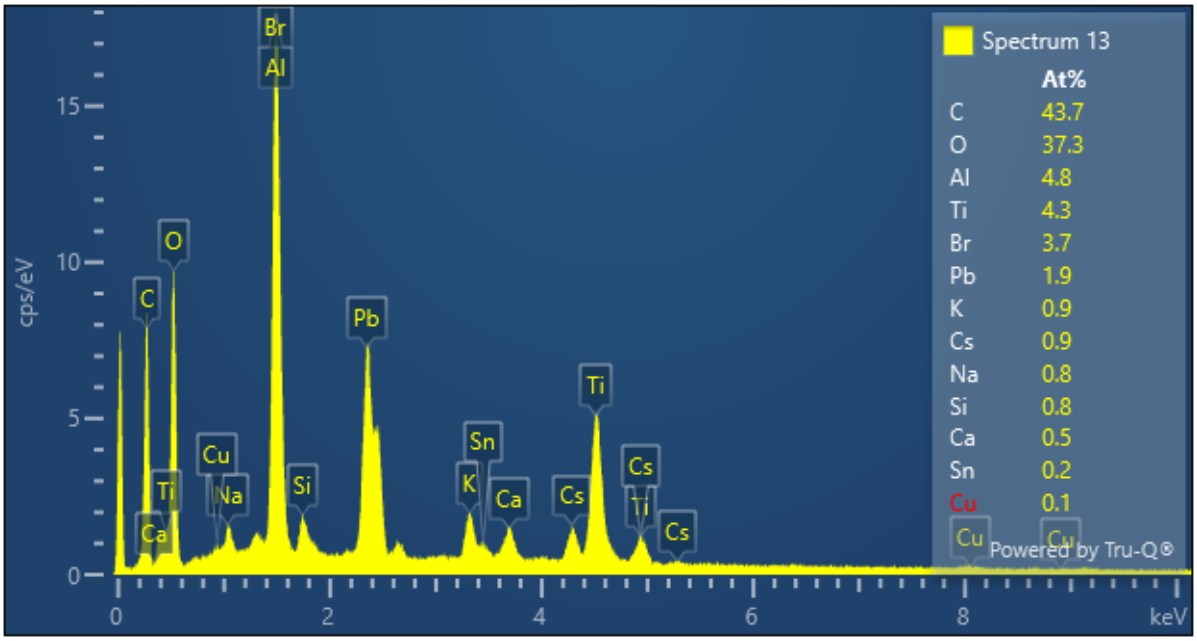

Appendix 1.5: EDX spectrum of the $CsPb_{0.99}Cu_{0.01}Br_3$ thin film cross section.

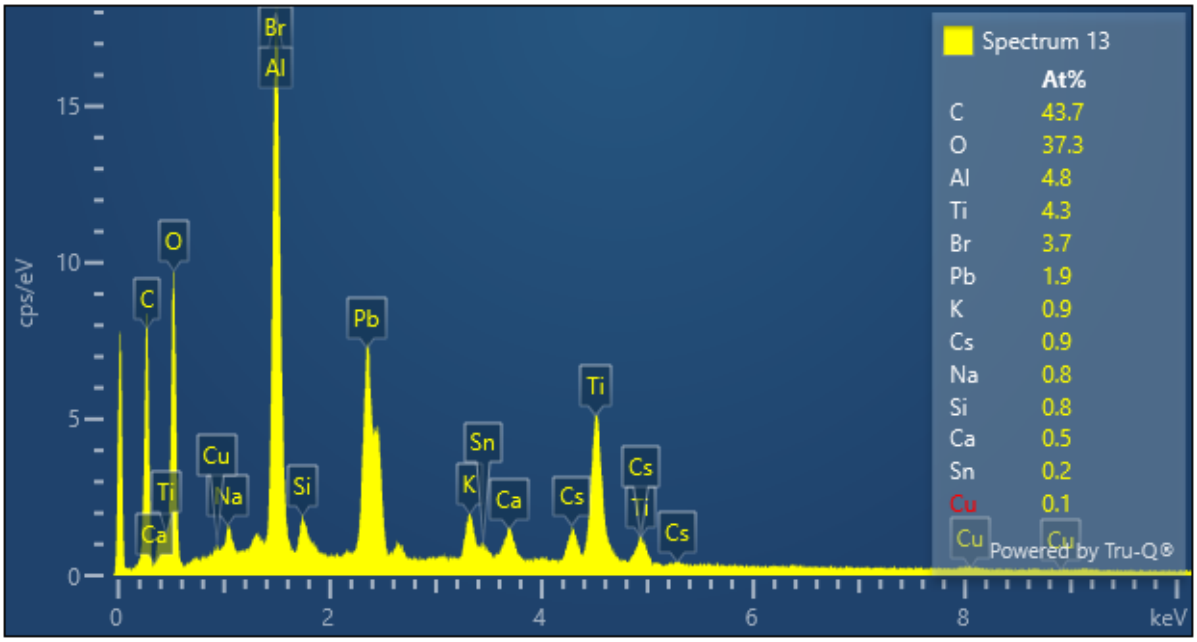

Appendix 1.6: EDX spectrum of the $CsPb_{0.99}Ni_{0.01}Br_3$ thin film cross section.

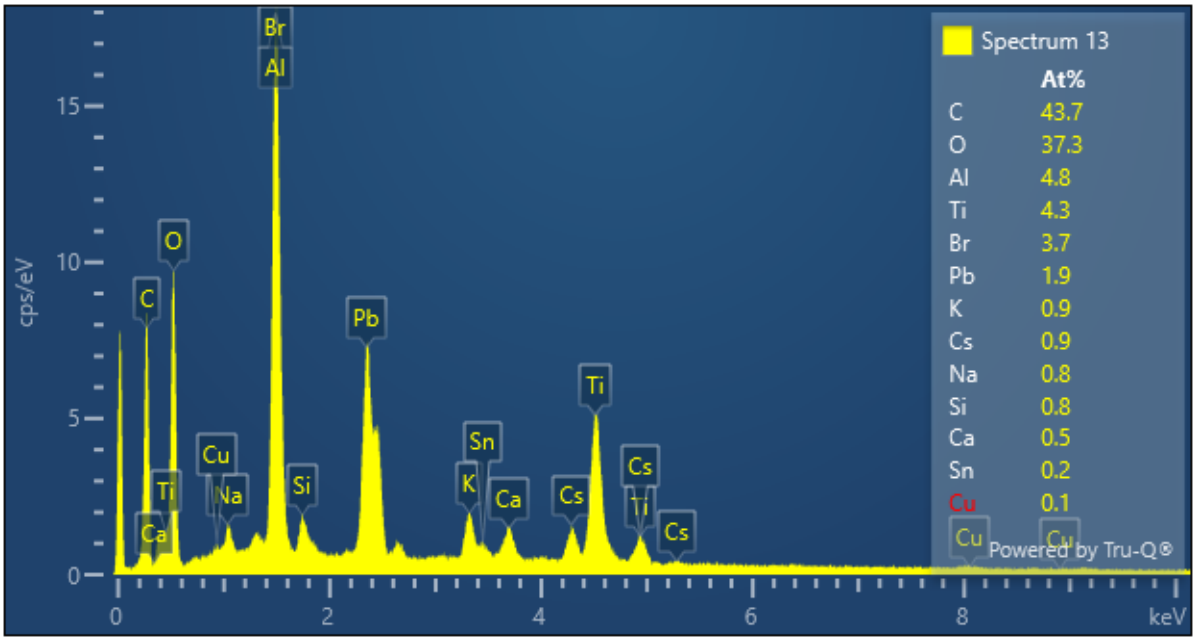

Appendix 1.7: EDX spectrum of the $CsPb_{0.99}Co_{0.01}Br_3$ thin film cross section.

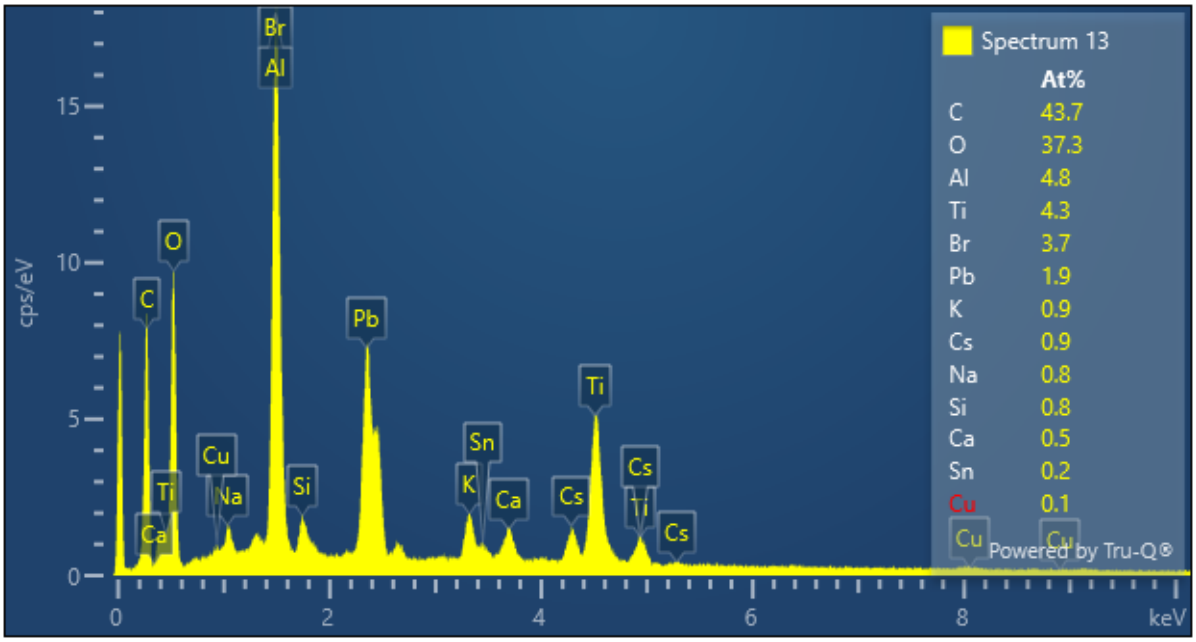

Appendix 1.8: EDX spectrum of the $CsPb_{0.99}Fe_{0.01}Br_3$ thin film cross section.

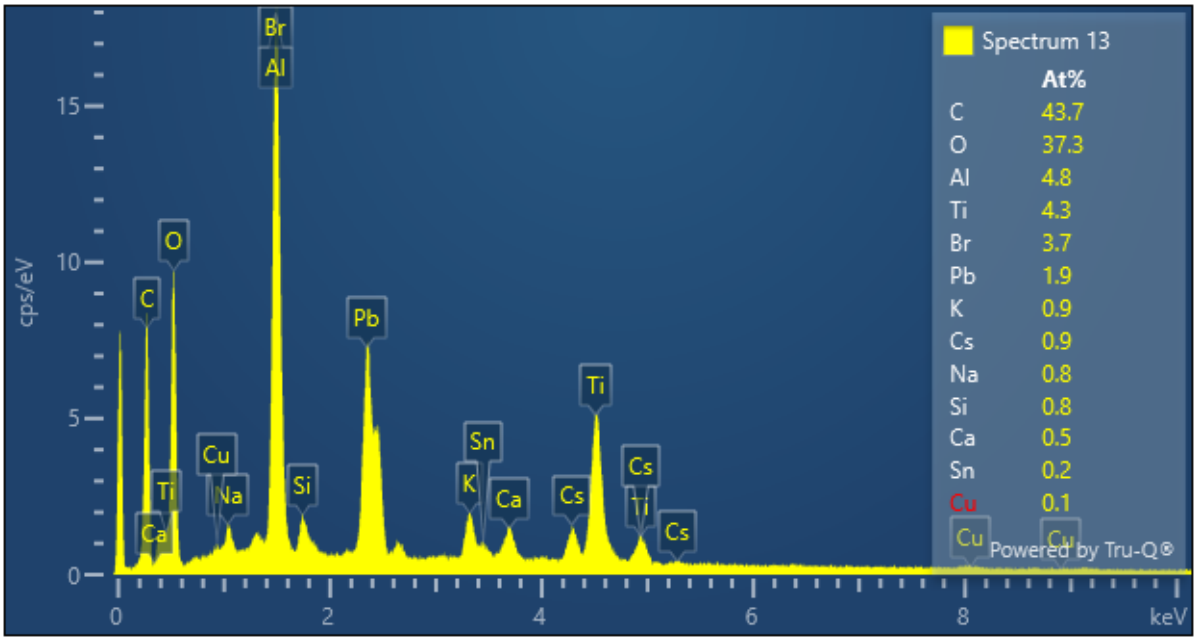

Appendix 1.9: EDX spectrum of the $CsPb_{0.99}Mn_{0.01}Br_3$ thin film cross section.

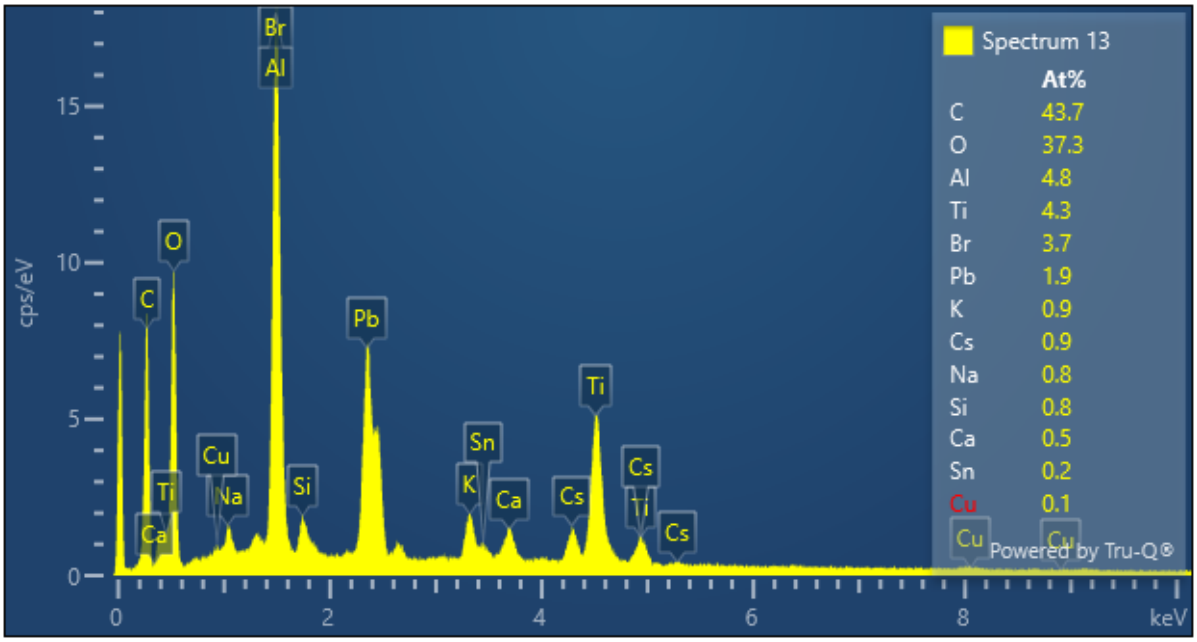

Appendix 1.10: EDX spectrum of the $CsPb_{0.97}Tb_{0.03}Br_3$ thin film cross section.

Appendix 2.

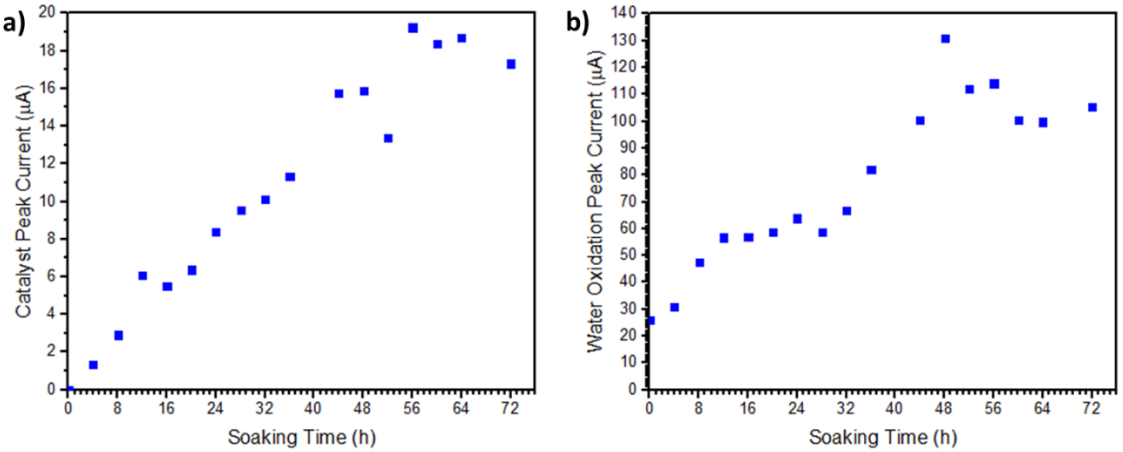

Appendix 2.1: Soaking study repeat. a) anodic peak current for the $Ir^{iii/iv}$ redox couple and b) water oxidation peak current at 1.66 V (VS RHE) after soaking the 1 cm^2 GS in the hom-WOC for 0 – 72 h.

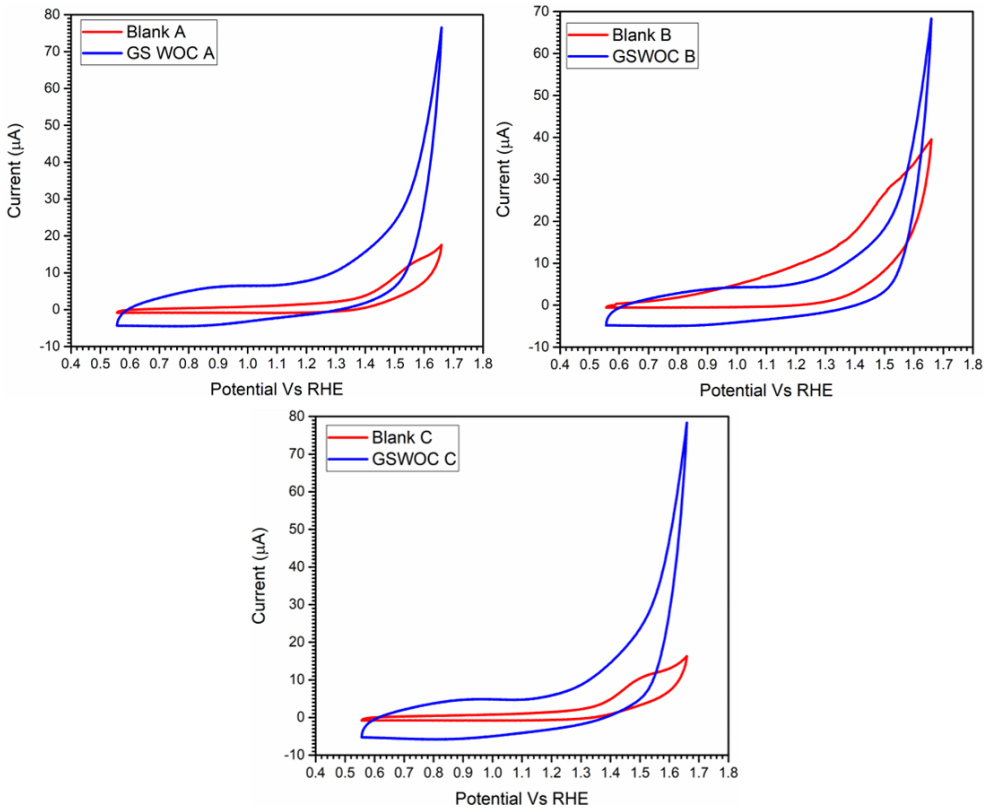

Appendix 2.2: Three CV scan repeats of the 70 µm thickness GS soaked in the Ir-based WOC for 52 h. Measured in 0.1 M KNO_3 at pH 2.5, at a scan rate of 50 mV s^{-1}. 10 scans were run and the 10^{th} scan is shown.

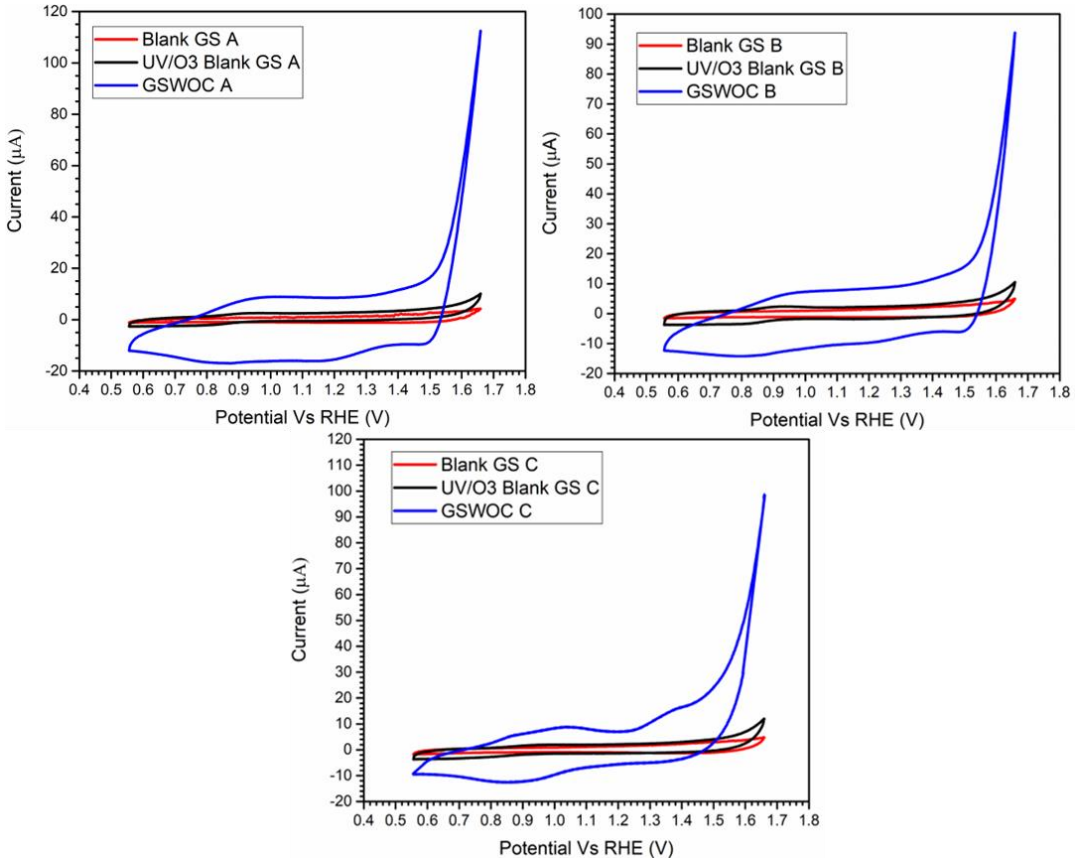

Appendix 2.3: Three CV scan repeats of the 70 µm thickness GS pre-treated with UV/ozone exposure, soaked in the Ir-based WOC for 52 h. Measured in 0.1 M KNO_3 at pH 2.5, at a scan rate of 50 mV s^{-1}. 10 scans were run and the 10^{th} scan is shown.

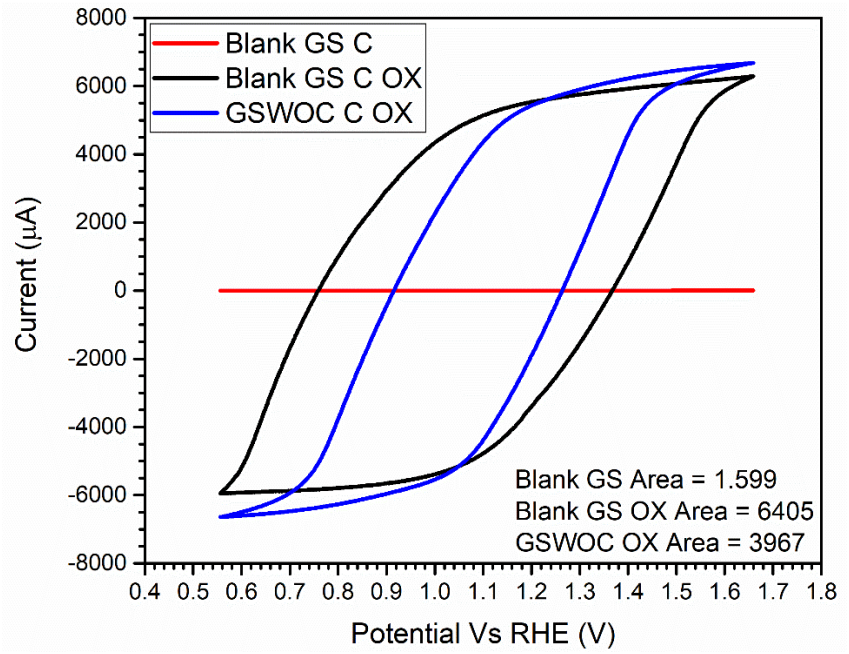

Appendix 2.4: CV of the untreated blank GS (red), CV of the GS electrochemically pre-treated with KH_2PO_4 at 2 V for 40 min (black). CV of the GS electrochemically pre-treated with KH_2PO_4 at 2 V for 40 min, then soaked in the Ir-based WOC for 52 h (blue) Scans measured in 0.1 M KNO_3 at pH 2.5, at a scan rate of 50 mV s^{-1}. 10 scans were run and the 10^{th} scan is shown. The calculated integrated areas under the scans are shown.

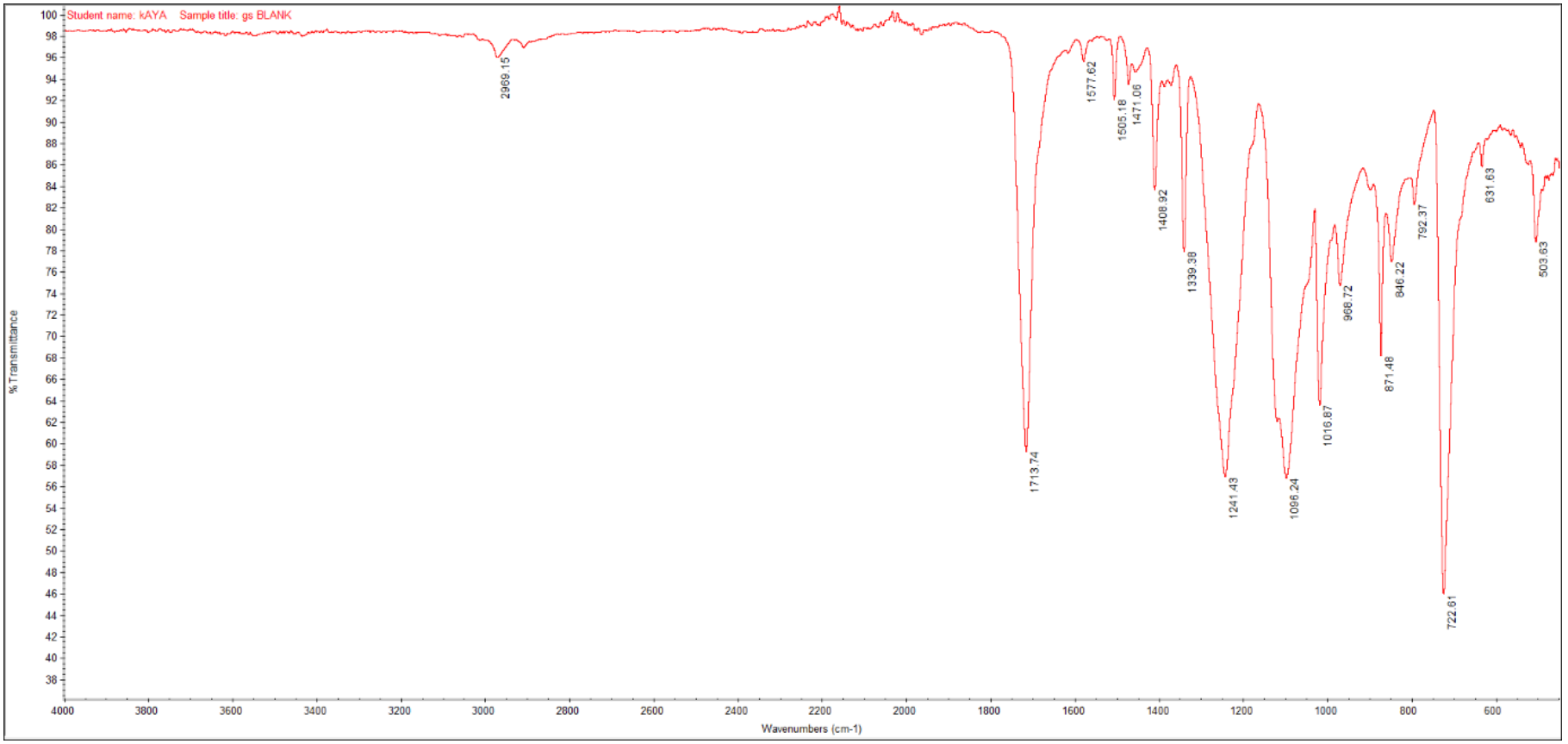

Appendix 2.5: FTIR spectrum of the blank GS

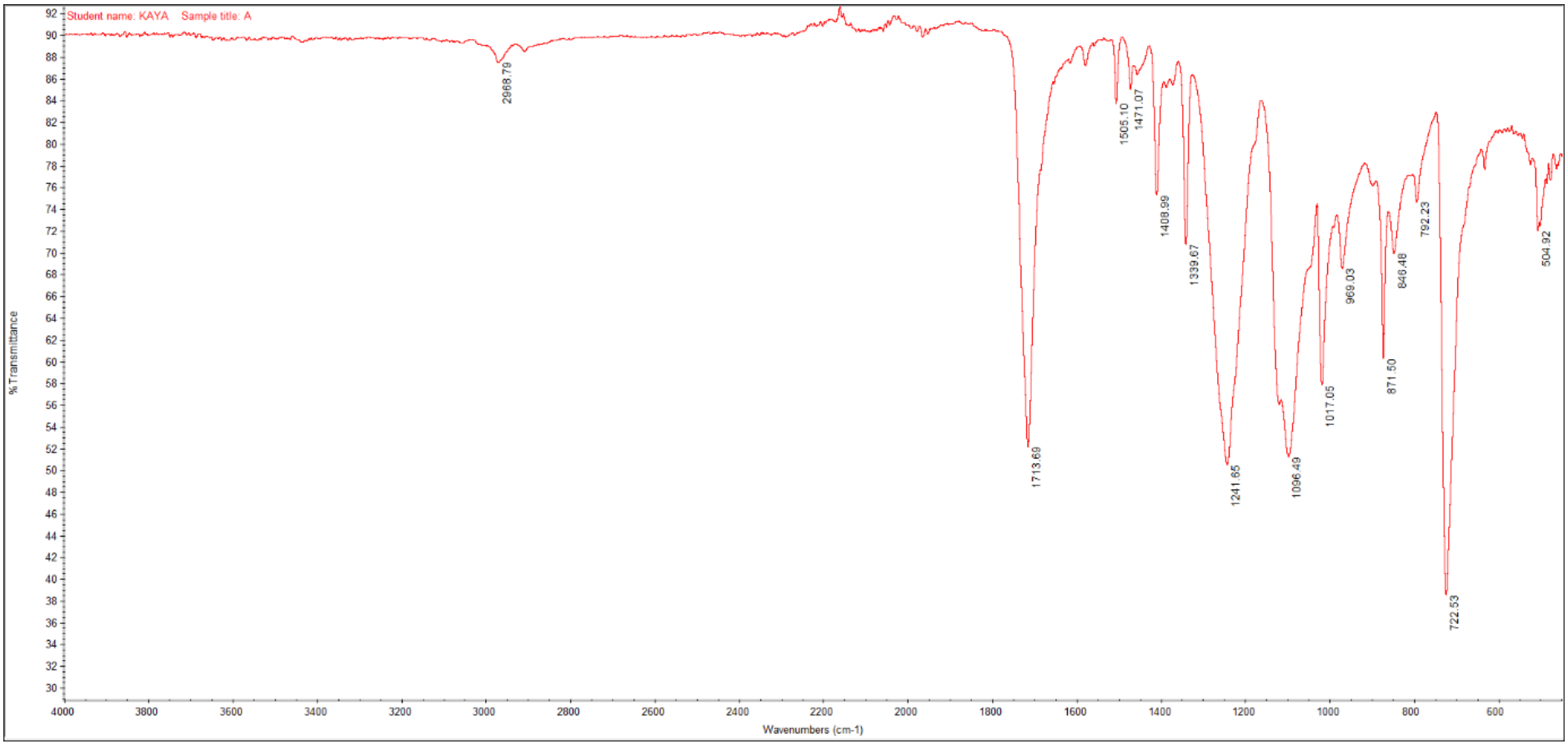

Appendix 2.6: FTIR spectrum of the blank GS after electrochemical treatment at 2 V for 40 min in KH_2PO_4.

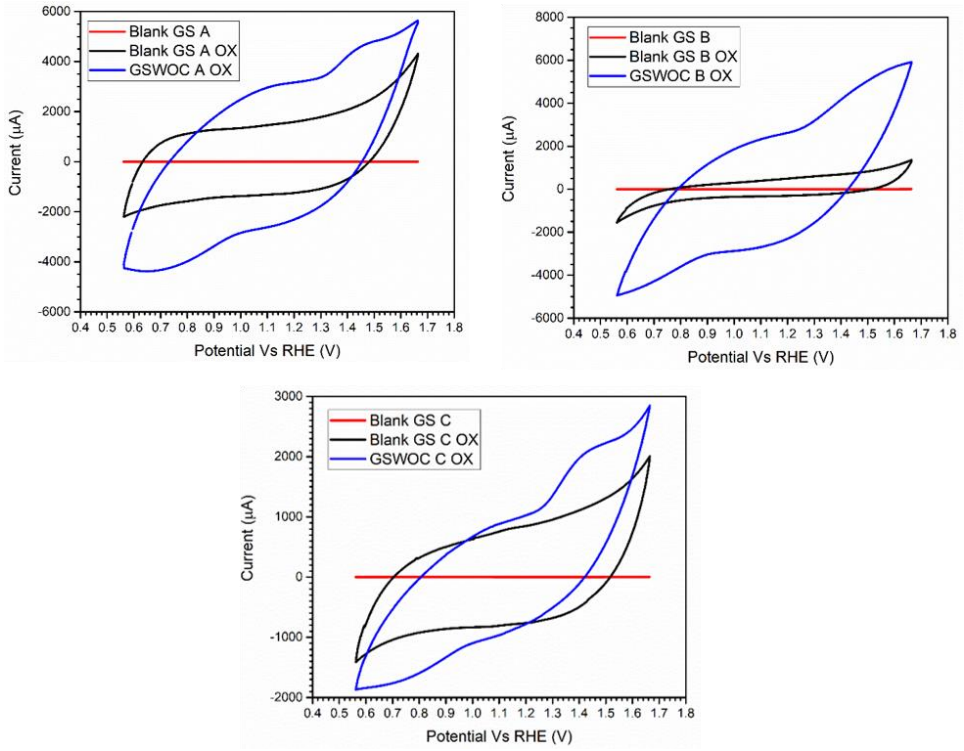

Appendix 2.7: Three CV scan repeats of the 70 µm thickness GS electrochemically treated at 2 V for 40 min in aqueous KH_2PO_4 then soaked in the Ir-based WOC for 52 h. Measured in 0.1 M KNO_3 at pH 2.5, at a scan rate of 50 mV s^{-1}. 10 scans were run and the 10^{th} scan is shown.

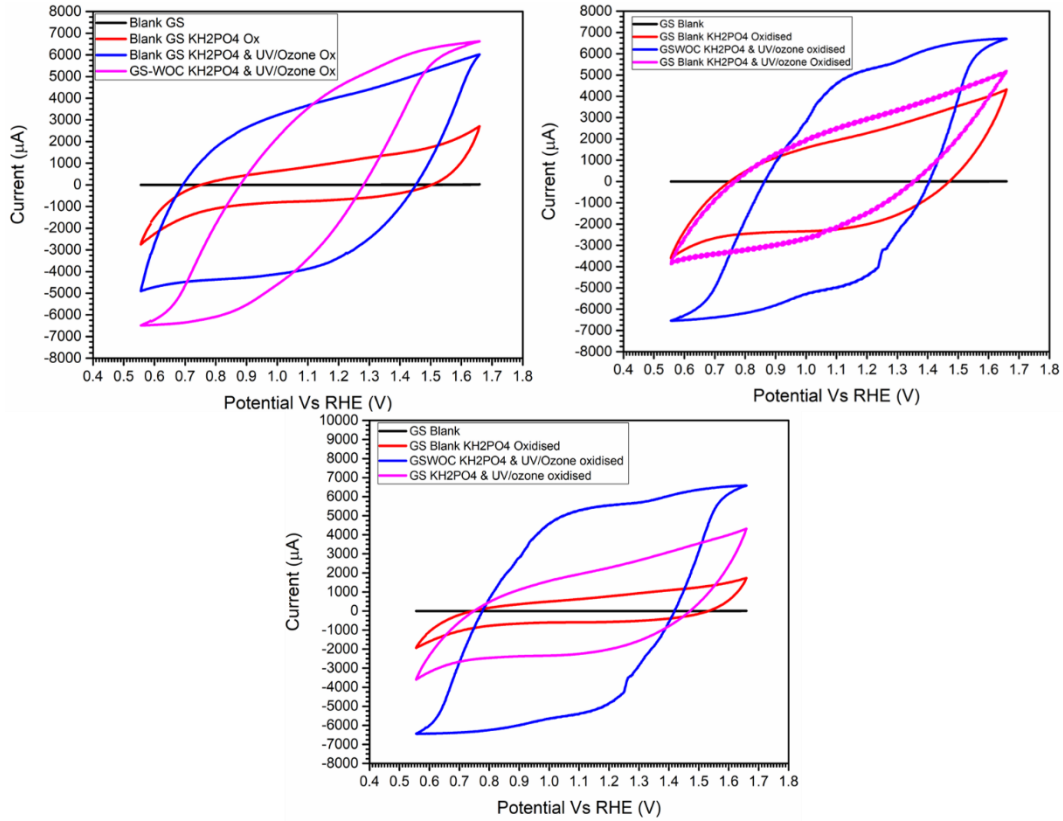

Appendix 2.8: Three CV scan repeats of the 70 µm thickness GS electrochemically treated at 2 V for 40 min in aqueous KH_2PO_4 then placed under a UV/ozone cleaner for 2 h before being soaked in the Ir-based WOC for 52 h. Measured in 0.1 M KNO_3 at pH 2.5, at a scan rate of 50 mV s^{-1}. 10 scans were run and the 10^{th} scan is shown.

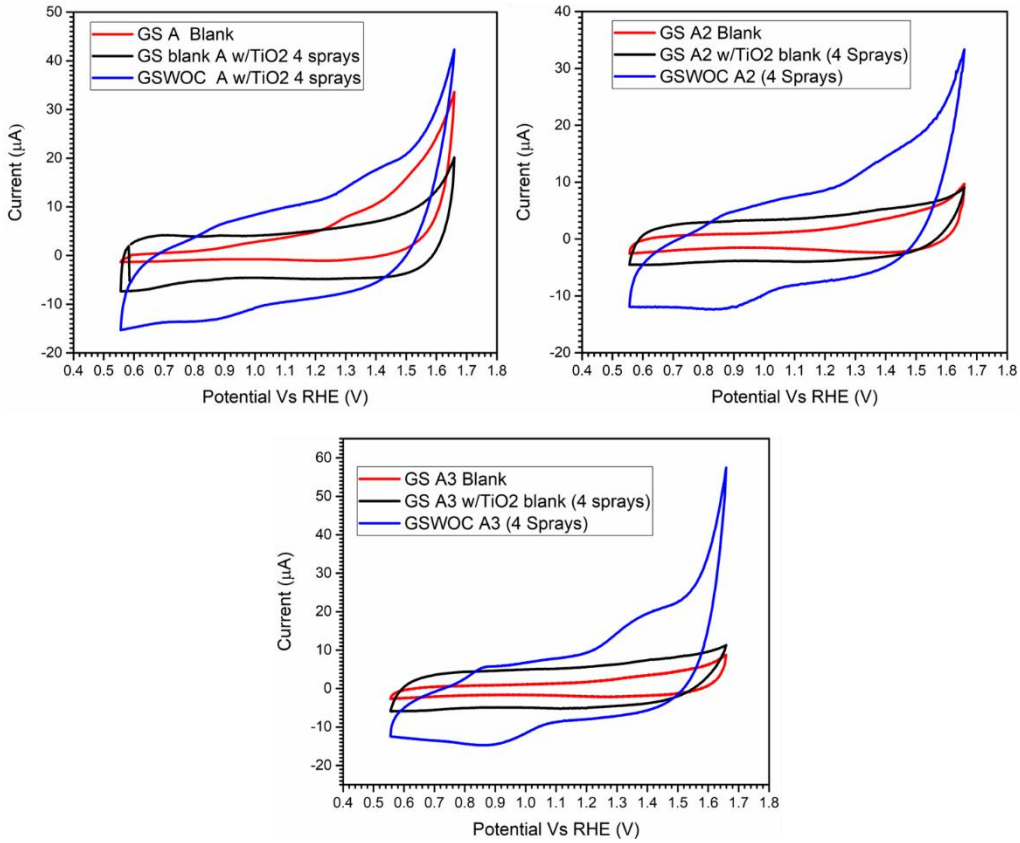

Appendix 2.9: Three CV scan repeats of the 70 µm thickness GS sprayed with TiO_2 precursor solution 4 times before being soaked in the Ir-based WOC for 52 h. Measured in 0.1 M KNO_3 at pH 2.5, at a scan rate of 50 mV s^{-1}. 10 scans were run and the 10^{th} scan is shown.

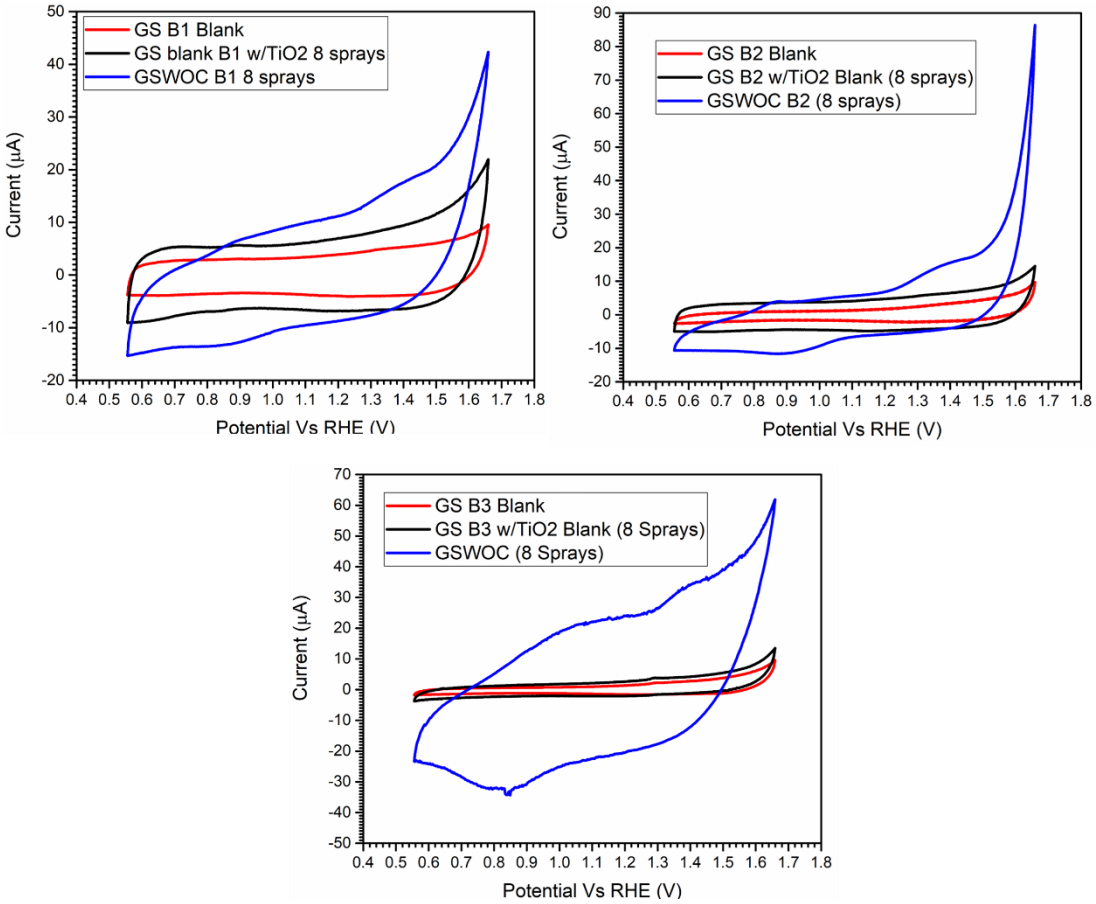

Appendix 2.10: Three CV scan repeats of the 70 µm thickness GS sprayed with TiO_2 precursor solution 8 times before being soaked in the Ir-based WOC for 52 h. Measured in 0.1 M KNO_3 at pH 2.5, at a scan rate of 50 mV s^{-1}. 10 scans were run and the 10^{th} scan is shown.

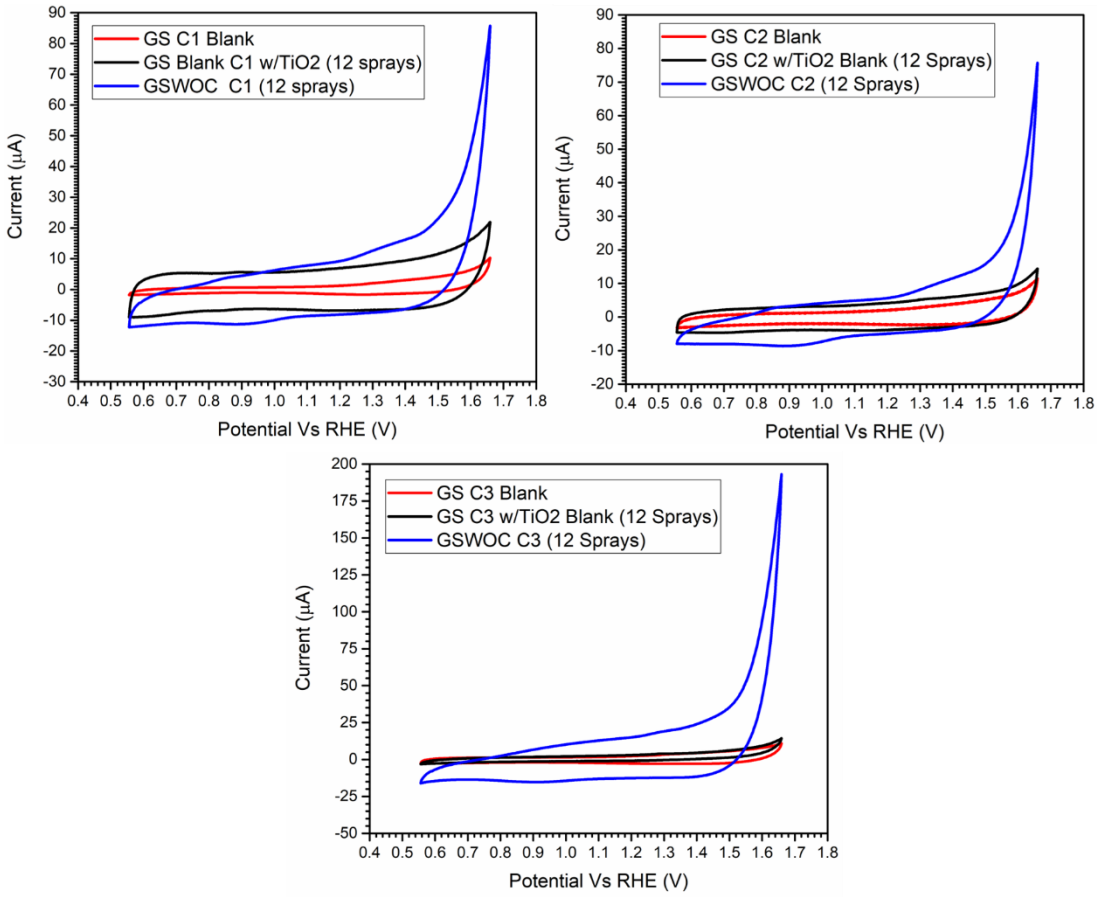

Appendix 2.11: Three CV scan repeats of the 70 µm thickness GS sprayed with TiO_2 precursor solution 12 times before being soaked in the Ir-based WOC for 52 h. Measured in 0.1 M KNO_3 at pH 2.5, at a scan rate of 50 mV s^{-1}. 10 scans were run and the 10^{th} scan is shown.

Appendix 2.12: Failed GS digestion attempt after 6 h under acidic microwave conditions.

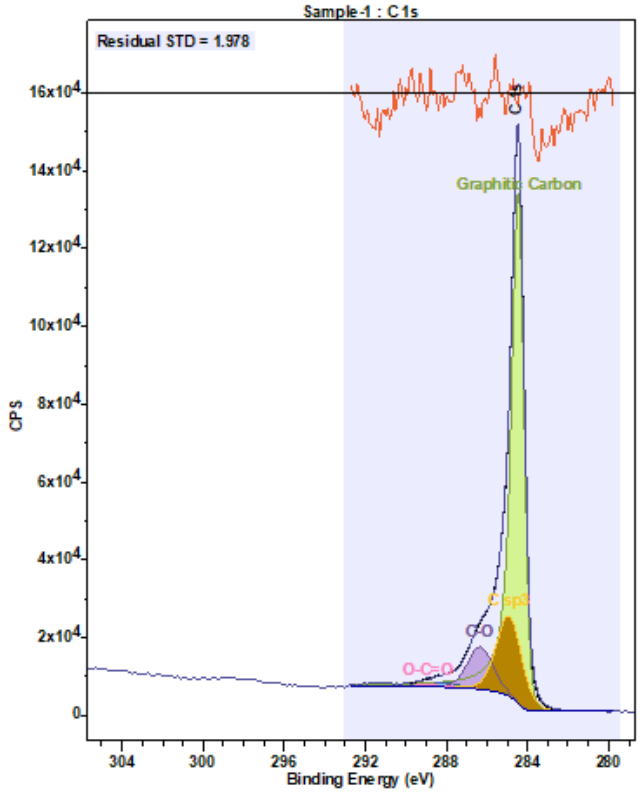

Appendix 2.13: Carbon XPS spectra of the untreated GS-WOC (70 µm.)

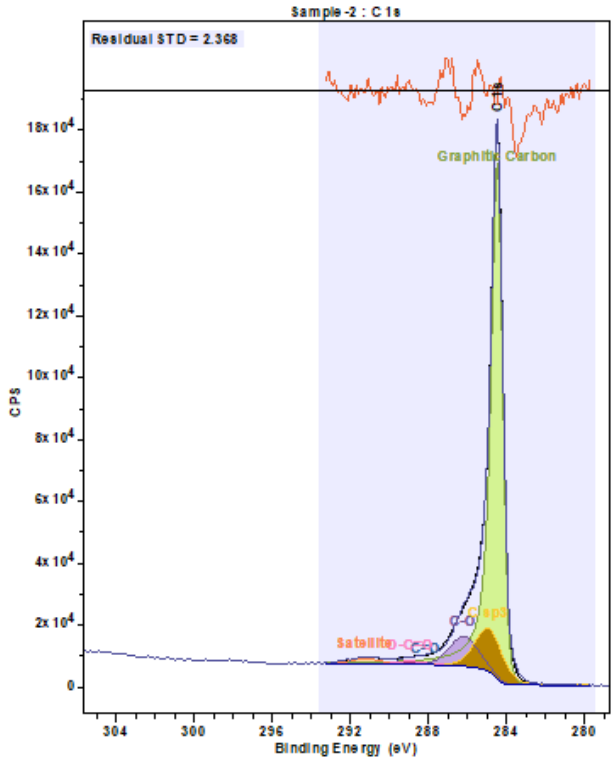

Appendix 2.14: Carbon XPS spectra of the UV/ozone treated GS-WOC (70 µm).

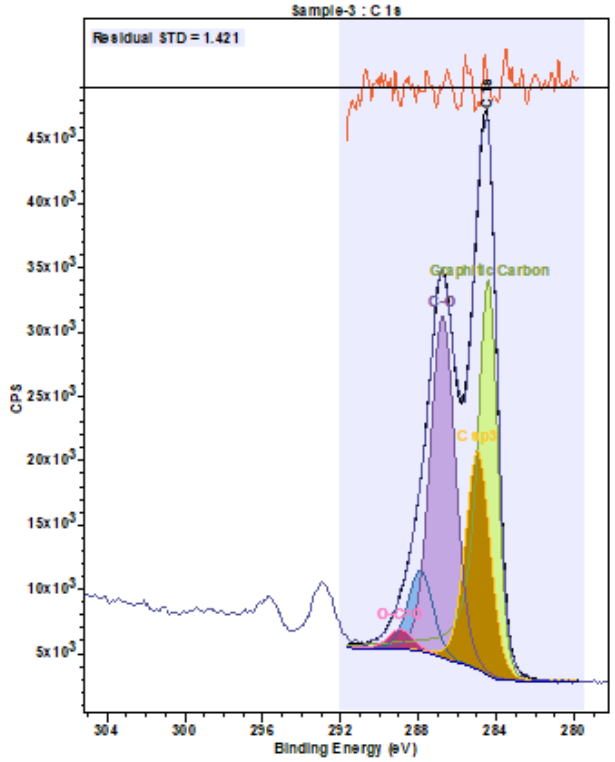

Appendix 2.15: Carbon XPS spectra of the electrochemically treated at 2 V for 40 min in KH_2PO_4 GS-WOC (70 µm).

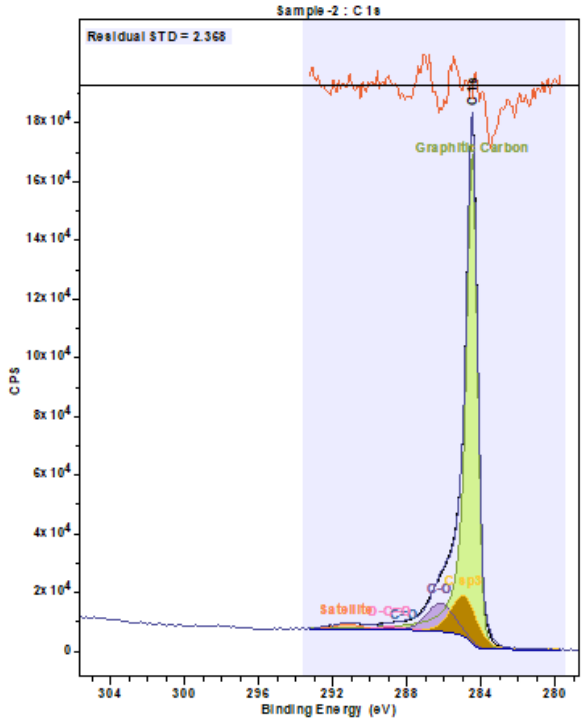

Appendix 2.16: Carbon XPS spectra of the electrochemically treated at 2 V for 40 min in KH_2PO_4 and then exposure to UV/ozone for 2 h, GS-WOC (70 µm).

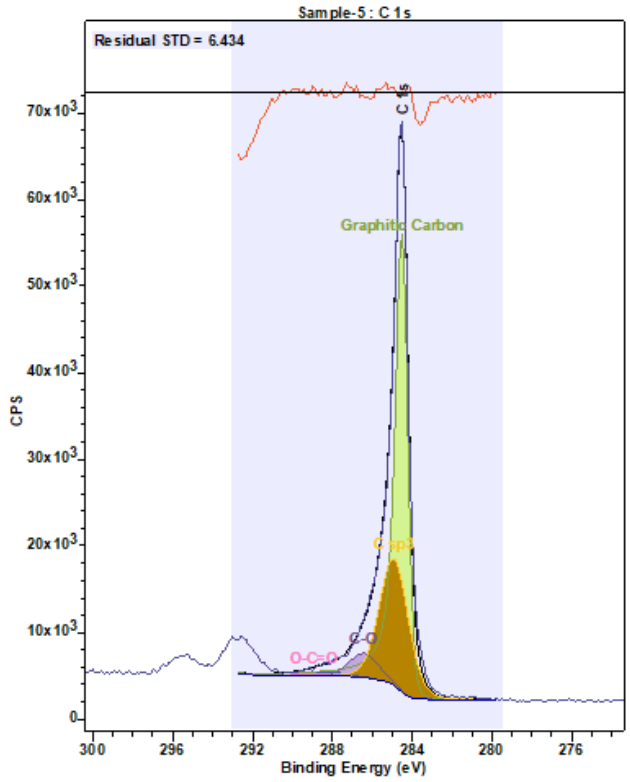

Appendix 2.17: Carbon XPS spectra of the GS-WOC (70 µm) where the GS was sprayed with TiO_2 precursor solution 12 times before the WOC was applied.

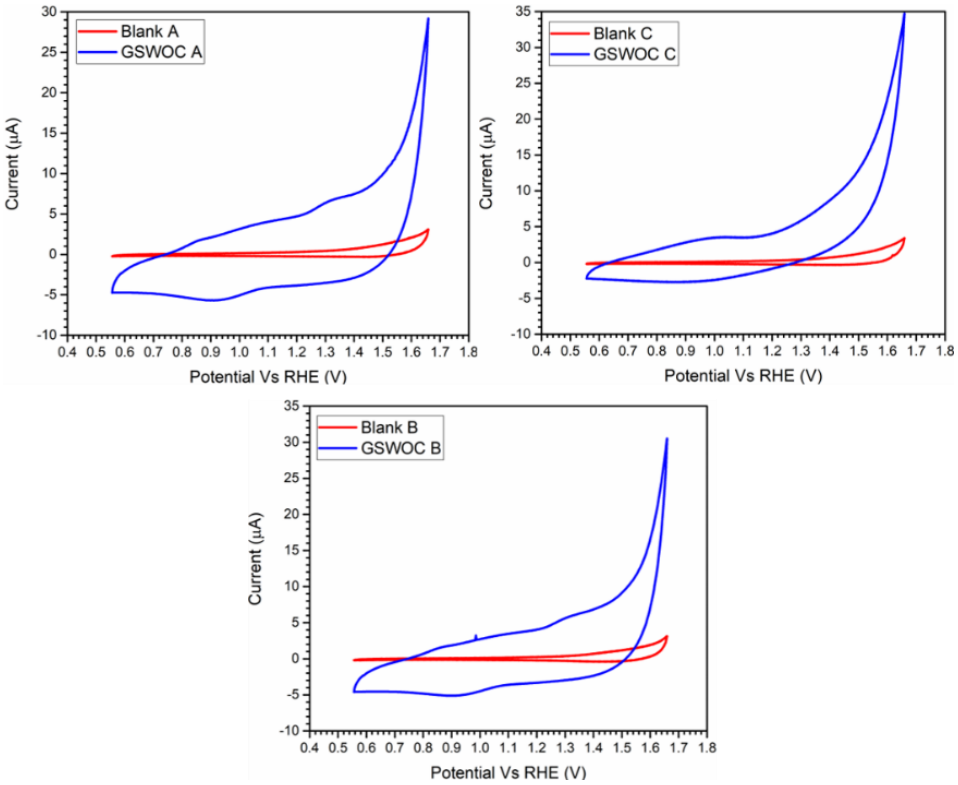

Appendix 2.18: Three CV scan repeats of the 25 µm thickness GS soaked in the Ir-based WOC for 52 h. Measured in 0.1 M KNO_3 at pH 2.5, at a scan rate of 50 mV s^{-1}. 10 scans were run and the 10^{th} scan is shown.

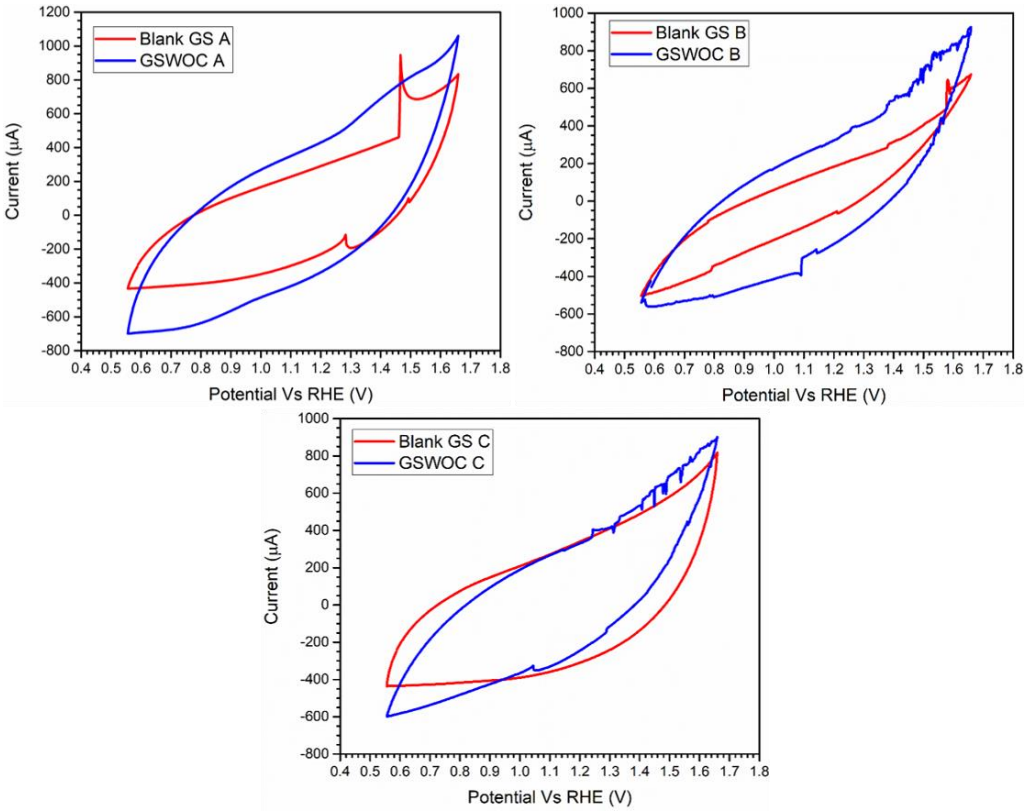

Appendix 2.19: Three CV scan repeats of the 160 µm thickness GS soaked in the Ir-based WOC for 52 h. Measured in 0.1 M KNO_3 at pH 2.5, at a scan rate of 50 mV s^{-1}. 10 scans were run and the 10th scan is shown.

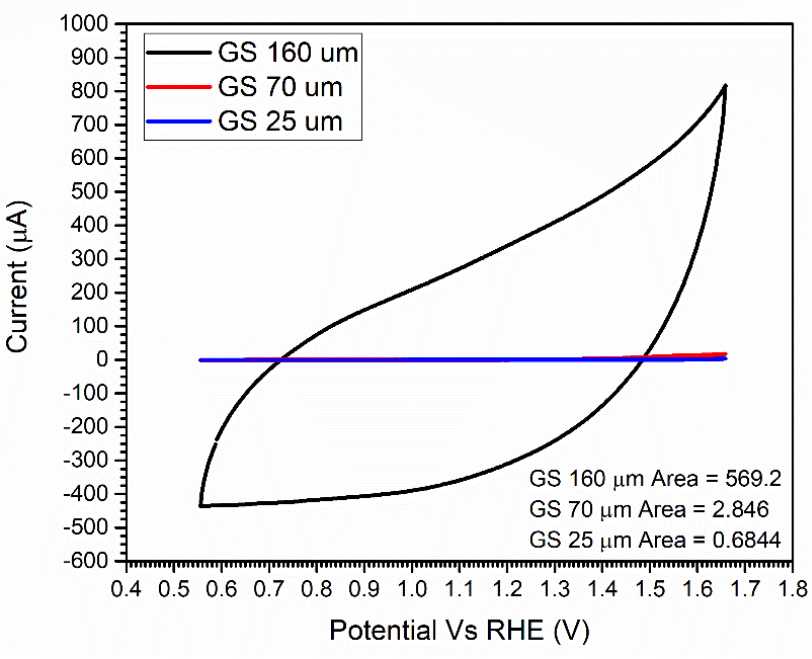

Appendix 2.20: CV of the untreated blank GS 70 µm thickness (red), 25 µm thickness (blue) and 160 µm thicknes (black). Scans measured in 0.1 M KNO_3 at pH 2.5, at a scan rate of 50 mV s^{-1}. 10 scans were run and the 10th scan is shown. The calculated integrated areas under the scans are shown.

Appendix 3.

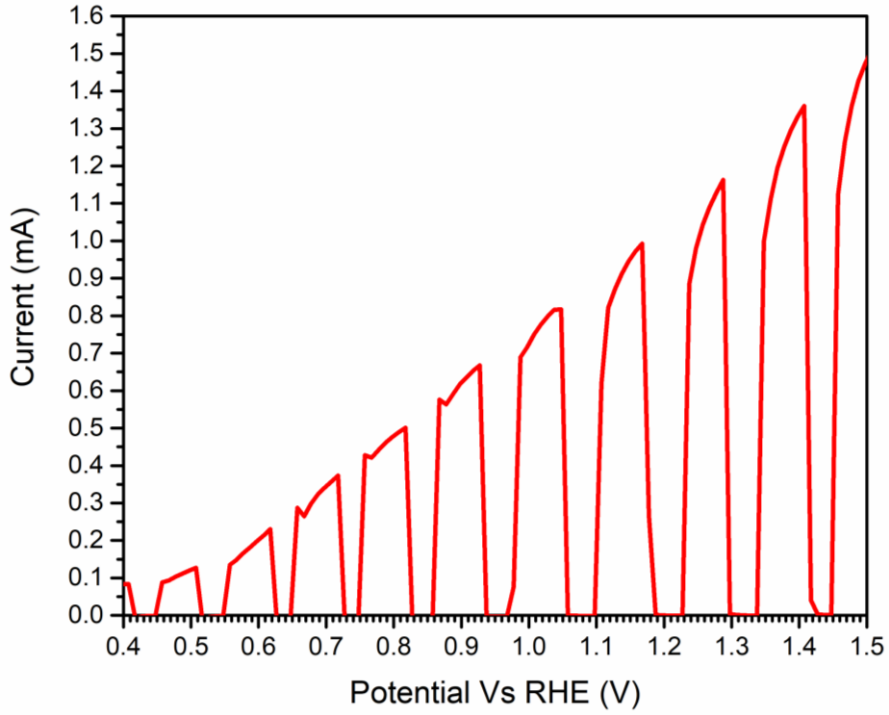

Appendix 3.1: Chopped LSV of the TiO_2|$CsPbBr_3$|Carbon|GSWOC (70 µm thickness GS) in 0.1M KNO_3, pH 2.5, under chopped 1 sun illumination. Scan rate of 50 mv s^{-1}

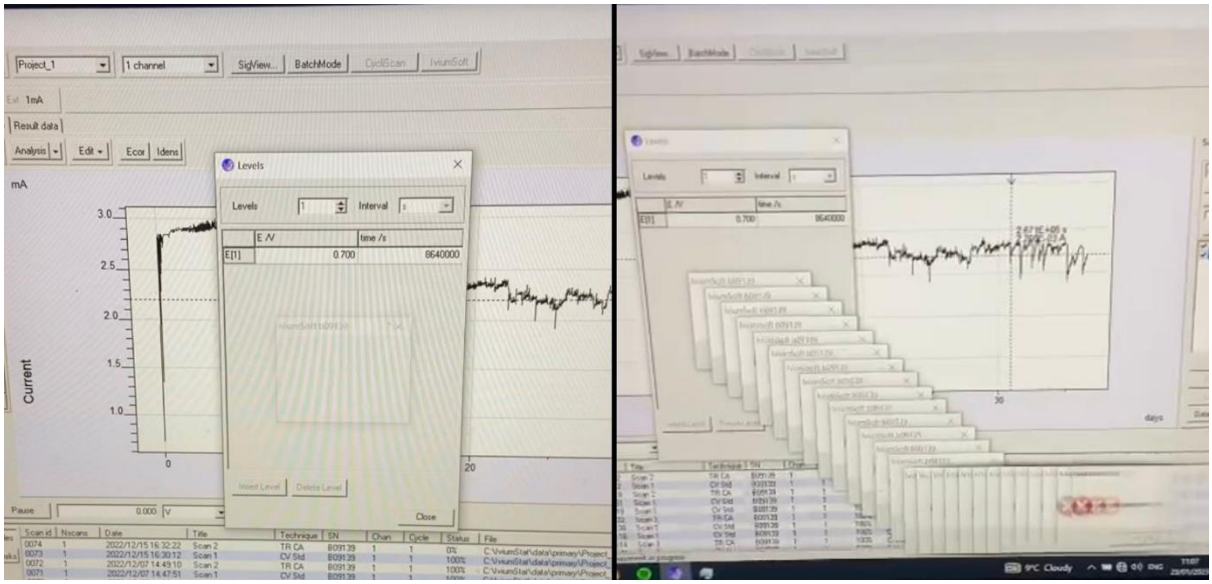

Appendix 3.2: Photographs of the chronoamperometric trace of TiO2/CsPbBr3/m-c/GSWOC (70 µm thickness GS) recorded at an applied potential of 1.06 V (vs RHE), in 0.1M KNO_3, pH 2.5, under continuous 1 sun illumination. Experiment was run for 36 days, however the Ivium software crashed and only the data up to 23 days was recovered. The current remained above 2 mA for the 36 days under operating conditions.

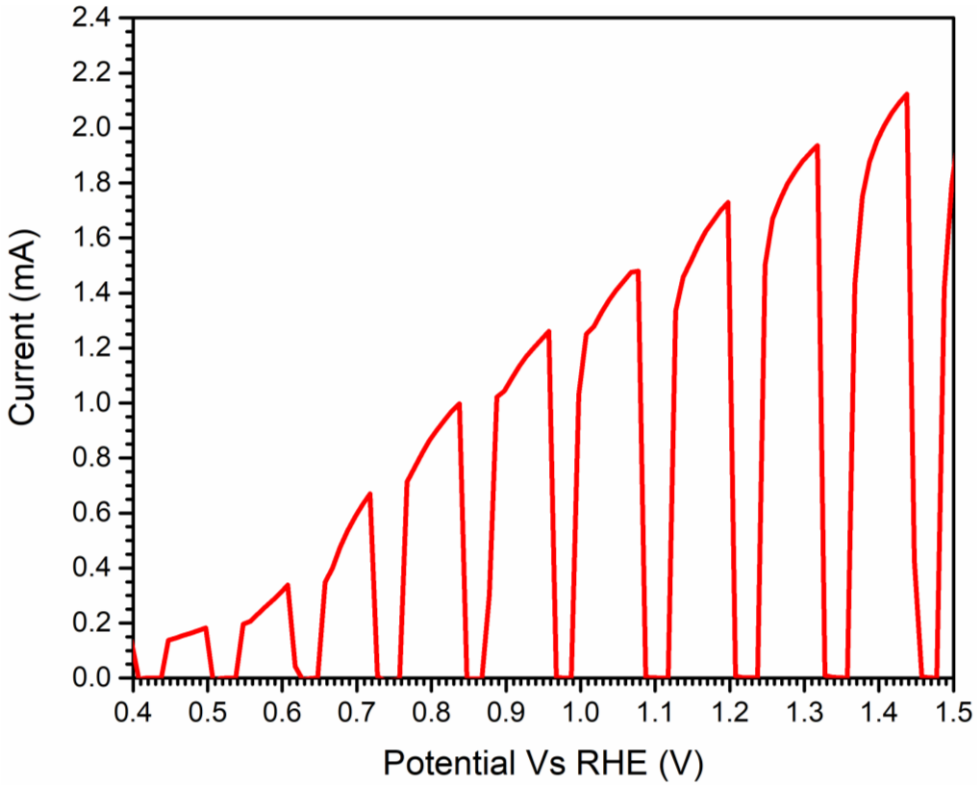

Appendix 3.3: Chopped LSV of the TiO_2|$CsPbBr_3$|Carbon|GSWOC (70 µm thickness GS), with the GS having been pre-treated with UV/ozone, in 0.1M KNO_3, pH 2.5, under chopped 1 sun illumination. Scan rate of 50 mv s^{-1}-